
IDENTIFICATION OF PATTERNS IN LONG-TERM OBSERVATIONS OF THE CLOUDY BOUNDARY LAYER

INAUGURAL-DISSERTATION
zur
Erlangung des Doktorgrades
der Mathematisch-Naturwissenschaftlichen Fakultät
der Universität zu Köln



vorgelegt von
Tobias Marke
aus Frechen

Köln, 2020

BERICHTERSTATTER:

Prof. Dr. Susanne Crewell

Prof. Dr. Clemens Simmer

TAG DER MÜNDLICHEN PRÜFUNG:

07.06.2019

CONTENTS

| | |
|---|------------|
| Abstract | 1 |
| Zusammenfassung | 3 |
| 1 Introduction | 7 |
| 1.1 Motivation | 7 |
| 1.2 Thesis Overview | 11 |
| 1.2.1 Publication I: Boundary layer classification | 12 |
| 1.2.2 Publication II: Low-level jet climatology | 13 |
| 1.2.3 Publication III: Land use induced water vapor patterns | 14 |
| 1.2.4 Publication IV: Statistical retrievals of liquid clouds | 15 |
| 1.2.5 Outline | 16 |
| 1.3 Theory | 16 |
| 1.3.1 Boundary layer wind and turbulence | 16 |
| 1.3.2 Observing atmospheric humidity and cloud properties | 20 |
| 2 Boundary layer classification | 25 |
| 3 Low-level jet climatology | 45 |
| 4 Land use induced water vapor patterns | 63 |
| 5 Statistical Retrievals of Liquid Clouds | 79 |
| 6 Discussion and Outlook | 97 |
| 6.1 Publication I: Boundary-layer classification | 97 |
| 6.2 Publication II: Low-level jet climatology | 99 |
| 6.3 Publication III: Land use induced water vapor patterns | 100 |
| 6.4 Publication IV: Statistical retrievals of liquid clouds | 102 |
| 6.5 Outlook | 104 |
| Literature | 113 |

ABSTRACT

Understanding atmospheric boundary layer (ABL) processes is a key aspect in improving parameterizations in weather forecast and climate prediction models, but also for renewable energy and air quality studies. The ABL, as the lowest part of the atmosphere, can be directly affected by heterogeneities in land surface properties like soil, vegetation and topography, creating patterns at different temporal and spatial scales. In this context, turbulent mixing plays an important role in connecting the atmosphere to the Earth's surface. The turbulent motions are responsible for the thermodynamic structure of the ABL by redistributing heat and moisture and the transport of constituents like aerosols and pollutants away from the surface. These processes are the main drivers for the development of ABL clouds, which in turn feed back to the ABL and surface through interaction with solar radiation, coupling to the large-scale circulation and precipitation formation. This links back to the aim of model improvement, since clouds are one of the largest source of uncertainty in global models. Therefore interdisciplinary research is required to capture the interplay between the different compartments of the Earth.

The *Transregional Collaborative Research Centre 32* (TR32) in its third phase is dedicated to find these patterns in the soil-vegetation-atmosphere system by a monitoring, modelling and data assimilation approach. Within the TR32 project D2 special emphasis is on measuring, modelling and understanding the spatio-temporal structures in land surface-atmosphere exchange at the Jülich ObservatorY for Cloud Evolution (JOYCE). For the typical ABL process scales of seconds to hours and meters to kilometers, ground-based remote sensing observations are well suited to continuously gather comprehensive information on the atmospheric state in a long-term perspective. With additional model simulations the conceptual process understanding can be improved.

This study focuses on the long-term characterisation of the cloudy boundary layer to identify patterns that can be further linked to surface properties at

JOYCE. For this purpose, a classification for characterizing ABL turbulence is developed ([Publication I](#)). The classification, based on Doppler wind lidar (DWL) data, identifies turbulence regions in the ABL and assigns a mixing source using multiple DWL quantities. In this way, convective, wind shear and cloud driven turbulence can be distinguished under most atmospheric conditions. The method is applied at two research sites, showing a distinct behavior for different climate regimes in terms of the diurnal and seasonal cycle of ABL development. In the analysis of the long-term data sets, nocturnal low-level jets (LLJ) are identified as an important source of shear generated mixing. Therefore, a long-term record of LLJ periods, compiled with DWL observations, is investigated in [Publication II](#). The high frequency of occurrence and wind speeds, associated with significant turbulence close to the surface, reveal the relevance of LLJs for wind energy applications. In addition, a strong interaction of the wind field with the surrounding topography can be seen in the DWL measurements, as well as in the results of a high-resolution large-eddy simulation (LES). Also during the day, when the buoyancy production represents the main factor of convective ABL mixing, the interaction between the land surface and the atmosphere is strongly influenced by surface properties. In particular, the local transport of water vapor in moist thermals is a key mechanism for the coupling of clouds to the underlying land surface and a spatially heterogeneous distribution of land use types can lead to patterns in atmospheric water vapor fields ([Publication III](#)). Besides a scanning microwave radiometer (MWR), also satellite and LES data are taken into account, showing a good agreement in identifying the direction of water vapor sources. Convective clouds, that are frequently forming in the ABL due to this convective humidity transport, often contain small amounts of liquid water. These thin liquid water clouds, with a low liquid water path (LWP), are important in terms of their interaction with radiation. In the range of low LWP values, the radiative fluxes are very sensitive to small changes in the amount liquid water contained in the clouds. For a correct representation of the cloud microphysical and optical properties, statistical retrievals using a neural network approach are developed in [Publication IV](#). The retrievals with low computational demand are derived from ground-based observations and make use of the distinct sensitivities in different spectral regimes. While the microwave regime suffers from high uncertainties in low LWP situations, the infrared regime reveals saturation effects for higher LWP. A combination of both spectral regimes yields the best results for the whole range of LWP values.

ZUSAMMENFASSUNG

Verständnis über Prozesse in der atmosphärischen Grenzschicht (ABL) ist ein Schlüsselaspekt für die Verbesserung von Parametrisierungen in Wetter- und Klimavorhersagemodellen, aber auch für Studien über erneuerbare Energien und Luftqualität. Die ABL, als unterster Teil der Atmosphäre, kann direkt von Heterogenitäten in Eigenschaften der Landoberfläche wie Boden, Vegetation und Topografie beeinflusst werden, was Muster auf verschiedenen zeitlichen und räumlichen Skalen erzeugt. In diesem Zusammenhang spielt die turbulente Durchmischung eine wichtige Rolle. Die turbulenten Bewegungen sind für die thermodynamische Struktur der ABL verantwortlich, was durch eine Umverteilung von Wärme, Feuchte und dem Transport von Bestandteilen wie Aerosolen und Schadstoffe von der Erdoberfläche in die Atmosphäre erzeugt wird. Diese Prozesse sind die hauptsächlichen Antriebe für die Entwicklung von ABL-Wolken, die wiederum durch Interaktion mit solarer Strahlung ABL und Landoberfläche beeinflussen und für eine Kopplung an die großskalige Zirkulation und Niederschlagsbildung sorgen. Dies führt auf das Ziel einer Verbesserung der Modelle zurück, da Wolken als eine der größten Quellen für Unsicherheiten in globalen Modellen gelten. Daher ist interdisziplinäre Forschung nötig, um die Wechselwirkungen zwischen den verschiedenen Bestandteilen der Erde zu erfassen.

Das *Transregional Collaborative Research Centre 32* (TR32), in seiner dritten Phase, engagiert sich diese Muster im System Boden-Vegetation-Atmosphäre zu finden, unter Zuhilfenahme von Beobachtungen, Modellierungen und Datenassimilationen. Innerhalb des TR32 Projekts D2 liegt ein besonderer Schwerpunkt auf der Messung, Modellierung und dem Erlangen von Erkenntnissen über zeitliche und räumliche Strukturen des Austausches zwischen Erdoberfläche und Atmosphäre am Jülich ObservatorY for Cloud Evolution (JOYCE). Für die typischen zeitlichen Skalen von Minuten bis Stunden und räumlichen Skalen von Meter bis Kilometer sind bodengebundene Beobachtungen besonders geeignet um kontinuierliche und umfassende Informationen über

den Zustand der Atmosphäre über lange Zeiträume zu erlangen. Mit zusätzlichen Modellsimulationen kann das konzeptionelle Verständnis der Prozesse verbessert werden.

Diese Studie legt den Fokus auf die langzeitliche Charakterisierung der bewölkten ABL zur Identifikation von Mustern, die darüber hinaus mit Eigenschaften der Erdoberfläche in der Umgebung von JOYCE in Verbindung gebracht werden können. Dafür wurde eine Klassifikation zur Charakterisierung der ABL-Turbulenz entwickelt (**Publication I**). Die Klassifikation basiert auf Doppler wind lidar (DWL) Daten, identifiziert turbulente Regionen in der ABL und weist, mit Hilfe von verschiedenen DWL Parametern, eine Quelle der Turbulenz zu. Somit kann die Klassifikation Turbulenz aufgrund von Konvektion, Windscherung und Wolken unterscheiden und unter fast allen atmosphärischen Bedingungen eingesetzt werden. Die Methode wurde an zwei Messstellen angewendet und zeigt ein unterschiedliches Verhalten für verschiedene klimatische Regime bezüglich des Tages- und Jahresgangs der ABL-Entwicklung. In der Analyse der langzeitlichen Daten wurden low-level jets (LLJ) als bedeutsame Quelle für Turbulenz, induziert durch Windscherung, identifiziert. Daher wurde eine Langzeitstudie von LLJ Perioden, detektiert durch DWL Beobachtungen, durchgeführt (**Publication II**). Die hohe Auftrittswahrscheinlichkeit und Windgeschwindigkeit zusammen mit signifikanter Turbulenz nahe der Erdoberfläche machen LLJ relevant für den Windenergiesektor. Zusätzlich ist eine Interaktion des Windfeldes mit der umgebenden Topografie in DWL Messungen und hoch aufgelösten large-eddy Simulationen (LES) zu sehen. Auch am Tag, wenn die Auftriebskraft den größten Anteil an der konvektiven ABL-Durchmischung ausmacht, sind Interaktionen zwischen der Landoberfläche und Atmosphäre stark durch Eigenschaften der Landoberfläche beeinflusst. Insbesondere der lokale Transport von Wasserdampf in feuchter Thermik ist ein wichtiger Faktor für die Kopplung von Wolken mit der Landoberfläche und räumlich heterogene Verteilungen von Landnutzungstypen können zu Mustern im Wasserdampffeld führen (**Publication III**). Neben eines Mikrowellenradiometer (MWR), werden auch Satellitendaten und LES eingesetzt und zeigen gute Übereinstimmungen bei der Detektion von Quellen des Wasserdampfs. Konvektive Wolken, die sich häufig durch diesen konvektiven Feuchtetransport in der ABL bilden, enthalten oft nur geringe Mengen an Flüssigwasser. Diese dünnen Flüssigwasserwolken, mit einem geringen Flüssigwasserpfad (LWP), sind wichtig in Bezug auf die Interaktion mit Strahlung. Im Bereich von geringen LWP Werten sind die Strahlungsflüsse sehr sensitiv zu kleinen Änderungen im Flüssigwassergehalt der Wolken. Um eine korrekte Darstellung der

mikrophysikalischen und optischen Eigenschaften der Wolken in Klimamodellen zu gewährleisten, werden statistische Retrieval mittels eines neuronalen Netzwerkes in **Publication IV** entwickelt. Diese Retrieval mit geringem Rechenaufwand werden durch bodengebundene Beobachtungen abgeleitet und machen sich verschiedene Sensitivitäten in unterschiedlichen Spektralbereichen zu Nutze. Während der Mikrowellenbereich unter hohen Unsicherheiten in Situationen mit geringem LWP leidet, zeigt der Infrarotbereich Sättigungseffekte für hohe LWP Werte. Eine Kombination beider Spektralbereiche liefert somit die besten Resultate für den gesamten LWP-Bereich.

1 INTRODUCTION

1.1 Motivation

The importance and motivation to study the boundary layer can be summarized by a statement in [Stull \(2012\)](#):

"That we live our lives within the boundary layer makes it a subject that touches us, and allows us to touch it."

The atmospheric boundary layer (ABL)¹ can be defined as the part of the troposphere that is directly influenced by the presence of the Earth's surface, with extents ranging from hundreds of meters up to a few kilometers. Relevant timescales for mid-latitude continental ABL processes are within an hour and reveal a strong diurnal cycle. During the course of a day, variations in the vertical distribution of heat, moisture and wind including turbulence can be observed, causing distinct stages of ABL development, as shown in [Figure 1.1](#). In disregard of low pressure frontal systems, the ABL can be primarily partitioned into a surface layer, a daytime mixed layer and a stable/residual layer occurring during the night. The bottom 10% of the ABL is called the surface layer, where mechanical generation of turbulence is dominant ([Stull, 2012](#)). The nighttime ABL is often characterized by a stable surface layer with shear generated turbulence aloft generated from an wind speed enhancement called low-level jet (LLJ). During the day, buoyant production increases due to the surface heating and surface driven convection represents the dominant source of mixing and is responsible for the formation of clouds at the top of the mixed layer. As the input of solar energy decreases shortly before sunset, turbulent motions decay in a sporadic and intermittent way in the residual layer. Pollutants, originating from the surface that were dispersed into the ABL due to the turbulent eddies at daytime, can remain in the residual layer. The different stages of ABL development are

¹also called planetary boundary layer (PBL)

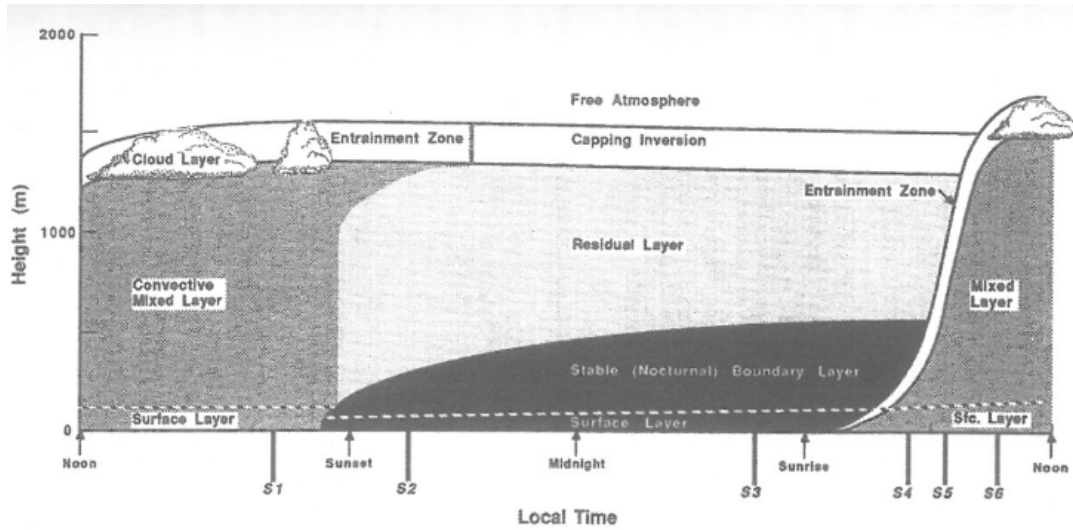


FIGURE 1.1: Schematic diurnal cycle of ABL development in fair weather (high pressure) situations (Stull, 2012).

not individual processes, but can be seen as a linked system. For instance in dry conditions, the surface evaporation as well as the latent heat flux is low and sensible heat flux is high, giving a deep ABL with less clouds during the day. This results in a strong stable layer at night due to increased surface cooling. But also a deep residual layer is formed, leading together with a high sensible heat flux to a fast mixed layer growth after sunrise (Betts, 2009).

Apart from the emission of pollutants, also other land surface-atmosphere interactions exist that depend on the properties of the soil, vegetation and topography. These interaction processes include surface fluxes of heat, moisture and momentum into the atmosphere and the modification of the wind flow by the terrain. Coupling processes and related feedback mechanisms are crucial to understand, as they are a key drivers for the weather and climate system and can not be regarded as independent components.

ABL clouds are one of the components showing, among water vapor, the strongest climate feedback and are known to be one of the largest source of uncertainty in general circulation models (GCMs) due to their radiative feedback (e.g. Bony et al., 2006; Webb et al., 2006). The transient clouds are usually on a subgrid-scale and can produce large errors in GCM and NWP models depending on the implemented parameterization (Stephens, 2005). Betts (2004) shows that accurate modeling of the climate and climate change over land critically depends on cloud coupling and states that there are strong daily feedback mechanisms between clouds, the surface energy budget and the partitioning between sensible and latent heat. Spatial variations in surface properties can influence ABL cloud formation (Rabin et al., 1990) and

in turn surface fluxes are affected by the cloud feedback through interaction with radiation (Freedman et al., 2001). In relation to clouds and the hydrological cycle also the moisture supply from the surface through evapotranspiration can be influenced by the land surface-atmosphere coupling (Heerwaarden et al., 2010) and convective precipitation is connected to the soil moisture distribution (Schär et al., 1999; Guo et al., 2006).

Not only convective processes, but also stably stratified conditions during night, responsible for the formation of fog and LLJs, are problematic in GCMs (Holtlag et al., 2013) leading to uncertainties in climate predictions (McNider et al., 2012). Critical aspects of the model spread are the representation of ABL turbulence, convective clouds and cloud microphysics that can not be resolved explicitly on a global scale for long time periods and need to be parameterized in GCMs (e.g. McFarlane, 2011). This complex system of parameterizations is leading to unrealistic cloud processes in current GCMs and therefore an uncertain estimate of the cloud response to climate change (IPCC, 2013). Also in numerical weather prediction (NWP) models and a more local scale, the implemented ABL parameterization scheme can significantly affect forecasts of winds and clouds with implications for the renewable energy sector (e.g. Storm et al., 2009; Perez et al., 2010; Muñoz-Esparza et al., 2012; Draxl et al., 2014; Krogsæter and Reuder, 2015) and for the society through severe weather events like thunderstorms (Cohen et al., 2015), tornadoes (Stensrud and Weiss, 2002), or flash floods (Zampieri et al., 2005).

In the past there have been numerous attempts to evaluate ABL parameterization schemes by comparing model output to observations in various climate regimes, mostly based on short-term field campaigns (e.g. Beesley et al., 2000; Betts, 2002; Hu et al., 2010). Often only near surface quantities are used for evaluation, resulting in a general undersampling and lack of continuous monitoring of the full ABL column and its diurnal cycle (Santanello et al., 2018). To study detailed feedback processes in the land surface-atmosphere system, also a coupling of the atmospheric model to a land surface model (LSM) and even the groundwater flow, as in Shrestha et al. (2014), is required. To evaluate the performance of the coupled models, the sensitivity of the model to the LSM needs to be considered and compared to observations. This is often achieved with case study analyses of specific events (Santanello et al., 2009; Santanello et al., 2011; Santanello et al., 2013; Milovac et al., 2016). In addition, several comprehensive short-term field campaigns were conducted to improve the process understanding of land surface-atmosphere interactions using a suite of ground-based remote sensing instrumentation and their synergies (Weckwerth et al., 2004; Beyrich et al., 2006; Wulfmeyer et al., 2011;

Späth et al., 2016; Macke et al., 2017; Wulfmeyer et al., 2018).

Also large-eddy simulation (LES) modeling is a valuable tool to study and evaluate land surface-atmosphere interactions and to foster the development of parameterizations in weather and climate models. Due to the high spatial resolutions of the models the three-dimensional atmospheric turbulence, by means of large eddies that are the main contributors to ABL transfer motions, can directly be resolved (Moeng, 1984). With the coupling to LSM, also the influence of surface heterogeneity can be assessed. One critical aspect in coupled LES modeling is the impact of surface heterogeneity scaling on the ABL structure (e.g. Patton et al., 2005; Courault et al., 2007; Brunzell et al., 2011). In addition, also the feedback mechanisms between the land surface and the ABL are studied. Bertoldi et al. (2007) and Huang and Margulis (2010) found feedbacks of the surface sensible heat flux and the variability of air temperature, which acts opposing to the wind speed and with differences for bare soil and vegetated areas. The partitioning in sensible and latent heat can result in related atmospheric patterns close to the surface, but also in higher altitudes (Shao et al., 2013). Furthermore, the soil moisture and evapotranspiration difference for various vegetation types can have a significant influence on ABL characteristics and cloud formation (Heerwaarden and Arellano, 2008; Vilà-Guerau de Arellano et al., 2014). Because of the complexity of widely used LES models and the incorporation of statistical relations, tests of the simulation results are needed and it is highly desirable to evaluate LES or prove conjectures arising from LES with observations (Stevens and Lenschow, 2001).

Ground-based remote sensing is very useful to sample the ABL over long time periods, but statistical model comparisons using multiyear data like in Sengupta et al. (2004), or even systematic evaluation approaches of ABL types in a weather forecast model (Harvey et al., 2015) are still sparse. In the study of Harvey et al. (2015) a method to diagnose boundary-layer types is used that demonstrates the potential for an objective classification of the cloudy ABL using Doppler wind lidar (DWL) observations (Harvey et al., 2013). With DWL, vertical profiles of the horizontal wind speed (Päschke et al., 2015) and higher-order moments of the vertical wind can be provided with high temporal resolution at many vertical levels, making it valuable for turbulence estimates in the ABL (Hogan et al., 2009; O'Connor et al., 2010). Therefore, DWL measurements are also widely used to assess turbulent LLJ characteristics (Banta et al., 2002; Bonin et al., 2015). The occurrence in low altitudes together with high wind speeds and strong intermittent turbulent motions, that are associated with LLJs, are strong impact factors for wind

energy applications (Emeis et al., 2007; Peña et al., 2016; Zhou and Chow, 2012). LLJs can also transport humidity and aerosols, leading to the formation of clouds and modified precipitation patterns (Higgins et al., 1997; Hu et al., 2010). During the day, surface driven convection is an important factor for the transport of water vapor into the ABL and is strongly influenced by surface characteristics. Spatiotemporal variations in the ABL water vapour field can be related to the land cover type as well as the topography and are important for ABL cloud formation (Adler et al., 2016; Späth et al., 2016). In these studies, ground-based remote sensing systems are deployed, which are favorable in observing these low clouds. Due to their complex interaction with radiation and feedback mechanisms to surface fluxes, the cloud microphysical and optical properties need to be determined accurately. The cloud fields are often broken and consist of optical thin clouds with a typical lifetime of minutes to hours, making accurate observations challenging (Turner et al., 2007b). Promising improvements in retrieving cloud properties were made by combining widely used microwave radiometer measurements with the infrared spectral regime (Turner, 2007). In this way, radiative transfer modeling can be improved, which is critical for GCMs (e.g. Cess et al., 1996).

1.2 Thesis Overview

To address the issue of lacking long-term observations in the cloudy ABL, the motivation here is to provide tools and in-depth observational and modeling studies for important ABL features, including land surface-atmosphere interactions. It is intended to strengthen the process understanding that eventually guides towards improvements in weather and climate models in the future. This is achieved within the *Transregional Collaborative Research Centre 32* (TR32), incorporating the Universities of Aachen, Bonn and Cologne and the Research Centre Jülich, bringing together disciplines like geography, hydrology, meteorology and mathematics. In the third phase of this interdisciplinary project the overall goal is to find spatial and temporal patterns of the soil-vegetation-atmosphere system using innovative monitoring, modelling and data assimilation approaches across different scales. The TR32 research group D2 is focusing on the identification and quantification of these interaction processes and patterns on the basis of novel and state-of-the-art remote sensing instruments. The majority of the study is conducted at the Jülich Observatory for Cloud Evolution-Central Facility (JOYCE-CF) described in Löhnert et al. (2015). In the framework of TR32 the following topics, depicted in Figure 1.2, are addressed in this thesis: (1) characterizing turbulence

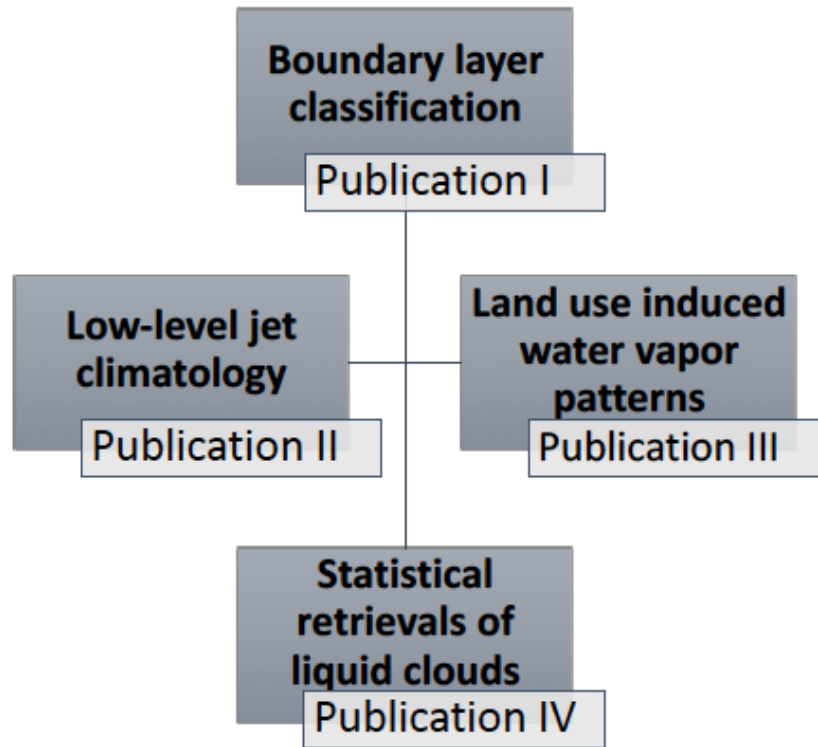


FIGURE 1.2: Overview of the thesis including all publications.

in the cloudy ABL using DWL measurements (**Publication I**), (2) investigating a long-term record of LLJs together with the simulated and observed interactions of the wind field with the topography (**Publication II**), (3) detecting atmospheric water vapor patterns in relation to the land use (**Publication III**) and (4) derivation of synergistic statistical retrievals for thin liquid water clouds (**Publication IV**). The outline of the thesis together with a brief overview and the interconnections of the publications is provided in the next sections.

1.2.1 Publication I: Boundary layer classification

In **Manninen et al. (2018)** (**Publication I**) an ABL classification using DWL data is developed. The method identifies turbulent parts of the ABL and objectively assigns a source of turbulent mixing. Besides surface driven convective mixing during the day also other sources, such as cloud and wind shear driven turbulence, can be distinguished. In addition, ABL clouds and the height of the ABL² are detected. The ABL classification builds upon the study of **Harvey et al. (2013)** that already showed to be valuable in terms of

²defined as the maximum height with a reliable aerosol signal

evaluating boundary layer types in a weather forecast model (Harvey et al., 2015). The bit field design of the classification, with a decision tree containing thresholds for the different DWL quantities, allows for a future implementation at different sites. Also a combination with additional instruments is possible to make use of their synergy and to complement and improve the classification, but also the knowledge on ABL development for evaluating ABL parameterizations.

The classification is based on the Halo Photonics Streamline DWL (Pearson et al., 2009) with 1.5 μm wavelength and 30 m vertical resolution, which is sensitive to the presence of aerosols and cloud droplets. As a first step the data processing method by Manninen et al. (2016) is implemented, leading to an increase in data availability by accounting for background signal artefacts especially in areas with low amounts of aerosol loading. With this background correction, reliable uncertainty estimates can be obtained, which is required in turbulent calculations.

Vertical profiles of Doppler velocity and attenuated backscatter are measured with 1 s integration time. With the hemispheric scanning capability also horizontal wind profiles can be derived. As input for the classification, profiles of attenuated backscatter, turbulent kinetic energy dissipation rate (O'Connor et al., 2010), derived from the vertical velocity standard deviation, vector wind shear and vertical velocity skewness are needed at a chosen temporal resolution of 3 min. Combining vertical velocity skewness and standard deviation as a measure of turbulence already showed to be useful to determine whether the turbulence is surface or cloud driven (Hogan et al., 2009).

The ability of the method to detect surface and cloud driven turbulence, as well as the coupling to surface, is demonstrated in two case studies. The classification is then applied to observations at two sites in different climatic regimes for over one year. The analysis of the long-term data set showed seasonal differences in the diurnal cycle of the identified types at the mid-latitude site JOYCE and a high-latitude site. At both sites enhanced nocturnal mixing due to wind shear was found and is potentially connected to the presence of LLJs. The ABL classification incorporates the same LLJ detection algorithm as in Publication II and the classification is used to identify turbulent regions and to extract further ABL characteristics in Publication III.

1.2.2 Publication II: Low-level jet climatology

For a better characterization of the turbulent properties of LLJs at JOYCE found in Publication I, a long-term LLJ analysis is conducted in Marke et

al. (2018) (Publication II). LLJ development is generally characterized by an increase of wind speed over a decoupled stable surface layer after Blackadar (1957). These jets play an important role with respect to the renewable energy sector and the production of wind energy. Therefore it is crucial to gain statistical knowledge on the occurrence, development and strength of the jets, but also the location of critical turbulence for wind turbines.

In order to detect LLJs, the algorithm developed in Tuononen et al. (2017), using a relative and absolute threshold in horizontal wind profiles, is applied to over four years of DWL data and is the same as in Publication I. In this study, the advantage of having long-term and continuous data samples at JOYCE is exploited. Supplementary observations of wind speed from the meteorological tower help to complement the DWL measurements below the first reliable height and the assessment of surface fluxes is useful for proving the concept of LLJ development, but also to study the influence of intermittent turbulence penetrating the stable surface layer.

Apart from the LLJ climatology, interactions of the wind field with the local topography are analyzed as a further objective in Publication II. Since DWL observations deliver mostly column information, an evaluation of the three-dimensional wind field using LES is desirable. LES modeling is valuable regarding the ability to scale the topography in different simulations for looking at sensitivities of the wind field to these perturbations. In a case study during a field campaign additional instrumentation like radiosondes are utilized to analyze the performance of the model for a LLJ situation. The model findings also feed back to a better interpretation of the long-term DWL measurements.

1.2.3 Publication III: Land use induced water vapor patterns

During nighttime, interactions of the wind field with the topography was demonstrated in Publication II. Also the study of Su et al. (2016) showed the importance of nocturnal LLJs, which can be responsible for cloud development. Likewise in daytime situations, when surface driven convection is strong, land surface properties are an important controlling factor for interaction processes. In Marke et al. (2020) (Publication III) the convective exchange of water vapor from the surface into the ABL is investigated at JOYCE. For this purpose, spatial information on the water vapor distribution is needed. The scanning microwave radiometer (MWR) as a passive

instrument is frequently used to retrieve humidity related quantities like integrated water vapor (IWV) or liquid water path (LWP) and already showed the ability to obtain spatial IWV gradients (Schween et al., 2011).

In this comprehensive study the spatial patterns in IWV from long-term scans of a MWR are connected to detailed knowledge on the land use around JOYCE. To distinguish local and large scale effects, but also to have independent estimates of the IWV distribution, satellite and reanalysis data are added to the analysis. Similar to Publication II, high-resolution LES shows to be beneficial for the process understanding, especially by altering the land use in the model input. In this way the effects of the land surface properties on surface fluxes and the transport of humidity into the ABL is evident. The resulting implications for ABL cloud formation are also addressed.

1.2.4 Publication IV: Statistical retrievals of liquid clouds

The liquid water clouds, found in Publication III, that formed under the influence of the land surface show characteristic features of convective ABL clouds. The clouds typically contain low amounts of liquid water (LWP below 100 g m^{-2})³ and are very frequent in most climate regimes (Turner et al., 2007a). Moreover radiative fluxes are especially sensitive to variations in cloud liquid water for these thin clouds, leading to large errors in radiative transfer calculations with implications for GCMs (e.g. Sengupta et al., 2003). Therefore an accurate determination of cloud microphysical and optical properties, like LWP and effective radius, is necessary and challenging at the same time (Turner et al., 2007b).

With different wavelengths also the interaction of atmospheric constituents with radiation changes. This can be utilized by combining spectrally diverse observations to determine the optimal frequency and instrument configuration. In Turner (2007) a synergy of the microwave and infrared spectral regime showed improvements compared to using a single spectral band. However, the retrieval derivation was done by a rather complex physical approach requiring prior knowledge on the atmospheric vertical structure for example from radiosondes. Thus, the study by Marke et al. (2016) (Publication IV) is evaluating the single instrument and synergistic retrieval accuracy for a computational less demanding statistical approach of neural network retrievals. With a data sample of single layer liquid water clouds, infrared and microwave observations are simulated to derive LWP and effective radius retrievals. First, the accuracy of the retrievals is assessed in

³referred to as thin clouds

a synthetic study before applying them to real measurements in a radiative closure study.

1.2.5 Outline

The thesis is constructed in the following way: The key theoretical aspects, covering the most important methods of this study, are given in [section 1.3](#). Following this, the previously introduced publications are presented. First, the *Boundary layer classification* as a tool to characterize turbulence is shown in [chapter 2](#). Then, [chapter 3](#) contains the *Low-level jet climatology* with the additional investigation of the interactions of the wind field with the local topography. This is followed by the second land surface-atmosphere interaction study *Land use induced water vapor patterns* in [chapter 4](#) covering the day-time convective exchange and liquid water cloud formation. For this type of cloud, the last study demonstrates the derivation of *Statistical retrievals of liquid clouds* in [chapter 5](#). Finally the results of the studies are discussed in [chapter 6](#) together with an outlook.

1.3 Theory

In the following, basic theory regarding the publications is presented. First, the principles of retrieving boundary layer wind and turbulence are shown. Then, techniques to observe atmospheric humidity and cloud properties are discussed.

1.3.1 Boundary layer wind and turbulence

Profile measurements of boundary layer wind from a ground-based perspective have a long history. Compared to in-situ and airborne observations, the full diurnal cycle can be captured vertically resolved and continuously. Frequently used techniques like sodar wind profiler are limited in the vertical extent ([Beyrich, 1997](#)) and radar wind profiler suffer from interference, ground clutter and can not obtain reliable results in the lowest few hundred meters ([Ecklund et al., 1988](#)). Meteorological towers and tethered balloons are also not able to retrieve the full ABL wind profile. Therefore, DWL as an optical remote sensing system is preferable for long-term operation and monitoring of ABL wind development. In addition, the small systems are portable and easy to deploy ([Pearson et al., 2009](#)).

According to [Weitkamp \(2005\)](#), the general lidar equation describing a single scattered return signal $P(R, \lambda)$ can be written as:

$$P(R, \lambda) = P_0 \frac{ct}{2} A \eta \frac{O(R)}{R^2} \beta(R, \lambda) \exp\left[-2 \int_0^R \alpha(r, \lambda) dr\right] \quad (1.1)$$

From the equation the quadratic decrease of the signal intensity with distance R is evident. The overlap function $O(R)$ is composed of geometric factors and describes the fraction of the laser beam that is imaged on the detector. Apart from instrument specific parameters like the average power of a laser pulse (P_0), pulse duration (t), area of receiver optics (A) and system efficiency (η), the backscatter term $\beta(R, \lambda)$ determines atmospheric contributions to the signal strength for the wavelength λ . It depends on the concentration of scattering material in the observed volume and the differential scattering cross section for the backward direction. Similar the transmission term $\exp[-2 \int_0^R \alpha(r, \lambda) dr]$, accounting for the extinction loss from the lidar to the particles and back, depends on the concentration and the extinction cross section.

Doppler lidar⁴ systems emit laser pulses at $1.5 \mu\text{m}$ (near-infrared). At this wavelength the radiation is scattered at aerosol and cloud particles (Mie scattering) and is less effected by molecular scattering. This also implies that this technique relies on a sufficient amount of aerosol contained in the atmosphere. On the other hand the signal is saturated by optically thick liquid water clouds. The part of the elastic backscattered signal that is detected at the telescope is compared to a local optical oscillator (LO) with a known frequency f_{LO} to determine the magnitude and sign of the frequency shift (heterodyne detection):

$$f_{LO} \pm (f_0 + \Delta f) \quad (1.2)$$

The frequency shift Δf , referring to the movement of the scattering particle, is known as the Doppler effect and can be inferred from a Fourier transform analysis ([Rye and Hardesty, 1993a](#); [Rye and Hardesty, 1993b](#)). With estimates of Δf , the radial velocities v_r can be calculated according to:

$$v_r = \frac{\lambda \Delta f}{2} \quad (1.3)$$

These DWL instruments operate with a high pulse repetition frequency (15 kHz) and an averaging time of usually 1 s for one beam to reduce speckle.

⁴here specifications of the *HALO Photonics* Streamline Doppler lidar available at JOYCE are described

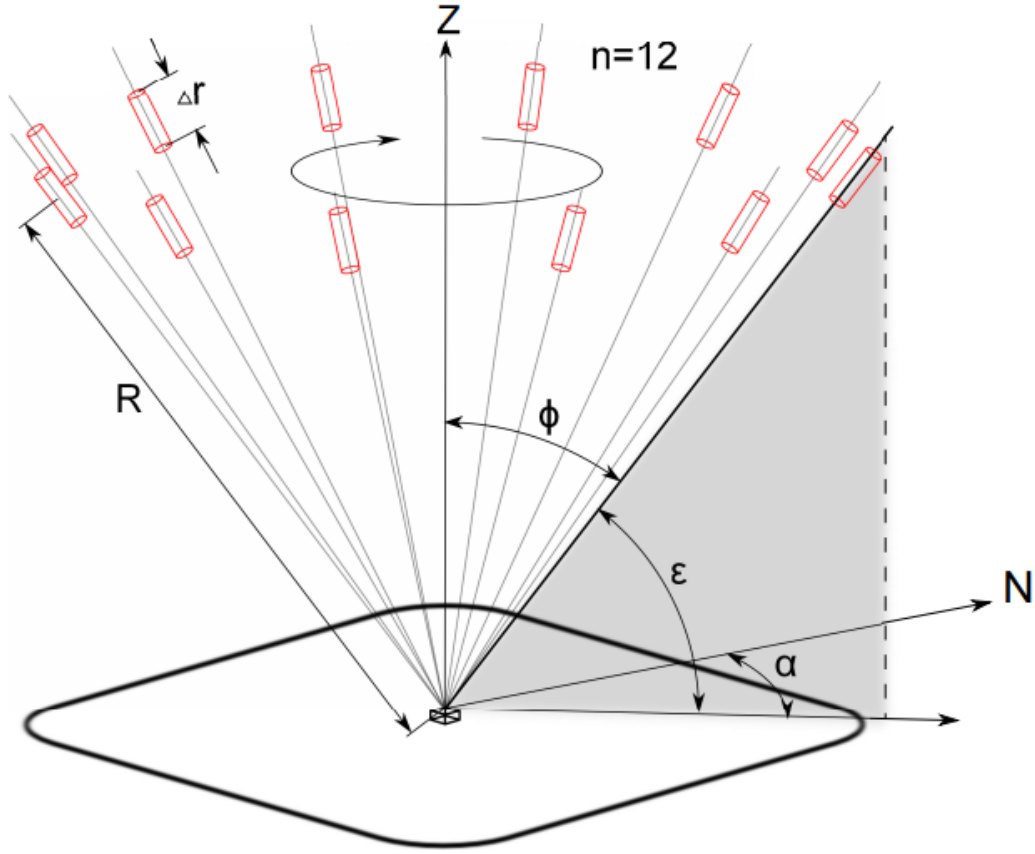


FIGURE 1.3: Schematic of a VAD scan with 12 beams (Päschke et al., 2015). The angle α corresponds to θ in the text.

With $\Delta R = ct/2$ from Equation 1.1 and c being the speed of light, a pulse duration t of 150 ns would result in a 22.5 m effective pulse length and the range resolution is determined from a range weighting function (Frehlich and Yadlowsky, 1994).

With the information of the radial wind component, the vertical wind can be directly estimated when pointing zenith. Due to the scanning capability of the DWL, also profiles of the horizontal wind vector can be derived with the assumption of a horizontal homogeneous wind field across the measurement volume. One of the methods to derive horizontal winds is the velocity-azimuth display (VAD) technique, which shows a better goodness-of-fit compared to the also widely used Doppler Beam Swinging (DBS) technique (Weitkamp, 2005). The VAD scan technique is the main method used to derive horizontal wind speed profiles in Publication I, Publication II and Publication III. VAD scans are composed of conical scans over the full azimuth angle θ at a fixed zenith angle ϕ with several beams (Figure 1.3). If the assumption of a homogeneous atmosphere during the scan is fulfilled, the observed radial velocities form a sine curve given by:

$$v_r = u \sin\theta \sin\phi + v \cos\theta \sin\phi + w \cos\phi \quad (1.4)$$

The least squares wind vector components (u, v, w) can be obtained by solving the overdetermined linear system $\mathbf{A}\mathbf{v} = \mathbf{V}_r$ using singular value decomposition (Päschke et al., 2015), where $\mathbf{v} = (u, v, w)^T$, $\mathbf{V}_r = (V_{r1} \dots V_{rn})^T$ and n is the number of beams. The n rows of matrix \mathbf{A} contain the unit vectors $\sin\theta_i \sin\phi \cos\theta_i \sin\phi \cos\phi$ (with $i = 1, \dots, n$). In Päschke et al. (2015) also a method to assess the deviations from a perfect sine curve fit is presented. These deviations can arise from turbulence due to convective motions, gravity waves or wind shear.

Doppler wind lidars provide the necessary high temporal and spatial resolution to obtain such turbulence estimates, especially the small-scale turbulence, from vertical velocity measurements. In particular the dissipation rate of turbulent kinetic energy (TKE) is of interest. TKE is an important parameter for studying atmospheric turbulence, since it is a measure of the intensity of turbulence and directly linked to the transport of momentum, heat and moisture in the ABL (Stull, 2012). The dissipation rate represents the transfer of energy to smaller turbulent eddies in the inertial sub-range of the energy spectrum (Figure 1.4) and describes the conversion of kinetic energy into heat in the viscous sub-range (Banakh et al., 1999). The inertial sub-range describes the part of the spectrum where energy produced by large eddies is decaying to smaller eddies. The turbulent energy spectrum $S(k)$ for isotropic turbulence after Kolmogorov (1991) can be given by:

$$S(k) = a\epsilon^{2/3}k^{-5/3}, \quad (1.5)$$

with $a = 0.55$ being the Kolmogorov constant (Paquin and Pond, 1971) and ϵ the dissipation rate (O'Connor et al., 2010). Furthermore, the wavenumber k can be related to a length scale $L = 2\pi/k$ by making use of the frozen turbulence hypothesis of Taylor (1935). Integrating the energy spectrum from Equation 1.5 is equivalent to the variance of the observed mean Doppler velocity $\sigma_{\bar{v}}$ (Bouniol et al., 2004) and yields for ϵ :

$$\epsilon = 2\pi\left(\frac{2}{3a}\right)^{3/2} \sigma_{\bar{v}}^3 (L^{2/3} - L_1^{2/3})^{-3/2} \quad (1.6)$$

The length scale L_1 can be approximated by the product of horizontal wind V and dwell time (acquisition time for radial velocity profile estimates) of the lidar and L is obtained by multiplying L_1 with the number of samples used to derive ϵ . This method assumes that variations in mean Doppler velocity

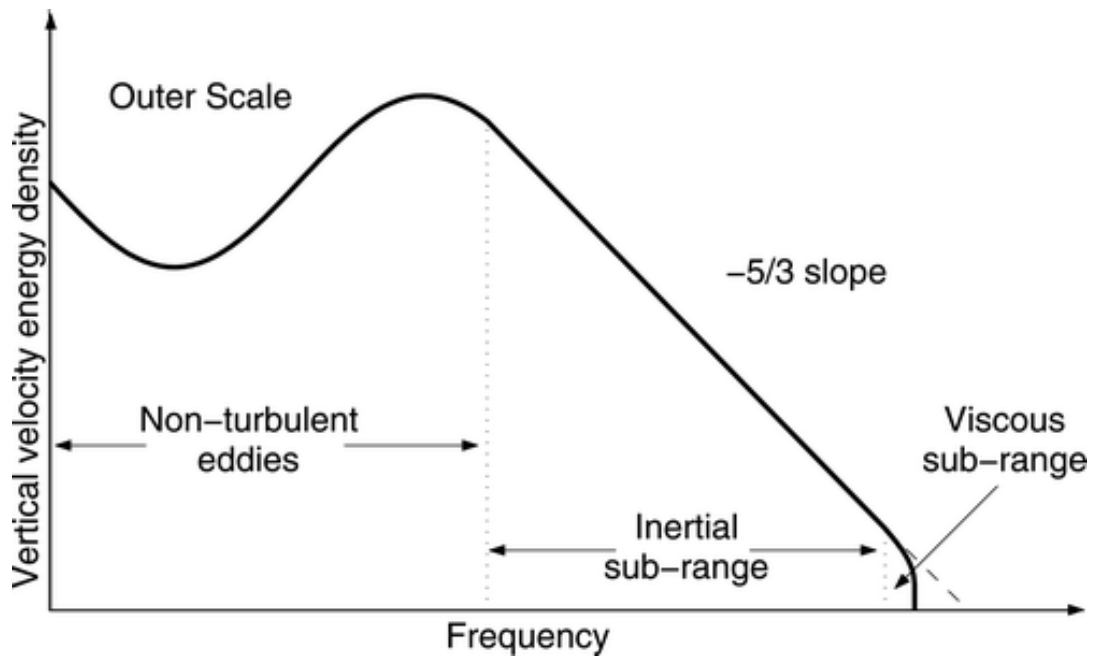


FIGURE 1.4: "Schematic of vertical velocity energy density spectra vs frequency conforming to Kolmogorov's hypothesis."
O'Connor et al. (2010)

are solely due to turbulence with scales inside the inertial sub-range (Frehlich and Cornman, 2002) and is used in Publication I and Publication III.

1.3.2 Observing atmospheric humidity and cloud properties

Atmospheric humidity is a key parameter to observe for vegetation-ABL interactions, but also for the surface energy balance and the hydrological cycle, can be estimated in different ways. Existing measurement techniques of the water vapor column amount range from satellite observations of the attenuation of reflected solar light from the surface in the near-infrared spectral regime (Gao and Kaufman, 2003), over radiosondes, to the Global Positioning System (GPS), making use of the zenith path delay (Bevis et al., 1992). For continuous observations of the full diurnal cycle under most weather conditions at a specific site, ground-based passive microwave radiometers are commonly used to derive integrated quantities like IWV and LWP, but also profiles of humidity and temperature (e.g. Löhnert and Crewell, 2003; Rose et al., 2005; Turner et al., 2007a). In the microwave spectrum, contributions to the extinction coefficient (Figure 1.5) are mainly due to absorption at the pressure-broadened rotational line of water vapor at 22.235 GHz and the oxygen complex (around 60 GHz). Furthermore, the water vapor and liquid

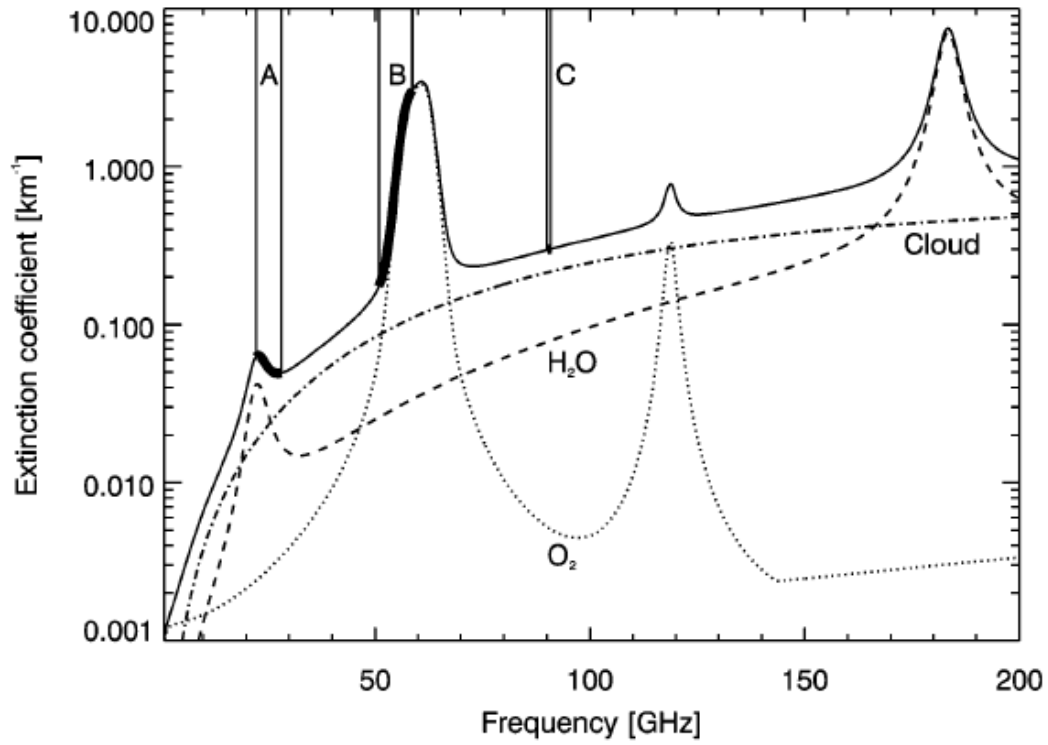


FIGURE 1.5: Extinction coefficient in the microwave spectral range, with contributions of oxygen, water vapor and liquid water. Löhnert et al. (2004)

water continuum add to the extinction of radiation and increases with frequency. Scattering processes for liquid water clouds by large cloud droplets or drizzle are only effective at frequencies above 100 GHz (Simmer, 1994).

Retrieval techniques often make use of the emission at two frequencies, located close to the 22.235 GHz water vapor line and in an atmospheric window region (e.g. 30 GHz). In this dual-channel approach, LWP and IWV can be retrieved simultaneously from atmospheric brightness temperatures (BT⁵) measurements, which has been applied for decades (Westwater, 1978). In order to convert BTs to estimates of IWV or LWP, statistical retrievals can be used (deployed in Publication III). For the retrieval development, radiative transfer calculations (e.g. Clough et al., 2005) need to be performed to relate BTs to the retrieval quantity. The input parameters such as profiles of temperature and humidity are usually obtained from radiosonde climatologies and are thus site specific. The information on the atmospheric state is then utilized to simulate BTs of the desired frequencies. Important factors that need to be accounted for in these calculations are, as mentioned before, microwave absorption due to water vapor and oxygen, as well as the water vapor continuum and liquid water (e.g. Liebe et al., 1991; Rosenkranz,

⁵describing the Planck equivalent blackbody temperature

1998). The retrieval coefficients are then inferred from regression techniques like multiple linear regression (e.g. Löhnert and Crewell, 2003), or neural network (Cadeddu et al. (2009), Marke et al. (2016), see Publication IV). Also physical retrievals exist, adding radar, lidar, radiosonde profiles, near surface observations and apriori knowledge for a better characterisation of the atmospheric state (Löhnert et al., 2004). To take into account non-linearities, the inversion can be done iteratively using optimal estimation (Rodgers, 2000). Hence, this approach is more accurate but also more computationally expensive compared to statistical methods (Turner et al., 2007a).

In general, reliable retrieval results can not be obtained during rainy conditions (Rose et al., 2005). Due to radiometric and absorption model uncertainties, as well as the deployed retrieval method and calibration procedure, a BT uncertainty of 0.5–1 K (Maschwitz et al., 2013) converts into retrieval accuracies of about 15–30 g m⁻² for LWP (Löhnert and Crewell, 2003) and 0.5–0.8 kg m⁻² for IWV (Steinke et al., 2015). Therefore, the relative retrieval uncertainty of LWP can be above 50% for thin liquid water clouds (LWP below 100 g m⁻²). This type of cloud is frequently occurring in various climate regimes, with percentages over 60% (Turner et al., 2007a). In addition, the sensitivity of shortwave and longwave radiative fluxes is high for clouds with low amounts of liquid water (Marchand et al., 2003). Due to the high abundance and radiative impact, it is crucial to accurately characterize radiative properties of thin liquid water clouds for a correct representation in climate models (Turner et al., 2007b). In order to describe interactions of clouds with radiation for a given wavelength, properties like cloud optical depth τ and effective radius r_{eff} can be used (Stephens, 1978; Hu and Stamnes, 1993; Turner et al., 2007b). With:

$$r_{eff} = \frac{\int_0^\infty r^3 n(r) dr}{\int_0^\infty r^2 n(r) dr} \quad (1.7)$$

being the effective radius as the area-weighted mean radius of cloud droplets with radius r and droplet size distribution (DSD) $n(r)$ (Hansen and Travis, 1974). If the droplets are large compared to the wavelength, cloud mean r_{eff} can be related to τ and LWP in a vertical uniform liquid water cloud by:

$$r_{eff} = \frac{3LWP}{2\tau\rho_l}, \quad (1.8)$$

where ρ_l is the liquid water density (Stephens, 1978). To obtain vertically resolved profiles of r_{eff} , MWR and radar observations are combined (Frisch et al., 1995). The radar reflectivity Z is proportional to the sixth moment

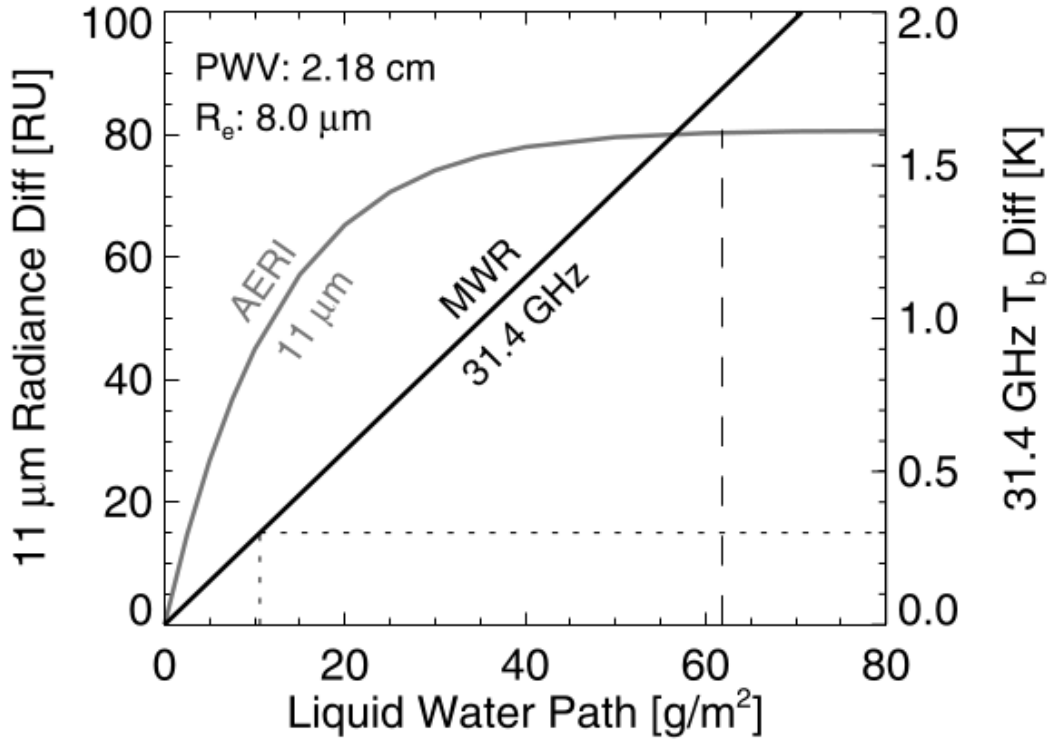


FIGURE 1.6: "Simulated cloudy minus clear sky radiance difference at 11 μm and 31.4 GHz for a range of LWP. [...]" **Turner (2007)**

of the DSD and distributes the MWR estimated LWP vertically within the cloud. Accounting for cloud top entrainment, r_{eff} as a function of height above cloud base (h) for non-drizzling clouds with known boundaries can be written as:

$$r_{eff}(h) = k_{rv} \left(\frac{\pi \rho_l \sum_{i=1}^n Z^{1/2}(h_i) \Delta h}{48LWP} \right)^{1/3} Z^{1/6}(h), \quad (1.9)$$

with assumptions on the DSD shape parameter contained in k_{rv} (**Knist, 2014**). Also infrared observations reveal sensitivities to changing amounts of liquid water contained in the clouds. Whereas for MWR a linear increase in downwelling radiance below 100 g m^{-2} is observed, the infrared sensitivity is much higher and exceeds the instrument uncertainty of 1 RU⁶ (**Figure 1.6**). At around 60 g m^{-2} saturation of the downwelling radiance is evident by the asymptotic behavior and the sensitivity drops below the uncertainty. Thus, the infrared spectral regime is suitable to retrieve low LWP values and can be combined with MWR observations to achieve a full coverage of the liquid water cloud LWP range, as demonstrated in **Turner (2007)** (see also **Publication IV**).

⁶1 RU (radiance unit) is $1 \text{ mW}(\text{m}^2 \text{ sr cm}^{-1})^{-1}$

2 BOUNDARY LAYER CLASSIFICATION

ATMOSPHERIC BOUNDARY LAYER CLASSIFICATION WITH DOPPLER LIDAR

A. Manninen, T. Marke, M. Tuononen, and E. O'Connor (2018). "Atmospheric Boundary Layer Classification With Doppler Lidar". In: *Journal of Geophysical Research: Atmospheres* 123.15. DOI: [10.1029/2017JD028169](https://doi.org/10.1029/2017JD028169)

© 2018 American Geophysical Union. All Rights Reserved.

RESEARCH ARTICLE

10.1029/2017JD028169

A. J. Manninen and T. Marke contributed equally to this work.

Key Points:

- Atmospheric boundary layer classification method objectively assigns a source for the turbulent mixing identified by Doppler lidar
- The site-independent method outputs a pixel-based classification for the turbulent source at high temporal and spatial resolution
- The method requires only Doppler lidar measurements but can be extended to use supplementary information as well

Correspondence to:

A. J. Manninen,
antti.j.manninen@helsinki.fi

Citation:


Manninen, A. J., Marke, T., Tuononen, M. J., & O'Connor, E. J. (2018). Atmospheric boundary layer classification with Doppler lidar. *Journal of Geophysical Research: Atmospheres*, 123. <https://doi.org/10.1029/2017JD028169>

Received 7 DEC 2017

Accepted 22 JUN 2018

Accepted article online 29 JUN 2018

Atmospheric Boundary Layer Classification With Doppler Lidar

A. J. Manninen¹ , T. Marke² , M. Tuononen^{1,3,4}, and E. J. O'Connor^{3,5} 

¹Department of Physics, University of Helsinki, Helsinki, Finland, ²Institute for Geophysics and Meteorology, University of Cologne, Cologne, Germany, ³Finnish Meteorological Institute, Helsinki, Finland, ⁴Vaisala Oyj, Vantaa, Finland, ⁵Department of Meteorology, University of Reading, Reading, UK

Abstract We present a method using Doppler lidar data for identifying the main sources of turbulent mixing within the atmospheric boundary layer. The method identifies the presence of turbulence and then assigns a turbulent source by combining several lidar quantities: attenuated backscatter coefficient, vertical velocity skewness, dissipation rate of turbulent kinetic energy, and vector wind shear. Both buoyancy-driven and shear-driven situations are identified, and the method operates in both clear-sky and cloud-topped conditions, with some reservations in precipitation. To capture the full seasonal cycle, the classification method was applied to more than 1 year of data from two sites, Hyytiälä, Finland, and Jülich, Germany. Analysis showed seasonal variation in the diurnal cycle at both sites; a clear diurnal cycle was observed in spring, summer, and autumn seasons, but due to their respective latitudes, a weaker cycle in winter at Jülich, and almost non-existent at Hyytiälä. Additionally, there are significant contributions from sources other than convective mixing, with cloud-driven mixing being observed even within the first 500 m above ground. Also evident is the considerable amount of nocturnal mixing within the lowest 500 m at both sites, especially during the winter. The presence of a low-level jet was often detected when sources of nocturnal mixing were diagnosed as wind shear. The classification scheme and the climatology extracted from the classification provide insight into the processes responsible for mixing within the atmospheric boundary layer, how variable in space and time these can be, and how they vary with location.

1. Introduction

Reliable representation of turbulent mixing within the atmospheric boundary layer (ABL) is essential for air quality studies, wind energy, and for weather and climate models (e.g., Garratt, 1994). Turbulent mixing is responsible for the redistribution of momentum, mass, temperature, and humidity within the ABL (Oke, 1992). In addition, turbulent processes govern the rate of exchange between the surface and the atmosphere and determine the transport of aerosol away from the surface (Fuentes et al., 2016; Kaimal & Finnigan, 1994). The sources of turbulent mixing include buoyancy production and wind shear production (Deardorff, 1972; Moeng & Sullivan, 1994) and are highly variable in time and space; therefore, accurate measurements (Baklanov et al., 2011) and representation in numerical models are a challenge (Holtzlag et al., 2013).

Buoyancy production, in terms of surface-driven convective mixing, is usually the dominant source of turbulent mixing in the ABL during the day (Oke, 1992), and also, radiative cooling in stratocumulus layers can drive top-down mixing from the cloud layer toward the surface during day and night (Hogan et al., 2009; Wood, 2012). Shear-driven production arises from shear in the near-surface wind profile induced by mechanical friction between the atmosphere and surface and from the shear associated with low-level jets (e.g., Banta et al., 2006; Tuononen et al., 2017).

Doppler lidar measurements provide sufficient temporal and spatial resolution for observing turbulent mixing in the ABL (e.g., Tucker et al., 2009) but have typically concentrated on particular quantities (O'Connor et al., 2010; Smalikho & Banakh, 2017; Vakkari et al., 2015) or processes (Barlow et al., 2011; Hogan et al., 2009; Su et al., 2016; Träumner et al., 2011) or deriving the mixing level height (Baars et al., 2008; Emeis et al., 2008; Pearson et al., 2010; Schween et al., 2014). To better comprehend the complex structure and evolution of the ABL, Harvey et al. (2013) introduced a profile-based Doppler lidar method for determining specific ABL types concentrating on whether the cloud-topped ABL was coupled to the surface.

Here we introduce a method that builds upon the method presented by Harvey et al. (2013) and which objectively assigns a source for the turbulent mixing identified in the ABL by Doppler lidar. The method combines

Table 1
Instrument Parameters During Standard Operation for the Halo Lidar at Hyytiälä (Jülich)

| Parameter | Value |
|----------------------------|--------------------------------|
| Wavelength | 1.5 μm |
| Detector | Heterodyne |
| Pulse repetition frequency | 15 kHz |
| Nyquist velocity | Approximately 20 m/s |
| Sampling frequency | 50 MHz |
| Velocity resolution | 0.038 m/s |
| Telescope | Monostatic optic-fiber coupled |
| Range resolution | 30 m |
| Pulse duration | 0.2 (0.15) μs |
| Lens diameter | 8 (7.5) cm |
| Lens divergence | 33 μrad |
| Minimum range | 90 m |
| Maximum range | 9,600 (8,400) m |
| Points per range bin | 10 |

multiple quantities derived from Doppler lidar measurements to output a pixel-based classification for the turbulent source at high temporal and spatial resolution (3 min and 30 m for the instruments used here). The method is robust for almost all situations except fog and precipitation and is intended to be site independent. Fog often impedes the propagation of the Doppler lidar signal and is mostly present at elevation, which are lower than the lowest observable Doppler lidar range gate 105 m. Contamination of lidar measurements from precipitation can be an issue, and the methodology could be improved with an inclusion of a robust method for detecting precipitation in Doppler lidar measurements which to the authors' knowledge does not exist yet. However, a simple precipitation detection method, which is described in section 3.2, was applied to the data set. In principle, this method can be applied to any Doppler lidar that provides measurements of vertical Doppler velocity and horizontal winds and requires only Doppler lidar; however, it is designed so that it can be easily extended with supplementary information, such as sensible heat flux measurements from a 3-D sonic anemometer.

For this study, we applied the classification method to long-term data sets (over 1 year) to capture a full seasonal cycle of the ABL using instruments at two sites in Europe. The instruments and their operating specifications, together with their locations, are described in section 2. The classification method is presented in section 3, which describes the lidar quantities that are required, together with their associated uncertainties, and the decision tree that is used to assign the source. In section 4, two case studies are highlighted to show how the method performs in both clear-sky and cloudy-topped ABL situations, and the results from the long-term climatological analysis at both sites are discussed.

2. Measurements

2.1. Halo Photonics Streamline Scanning Doppler Lidar

The Halo Photonics Streamline Doppler lidar (Pearson et al., 2009) is a pulsed lidar system with a heterodyne detector operating in the near-infrared spectral region. This instrument has full hemispheric scanning capability and provides range-resolved profiles of backscattering signal and radial Doppler velocity with user-selectable resolution. The instrument parameters during standard operation for the two instruments considered here are given in Table 1. To obtain reliable uncertainty estimates, Manninen et al. (2016) showed that the Halo lidar signal output often requires further processing to account for artifacts in the instrument background signal. This extra processing also has a major impact on the data availability, especially in regions with a low aerosol loading. The extra processing does not affect the Doppler velocities. After the background correction, new measurement uncertainties are derived from the corrected signal (O'Connor et al., 2010; Rye & Hardesty, 1993), which will then propagate through to the products derived from the lidar signal and radial Doppler velocity. Profiles of calibrated attenuated backscatter coefficient (β) are also derived (Westbrook et al., 2010), if the telescope function is known (Hirsikko et al., 2014).

2.2. Site and Data Set Description

To evaluate the ABL classification, Halo lidar measurements from two locations are utilized: Hyytiälä, Finland, and Jülich, Germany. Both locations represent a maritime to continental environment in the high and middle latitudes, respectively. The data set used in this study consists of Halo lidar measurements performed between 1 September 2015 and 15 November 2016 at Hyytiälä and from 1 May 2015 to 31 December 2016 at Jülich.

Hyytiälä hosts the Station for Measuring Ecosystem-Atmosphere Relations-II (Hari & Kulmala, 2005) operated by the University of Helsinki and is located in the southwestern part of Finland (61.845°N, 24.289°E). The site is about 190 km north of Helsinki and 150 km from the shores of the Gulf of Bothnia in the west. The site represents a typical rural boreal forest environment and was established to teach and study forestry in 1910. Together with forest science research, atmospheric measurements have been performed at the station since the 1980s, and the Station for Measuring Ecosystem-Atmosphere Relation-II station has been operational since 1995. The station is embedded within the Aerosols, Clouds and Trace gases Research Infrastructure (ACTRIS), Integrated Carbon Observation System, and Long-Term Ecosystem Research in Europe infrastructures.

The Halo lidar, operated by the Finnish Meteorological Institute, has been operating continuously at the station since 2013, following the operational scanning strategy outlined in Hirsikko et al. (2014). The scanning sequence for this period comprised the following: VAD scan at 30° elevation from horizontal with 23 beams (excluding one blocked beam) every 30 min, three-beam Doppler beam swinging (DBS) scan at 70° elevation every 30 min, and range height indicator scan and custom sector scan every 30 min with slightly varying integration times. When not scanning, the instrument was performing vertical stare measurements with 10-s integration time. For Hyytiälä, only the DBS scans were used for the Halo lidar wind retrievals.

The Jülich Observatory for Cloud Evolution (JOYCE) is embedded in the German Research Foundation (DFG) Transregional Collaborative Research Centre Transregio32 Patterns in Soil-Vegetation-Atmosphere Systems—Monitoring, modeling and data assimilation of the Universities of Aachen, Bonn, Cologne, and the Research Centre Jülich. The JOYCE instrumentation aims to observe the variability of atmospheric water cycle variables, helping to understand the interactions between soil, vegetation, and atmosphere through spatially and temporally highly resolved measurements. As a registered DFG Research Infrastructure, JOYCE has recently (beginning of 2016) been funded as a DFG Core Facility in order to professionally manage user access to JOYCE instruments, observation data, and scientific expertise. Internationally, JOYCE is a Cloudnet observatory embedded within the European Horizon2020 Research Infrastructure ACTRIS-2. In March 2016 the European Strategy Forum for Research Infrastructures officially adopted ACTRIS. Most of the instruments (including the Doppler lidar) are located on the roof of the Institute for Energy and Climate Research-Troposphere IEK-8 at the Research Centre Jülich, which is embedded in an agricultural dominated landscape (50.909°N, 6.414°E, 111 masl).

At Jülich, the operational scanning strategy consists of a 75° elevation VAD scan with 36 beams every 15 min. Every 5 min a DBS scan is conducted with the same elevation angle. Since 1 June 2015 an additional VAD scan with only three beams was set up following the DBS scan. Furthermore, a range height indicator scan at 0° azimuth is performed every hour with 5° increments, resulting in 37 beams. For the remainder of the time, vertical stare measurements are carried out with 1-s integration time. For Jülich, only the VAD scans were used for the Halo lidar wind retrievals. To filter atmospheric lidar signal from noise, we have selected a conservative signal-to-noise (SNR) threshold of −20 dB at both sites.

3. Methodology

3.1. Calculation of the Required Quantities From Doppler Lidar Measurements

The ABL classification method requires the following lidar quantities as inputs: attenuated backscatter coefficient, vertical velocity skewness, dissipation rate of turbulent kinetic energy (TKE), vertical profiles of horizontal wind, and vector wind shear. These lidar quantities are derived from the data corrected following Manninen et al. (2016) and generated at the original vertical resolution and selected temporal resolution, unless otherwise mentioned. The choice of temporal resolution depends on the signal strength and data availability, that is, the aerosol loading in the region where the Halo lidar is located; more averaging is required in clean air situations. In addition, it is necessary to ensure that the turbulent length scales imposed by the choice of temporal resolution encompass eddies that remain within the inertial subrange (Frehlich & Cornman, 2002; O'Connor et al., 2010). Hence, for the sites investigated here, 3 min was determined as the temporal

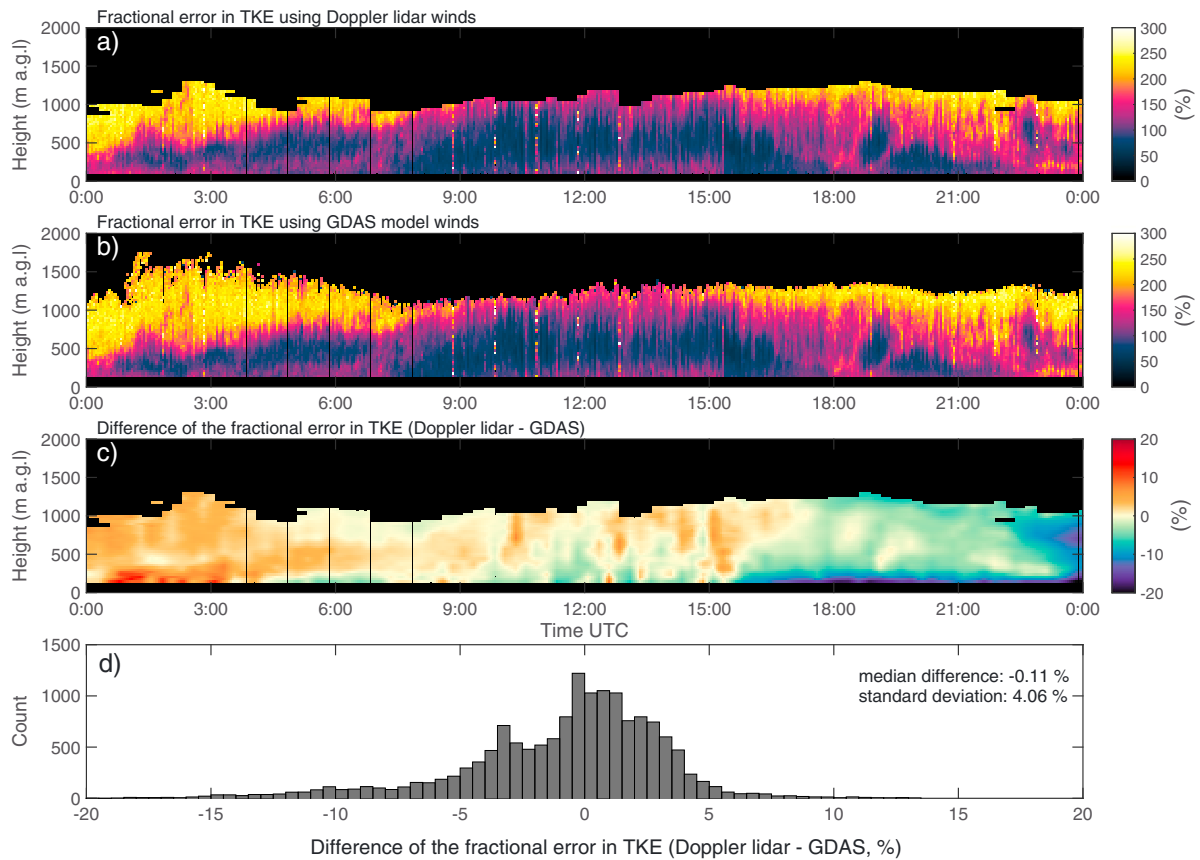


Figure 1. Time-height plots of fractional error in ϵ using (a) Doppler lidar winds and (b) GDAS model winds calculated from measurements on 9 March 2016 at Jülich, Germany. (c) Time-height plot and (d) histogram of the difference in the two fractional errors (Doppler lidar-GDAS). GDAS = Global Data Assimilation System; TKE = turbulent kinetic energy.

resolution limit for generating the ABL classification. Vertical velocity skewness requires a longer time window (e.g., Harvey et al., 2013; Hogan et al., 2009), which is further discussed below.

The height of the aerosol layer, in terms of the Halo lidar measurements, is calculated from the averaged attenuated backscatter coefficients (β). The height is utilized to limit the calculations to the height ranges with sufficient atmospheric signal. Clouds are detected from the β values by selecting a threshold from the literature: $10^{-5} \text{ m}^{-1} \cdot \text{sr}^{-1}$ (e.g., Harvey et al., 2013; Hogan et al., 2009; Westbrook et al., 2010). Ideally, the cloud detection scheme should include objective cloud-precipitation discrimination.

The uncertainty in attenuated backscatter coefficient σ_{β} is calculated by

$$\sigma_{\beta} = \frac{1}{\sqrt{n_p}} \left(1 + \left(\frac{1}{|\text{SNR}|} \right) \right), \quad (1)$$

where n_p is the number of pulses per ray and SNR is the signal-to-noise ratio. Since the β value at cloud base is at least 2 orders of magnitude above aerosol β values, and usually have high SNR, we consider that σ_{β} has little impact on the simple threshold-based cloud detection method.

The vertical velocity variance and skewness are calculated from the vertically pointing radial Doppler velocities by using a method presented by Rimoldini (2014), which provides higher-order moments unbiased by random uncertainties or sample size. The vertical velocity skewness is used to diagnose whether the turbulence is cloud driven, as discussed in section 3.2.2. Uncertainties of velocity variance and skewness were estimated by using bootstrapping technique (e.g., Kleiner et al., 2014). To capture reliable skewness of vertical air motion in the ABL, a 60-min time window was determined to be suitable. Skewness calculated with

the 60-min window is then subsampled to 3 min with linear interpolation to match the temporal resolution of other lidar quantities. Skewness is highly noisy quantity, and thus, in the results presented here, median filtering is applied using a window size of 10 consecutive 3-min profiles and 3 range gates.

In order to associate a source of the mixing process, the most important part of the classification is the identification of the turbulent regions of the ABL. Hogan et al. (2009) discussed that a combination of vertical velocity skewness and variance (σ_v^2) can be used to detect turbulence. In this study, the presence of turbulent mixing is diagnosed from the dissipation rate of TKE, which is calculated from vertically pointing data using the method presented by O'Connor et al. (2010):

$$\epsilon = 2\pi \left(\frac{2}{3a} \right)^{3/2} \sigma_w^3 \left(L^{2/3} - L_1^{2/3} \right)^{-3/2}, \quad (2)$$

where the $a = 0.55$ is the Kolmogorov constant, σ_w is the standard deviation of the mean radial velocity of a selected time averaging window (O'Connor et al., 2005), L is the length scale of the largest eddies that pass completely through the lidar beam during the averaging window, and L_1 describes the length scale of the scattering volume dimension per single sample in the averaging window. It is important to note that, if present, the impact of wave motions to the observed σ_w and henceforth to the ϵ should be taken into account because the wave motions do not cause turbulent mixing (Bonin et al., 2018).

The method also provides an uncertainty estimate for ϵ , described in terms of fractional error, $\Delta\epsilon/\epsilon$, where $\Delta\epsilon$ is the absolute error in TKE dissipation rate (for further details, see O'Connor et al., 2010). Horizontal winds are required to estimate the length scales L and L_1 , and these may be provided by the instrument itself, if scanning capable, or by supplementary sources such as radiosonde, wind profiler, or weather forecast models (O'Connor et al., 2010). Low SNR or highly turbulent conditions can impact the Doppler lidar wind retrievals (Newsom et al., 2017; Päsche et al., 2015), in which case, when Halo lidar horizontal winds are not available, horizontal winds provided by, for example, the Global Data Assimilation System, GDAS (GDAS, 2016) can be used instead.

To investigate how the uncertainty in ϵ estimate change when model winds are used instead of winds retrieved with Doppler lidar, we calculated ϵ using (2) with both wind data sets and compared the resulting fractional errors in ϵ . Figure 1 shows an example day from 9 March 2016, Jülich, Germany, where Halo lidar winds could be retrieved throughout the ABL. The median difference in fractional error in ϵ was 0.11% with standard deviation of 4.1%. Given that a typical threshold value for reliable ϵ estimates can be as high as 300%, as suggested by O'Connor et al. (2010), the additional uncertainty arising from using GDAS model winds is considered to be insignificant. However, in the results presented in this paper we have used only the Halo lidar winds.

Wind shear, which is also a source of turbulent mixing, can be derived from the Doppler lidar retrievals of horizontal wind. The vector wind shear is given by, for example, ICAO (2005):

$$\text{vector wind shear} = \frac{(\Delta u^2 + \Delta v^2)^{1/2}}{\Delta z}, \quad (3)$$

where the vector difference of the u and v wind components is divided by the height difference Δz between the two altitudes over which the wind shear is calculated. Here the vector wind shear is calculated over three range gates ($\Delta z = 90$ m). The uncertainty in vector wind shear is obtained by propagating the uncertainty in the winds. In good conditions, the uncertainty in horizontal wind is of the order 0.2 m/s for VAD scans, but inhomogeneous flow in strongly turbulent mixing layers can increase the uncertainty significantly (Päsche et al., 2015). Thus, we assume that, when present, convective mixing is the dominant cause of turbulence within the ABL and neglects the influence of vector wind shear. Wind shear is not calculated when Doppler lidar winds are not available.

For additional information, the low-level jet (LLJ) detection algorithm presented by Tuononen et al. (2017) is applied. LLJs have been shown to cause shear-driven turbulence above and below the jet nose, especially in the nighttime ABL (Banta et al., 2006; Cuxart & Jiménez, 2007) and also during daytime in coastal locations (Tuononen et al., 2017). In the results presented here, only the presence and the height of the detected LLJs are shown, but LLJs are not explicitly diagnosed as the turbulent source, as automated attribution is still under evaluation.

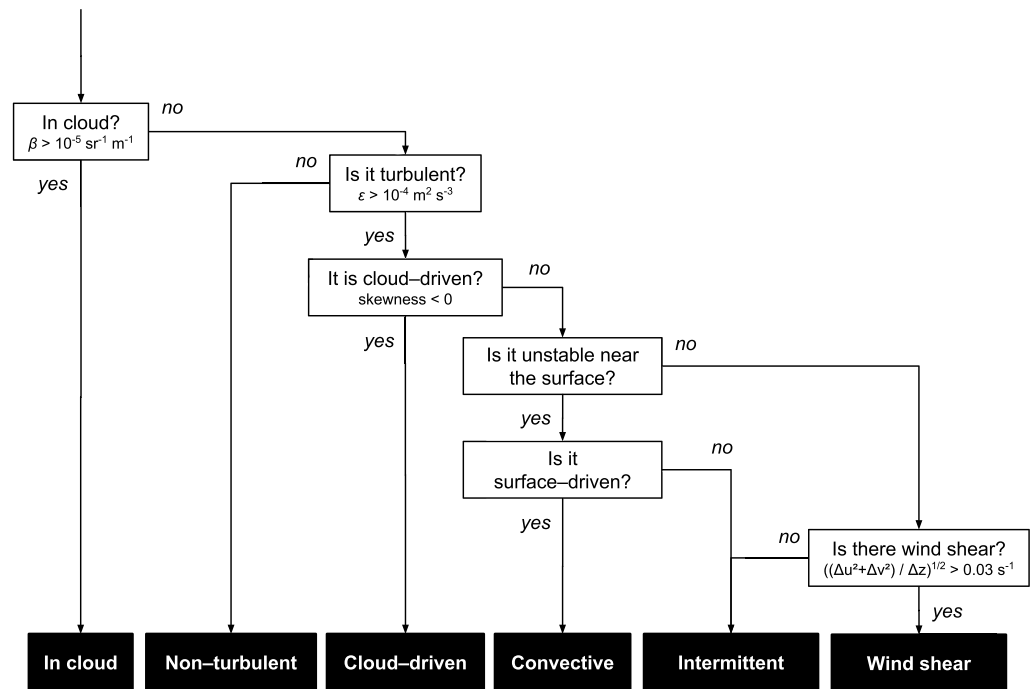


Figure 2. Schematic of the atmospheric boundary layer turbulent mixing source decision tree.

3.2. Generating the ABL Classification Product

The main product of the method presented in this paper is a classification bit field, in which each bit contains the relevant information obtained from each individual quantity required for the boundary layer classification. The two masks, generated using the decision tree logic, are derived from the bit field. This approach allows straightforward implementation of future developments, such as improved methods and supplementary information (e.g., surface stability), through which new bits can be added to the bit field, without changing the current logic. The decision tree logic can be modified without modifying the bits, and more classes can be added by including the new bits when deriving masks from the bit field. The bit field can be represented by two fields, one identifying the presence of turbulent mixing and whether it is associated with clouds, the surface, or neither (section 3.2.1) and one presenting the diagnosed dominant source of mixing (section 3.2.2). These fields are generated at the same time-height resolution as the input lidar quantities. The classification product classes are denoted in *italics*.

Precipitation cases are identified profile by profile from the vertical velocity data by using the assumption that all precipitation has a fall velocity greater than 1 m/s. Since turbulent motions can also exceed 1 m/s, a pixel-by-pixel approach will not suffice. However, a mean negative Doppler velocity averaged over a larger time and vertical window is also not a sufficient discriminator, since large turbulent eddies can also result in a mean negative Doppler velocity at the time and spatial scales that would seem suitable for detecting precipitation. Hence, we use the additional criterion that 95% of the Doppler velocities within the averaging window must also be < -1 m/s; the entire profile within which any pixel meets these criteria is then diagnosed as containing precipitation. An averaging window of 3×7 pixels (equivalent to 9 min and 210 m) was applied to the 3-min averaged profiles; since precipitation is more coherent in the vertical dimension, enlarging the window in the vertical direction provides more values from which to compute the 95th percentile and is a compromise between obtaining a robust result and retaining the temporal resolution necessary to capture some precipitation features. This precipitation diagnostic may not be suitable in locations where there is significant large-scale vertical motion arising from orographic features or strong convection. At the two locations in this study, the precipitation diagnostic removed about 1% of the profiles at Hyytiälä and about 2% at Jülich.

3.2.1. Surface-Driven Versus Cloud-Driven Turbulent Mixing

The presence of turbulence is obtained from ϵ using a threshold-based approach. Previous studies suggest $\epsilon > 10^{-4} \text{ m}^2/\text{s}^3$ as a suitable threshold value (e.g., Borque et al., 2016; O'Connor et al., 2010; Vakkari et al., 2015).

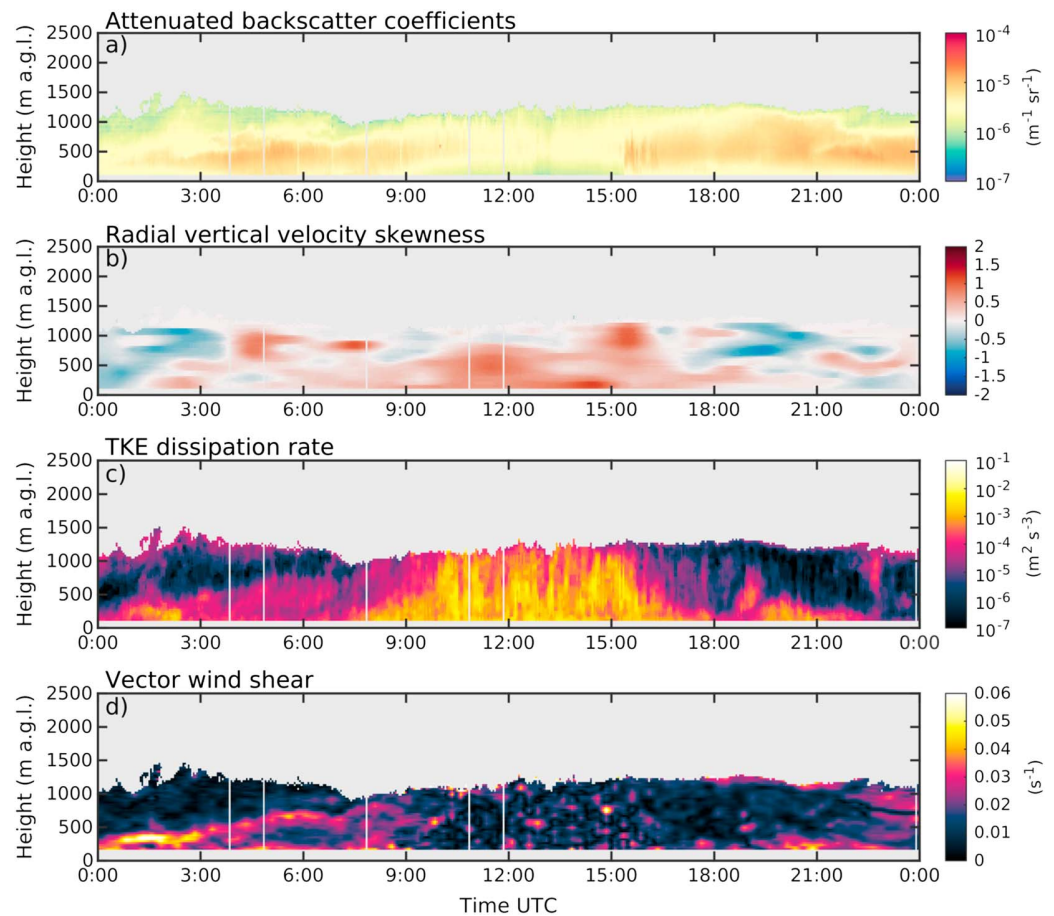


Figure 3. Time-height plots of (a) attenuated backscatter coefficient, β , (b) vertical velocity skewness, (c) TKE dissipation rate, ϵ , and (d) vector wind shear, calculated from Doppler lidar measurements on 9 March 2016 at Jülich, Germany. Solar noon is about 11:45 UTC. TKE = turbulent kinetic energy.

We selected $\epsilon > 10^{-5} \text{ m}^2/\text{s}^3$ as our threshold for detecting turbulent mixing and a threshold of $\epsilon > 10^{-4} \text{ m}^2/\text{s}^3$ for detecting surface-connected mixing, as discussed below. Pixels above the $\epsilon > 10^{-5} \text{ m}^2/\text{s}^3$ threshold are determined to be turbulent and below the threshold as *noturbulent*. The presence of cloud in a profile is also determined using a threshold value, $\beta > 10^{-5} \text{ m}^{-1} \cdot \text{sr}^{-1}$ being labeled as *in cloud*.

When the ABL is topped by stratocumulus clouds, cloud-top radiative cooling can be the dominant driver for turbulent mixing within the ABL (Wood, 2012), which resembles the inverse of surface-driven turbulence (Hogan et al., 2009) and can be recognized from the vertical velocity skewness. In order to determine whether turbulent mixing is associated with a cloud layer, labeled *cloud driven*, the cloud base height is first obtained and then a top-down approach is used to find all consecutive range gates below the cloud with $\epsilon > 10^{-5} \text{ m}^2/\text{s}^3$ and containing negative vertical velocity skewness. Similarly, *surface connected* is resolved with a bottom-up approach by searching the profile upward until the first range gate where $\epsilon < 10^{-4} \text{ m}^2/\text{s}^3$ is found, starting at the lowest reliable range gate of the Halo lidar (105 m). Any remaining range gates where $\epsilon > 10^{-5} \text{ m}^2/\text{s}^3$ are labeled as *unconnected*. In principle, the regions labeled surface connected comprise the mixing layer, from which the mixing layer height can be produced, a valuable parameter for many applications. Cases where the surface-connected and cloud-driven turbulence are coupled, special care should be taken in determining the height of the mixing layer since ascending and descending plumes have been observed to pass through the interface between positive and negative skewness layers indicating surface-connected and cloud-driven layers, respectively (Hogan et al., 2009).

3.2.2. Identifying the Turbulent Mixing Source

The source of turbulent mixing is derived using decision tree-based logic, as presented in Figure 2, which requires an additional input describing the atmospheric thermodynamic stability close to the surface.

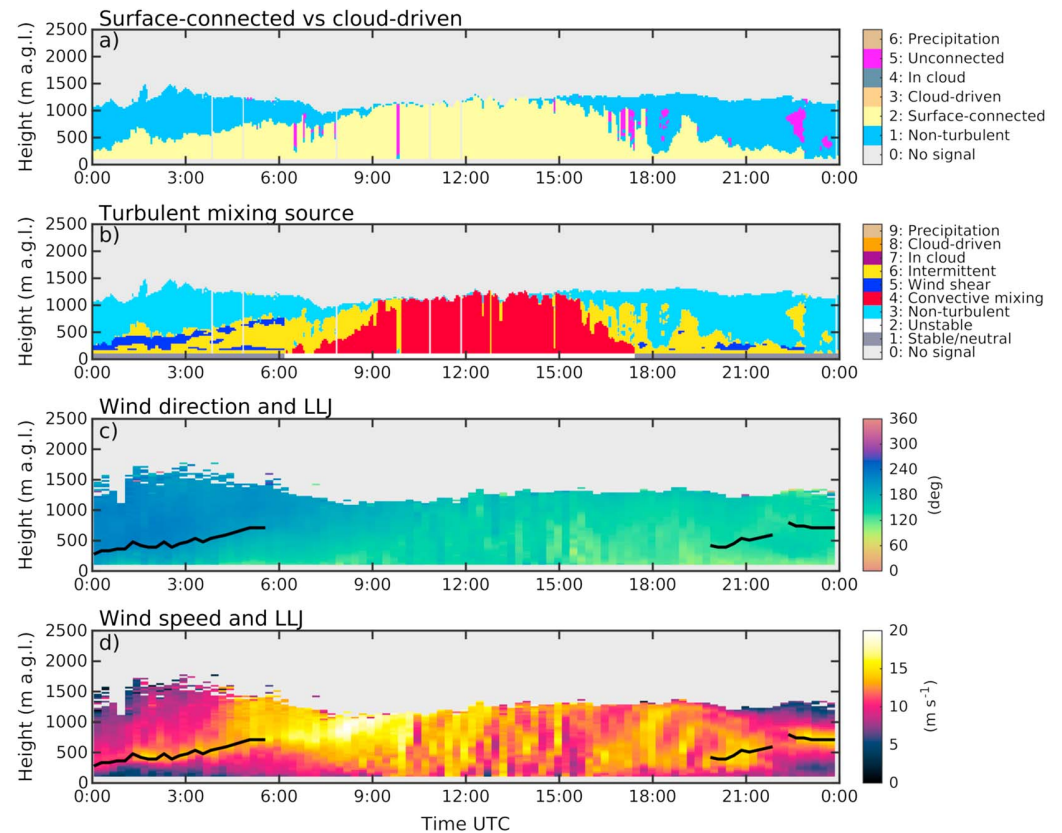


Figure 4. Time-height plots of atmospheric boundary layer classification showing (a) connection with the surface (i.e., surface driven versus cloud driven) and (b) the turbulent mixing source, together with time-height plots of (c) wind direction and (d) wind speed on 9 March 2016 at Jülich, Germany. The black lines on the two lower panels show LLJ altitude identified using the method presented by Tuononen et al. (2017). LLJ = low-level jet.

First, pixels are identified as being in cloud or not. Then, turbulent pixels are separated from nonturbulent and cloud-driven pixels are identified. Other turbulent pixels are then classified depending on the atmospheric stability close to the surface, whether they are in contact with the surface, and whether there is wind shear present.

In the absence of ancillary measurements, it is assumed that the daytime ABL is unstable, and the nighttime ABL is neutral or stably stratified (e.g., Garratt, 1994; Oke, 1992), with sunrise and sunset calculated using the method described in Ibrahim and Afshin (2008). In unstable situations, *convective* mixing is assumed to be the dominant source of turbulence for pixels labeled surface connected. It is important to note that the ABL does not become unstable immediately after sunrise but that it takes some time, the length of which depends, for example, on solar angle, cloud cover, and surface characteristics (Ketzler, 2014).

In stable or neutral conditions, any turbulence in the presence of significant wind shear, defined as $> 0.03 \text{ s}^{-1}$, is assigned the class *wind shear*, which may include surface-connected and unconnected pixels (but not cloud driven), and is often seen in the presence of a LLJ as in the case study discussed in section 4.1. This class is not assigned in unstable situations as it is assumed that any mechanically driven turbulence is dominated by thermally driven turbulence.

For all remaining unassigned pixels, turbulence is assumed to arise from decaying convective eddies after sunset or from other intermittent sources (Lothon et al., 2014) and labeled as *intermittent*.

4. Results and Discussion

We first present two case studies, a clear-sky day from Jülich and a cloud-topped ABL from Hyytiälä, to illustrate the detailed performance of the classification scheme on a daily basis. The ABL classification scheme is

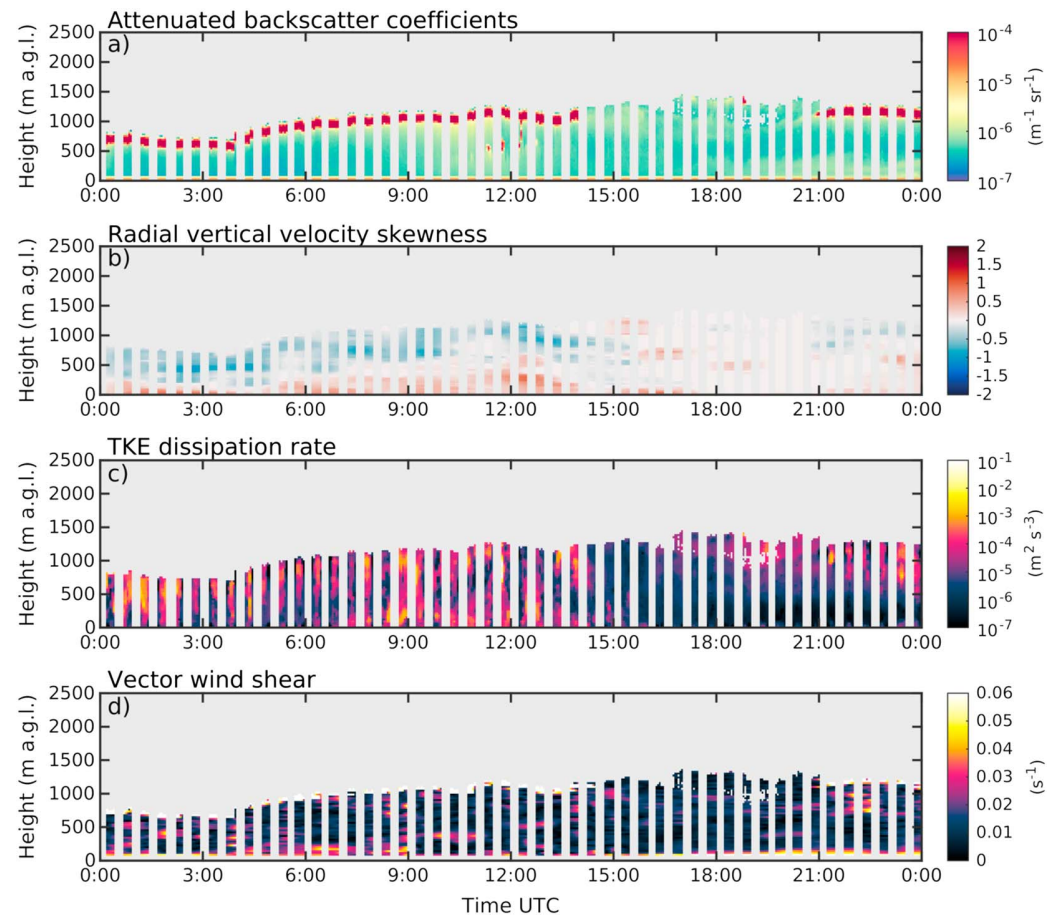


Figure 5. Time-height plots of (a) attenuated backscatter coefficient, β , (b) vertical velocity skewness, (c) TKE dissipation rate, ϵ , and (d) vector wind shear, calculated from Doppler lidar measurements on 22 September 2016 at Hyttiälä, Finland. Vertical gray lines indicate periods when the Doppler lidar was scanning. Solar noon is about 10:15 UTC. TKE = turbulent kinetic energy.

then applied to more than 1 year of data from both sites to display how the classification scheme is used to investigate the relative proportion of surface-driven, cloud-driven, and other turbulent sources, their diurnal cycle, and their seasonal variation.

4.1. Clear-Sky Case Study

Figure 3 displays lidar quantities calculated from the Halo lidar data for a clear-sky day in Jülich, Germany. The development of the ABL structure is typical for a clear-sky day between spring and early autumn in a midlatitude and semiurban environment. Sunrise is at 06:08 UTC, and a layer with high TKE dissipation rate values ($\epsilon > 10^{-3} \text{ m}^2/\text{s}^3$) and generally positive skewness values can be seen growing to reach about 1,200 m by 10:00 UTC, indicative of surface-driven convective mixing. This layer then begins reducing in altitude after 16:00 as the turbulent mixing associated with surface heating weakens, as expected with sunset at 17:24 UTC. The ABL classification product displayed in Figure 4, diagnosed using the decision tree (Figure 2), produces the same result, *surface-connected* mixing with a convective source during the daytime.

However, there are other turbulent features present in the ABL. Between 00:00 and 09:00 UTC there is significant turbulent mixing at altitudes up to 500 m or more, the upper boundary of which coincides with a strong gradient in the attenuated backscatter field. This early morning turbulent mixing correlates well with an elevated layer of strong vector wind shear ($> 0.03 \text{ s}^{-1}$) as does another elevated turbulent layer after sunset between 17:30 and 22:30 UTC. Applying the LLJ algorithm to the horizontal wind profiles, displayed in Figure 4, shows that LLJs are present at these times and at appropriate altitudes, since the strongest wind shear associated with LLJs is usually below the jet maximum. There is also strong near-surface shear cou-

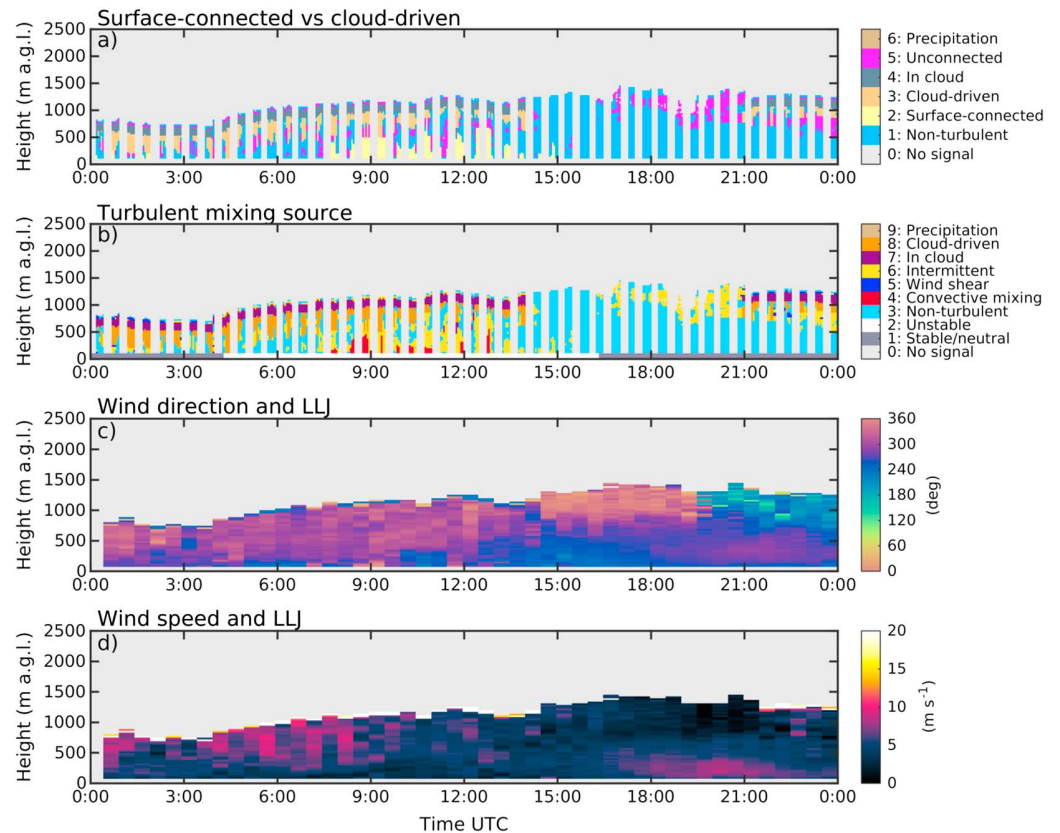


Figure 6. Time-height plots of ABL classification showing (a) connection with the surface (i.e., surface driven versus cloud driven) and (b) the turbulent mixing source, together with time-height plots of (c) wind direction and (d) wind speed on 22 September 2016 at Hyytiälä, Finland. Vertical gray lines in (a) and (b) indicate periods when the Doppler lidar was scanning. LLJ = low-level jet.

pled with turbulence detected between 00:00 and 4:00 UTC and between 18:00 and 24:00 UTC, presumably a result of the surface friction. These features are also captured in the classification product as wind shear and may be surface connected or unconnected. Turbulent features without an objectively determined source are labeled as intermittent. In this pixel-by-pixel approach we assume that convective mixing dominates any wind shear, since convection also manifests apparent wind shear at the 3-min resolution used here (due to updrafts and downdrafts being advected over the site). Outside convective regions, pixels classified as intermittent might also be a result of wind shear but not directly affected by wind shear. For interpreting wind shear-affected regions, temporal and spatial consistency of the classification should be considered, and the wind shear threshold sensitivity tests should be carried out at several sites.

Note that there are weak features that could be interpreted as decaying turbulence in Figure 3c, such as after 16:00 UTC up to 1 km, but since $\epsilon < 10^{-4} \text{ m}^2/\text{s}^3$ the decaying turbulence is labeled accordingly as nonturbulent in Figures 4a and 4b. This is a consequence of the relatively high fractional errors in dissipation rate for low ϵ values.

4.2. Cloud-Topped Case Study

Figure 5 displays the same lidar quantities as in Figure 3 calculated from the Halo lidar data for a nonprecipitating stratocumulus cloud-topped case in Hyytiälä, Finland. Exhibiting high attenuated backscatter ($\beta > 10^{-4} \text{ m}^{-1} \cdot \text{s}^{-1}$), the stratocumulus cloud layer is clearly visible in Figure 5a at altitudes ranging from 500 m between 00:00 and 04:00 UTC and rising to about 1,000 m by 06:00 UTC. The stratocumulus layer persists until 14:00 UTC and then reappears in the evening after 21:00 UTC, with clear skies in between. A deep layer of high dissipation rate ($\epsilon > 10^{-4} \text{ m}^2/\text{s}^3$) and negative skewness values is associated with the cloud layer and is not present during the clear-sky period in the afternoon. In the morning, between 00:00 and 05:00 UTC, this layer

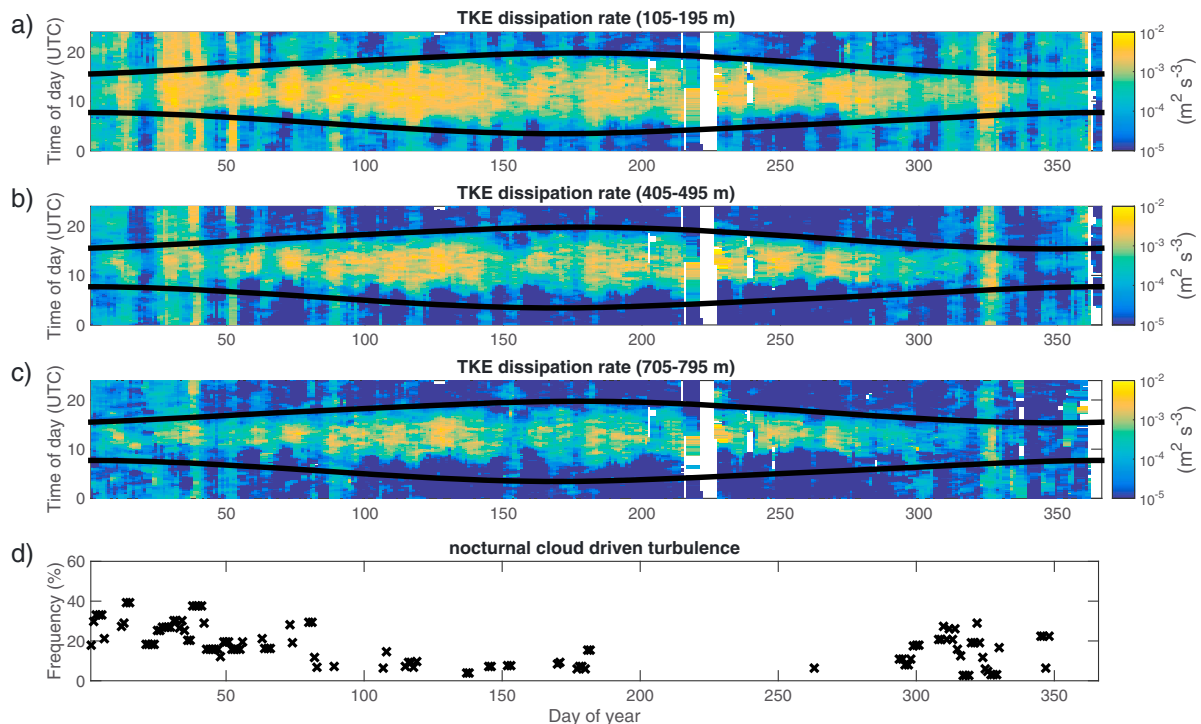


Figure 7. Time-of-day versus day-of-year plot of TKE dissipation rate ϵ values from Jülich, Germany, averaged over altitude ranges: (a) 105–195 m above ground level (agl), (b) 405–495 m agl, and (c) 705–795 m agl. Black lines in (a)–(c) show sunrise and sunset. Panel (d) presents the frequency of occurrence of nocturnal cloud-driven turbulence. A moving median filter of 5 days and 30 min has been applied to the data. Data period is between 1 May 2015 and 31 December 2016. TKE = turbulent kinetic energy.

can be seen to reach from cloud base down to about 200-m altitude between 00:00 and 05:00 UTC (Figures 5b and 5c), below which exists a layer with positive skewness values, indicating that although cloud-driven turbulent mixing dominates most of the ABL depth, it is not able to mix through to the surface. Once the cloud layer is not present, after 14:00 UTC, the turbulent mixing associated with the cloud also disappears rapidly, with the skewness values switching from negative to positive in the absence of any turbulent source. Negative skewness values return in the evening at 21:00 UTC and at 1,000 m when the stratocumulus layer reappears, with a turbulent layer growing below cloud base.

After sunrise at 04:24 UTC, a turbulent layer with positive skewness values indicating surface-driven mixing grows from the surface to reach 800 m by 14:00 UTC, before decaying again toward sunset at 16:29 UTC. Although relatively high dissipation rate values are present throughout much of the ABL between 00:00 and 15:00 UTC, strong gradients in vertical velocity skewness and dissipation rate suggest that there are two turbulent layers and little mixing across the boundary between them. These features are captured in the ABL classification product in Figure 6, which shows separate regions of mixing: one connected to clouds (cloud driven), one connected to the surface (surface connected) and associated with convective mixing. Cumulus clouds at 500 m in altitude are present around 12:00 UTC, and correctly identified by the classification as being surface connected, due to the positive skewness values and connection of the turbulent layer to the surface. There are also regions labeled intermittent or wind shear where the turbulent ABL has been identified, but, due to alternating positive and negative patterns observed in the vertical velocity skewness (e.g., between 22:00 and 23:00 UTC), the objective nature of the classification scheme does not issue a definitive association with the surface or cloud layer.

Hence, the classification scheme is able to distinguish between coupled and decoupled clouds, identify the layer of mixing associated with clouds and whether it dominates any surface-driven mixing, and aid in determining whether cumulus clouds formed underneath a stratocumulus cloud layer act to couple the stratocumulus layer to the surface (Krueger et al., 1995; Wood, 2012).

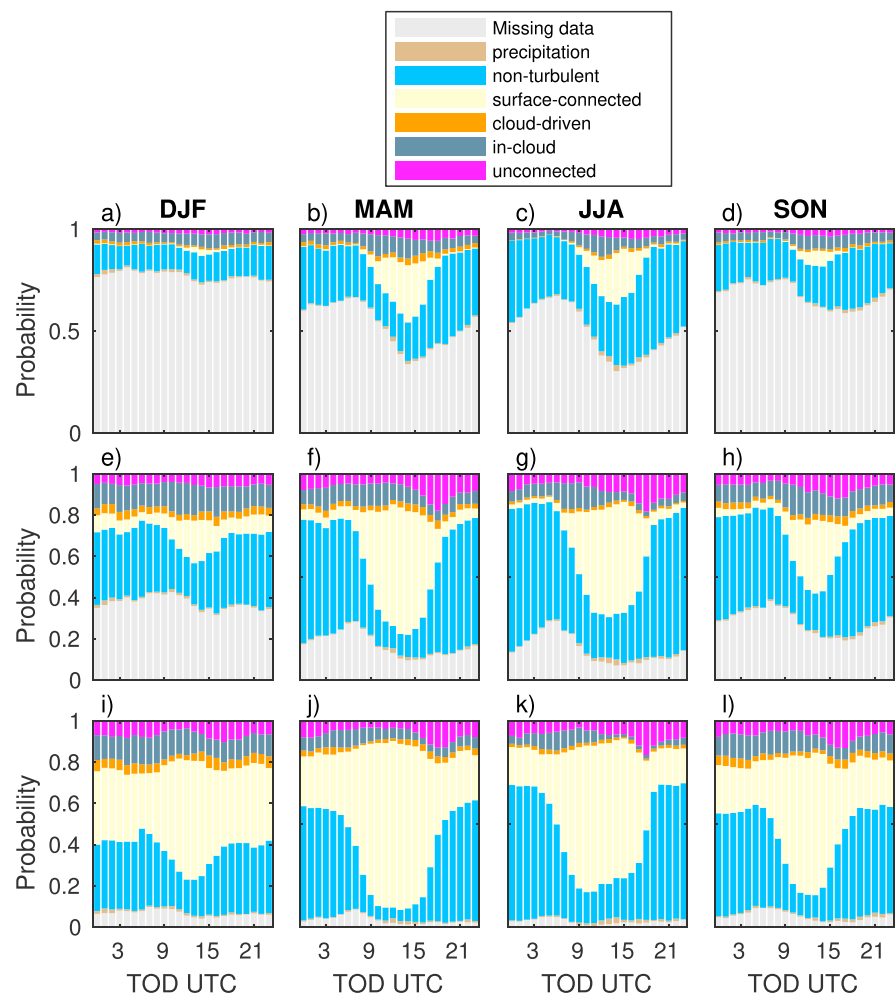


Figure 8. Seasonal average diurnal cycle of the probability of turbulence over Jülich, Germany, to be associated with the surface, cloud, or neither, calculated for three different height ranges: (a–d) 1,065–1,515 m above ground level (agl), (e–h) 585–1,035 m agl, and (i–l) 105–555 m agl. Measurement period covers 1 May 2015 to 31 December 2016. DJF = December–February; MAM = March–May; JJA = June–August; SON = September–November; TOD = time of day; UTC = universal time coordinated.

4.3. Climatological Analysis

Figure 7 displays TKE dissipation rate with respect to the time of day and day of year from Jülich, Germany. There is a clear diurnal and seasonal cycles, and the presence of strong dissipation rate generally lies between sunrise and sunset. The time lag between sunrise and the onset of turbulence increases with altitude, and, above 400 m, the atmosphere is typically calm before sunrise and after sunset. However, there are also periods where there is no diurnal cycle, visible in the plots as vertical bands of high dissipation rate, and these are connected to days where turbulence in the ABL is mainly driven by clouds (Figure 7d, which shows the percentage of nighttime profiles per day with at least one pixel of cloud-driven turbulence).

To investigate the seasonal changes in the diurnal cycle of the mixing in the ABL, the data sets from both sites were divided into four seasons: winter (December–February), spring (March–May), summer (June–August), and autumn (September–November). The seasonal changes in the diurnal cycle of the probability for the turbulence to be connected with the surface, or not, are shown for Jülich in Figure 8 and for Hyytiälä in Figure 9. In both figures, the statistics were calculated over three different altitude ranges, selected so that the ABL development at both sites could be compared despite the differences in their average daily maximum ABL height. The amount of missing data increases with altitude at both sites, as expected since SNR reduces with range, and signal is usually confined to the ABL. After background correction, the same conservative SNR

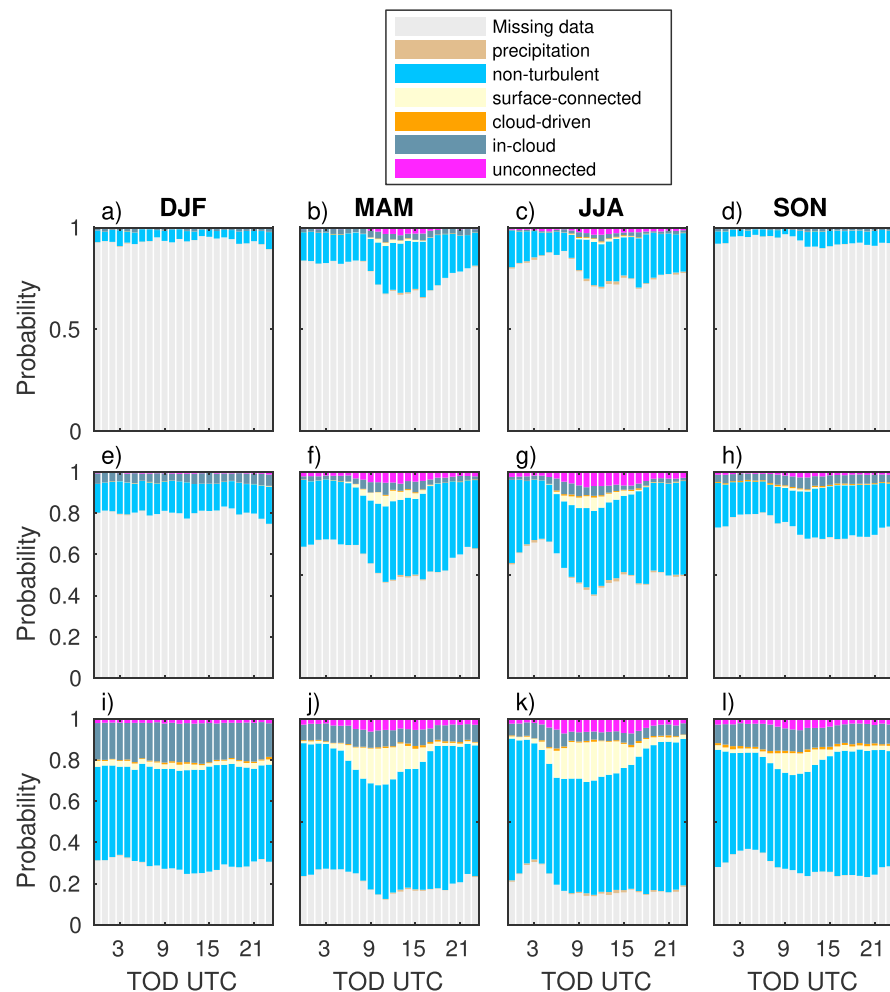


Figure 9. Seasonal average diurnal cycle of the probability of turbulence over Hyytiälä, Finland, to be associated with the surface, cloud, or neither, calculated for three different height ranges: (a–d) 1,065–1,515 m above ground level (agl), (e–h) 585–1,035 m agl, and (i–l) 105–555 m agl. Measurement period covers 1 September 2015 to 15 November 2016. DJF = December–February; MAM = March–May; JJA = June–August; SON = September–November; TOD = time of day; UTC = universal time coordinated.

threshold of -20 dB (0.01) was chosen for both sites; thus, the large difference in the amount of missing data between the sites portrays how much the aerosol loading impacts data availability. Jülich exhibits a clear seasonal and diurnal dependence in data availability for the highest altitude range, with most missing data during winter ($> 70\%$) and least during summer afternoons ($< 40\%$), directly responding to the large seasonal variation in ABL depth in the midlatitudes. At Hyytiälä, a high-latitude site, the amount of missing data is consistently above 70% for the highest altitude range in all seasons, and it is the medium altitude range that resembles more closely the upper altitude range at Jülich. The ABL does reach $1,500$ m in summer over Hyytiälä, but the corresponding dilution of the already low aerosol loading through the deeper ABL often results in SNR that is too weak to generate reliable lidar quantities for classification. The ABL height in winter at Hyytiälä rarely reaches 500 m, hence the very low data availability above 500 m.

During spring (Figures 8b, 8f, and 8j and 9b, 9f, and 9j) and summer (Figures 8c, 8g, and 8k and 9c, 9g, and 9k), both sites display a clear diurnal cycle in the probability of turbulence connected with the surface: high during the day (Jülich $> 80\%$ and Hyytiälä $> 30\%$) and low during nighttime (Jülich $< 20\%$ and Hyytiälä $< 10\%$). A similar but weaker diurnal cycle is evident at both sites during autumn (Figures 8l and 9l): high during the day (Jülich $> 60\%$ and Hyytiälä $> 20\%$) and low during nighttime (Jülich $< 20\%$ and Hyytiälä $< 10\%$).

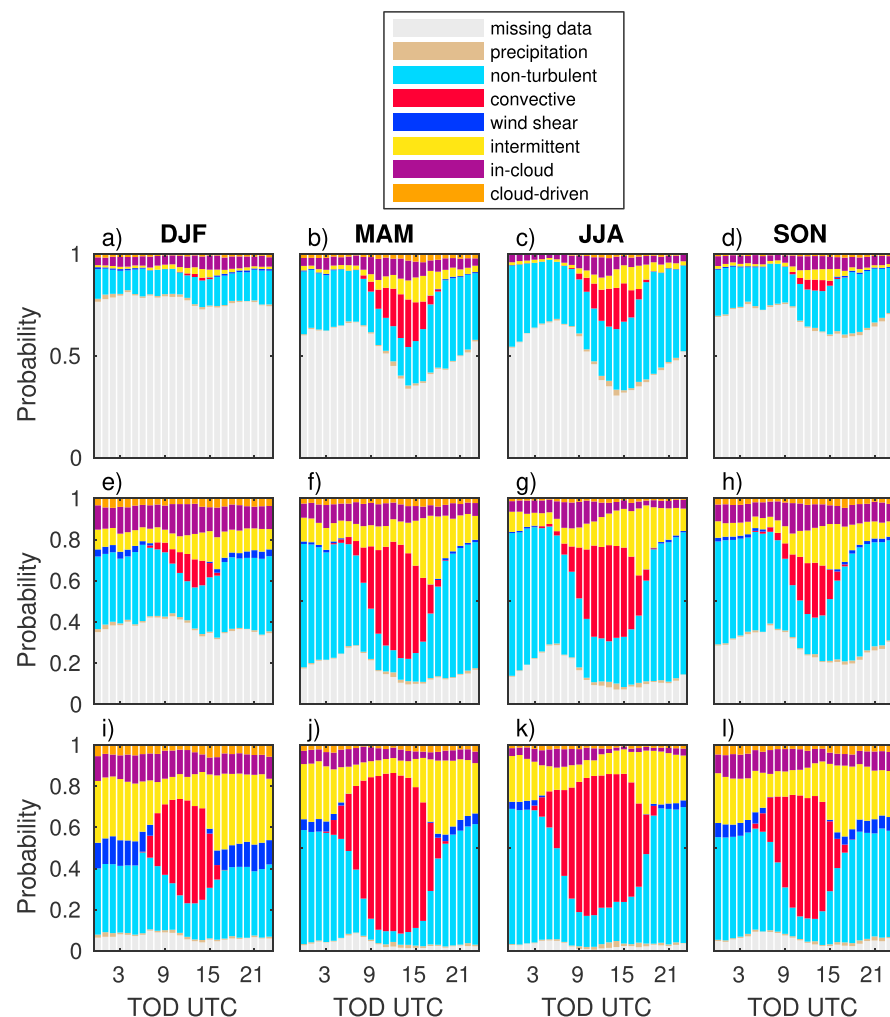


Figure 10. Seasonal average diurnal cycle of the probability for each identified source causing mixing in the atmospheric boundary layer over Jülich, Germany, calculated for three different height ranges: (a–d) 1,065–1,515 m above ground level (agl), (e–h) 585–1,035 m agl, and (i–l) 105–555 m agl. Measurement period covers 1 May 2015 to 31 December 2016. DJF = December–February; MAM = March–May; JJA = June–August; SON = September–November; TOD = time of day; UTC = universal time coordinated.

The probability for unconnected turbulence is highest during spring and summer, especially in the middle height range of 585–1,035 m above ground level (agl) and also noticeable at other height ranges at Jülich (Figures 8f and 8g) and also displays a weak diurnal cycle. This cycle is most obvious during summer, where the probability of unconnected turbulence increases during the afternoon around 18:00 UTC at Jülich. Hence, it is associated with the decay of what was the surface-driven convective mixing layer after the residual layer decouples from the surface. Diurnal cycle in the unconnected turbulence is weaker at Hyytiälä and only noticeable at the middle height range (Figures 9f and 9g).

Figures 8 and 9 also show that clouds influence mixing in the ABL at both sites. There is a strong seasonal variation in cloud presence at each altitude range, with Hyytiälä having probabilities above 30% in winter and 10% in summer at the lowest altitude range, but the diurnal variation is not so pronounced, especially in winter, spring, and autumn. In summer, there are fewer clouds during the day (Hyytiälä) or in late afternoon (Jülich) but these figures do not necessarily capture the full cloud cover, since there may be clouds associated with the ABL above the altitude range maximum (1,515 m agl) selected here.

In Figures 10 and 11 we investigate the seasonal and diurnal cycles in the source of mixing that has been assigned. These figures clearly show the strong diurnal variation in surface-connected convective mixing at

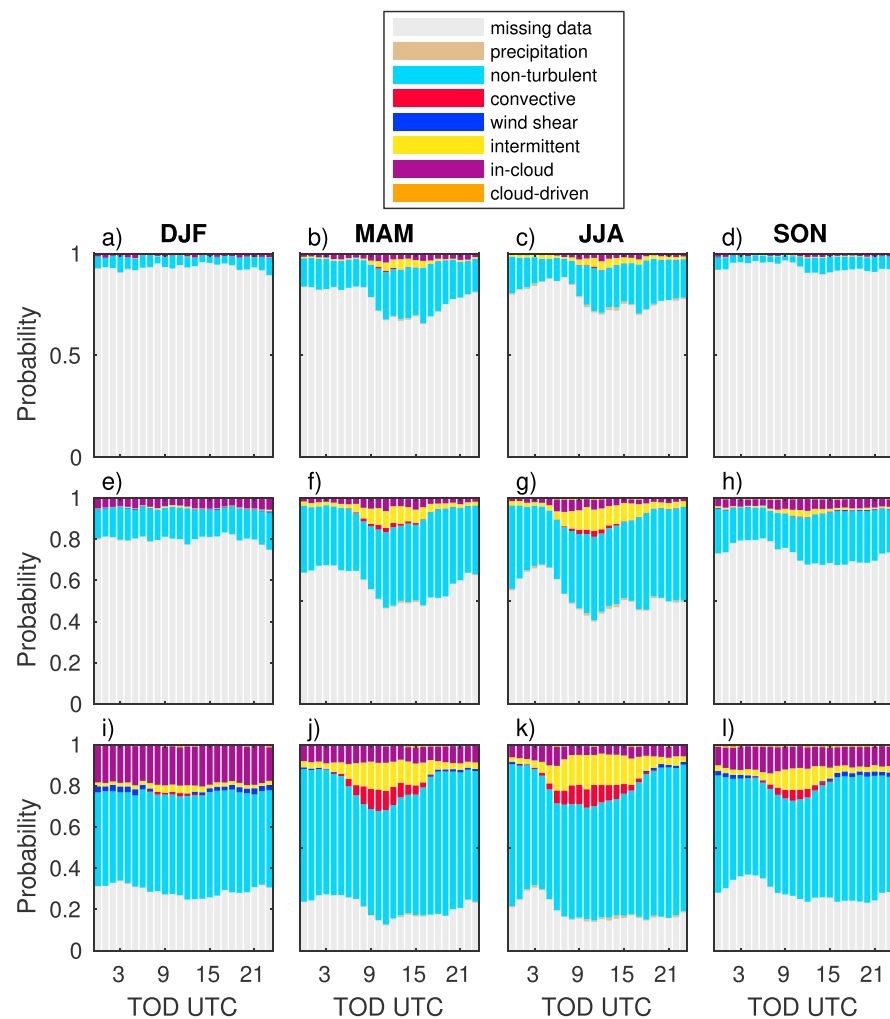


Figure 11. Seasonal average diurnal cycle of the probability for each identified source causing mixing in the atmospheric boundary layer over Hyytiälä, Finland, calculated for three different height ranges: (a–d) 1,065–1,515 m agl, (e–h) 585–1,035 m agl, and (i–l) 105–555 m agl. Measurement period covers 1 September 2015 to 15 November 2016. Measurement period covers 1 May 2015 to 31 December 2016. DJF = December–February; MAM = March–May; JJA = June–August; SON = September–November; TOD = time of day; UTC = universal time coordinated.

both sites and also show the variation in the convective boundary layer with the season. At Jülich, convective mixing at low altitudes clearly dominates ABL mixing during spring, summer, and autumn daytime, but the relative dominance decreases with increasing altitude. Figure 10 shows that convective mixing rarely reaches above 1 km in autumn and winter. A similar picture is seen in Hyytiälä (Figure 11), except that surface-driven convective mixing only dominates during spring and summer at low altitudes and rarely reaches 600 m during autumn and never in winter.

At both sites there is a significant fraction of the time where turbulent mixing is present in the lowest altitude range at night, close 20% in summer but exceeding 40% in winter. At Hyytiälä, most of the nighttime turbulence is associated with cloud, whereas at Jülich, there are larger contributions from other sources. Both sites show a clear seasonal variation in nighttime mixing associated with wind shear at low altitudes, with more observed during autumn and winter than during spring and summer. At Jülich, wind shear is diagnosed almost 10% of the time at night during winter, together with a much higher fraction of intermittent turbulence, where a source of mixing was not assigned. It is thought that LLJs may be partially responsible for the high occurrence of mixing close to the surface at night in Jülich.

Similar seasonal and diurnal variabilities in the extent of the mixed-layer were found over Jülich by Schween et al. (2014) and over Trainou in France by Pal et al. (2015), including the day-to-day variability. However, they limited their studies to identifying the mixed-layer height.

5. Conclusions

In this study, we present a method for objectively classifying turbulent mixing within the ABL using Doppler lidar. The method identifies the presence of turbulence and then assigns a turbulent source by combining several lidar quantities: attenuated backscatter coefficient, vertical velocity skewness, TKE dissipation rate, and vector wind shear. The range of complexity exhibited by ABL mixing was simplified by concentrating on only a finite number of classes and situations that can be identified reliably from Doppler lidar measurements. For instance, we have defined that convective mixing is surface-driven only, even though there are situations where elevated convection can also occur (Geerts et al., 2017).

The method operates in all weather conditions, both clear-sky and cloud-topped, and can provide an ABL classification at high temporal (3 min) and vertical resolution (30 m). The method was applied to extended data sets from Doppler lidar measurements at two locations in different environments, Jülich, Germany, and Hyttälä, Finland, and was shown to be capable of classifying complex ABL structures. Some limitations were identified, such as insufficient instrument sensitivity during periods with very low aerosol concentrations and difficulties in precipitation discrimination. Synergy with additional instruments would improve this classification method, through providing robust precipitation discrimination or determining the atmospheric thermodynamic stability (e.g., utilizing a vertical temperature gradient from a meteorological tower or the sensible heat flux from eddy covariance measurements). However, this method was designed to operate on Doppler lidar measurements alone since colocated supplementary measurements are not always available at every Doppler lidar site.

Statistical analysis of the data sets measured at Hyttälä and Jülich showed a very clear seasonal variation in the diurnal cycle for both the probability of turbulence to be associated with the surface, or not, and in the probability of the turbulent mixing source. For these sites, spring, summer, and autumn seasons display a clear diurnal cycle, with surface-driven convection a dominant source of mixing within the ABL during the day, as expected. In winter, as a consequence of their respective latitudes, the diurnal cycle is much weaker at Jülich and almost nonexistent at Hyttälä. However, there are significant contributions from other sources, with cloud-driven mixing being observed even within the first 500 m from the surface. Also evident is the considerable amount of nocturnal mixing within the lowest 500 m at both sites, especially during the winter. The presence of a LLJ was often detected when sources of nocturnal mixing were diagnosed as wind shear. LLJs are clearly an important source of mixing, promoting mixing especially below the jet.

The classification scheme and the climatology extracted from the classification provide insight into the processes responsible for mixing within the ABL, how variable in space and time these can be, and how they vary with location.

Acknowledgments

The data supporting the analysis and conclusions can be accessed at <https://doi.org/10.5281/zenodo.1249433>. This work was partly supported by the European Commission via projects ACTRIS and ACTRIS2, U.S. Department of Energy via the Office of Science (BER), and Academy of Finland via Center of Excellence in Atmospheric Sciences. M. Tuononen was supported by the Maj ja Tor Nesslingin Säätiö (grants 201500300 and 201600003). This work was also supported by the Academy of Finland Center of Excellence programme (grant 307331) and the U.S. Department of Energy (grant DE-SC0017338). Contribution to the instrumentation of JOYCE and its maintenance, as well as the funding of T. Marke, is realized by the Transregional Collaborative Research Center (TR32) *Patterns in Soil-Vegetation-Atmosphere Systems*, which is funded by the German Science Foundation (DFG).

References

- Baars, H., Ansmann, A., Engelmann, R., & Althausen, D. (2008). Continuous monitoring of the boundary-layer top with lidar. *Atmospheric Chemistry and Physics*, 8, 7281–7296. <https://doi.org/10.5194/acp-8-7281-2008>
- Baklanov, A. A., Grisogono, B., Bornstein, R., Mahrt, L., Zilitinkevich, S. S., Taylor, P., et al. (2011). The nature, theory, and modeling of atmospheric planetary boundary layers. *Bulletin of the American Meteorological Society*, 92, 123–128. <https://doi.org/10.1175/2010BAMS2797.1>
- Banta, R. M., Pichugina, Y. L., & Brewer, W. A. (2006). Turbulent velocity-variance profiles in the stable boundary layer generated by a nocturnal low-level jet. *Journal of the atmospheric sciences*, 63, 2700–2719.
- Barlow, J. F., Dunbar, T. M., Nemitz, E. G., Wood, C. R., Gallagher, M. W., Davies, F., et al. (2011). Boundary layer dynamics over London, UK, as observed using Doppler lidar during REPAREE-II. *Atmospheric Chemistry and Physics*, 11, 2111–2125. <https://doi.org/10.5194/acp-11-2111-2011>
- Bonin, T. A., Carroll, B. J., Hardesty, R. M., Brewer, W. A., Hajny, K., Salmon, O. E., & Shepson, P. B. (2018). Doppler lidar observations of the mixing height in Indianapolis using an automated composite fuzzy logic approach. *Journal of Atmospheric and Oceanic Technology*, 35, 473–490. <https://doi.org/10.1175/JTECH-D-17-0159.1>, <http://journals.ametsoc.org/doi/10.1175/JTECH-D-17-0159.1>
- Borquez, P., Luke, E., & Kollias, P. (2016). On the unified estimation of turbulence eddy dissipation rate using Doppler cloud radars and lidars: Radar and lidar turbulence estimation. *Journal of Geophysical Research: Atmospheres*, 121, 5972–5989. <https://doi.org/10.1002/2015JD024543>
- Cuxart, J., & Jiménez, M. A. (2007). Mixing processes in a nocturnal low-level jet: An LES study. *Journal of the Atmospheric Sciences*, 64, 1666–1679. <https://doi.org/10.1175/JAS3903.1>
- Deardorff, J. W. (1972). Numerical investigation of neutral and unstable planetary boundary layers. *Journal of the Atmospheric Sciences*, 29, 91–115. [https://doi.org/10.1175/1520-0469\(1972\)029<0091:NIONAU>2.0.CO;2](https://doi.org/10.1175/1520-0469(1972)029<0091:NIONAU>2.0.CO;2)

- Emeis, S., Schäfer, K., & Munkel, C. (2008). Surface-based remote sensing of the mixing-layer height—A review. *Meteorologische Zeitschrift*, 17, 621–630. <https://doi.org/10.1127/0941-2948/2008/0312>
- Frehlich, R., & Cornman, L. (2002). Estimating spatial velocity statistics with coherent Doppler lidar. *Journal of Atmospheric and Oceanic Technology*, 19, 355–366. <https://doi.org/10.1175/1520-0426-19.3.355>
- Fuentes, J. D., Chamecki, M., Nascimento dos Santos, R. M., Von Randow, C., Stoy, P. C., Katul, G., et al. (2016). Linking meteorology, turbulence, and air chemistry in the Amazon rain forest. *Bulletin of the American Meteorological Society*, 97, 2329–2342. <https://doi.org/10.1175/BAMS-D-15-00152.1>
- GDAS (2016). Global Data Assimilation System.
- Garraff, J. (1994). Review: The atmospheric boundary layer. *Earth-Science Reviews*, 37, 89–134. [https://doi.org/10.1016/0012-8252\(94\)90026-4](https://doi.org/10.1016/0012-8252(94)90026-4)
- Geerts, B., Parsons, D., Ziegler, C. L., Weckwerth, T. M., Biggerstaff, M. I., Clark, R. D., et al. (2017). The (2015), plains elevated convection at night field project. *Bulletin of the American Meteorological Society*, 98, 767–786. <https://doi.org/10.1175/BAMS-D-15-00257.1>
- Hari, P., & Kulmala, M. (2005). Station for measuring ecosystem-atmosphere relations (SMEAR II). *Boreal Environment Research*, 10, 315–322.
- Harvey, N. J., Hogan, R. J., & Dacre, H. F. (2013). A method to diagnose boundary-layer type using Doppler lidar: A method to diagnose boundary-layer type. *Quarterly Journal of the Royal Meteorological Society*, 139, 1681–1693. <https://doi.org/10.1002/qj.2068>
- Hirsikko, A., O'Connor, E. J., Komppula, M., Korhonen, K., Pfüller, A., Giannakaki, E., et al. (2014). Observing wind, aerosol particles, cloud and precipitation: Finland's new ground-based remote-sensing network. *Atmospheric Measurement Techniques*, 7, 1351–1375. <https://doi.org/10.5194/amt-7-1351-2014>
- Hogan, R. J., Grant, A. L. M., Illingworth, A. J., Pearson, G. N., & O'Connor, E. J. (2009). Vertical velocity variance and skewness in clear and cloud-topped boundary layers as revealed by Doppler lidar. *Quarterly Journal of the Royal Meteorological Society*, 135, 635–643. <https://doi.org/10.1002/qj.413>
- Holtzlag, A. A. M., Svensson, G., Baas, P., Basu, S., Beare, B., Beljaars, A. C. M., et al. (2013). Stable atmospheric boundary layers and diurnal cycles: Challenges for weather and climate models. *Bulletin of the American Meteorological Society*, 94, 1691–1706. <http://journals.ametsoc.org/doi/abs/10.1175/BAMS-D-11-00187.1>
- ICAO (2005). Manual on low-level wind shear (Tech. Rep.). International Civil Aviation Organization.
- Ibrahim, R., & Afshin, A. (2008). Solar position algorithm for solar radiation applications (Tech. Rep. NREL/TP-560-34302). National Renewable Energy Laboratory NREL.
- Kaimal, J. C., & Finnigan, J. J. (1994). *Atmospheric boundary layer flows: Their structure and measurement*. New York, NY: Oxford University Press.
- Ketzler, G. (2014). The diurnal temperature cycle and its relation to boundary-layer structure during the morning transition. *Boundary-Layer Meteorology*, 151, 335–351. <https://doi.org/10.1007/s10546-013-9898-7>, <http://link.springer.com/10.1007/s10546-013-9898-7>
- Kleiner, A., Talwalkar, A., Sarkar, P., & Jordan, M. I. (2014). A scalable bootstrap for massive data. *Journal of the Royal Statistical Society: Series B (Statistical Methodology)*, 76, 795–816. <https://doi.org/10.1111/rssb.12050>, <http://doi.wiley.com/10.1111/rssb.12050>
- Krueger, S. K., McLean, G. T., & Fu, Q. (1995). Numerical simulation of the stratus-to-cumulus transition in the subtropical marine boundary layer. Part II: Boundary-layer circulation. *Journal of the Atmospheric Sciences*, 52, 2851–2868. [https://doi.org/10.1175/1520-0469\(1995\)052<2851:NSOTST>2.0.CO;2](https://doi.org/10.1175/1520-0469(1995)052<2851:NSOTST>2.0.CO;2)
- Lothou, M., Lohou, F., Pino, D., Couvreur, F., Pardyjak, E. R., Reuder, J., et al. (2014). The BLLAST field experiment: Boundary-layer late afternoon and sunset turbulence. *Atmospheric Chemistry and Physics*, 14, 10,931–10,960. <https://doi.org/10.5194/acp-14-10931-2014>, <http://www.atmos-chem-phys.net/14/10931/2014/>
- Manninen, A. J., O'Connor, E. J., Vakkari, V., & Petäjä, T. (2016). A generalised background correction algorithm for a Halo Doppler lidar and its application to data from Finland. *Atmospheric Measurement Techniques*, 9, 817–827. <https://doi.org/10.5194/amt-9-817-2016>
- Moeng, C.-H., & Sullivan, P. P. (1994). A comparison of shear- and buoyancy-driven planetary boundary layer flows. *Journal of the Atmospheric Sciences*, 51, 999–1022. [https://doi.org/10.1175/1520-0469\(1994\)051<0999:ACOSAB>2.0.CO;2](https://doi.org/10.1175/1520-0469(1994)051<0999:ACOSAB>2.0.CO;2)
- Newsom, R. K., Brewer, W. A., Wilczak, J. M., Wolfe, D. E., Oncley, S. P., & Lundquist, J. K. (2017). Validating precision estimates in horizontal wind measurements from a Doppler lidar. *Atmospheric Measurement Techniques*, 10, 1229–1240. <https://doi.org/10.5194/amt-10-1229-2017>
- O'Connor, E. J., Hogan, R. J., & Illingworth, A. J. (2005). Retrieving stratocumulus drizzle parameters using Doppler radar and lidar. *Journal of Applied Meteorology*, 44, 14–27.
- O'Connor, E. J., Illingworth, A. J., Brooks, I. M., Westbrook, C. D., Hogan, R. J., Davies, F., & Brooks, B. J. (2010). A method for estimating the turbulent kinetic energy dissipation rate from a vertically pointing Doppler lidar, and independent evaluation from balloon-borne in situ measurements. *Journal of Atmospheric and Oceanic Technology*, 27, 1652–1664. <https://doi.org/10.1175/2010JTECHA1455.1>
- Oke, T. R. (1992). *Boundary layer climates*, Routledge, London; New York, 2nd edn.
- Pal, S., Lopez, M., Schmidt, M., Ramonet, M., Gibert, F., Xueref-Remy, I., & Ciais, P. (2015). Investigation of the atmospheric boundary layer depth variability and its impact on the 222 Rn concentration at a rural site in France: Impact of ABL depth variability on radon. *Journal of Geophysical Research: Atmospheres*, 120, 623–643. <https://doi.org/10.1002/2014JD022322>
- Päschke, E., Leinweber, R., & Lehmann, V. (2015). An assessment of the performance of a 1.5 µm Doppler lidar for operational vertical wind profiling based on a 1-year trial. *Atmospheric Measurement Techniques*, 8, 2251–2266. <https://doi.org/10.5194/amt-8-2251-2015>
- Pearson, G., Davies, F., & Collier, C. (2009). An analysis of the performance of the UFAM pulsed Doppler lidar for observing the boundary layer. *Journal of Atmospheric and Oceanic Technology*, 26, 240–250. <https://doi.org/10.1175/2008JTECHA1128.1>
- Pearson, G., Davies, F., & Collier, C. (2010). Remote sensing of the tropical rain forest boundary layer using pulsed Doppler lidar. *Atmospheric Chemistry and Physics*, 10, 5891–5901. <https://doi.org/10.5194/acp-10-5891-2010>
- Rimoldini, L. (2014). Weighted skewness and kurtosis unbiased by sample size and Gaussian uncertainties. *Astronomy and Computing*, 5, 1–8. <https://doi.org/10.1016/j.ascom.2014.02.001>, <http://linkinghub.elsevier.com/retrieve/pii/S2213133714000092>
- Rye, B. J., & Hardesty, R. M. (1993). Discrete spectral peak estimation in incoherent backscatter heterodyne lidar. I. Spectral accumulation and the Cramer-Rao lower bound. *Geoscience and Remote Sensing, IEEE Transactions on*, 31, 16–27. <https://doi.org/10.1109/36.210440>
- Schween, J. H., Hirsikko, A., Löhnert, U., & Crewell, S. (2014). Mixing-layer height retrieval with ceilometer and Doppler lidar: From case studies to long-term assessment. *Atmospheric Measurement Techniques*, 7, 3685–3704. <https://doi.org/10.5194/amt-7-3685-2014>
- Smalikho, I. N., & Banakh, V. A. (2017). Measurements of wind turbulence parameters by a conically scanning coherent Doppler lidar in the atmospheric boundary layer. *Atmospheric Measurement Techniques*, 10, 4191–4208. <https://doi.org/10.5194/amt-10-4191-2017>
- Su, J., Felton, M., Lei, L., McCormick, M. P., Delgado, R., & St. Pé, A. (2016). Lidar remote sensing of cloud formation caused by low-level jets: Cloud formation caused by low-level jets. *Journal of Geophysical Research: Atmospheres*, 121, 5904–5911. <https://doi.org/10.1002/2015JD024590>

- Träumner, K., Kottmeier, C., Corsmeier, U., & Wieser, A. (2011). Convective boundary-layer entrainment: Short review and progress using Doppler lidar. *Boundary-Layer Meteorology*, 141, 369–391. <https://doi.org/10.1007/s10546-011-9657-6>
- Tucker, S. C., Senff, C. J., Weickmann, A. M., Brewer, W. A., Banta, R. M., Sandberg, S. P., et al. (2009). Doppler lidar estimation of mixing height using turbulence, shear, and aerosol profiles. *Journal of Atmospheric and Oceanic Technology*, 26, 673–688. <https://doi.org/10.1175/2008JTECHA1157.1>
- Tuononen, M., O'Connor, E. J., Sinclair, V. A., & Vakkari, V. (2017). Low-level jets over Utö, Finland, based on Doppler lidar observations. *Journal of Applied Meteorology and Climatology*, 56, 2577–2594. <https://doi.org/10.1175/JAMC-D-16-0411.1>
- Vakkari, V., O'Connor, E. J., Nisantzi, A., Mamouri, R. E., & Hadjimitsis, D. G. (2015). Low-level mixing height detection in coastal locations with a scanning Doppler lidar. *Atmospheric Measurement Techniques*, 8, 1875–1885. <https://doi.org/10.5194/amt-8-1875-2015>
- Westbrook, C. D., Illingworth, A. J., O'Connor, E. J., & Hogan, R. J. (2010). Doppler lidar measurements of oriented planar ice crystals falling from supercooled and glaciated layer clouds. *Quarterly Journal of the Royal Meteorological Society*, 136, 260–276. <https://doi.org/10.1002/qj.528>
- Wood, R. (2012). Stratocumulus clouds. *Monthly Weather Review*, 140, 2373–2423. <https://doi.org/10.1175/MWR-D-11-00121.1>

3 LOW-LEVEL JET CLIMATOLOGY

LONG-TERM OBSERVATIONS AND HIGH-RESOLUTION MODELING OF MID-LATITUDE NOCTURNAL BOUNDARY LAYER PROCESSES CONNECTED TO LOW-LEVEL JETS

T. Marke, S. Crewell, V. Schemann, J. Schween, and M. Tuononen (2018). “Long-term observations and high-resolution modeling of midlatitude nocturnal boundary layer processes connected to low-level jets”. In: *Journal of Applied Meteorology and Climatology* 57.5. DOI: [10.1175/JAMC-D-17-0341.1](https://doi.org/10.1175/JAMC-D-17-0341.1)
© 2018 American Meteorological Society.

Long-Term Observations and High-Resolution Modeling of Midlatitude Nocturnal Boundary Layer Processes Connected to Low-Level Jets

TOBIAS MARKE, SUSANNE CREWELL, VERA SCHEMANN, AND JAN H. SCHWEEN

Institute for Geophysics and Meteorology, University of Cologne, Cologne, Germany

MINTTU TUONONEN

Finnish Meteorological Institute, Helsinki, and Vaisala Oyj, Vantaa, and Department of Physics, University of Helsinki, Helsinki, Finland

(Manuscript received 6 December 2017, in final form 9 March 2018)

ABSTRACT

Low-level-jet (LLJ) periods are investigated by exploiting a long-term record of ground-based remote sensing Doppler wind lidar measurements supported by tower observations and surface flux measurements at the Jülich Observatory for Cloud Evolution (JOYCE), a midlatitude site in western Germany. LLJs were found 13% of the time during continuous observations over more than 4 yr. The climatological behavior of the LLJs shows a prevailing nighttime appearance of the jets, with a median height of 375 m and a median wind speed of 8.8 m s^{-1} at the jet nose. Significant turbulence below the jet nose only occurs for high bulk wind shear, which is an important parameter for describing the turbulent characteristics of the jets. The numerous LLJs (16% of all jets) in the range of wind-turbine rotor heights below 200 m demonstrate the importance of LLJs and the associated intermittent turbulence for wind-energy applications. Also, a decrease in surface fluxes and an accumulation of carbon dioxide are observed if LLJs are present. A comprehensive analysis of an LLJ case shows the influence of the surrounding topography, dominated by an open pit mine and a 200-m-high hill, on the wind observed at JOYCE. High-resolution large-eddy simulations that complement the observations show that the spatial distribution of the wind field exhibits variations connected with the orographic flow depending on the wind direction, causing high variability in the long-term measurements of the vertical velocity.

1. Introduction

One of the dominant nocturnal atmospheric boundary layer processes over land areas is the decoupling of the lower troposphere from the friction-governed surface layer, leading to the formation of a distinct maximum in the vertical profile of the horizontal wind speed, called a low-level jet (LLJ). The nighttime development of a stable surface layer results in a decrease in surface friction in the decoupled residual layer above and hence an inertial oscillation (Blackadar 1957). The wind speed maximum of LLJs is typically found between 100 and 1000 m (Tuononen et al. 2015), and the wind shear below this jet maximum leads to the generation of turbulence (Banta et al. 2002). Turbulent motions related to the LLJs are often intermittent and highly energetic, which is crucial for wind-energy applications (Emeis et al.

2007; Peña et al. 2016). Especially in the region of the rotor height, LLJ events can have an impact on the performance and lifetime of a wind turbine (Zhou and Chow 2012). On the other hand, the increased wind speed makes places with frequently occurring LLJs, such as the Great Plains region, favorable for wind-energy production (Storm et al. 2009).

LLJs can also be associated with local transport of aerosols and water vapor, controlling the evolution of clouds and precipitation by horizontal convergence and uplifting of atmospheric constituents (Su et al. 2016). The transferring motions and moisture transport between the surface and the atmosphere also directly affect synoptic-scale systems, leading to changes in precipitation patterns (Higgins et al. 1997). At the surface, the momentum decoupling during nighttime LLJs can reduce surface fluxes, leading to an accumulation of atmospheric gases (Mathieu et al. 2005). This process is limited by intermittent turbulence that reaches the surface and hence weakens the stabilization and depth of

Corresponding author: Tobias Marke, tmarke@meteo.uni-koeln.de

the nocturnal boundary layer. The correct representation of LLJ-related turbulence effects is therefore crucial for predictions in atmospheric weather and climate models at different resolutions (Stensrud 1996; Holtslag et al. 2013).

The forcing mechanisms of continental LLJs in the midlatitudes have been extensively studied, especially in the Great Plains (Mitchell et al. 1995; Zhong et al. 1996), and a more complete review can be found in Stensrud (1996). The identification of LLJs in earlier studies was based on radiosonde observations (Bonner 1968; Whiteman et al. 1997) or meteorological-tower measurements (Dörenkämper et al. 2015). Even though these observations provide good vertical resolution, they are lacking in temporal resolution (radiosondes) and vertical extent (towers). Therefore, many previous studies have utilized remotely sensing radio acoustic or (ultra-high frequency) radar wind profilers to obtain detailed case analyses and continuous long-term records of LLJs (e.g., Baas et al. 2009; Lampert et al. 2016; Mitchell et al. 1995). Doppler wind lidars (DWLs), which are an emerging tool in ground-based remote sensing networks such as the European Earth System Science and Environmental Management European Cooperation in Science and Technology (COST) Action ES1303 network or the ground-based remote sensing network in Finland (Hirsikko et al. 2014), show considerable potential for observing winds and turbulent parameters at high spatial and temporal resolution. The study by Tuononen et al. (2017) showed the capability of a DWL to identify LLJs for a multiyear dataset, and Lampert et al. (2015) used a 1-yr dataset to derive statistics related to LLJ occurrence and parameters of the Weibull distribution. By continuously providing accurate estimates of the vertical wind component, DWLs are furthermore able to quantify turbulent motions (O'Connor et al. 2010) and detect clouds and the aerosol layer.

In this study, long-term (2012–16) DWL measurements at the Jülich Observatory for Cloud Evolution (JOYCE; Löhnert et al. 2015) in western Germany are used together with a detailed case analysis, combining ground-based remote sensing, radiosondes (RS), and large-eddy simulation (LES) model output, to investigate local nocturnal boundary layer processes. The research focus of this study encompasses the climatological behavior (or “climatology”) of LLJs, their turbulence characteristics, and their influence on the surface fluxes using a long-term record of DWL, tower, and eddy-covariance (EC) measurements. A detailed case analysis reveals the local LLJ effects related to the topography by observations and LES. The chosen case analysis was carried out during the High Definition Cloud and Precipitation for Advancing

Climate Prediction [HD(CP)²] Observational Prototype Experiment (HOPE) field campaign in April and May of 2013 (Macke et al. 2017). The HOPE campaign was conducted to provide ground-based information on land surface–atmosphere interactions including clouds and precipitation in the boundary layer and to evaluate the LES extension of the atmospheric Icosahedral Non-hydrostatic (ICON) model (Dipankar et al. 2015).

This article is built in the following way. Section 2 describes the measurement site, including the deployed instruments utilized in this study. Subsequently in section 3 the dataset of the DWL is introduced together with the LLJ identification and the model setup. The results of the LLJ climatology, the turbulence characteristics, and the surface fluxes are presented and discussed in section 4, followed by the case analysis during the HOPE campaign that investigates topographic effects supported by LES in section 5. A summary is given and conclusions about the presented results are drawn in section 6.

2. Description of measurement site and instruments

a. JOYCE site and supporting instruments

The observational data are provided by the JOYCE site located in western Germany (50°54′31″N, 6°24′49″E at 111 m MSL; Fig. 1a), which is operated jointly by the Institute for Geophysics and Meteorology at the University of Cologne, the Meteorological Institute of the University of Bonn, and the Institute of Energy and Climate Research (IEK-8) at the Forschungszentrum Jülich. The JOYCE supersite is embedded in a rural environment with different crop types and provides a constantly growing multiyear dataset for detailed insight into boundary layer processes and patterns related to surface conditions (Löhnert et al. 2015). The mostly flat topography is dominated by two open-pit mines east and southwest of the site and a mine dump hill (Sophienhöhe), 200 m higher than the JOYCE site, to the northeast (Fig. 1c). A plain at around 100 m MSL stretches from southeast to northwest, including a riverbed of the Rur River and with a slight slope to the northwest. Together with the Eifel region, which is approximately 20 km to the south with hills of around 800 m MSL (Fig. 1b), the valley shows a potential channeling effect of the wind, with the Sophienhöhe as a northeast border. In a circle of 1 km around the JOYCE site, the topography shows a maximum height of 120.3 m MSL and a standard deviation of 5.7 m. The maximum height increases to 296.6 m MSL with a standard deviation of 48.9 m for a 5-km circle.

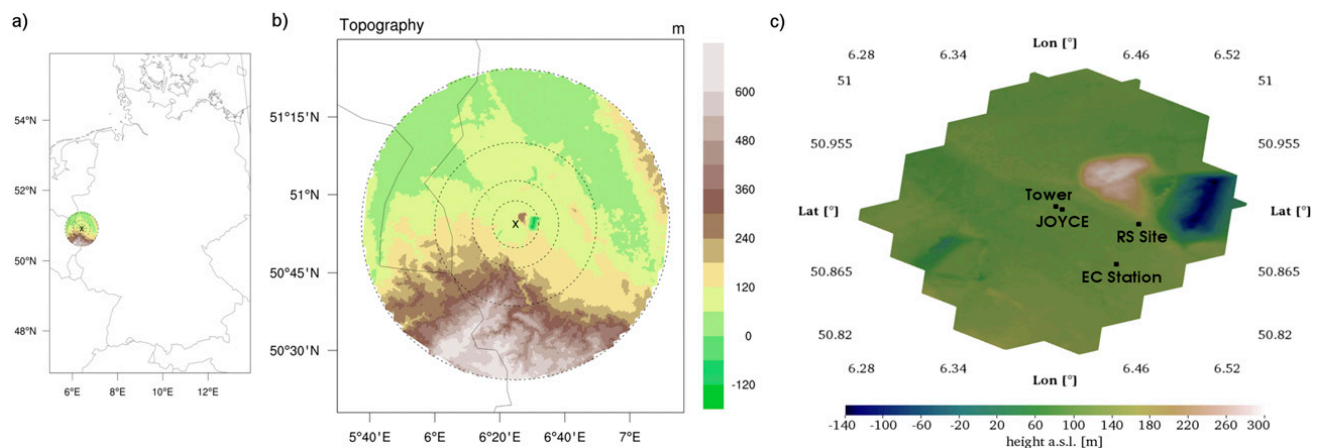


FIG. 1. (a) Location and (b) topographic maps of the ICON-LEM circular domains and the position of the JOYCE site (black X) within Germany. (c) A segment of the innermost domain (10-km radius and 78-m horizontal resolution) centered around the JOYCE site, also indicating the measurement sites and instruments deployed in this study.

The majority of the JOYCE instrumentation has been operational since 2012 and includes a DWL, cloud radar, microwave radiometer, and ceilometer. The long-term and continuous dataset of JOYCE provides temporal highly resolved cloud micro- and macrophysical observations, as well as a characterization of the environment in which they evolve. As an additional observational support during the HOPE campaign, from two to seven radiosonde launches per day were conducted from a nearby station. The launch site of the radiosondes (labeled as “RS Site” in Fig. 1) is located 3.8 km east of the site at the southeastern corner of the Sophienhöhe.

A 120-m-high meteorological tower is located approximately 330 m northwest of JOYCE (labeled as “Tower” in Fig. 1). The tower is equipped with cup anemometers and wind vanes at 30, 50, and 120 m, allowing simultaneous measurement of the wind speed and the wind direction. To observe the atmosphere–land surface interactions, several EC stations are deployed around JOYCE. For this study, the EC station at the agricultural flatland site Selhausen is used, which is located 5 km southeast of the JOYCE site (labeled as “EC Station” in Fig. 1). The measurement devices (sonic anemometer and open-path gas analyzer) are deployed at a height of 2.46 m above the ground. The averaging interval of the data obtained with a measurement frequency of 20 Hz is set to 30 min, and the quality assessment and quality control of the measurements, together with the instrument setup, are explained in Mauder et al. (2013).

b. Doppler wind lidar

The Halo Photonics Streamline DWL (Pearson et al. 2009), the main instrument for this study, was installed on the roof of the IEK-8 building, which is referred to as the JOYCE site. The DWL measures the backscattered

light from an emitted laser beam at $1.5 \mu\text{m}$. The analysis of the Doppler shift provides an estimate of the wind speed along the line of sight. The combination of several inclined beams allows the derivation of the three components of the wind vector and therefore also the wind direction. The attenuated backscatter coefficient can be calculated by the amount of received backscattered light, which mainly depends on the number and size of aerosol and/or cloud particles in the measured volume.

At JOYCE the DWL operational schedule consists of four conical scans per hour with 36 beams at 75° elevation and a duration of approximately 3 min. This velocity azimuth display method provides accurate wind estimates, even in turbulent situations (Päschke et al. 2015). For the remainder of the hour, the instrument points vertically, with a temporal resolution of 1.67 s. The vertical measurements provide profiles of the vertical velocity, which in turn can be used for turbulence estimates by calculating the standard deviation for each range gate (Schween et al. 2014). The vertical resolution is 30 m, with the first reliable range gate, as determined by the signal-to-noise ratio, usually at 105 m above the instrument (fourth range gate).

3. Data and methods

The DWL at JOYCE has been measuring continuously since March of 2012, and the LLJ classification, described in the following section, was applied through the end of 2016. Because of measurement gaps, the resulting dataset contains 1518 days of DWL observations that are analyzed in this study. The HOPE campaign at JOYCE was conducted from 3 April to 31 May 2013 to study the frequently occurring formation of boundary layer cloud during the spring season.

a. Low-level jet detection

In previous studies various criteria were used to detect LLJs in long-term observations to compile an LLJ climatology. In the study by [Bonner \(1968\)](#), LLJs are identified by detecting a wind speed maximum and a 50% decrease above the jet in the lowest 3 km. The LLJ detection algorithm of [Baas et al. \(2009\)](#) uses an absolute and relative criterion for the wind speed maximum and the corresponding minimum above, which is also used in a similar way in [Lampert et al. \(2015\)](#).

In this study, the LLJ identification of [Tuononen et al. \(2017\)](#) is applied to the DWL measurements between 2012 and 2016. In addition, tower measurements at 30 and 50 m are used to fill the observational gap of the DWL below 105 m. A comparison of hourly averaged wind speed measurements during nighttime at 120 m from the tower and the DWL vertical profile reveals a high correlation of 0.95 during the observational period (not shown). Despite the high correlation, the tower measurements are only used when the wind speed difference to the DWL at 120 m does not exceed 2 m s^{-1} . In this way, false classifications due to large deviations between the tower and DWL can be avoided, as a smooth transition of the wind speed between the tower and DWL is ensured and about 13% of the otherwise detected LLJs are neglected.

The LLJ identification algorithm requires a relative and an absolute criterion to be fulfilled to detect an LLJ. The maximum wind speed in each profile must be at least 2 m s^{-1} higher and 25% stronger than the minimum above and below the jet between 30 and 1485 m. In this way small variations in weak wind situations and turbulent fluctuations for stronger winds are prevented from being falsely identified as an LLJ.

After this first step of LLJ identification, the following consistency checks are applied to distinguish between a temporal and spatial continuation of an LLJ and a newly formed LLJ. For an LLJ continuation, the strength and direction of the LLJ maximum should not change by more than 30% and 45° , respectively, between two consecutive profiles measured every 15 min and the LLJ height should stay within four range gates (120 m). In addition to the algorithm of [Tuononen et al. \(2017\)](#), it is required that no data gaps occur between two detected wind speed maxima. Only coherent LLJs that are persistent for at least 1 h are considered. The LLJ speed and direction in this study refer to the measured value at the location of the wind speed maximum, which is referred to as the LLJ height or jet nose.

b. ICON-LEM

The ICON model ([Zängl et al. 2015](#)) was developed in a collaboration between the German Weather Service

[Deutscher Wetterdienst (DWD)] and the Max Planck Institute for Meteorology (MPI-M) as a new modeling system. Within the framework of the HD(CP)² project, the ICON Large-Eddy Model (ICON-LEM) was designed to conduct LES over the whole of Germany to improve moist processes in climate prediction models ([Heinze et al. 2017](#)) and is still under development. In this study, the ICON-LEM simulation of one day (2 May 2013) is used to compare with measurements obtained from the HOPE campaign in Jülich and to provide a spatial representation of the wind field. ICON-LEM has already proven to be in agreement with HOPE observations concerning turbulence, column water vapor, and cumulus clouds (when compared with satellite observations), especially for higher grid resolutions ([Heinze et al. 2017](#)).

Here, a setup that is similar to that of [Heinze et al. \(2017\)](#) is used and includes four nests with circular domains centered around JOYCE ([Fig. 1b](#)). The nests start with a radius of 110 km and a horizontal resolution of 624 m and end with a radius of 10 km and a horizontal resolution of 78 m, which is used in this study. The vertical extent of the simulated domain is about 20 km, with a minimal layer thickness of 20 m and 33 levels in the lowest 2 km. The operational COSMO model covering the German domain (COSMO-DE), as described in [Baldauf et al. \(2011\)](#), is used as forcing data. The utilized model domain with the highest horizontal resolution (78 m), together with the implementation of the topography, can be seen in [Fig. 1](#). The simulation is stored as profiles for the JOYCE site with a 9-s output time and as 3D fields for the whole domain every 10 min. The simulations of this study were conducted on the general purpose Jülich Research on Exascale Cluster Architectures (JURECA) supercomputer, which is operated by the Jülich Supercomputing Centre (JSC) at Forschungszentrum Jülich ([Krause and Thörnig 2016](#)). The visualizations of the ICON-LEM model domain are realized using the ParaView software package ([Ayachit 2015](#)).

4. Statistical analysis of LLJs

Before evaluating specific nocturnal boundary layer processes related to the presence of LLJs measured by an EC station in [section 4b](#), the climatology and statistics of LLJs and their turbulent properties are analyzed.

a. Climatology of LLJs and their turbulent characteristics

The application of the LLJ detection to the DWL measurements (1518 analyzed days) results in 1020 days

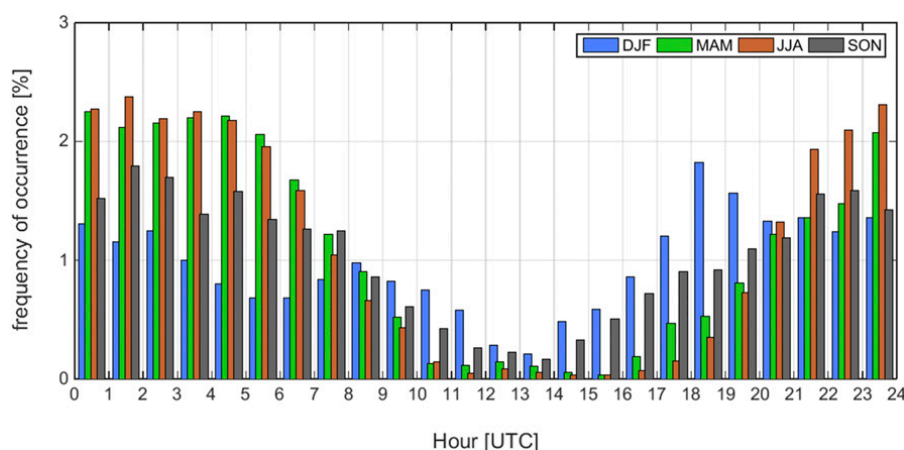


FIG. 2. LLJ frequency of occurrence per hour of the day and for each season relative to the total amount of detected LLJs at JOYCE [local time = UTC + 1 h (winter) or 2 h (summer)]. For an equal number of the different seasons, only LLJs between March 2012 and February 2015 are considered. Total frequencies of occurrence per season are 23% for DJF, 26% for MAM, 26% for JJA, and 25% for SON.

with a detected LLJ of more than 1 h. The data sample includes 1958 periods of continuously detected LLJs, encompassing 17987 vertical wind profiles and a total frequency of occurrence of 13% during the observational period. In general, the relative occurrence of LLJs reveals a clear diurnal cycle with fewer LLJs during daytime (Fig. 2). The median LLJ height and wind speed during the observational period are 375 m and 8.8 m s^{-1} , respectively.

When sorting all detected LLJs according to the different seasons between March 2012 and February 2015 for an equality of the seasons, it is evident from Fig. 2 that the lowest occurrence of LLJs (23%) is during the winter months [December–February (DJF)]. This result is probably due to a weaker diurnal cycle and therefore a less pronounced temperature difference between day and night, which hampers the jet formation. Also, cloud occurrence is higher in winter, as determined by a 905-nm Vaisala, Inc., CT25k ceilometer at JOYCE, with a mean daily cloud cover of 0.62 as compared with 0.50 for March–May (MAM), 0.47 for June–August (JJA), and 0.55 for September–November (SON). The higher cloud occurrence leads to less radiative cooling in the evening, which is necessary for a decoupling from the friction-governed surface layer and leads to fewer LLJs on winter nights. Between sunrise and sunset, however, the higher cloud cover reduces convective motions and thus the coupling strength, which in turn increases the chance of an LLJ to form. During the shorter daylight period in DJF and SON, LLJ occurrence is increased relative to the summer season, and the peak in wintertime LLJs appears during the evening transition time around 1800 UTC.

The spring (MAM), summer (JJA), and autumn (SON) diurnal cycles are similar, with a slight shift in the decrease in LLJ occurrence in the morning hours and an increase during the evening transition as a result of the different sunrise and sunset times. The relative occurrence in SON is less than in spring and summer during the night, whereas MAM and JJA have the fewest daytime appearances of LLJs. This seasonal difference in LLJ occurrence is in agreement with the LLJ climatology of Baas et al. (2009) at a topographically flat site approximately 200 km away from JOYCE. The differences are explained by a stronger coupling of the boundary layer and the surface in summer during daytime, resulting in a larger amplitude of the nocturnal inertial oscillation. In winter, the higher frequency of cloudy periods with more geostrophic forcing and weaker stable stratification leads to a lower occurrence of LLJs. The results in Fig. 2 are also in good agreement with those from the study by Lampert et al. (2015) for a 1-yr dataset obtained from a similar site that is located 300 km northeast of JOYCE. Note that even such details as the early-morning and late-evening relative maxima in winter occur (see Fig. 5 in Lampert et al. 2015).

A further distinction in the forcing mechanisms of the LLJs is reflected in the distribution of the LLJ direction in comparison with the prevailing wind direction at the median height of all LLJs (375 m). In DJF (and in a similar way for SON) a bimodal distribution of southwesterly–westerly (220° – 280° ; 55% of all DJF cases) and southeasterly (105° – 165° ; 25% of all DJF cases) jets can be identified (Fig. 3d), with southwest being the main wind direction at JOYCE in summer and winter (Figs. 3a,b). To relate the observed LLJ wind directions

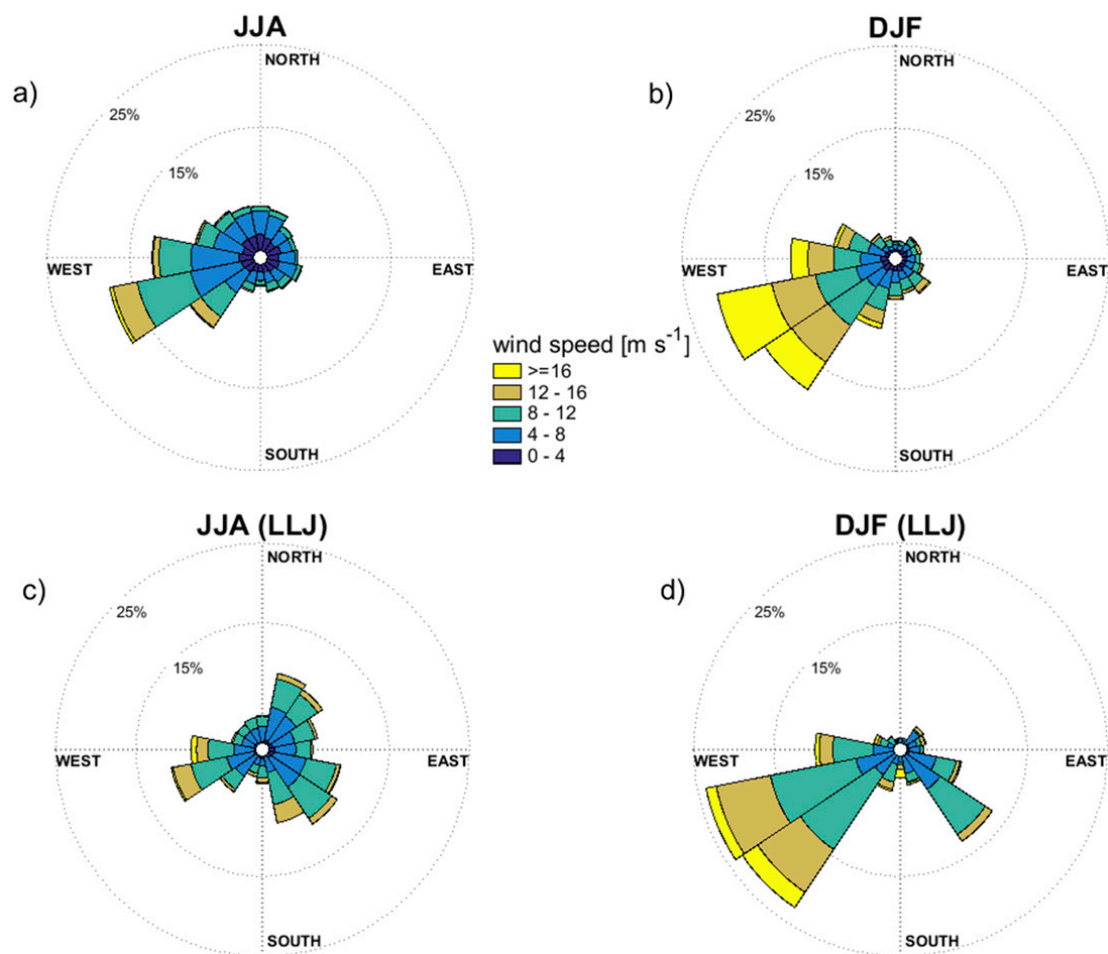


FIG. 3. Wind direction (wind rose) and wind speed (color code) measured at (a),(b) 375 m and (c),(d) the LLJ core at JOYCE between March 2012 and December 2016. The wind roses show results for (left) JJA and (right) DJF.

to the synoptic situation, the 975-hPa geopotential height of the reanalysis product known as ERA-Interim (Dee et al. 2011) is implemented in the Jenkinson–Collison circulation weather type (CWT) classification (Jenkinson and Collison 1977) using the “COST 733” software (Philipp et al. 2016). The CWT model estimates the prevailing wind direction (W, NW, N, NE, E, SE, S, or SW) or the type of circulation [cyclonic (C) or anticyclonic (AC)] four times per day (0000, 0600, 1200, and 1800 UTC). The CWTs are estimated on the basis of the variability of 16 grid points around the JOYCE site with an extent of 5° east–west \times 3° north–south.

Overall, about 50% of the CWT classes are detected as W and SW, which is in agreement with the wind roses in Figs. 3a and 3b. The southwest LLJs can therefore be related to the forcing of common southwesterly winds with low pressure to the northwest and high pressure to the southeast. Only 6% of all CWT classes are identified as SE for all wintertime LLJs and 9% for the summertime LLJs. The LLJs originating from this sector (Figs. 3c,d) thus cannot be explained by synoptic forcing,

but are most probably connected to a channeling effect by the wide Rur River valley from southeast to northwest. For JJA (and similar for MAM) the distribution of the LLJ direction is broader (Fig. 3c), with a third peak in the northeast (10° – 70° ; 21% of all JJA cases) connected to an NE circulation weather type, detected in 15% of the summertime LLJ cases. It is also evident that the months DJF have higher wind speeds, since the LLJ speed is higher than 12 m s^{-1} in 26% of all cases in DJF and only in 12% of all cases in JJA. The median jet speeds are 8.3 m s^{-1} for JJA and 9.8 m s^{-1} for DJF, and the median LLJ heights in JJA (375 m) and DJF (345 m) only differ by one DWL range gate.

For the height of the LLJ maximum in the whole observational time period of March 2012–December 2016, 87% of the LLJs have their wind speed maximum below 600 m (Fig. 4a) and 2965 (16%) LLJs occurred below 200 m, which is within the range of wind-turbine rotors. Intermittent turbulence in this region could increase turbine loading through wind shear over the area of the rotor (Peña et al. 2016). For the purpose of

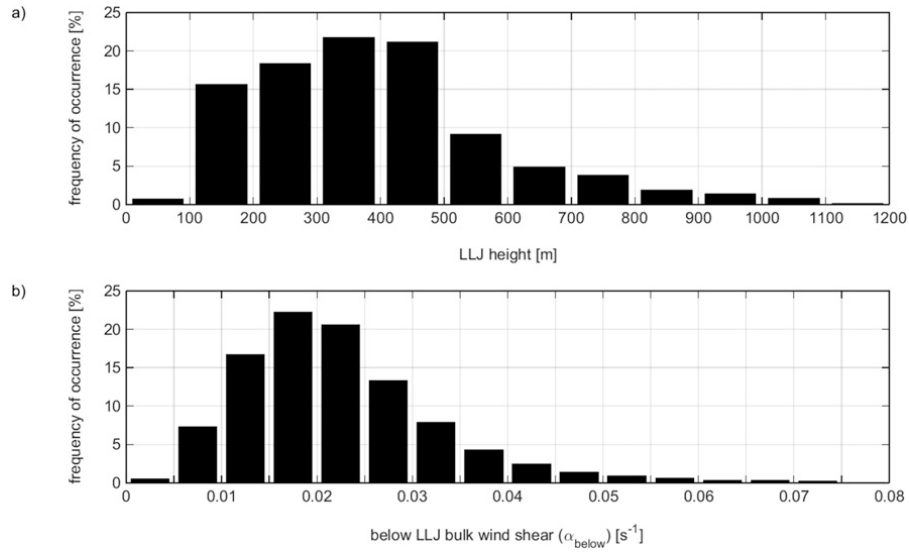


FIG. 4. (a) Height of the LLJ maximum wind speed (bin size = 100 m) and (b) below-LLJ bulk wind shear α_{below} (bin size = 0.005 s^{-1}). The data sample contains all detected LLJs between March 2012 and December 2016 at JOYCE.

analyzing the generation of turbulence below the LLJ as an important attribute for wind-energy applications, the dataset is classified according to the bulk wind shear below the jet, similar to [Tuononen et al. \(2017\)](#):

$$\alpha_{\text{below}} = \frac{U_{\text{LLJ}} - U_{\text{min,below}}}{h_{\text{LLJ}} - h_{\text{min,below}}}, \quad (1)$$

where U_{LLJ} is the wind speed maximum at the height h_{LLJ} and $U_{\text{min,below}}$ is the detected wind speed minimum below the jet with the height $h_{\text{min,below}}$.

To investigate the directional shear, vertical profiles of the vector wind shear U_{shear} can be derived as

$$U_{\text{shear}} = \frac{(\delta u^2 + \delta v^2)^{1/2}}{\delta z}, \quad (2)$$

with differences of the south-to-north v and west-to-east u wind components over a height range δz of 60 m (two range gates).

From Eq. (1), high values of α_{below} represent rapidly increasing wind speeds within a short vertical distance from the surface to the jet nose and therefore a strong gradient (and vice versa). To investigate the turbulence characteristics depending on α_{below} , 30-min standard deviations σ_w of the vertical wind speed around the time of occurrence of the LLJ are derived as an indicator for turbulence. This can be accomplished because of the high temporal resolution of the vertical measurements. In addition, profiles of the horizontal wind speed and vector wind shear U_{shear} [Eq. (2)] of the LLJ periods are extracted from the dataset. The profiles are averaged

and scaled by the LLJ speed and height of the LLJ (Fig. 5).

The dataset of wind speed, wind shear, and σ_w profiles during LLJ periods is classified according to the median of the α_{below} distribution (0.02 s^{-1} ; Fig. 4b) into low-gradient ($\alpha_{\text{below}} < 0.02 \text{ s}^{-1}$) jets (Figs. 5a–d) and strong-gradient jets, with α_{below} being higher than the median (Figs. 5e–h). The low-gradient jets reveal a median jet-nose height of 465 m and a median wind speed of 8.7 m s^{-1} . In comparison, the strong-gradient LLJs with $\alpha_{\text{below}} > 0.02 \text{ s}^{-1}$ show not only a lower jet-nose height (315 m) but also higher wind speeds (10.2 m s^{-1}). The strong winds inhibit a further vertical growth of the stable layer and are caused by high nocturnal cooling rates and low geostrophic forcing ([Baas et al. 2009](#)). Also the stratification is more stable, resulting in a stronger decoupling; according to [Emeis \(2017\)](#) the magnitude of the wind shear in the subjet layer depends on the vertical temperature gradient below the jet.

For the low-gradient jets, U_{shear} also remains small (Fig. 5b), which is expected because U_{shear} and α_{below} are related to each other. Despite there being some variations in U_{shear} with height, however, no significant turbulence can be seen below and above the jet (Fig. 5c). The strong-gradient LLJs in contrast show high averaged vector wind shear values (U_{shear} up to 0.04 s^{-1}) below the jet nose in the region of strongly decreasing wind speeds with height. This result supports the findings of [Svensson and Holtslag \(2009\)](#), who showed a stronger turning of the wind for a shallower boundary layer height, which is here assumed to be related to the LLJ height. The strongest averaged turbulence (up to

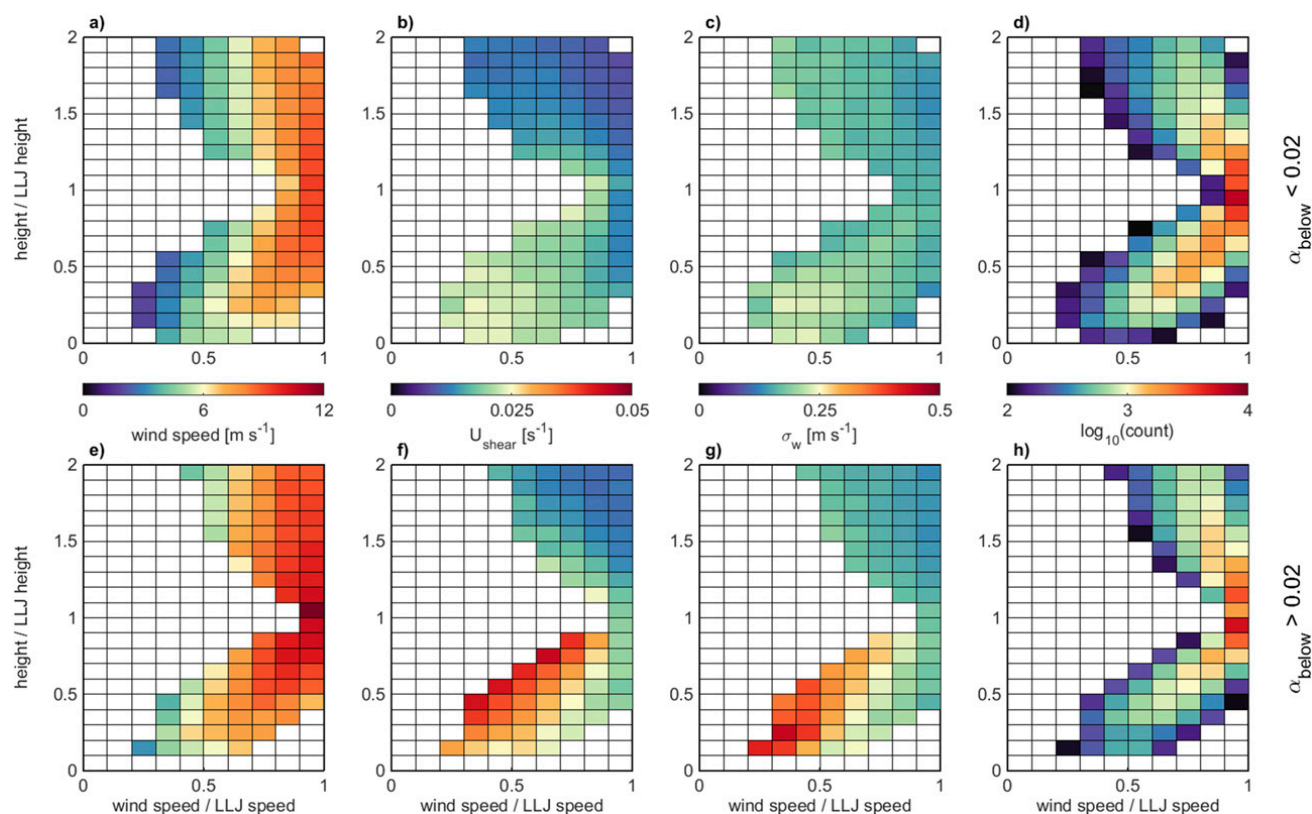


FIG. 5. Distributions of (a),(e) average wind speed, (b),(f) vector wind shear U_{shear} , (c),(g) vertical velocity standard deviation σ_w , calculated over 30 min, and (d),(h) number of observations as a function of normalized wind speed (abscissa) and height (ordinate) of the LLJ for cases with (top) low and (bottom) strong wind shear. Only pixels with at least 100 measurements are shown.

0.4 m s^{-1}) can be found close to the surface below the region of high U_{shear} values (Fig. 5g). Because of the low LLJ heights in this class, the mean height in the 0.1–0.2 height bin is 117.2 m, which is within the rotor height of wind turbines.

b. Influences on the surface fluxes

Note that the lowest 105 m cannot be captured by the DWL. To get information about the differences in turbulence and transport processes closer to the surface, measurements from the EC station 5 km to the southeast of the JOYCE site are evaluated for nocturnal LLJ and no-LLJ periods when no clouds are detected by the DWL (Table 1). The cloud detection is based on a threshold value ($10^{-4} \text{ m}^{-1} \text{ sr}^{-1}$) of the attenuated backscatter measured by the DWL. The largest, statistically significant spread between the two data samples of LLJ and no-LLJ periods is observed during DJF, when there is less influence from the vegetation (maximum vegetation height of 0.4 m) on the surface fluxes. The surface friction is also smaller, leading to decreased turbulent exchange processes.

The LLJ develops above the barrier for heat and momentum fluxes formed by the stable surface layer, as

described in Businger (1973). Thereafter, the turbulence near the surface dissipates and strong wind shear associated with a generation of turbulence is present above the surface layer. This is shown in Fig. 5, where the turbulence occurs below the largest shear.

TABLE 1. Median flux values of latent and sensible heat, as well as the net ecosystem CO_2 exchange, friction velocity, Monin–Obukhov stability parameter, standard deviation of the vertical velocity, air pressure, and CO_2 content during periods without LLJs (second column) and with LLJs (third column). The data are obtained at a height of 2.46 m from the EC station using 30-min means during nighttime (from 1 h after sunset until 1 h before sunrise) in DJF between 2012 and 2016. Only times with no clouds identified by the DWL are considered. All distributions are statistically different as based on a 99% confidence interval.

| | No LLJ (4039 cases) | LLJ (698 cases) |
|---|---------------------|-----------------|
| LH (W m^{-2}) | 6.25 | 0.65 |
| SH (W m^{-2}) | −23.97 | −11.73 |
| NEE ($\mu\text{mol m}^{-2} \text{ s}^{-1}$) | 0.94 | 0.74 |
| u_* (m s^{-1}) | 0.18 | 0.11 |
| z/L | 0.06 | 0.16 |
| σ_w (m s^{-1}) | 0.07 | 0.02 |
| p_{air} (hPa) | 1006.61 | 1008.79 |
| CO_2 (ppm) | 401.2 | 411.6 |

The decoupling and reduction of turbulence at the surface during LLJ periods is reflected in the EC measurements by a decrease in the friction velocity u_* and in the vertical velocity standard deviation relative to no-LLJ periods. Also, the higher median value of 0.16 of the Monin–Obukhov stability parameter z/L indicates a more stable regime during the presence of LLJs than during the no-LLJ cases (0.06), which reduces the exchange processes and increases the concentration of emitted gases. This is evident with regard to the increased CO_2 value measured by the EC station during the LLJ periods (411.6 ppm). The increase of 10.4 ppm relative to the no-LLJ periods accounts for more than 40% of the complete CO_2 data-sample standard deviation. The accumulation of near-surface CO_2 during the presence of an LLJ through an elevated wind shear layer acting as a barrier for surface–atmosphere exchange processes is in agreement with the findings of Mathieu et al. (2005).

Also, the latent heat flux LH of 0.65 W m^{-2} during the LLJ periods is much smaller than for the no-LLJ cases (6.25 W m^{-2}). The sensible heat flux SH being closer to zero during LLJ cases and a decrease of more than 20% in the median net ecosystem CO_2 exchange (NEE) supports the assumption of a decoupled surface layer in which all fluxes are reduced. The higher air pressure indicates a synoptic feature of a higher occurrence of LLJs during anticyclonic high pressure flow at this site between December and February.

The turbulence during the LLJ periods is not totally diminished because of an intermittent downward transport of momentum and turbulence, which was also found in EC measurements during LLJs in the study of Prabha et al. (2007). This interaction of the surface layer with the upper-level flow is defined by Mahrt and Vickers (2002) as an upside-down boundary layer. For a detailed study of these interaction processes, as well as a possible recoupling of the layers, tower measurements of the vertical turbulence structure below 100 m could be beneficial.

5. LLJ interaction with the topography

Because the influence of the surrounding topography is of high interest for the interpretation of wind measurements and their representativeness, the hypothesis of a significant effect on the wind field caused by small deviations from flat terrain is investigated in the following. The most prominent feature of the orography in the vicinity of the JOYCE site is a mine dump hill at a distance of approximately 1.8 km to the northeast of the DWL and around 200 m higher than the measurement site. Together with the open-pit mine, which

is connected to the southeast of the hill, a heterogeneous orographic surrounding is present. The influence of the hill on the wind field is investigated by means of a case analysis during the HOPE campaign on 2 May 2013, where radiosondes and the ICON-LEM simulation are available for comparison with the DWL measurements.

On this day, with a sunset time of 1851 UTC, an easterly CWT is classified at 1800 UTC. After the breakdown of the convective boundary layer around 1630 UTC, the wind speed measured by the DWL increases below 600 m (Fig. 6a). After 1815 and 2130 UTC two LLJ periods are detected by the DWL, whereas from 1945 until 2130 UTC no further LLJs periods of at least 1 h are detected, since the coherence checks in the algorithm are not fulfilled. In this case the LLJ height between two consecutive profiles differs by more than 120 m. Although the high wind speed is contained throughout the shown time period, the wind direction changes from northeast to southeast (Fig. 7). Therefore, the two detected LLJs can be seen as separate events.

The LLJ classification is also applied to the profiles of the ICON-LEM simulation. The coherence check of the time step between two consecutive wind speed maxima needs to be modified because of the different temporal resolution of the model. A new jet in the ICON-LEM LLJ detection is labeled when a gap of more than 18 s occurs, which is 2 times the output time and similar to the DWL LLJ detection, as described in section 3a. In that way, an LLJ is identified continuously from 1730 to 2200 UTC (Fig. 6b), which is more than 1 h earlier and more persistent than the DWL observations. When bringing the model data to the DWL resolution and applying the same thresholds as for the DWL, the coherent LLJ detection ends at 2015 UTC (Fig. 6c).

In general, the vertical extent and growth of the layer with increased wind speeds between 1730 and 1830 UTC is larger in ICON-LEM. The wind maximum is also sharper and higher in the model. ICON-LEM still captures the main features of the observed wind profiles, however, especially between 1815 and 1945 UTC, when an LLJ is detected by using the DWL observations and the model simulations. This motivates us to use the ICON-LEM simulations as a tool for the investigation of the spatial structure of the wind field.

a. Influence of a scaled topography on the wind field in ICON-LEM

Scaling the topography in the ICON-LEM simulations provides a valuable tool for analyzing the sensitivity of the wind field to heterogeneous terrain.

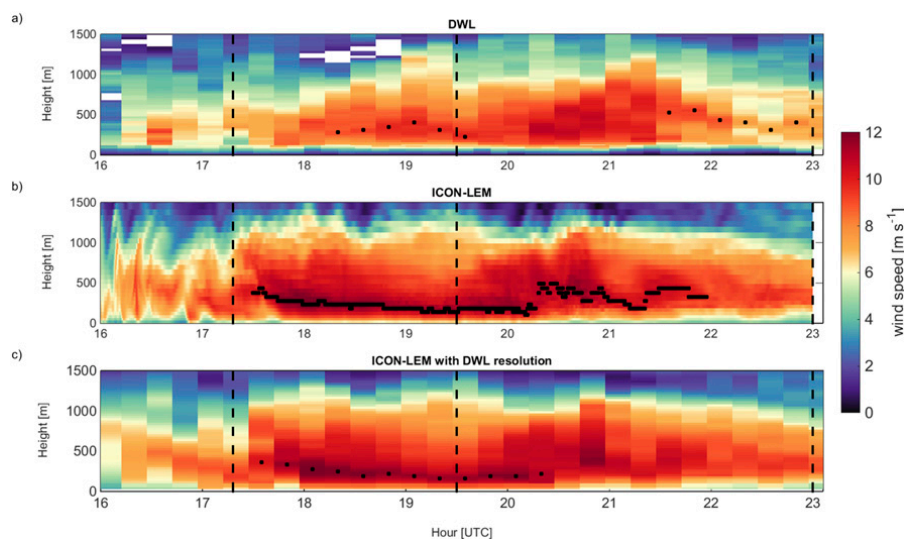


FIG. 6. Wind speed (a) measured by the DWL and tower and (b) simulated by ICON-LEM with an output every 9 s and (c) with the DWL resolution on 2 May 2013 [local time = UTC + 1 h (winter) or 2 h (summer)]. The location of the LLJ height, detected by the LLJ classification, is marked with black dots. The vertical black dashed lines show the selected times for the case analysis in [section 5c](#). Note that on this day the ICON-LEM simulation and the tower measurements are only available until 2300 UTC.

Therefore, streamlines are calculated on 2 May 2013 (2300 UTC) for the lowest 10 model levels of the 3D ICON-LEM simulations with the original topography, but also scaled by factors of 0.5 and 1.5. The scaling factors are a reduction and increase, respectively, of 50% to ensure a significant difference in the model simulations with respect to the topographic effect on the wind field, which is still reasonable for the model setup. More extreme factors might enhance the spinup time or introduce artificial perturbations (because the initial data still include the orography implicitly), whereas less-

strong scaling factors might not show any significant difference. During this time a southeasterly LLJ is present, which is shown to be likely connected to a channeling effect as described in [section 4a](#).

When scaling down the topography by a factor of 0.5, it is evident from [Fig. 8b](#) that the wind field is less influenced by the orography across the whole domain. The wind speed increases faster with height than in the original simulation ([Fig. 8a](#)). The upscaled simulation shows a significant reduction in wind speed, however, especially close to the surface in the region of the

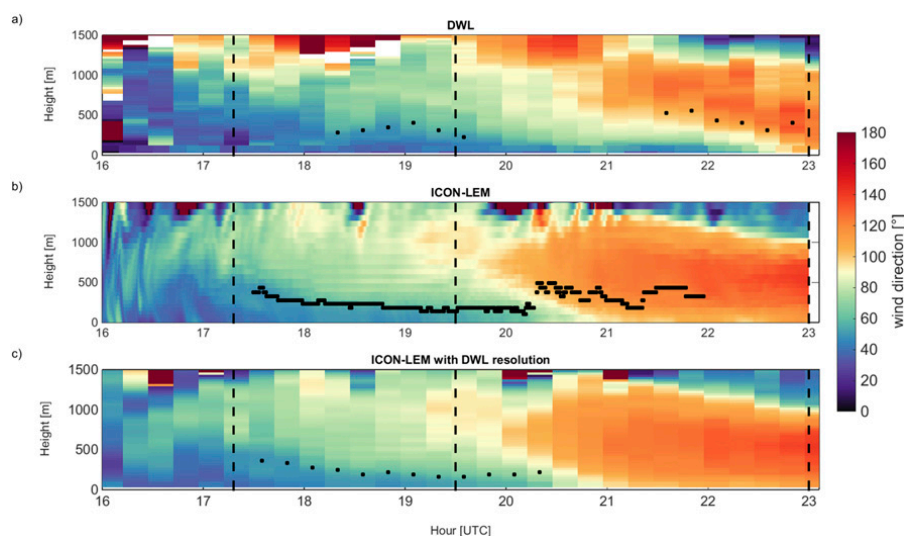


FIG. 7. As in [Fig. 6](#), but for wind direction.

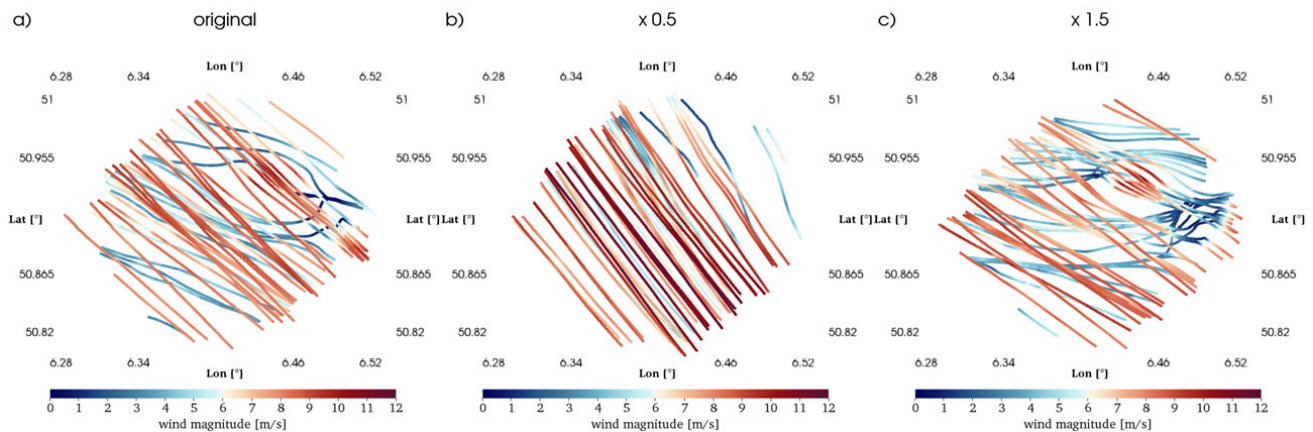


FIG. 8. Streamlines for the 3D ICON-LEM domain snapshot on 2 May 2013 (2300 UTC; southeasterly wind direction). The lowest 10 model levels (up to 790 m MSL) are shown, with the lowest wind speeds (blue) occurring close to the surface and increasing with height. Three simulations are conducted using (a) the original topography and topography that is scaled by factors of (b) 0.5 and (c) 1.5.

open-pit mine (Fig. 8c). The wind speed then increases again over the top of the hill. The topography is also influencing the wind direction by up to 45° for the lower elevations, which can be seen by the more easterly streamlines in the upscaled and original simulations. This finding indicates that the small but close hill to the northeast of the JOYCE site can act as an additional barrier to the channeling effect induced by the large-scale topography surrounding the site.

b. Comparison of observations and ICON-LEM for a nocturnal LLJ

For a better comparison of the measurements and model output, profiles of wind speed, wind direction, vertical wind speed, and potential temperature around the time of the LLJ presence are shown in Fig. 9. Because the vertical velocity is highly variable in both space and time, the ICON-LEM and DWL profiles need to be averaged. The DWL vertical velocity measurements are therefore averaged to 30 min. To account for a similar variability in the ICON-LEM vertical wind, but also to obtain simulated quantities that are comparable to the DWL scans, a spatial average of the model output is calculated. The $1.9 \times 1.9 \text{ km}^2$ area around the JOYCE site (see the black-outlined square in Fig. 10) is selected such that it covers the same area as the DWL scan during 30 min: winds with an average speed of 8 m s^{-1} (which is found during this time period) would travel 14 km during 30 min. At 470 m, which is approximately in the middle of the considered height range, the diameter of the DWL scan at 75° elevation is 250 m. This results in the same surface area as chosen for averaging the ICON-LEM output ($14 \text{ km} \times 0.25 \text{ km} = 3.61 \text{ km}^2 = 1.9 \times 1.9 \text{ km}^2$). Three times are considered in the case analysis, including the LLJ initiation phase at 1720 UTC, the developed LLJ at 1930 UTC, and a weaker LLJ phase with a change of direction at 2300 UTC.

For the times 1720 and 2300 UTC profiles from radiosonde ascents are also available.

In general, the wind speed and direction profiles show good agreement (Figs. 9a,b,e,f,i,j), with only ICON-LEM overestimating the wind speed. In the evening transition period around 1720 UTC, turbulence is still present up to the mixing height at 285 m (dashed lines in Figs. 9a–d), defined as the height at which the standard deviation of the vertical velocity over 30 min drops below 0.4 m s^{-1} , which can be used as an indicator for vertical mixing (Schween et al. 2014). Therefore, the 30-min standard deviation of the DWL is highest within the mixing layer (Fig. 9c). The turbulent motion, as well as the distance of the radiosonde launch site to the DWL, can explain parts of the deviations between the wind speed profiles below 300 m. In addition, the launch site is located at the southeastern corner of the hill and is therefore not shaded from the northeasterly wind.

During the LLJ period at 1930 UTC (Figs. 9e–h) the turbulence only reaches up to 135 m and the LLJ has formed with a maximum wind speed of 9.8 m s^{-1} at 225 m, as determined by the DWL (Fig. 9e). The wind direction close to the ground is still northeasterly, and it turns clockwise toward the geostrophic wind with height (Fig. 9f). For the ICON-LEM potential temperature profile, stable stratification can be identified, especially above the mixing-layer height from the DWL (Fig. 9h). The DWL shows increased positive vertical velocity values of up to 0.5 m s^{-1} around 600 m, a result that is not captured by ICON-LEM.

With a change in near-surface wind direction to southeasterly at 2300 UTC (Fig. 9j), the distinct LLJ profile vanishes together with the vertical updraft (Figs. 9i,k). The potential temperature profile measured by the RS shows a stable surface layer up to about 150 m and a neutral stratified layer until 600 m, followed again

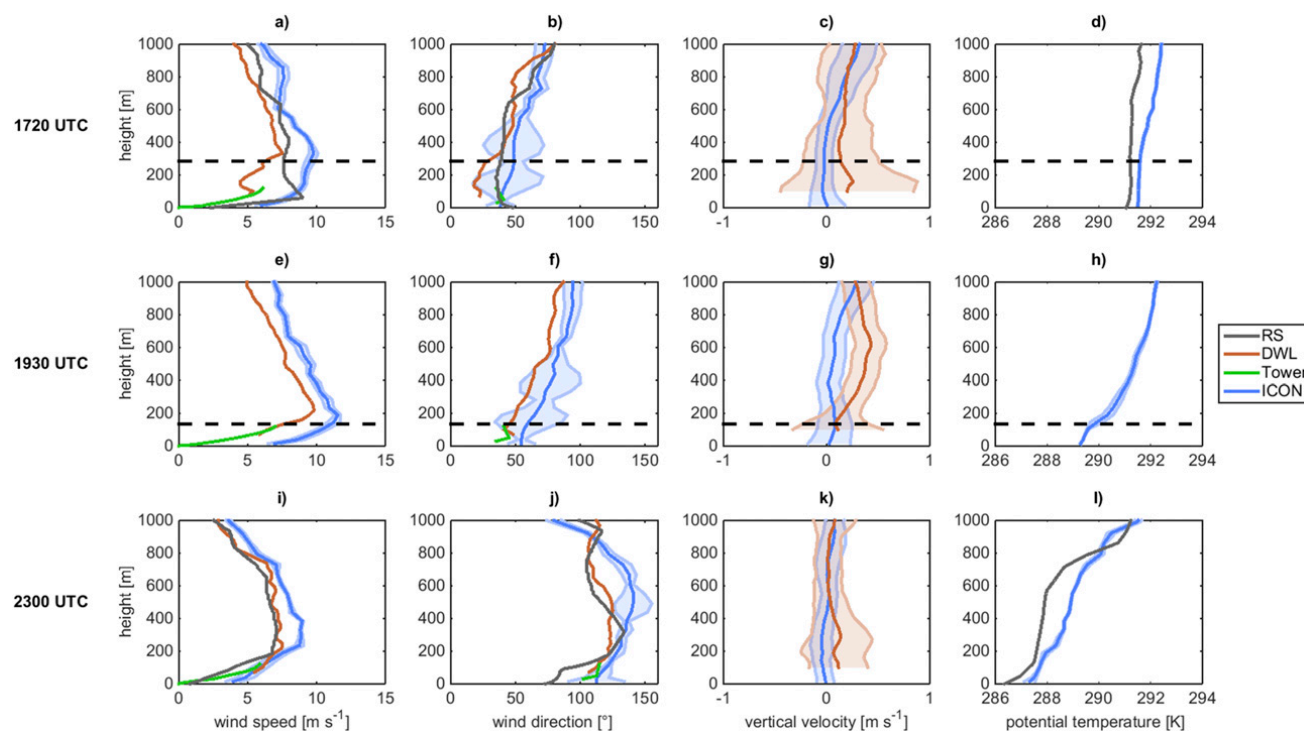


FIG. 9. Case analysis on 2 May 2013 with profiles of (a),(e),(i) wind speed, (b),(f),(j) wind direction, (c),(g),(k) vertical velocity, and (d),(h),(l) potential temperature. The measurements from RSs (gray line), DWL (red line), and the tower (green line), as well as the ICON-LEM output (blue line), are shown for (top) 1720, (middle) 1930, and (bottom) 2300 UTC. The ICON-LEM profiles are spatially averaged over $1.9 \text{ km} \times 1.9 \text{ km}$ and the standard deviation [for wind direction calculated with the method of Yamartino (1984)] is shaded in light blue. The DWL vertical velocity is temporally averaged over 30 min, with the standard deviation given in reddish shading. The mixing-layer height after Schween et al. (2014) is shown by a black dashed line.

by a stable layer. This might indicate a decoupling at the surface from the adjacent residual layer reaching up to 600 m. These are favorable conditions for an LLJ, which is also detected using the DWL measurements.

c. Topographic influence on the vertical wind

To understand the differences in the vertical wind between ICON-LEM and the DWL, the vertical

velocity of the 3D ICON-LEM domain is evaluated at 300 m MSL (Fig. 10). This height is chosen to be above the highest surface point in the model domain. During the LLJ period at 1930 UTC the vertical velocities simulated by ICON-LEM reveal updrafts on the windward side and downdraft motions leeward of the hill with the wind coming from the northeast (Fig. 10b). Thus, the orographic disturbance induces vertical wind

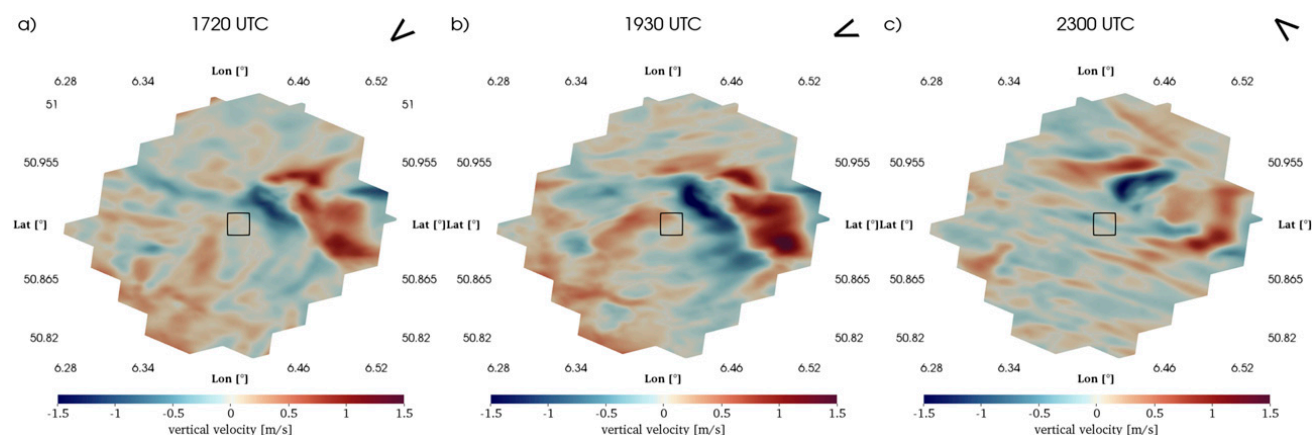


FIG. 10. Vertical velocity at 300 m MSL of the ICON-LEM domain snapshots at (a) 1720, (b) 1930, and (c) 2300 UTC 2 May 2013. The black-outlined square denotes the $1.9 \text{ km} \times 1.9 \text{ km}$ area around the JOYCE site, where the average vertical velocity profiles from Fig. 9 are calculated. The black arrow in the top-right corner of (a)–(c) shows the wind direction at JOYCE around 300 m.

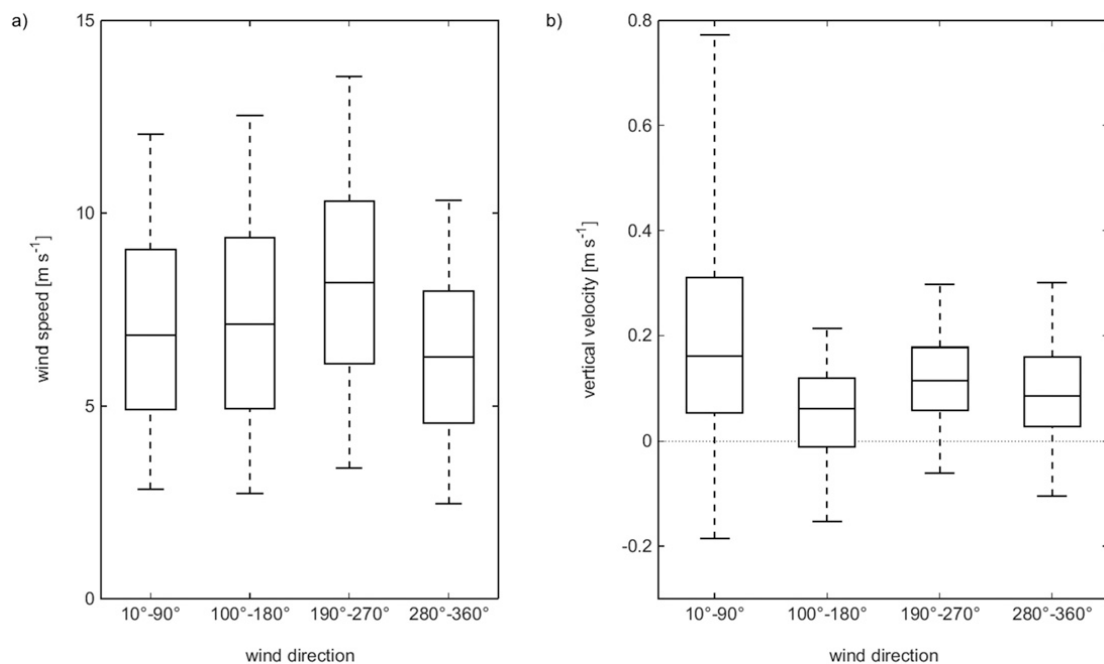


FIG. 11. Box plots showing the 5th, 25th, 50th, 75th, and 95th percentiles of (a) wind speed and (b) 30-min averages of the vertical velocity measured by the DWL between 225 and 705 m. Only LLJs below 500 m during nighttime (from 1 h after sunset until 1 h before sunrise) and clear-sky (DWL backscatter $< 10^{-4} \text{ m}^{-1} \text{ sr}^{-1}$) conditions are included. The wind speed between 105 and 225 m needs to be above 4 m s^{-1} , and the data are binned according to the wind direction (bin size = 80°) in this range with 10° separation. The numbers of cases are 1310 (10° – 90°), 2564 (100° – 180°), 2142 (190° – 270°), and 525 (280° – 360°).

variations up to approximately 3 m s^{-1} , with the JOYCE site located in an updraft region, as also was seen by the DWL (Fig. 9g). The strong gradients in the ICON-LEM vertical wind field can explain the deviations to the observations by a slight spatial displacement. At 2300 UTC the simulated spatial pattern in the vertical velocity (Fig. 10c) is changed according to the turning of the wind direction and a wavelike structure is visible, caused by the wind first flowing down the depression of the pit mine and then uphill.

The results of the case analysis suggest that the updrafts measured at the JOYCE site are caused by the topography for northeasterly winds. In the following, we investigate if this statement can be verified using long-term measurements. Therefore, the DWL dataset from 2012 to 2016 is sampled for LLJs below 500 m during clear-sky conditions, since drizzle events could influence the vertical velocity estimates. Furthermore, it is required that the wind speed between 105 and 225 m exceeds 4 m s^{-1} to ensure a sufficiently strong updraft. Convective motions are excluded by only considering nighttime cases. The data sample of wind speed and 30-min averages of the vertical wind above the summit of the hill (from 225 to 705 m) is classified into different directional classes to investigate the effect of the hill to the northeast (10° – 90°) relative to the other directions (Fig. 11).

The wind speed distribution of the direction in the range of 190° – 270° reveals higher values, with a median value of 8.2 m s^{-1} that exceeds the median values in the other directional classes by 1.1 – 1.9 m s^{-1} (Fig. 11a). Although the effect is small relative to the range of observed wind speed values (standard deviation around 3 m s^{-1}), a possible explanation could be the influence of frontal systems predominantly coming from the southwest.

Despite lower wind speeds, a significant shift to higher positive vertical wind speed values and by far the highest variability can be found in the 10° – 90° directional class (Fig. 11b). The 75th percentile (0.3 m s^{-1}) of the 10° – 90° class is around or even higher than the 95th percentiles of the other distributions. The longer tail toward negative vertical velocity values observed for the northeasterly wind directions could be explained by a slight shift of the updraft region after the descending motions at the leeward side of the hill, as seen in the ICON-LEM simulation, or a higher degree of turbulence induced by the topography. The overall shift to positive values indicated by all distributions of the vertical velocity is probably due to a small offset of the instrument on the order of a few centimeters per second. It can be conclusively stated from the model simulations and the DWL observations that the moderate topography around JOYCE shows sufficient heterogeneity to cause significant disturbances in the wind field.

6. Summary and conclusions

The LLJ climatology obtained from the long-term observations (March 2012–December 2016) by the Doppler wind lidar at the JOYCE site in western Germany shows a clear diurnal cycle of the occurrence of LLJs, favoring the nighttime appearance of the jets. In total, LLJs are detected in 13% of the observational period. Seasonal differences in the diurnal LLJ frequency of occurrence can mostly be attributed to the length of the day. Fewer but stronger LLJs occur in the winter months, because of the lower temperature gradients between day and night and strong geostrophic forcing. An analysis of the synoptic situation using circulation weather types showed that the predominant southwesterly direction of the jets is in agreement with the general circulation around JOYCE. The southeasterly LLJs cannot be associated with the synoptic forcing but rather are more related to a local channeling effect.

The turbulent characteristics of the LLJs, provided by the Doppler wind lidar, showed notably higher vector wind shear below the jet nose for LLJs with strongly decreasing wind speeds below the jet. When dividing all LLJs according to the bulk wind shear, significant turbulent motions can only be found close to the surface for jets with high bulk wind shear. The characterization of the turbulence associated with LLJs shows the importance for wind-energy production, since a large number of LLJs (2965; 16% of all jets) are detected in the range of the rotor height below 200 m.

Evaluation of the nighttime EC-station measurements proves the concept of [Businger \(1973\)](#) of a decoupled surface layer during LLJ events. The strong wind shear associated with the LLJ together with the nonturbulent stable layer hampers upward mixing, which leads to an accumulation of carbon dioxide (CO₂) and a reduction of the heat and momentum fluxes in the stable surface layer. Turbulent mixing found at the surface might be generated by a recoupling of the flow through intermittent downward transport of jet-induced turbulence. This concept of an upside-down boundary layer is explained by [Mahrt and Vickers \(2002\)](#) and could be further analyzed using detailed measurements of the vertical structure of near-surface turbulence.

In the comprehensive case analysis, a strong interaction of the winds with the topography, dominated by a 200-m-high hill and a pit mine close to the measurement site, can be observed during an LLJ event. The DWL shows high positive vertical velocities for northeasterly LLJs, when the wind is flowing over the hill toward the instrument's field of view. High-resolution simulations of ICON-LEM, as a self-consistent representation of the atmosphere, help in the analysis of the spatial variations of the wind field. The vertical velocities reveal a wave structure induced by

the hill and pit mine, which are also influencing the wind speed and direction. From a long-term perspective, this influence introduces a much stronger variability in the vertical wind for the location of the DWL, depending on the wind direction.

The results of the long-term assessment, as well as the model simulations presented in this study, stress the importance of analyzing LLJs and their local effects. The LLJ identification algorithm of [Tuononen et al. \(2017\)](#) proved to be able to identify LLJs objectively by utilizing a multiyear dataset of high temporal and vertical resolution Doppler lidar measurements. The method can further be used for evaluating model performance in terms of the correct representation of LLJ characteristics. By including additional information on atmospheric turbulence, which can be derived from Doppler wind lidars, the impact of LLJs on wind turbines can be examined.

Acknowledgments. The authors acknowledge the Transregional Collaborative Research Centre (TR32) “Patterns in Soil-Vegetation-Atmosphere Systems” funded by the German Science Foundation (DFG), which has continuously contributed to the instrumentation of JOYCE and its maintenance as well as funding T. Marke. The measurement infrastructure providing EC data was supported by the Terrestrial Environmental Observatories (TERENO), funded by the Helmholtz Association. Part of the work has been granted by Energy Transition and Climate Change (ET-CC) under DFG Grant ZUK 81. The ICON-LEM simulations are incorporated by the HD(CP)² research initiative funded by the German Ministry for Education and Research (BMBF). Furthermore, the authors gratefully acknowledge the computing time granted by the John von Neumann Institute for Computing and provided on the supercomputer JURECA at the JSC. Access to the meteorological tower observations was made possible through Axel Knaps from the Research Centre Jülich. The work of M. Tuononen is funded by the Maj and Tor Nessling Foundation (Grants 201500300 and 201600003).

REFERENCES

- Ayachit, U., 2015: *The ParaView Guide: A Parallel Visualization Application*. Kitware, Inc., 340 pp.
- Baas, P., F. C. Bosveld, H. Klein Baltink, and A. A. M. Holtslag, 2009: A climatology of nocturnal low-level jets at Cabauw. *J. Appl. Meteor. Climatol.*, **48**, 1627–1642, <https://doi.org/10.1175/2009JAMC1965.1>.
- Baldauf, M., A. Seifert, J. Förstner, D. Majewski, M. Raschendorfer, and T. Reinhardt, 2011: Operational convective-scale numerical weather prediction with the COSMO model: Description and sensitivities. *Mon. Wea. Rev.*, **139**, 3887–3905, <https://doi.org/10.1175/MWR-D-10-05013.1>.

- Banta, R., R. K. Newsom, J. K. Lundquist, Y. L. Pichugina, R. L. Coulter, and L. Mahrt, 2002: Nocturnal low-level jet characteristics over Kansas during CASES-99. *Bound.-Layer Meteor.*, **105**, 221–252, <https://doi.org/10.1023/A:1019992330866>.
- Blackadar, A. K., 1957: Boundary layer wind maxima and their significance for the growth of nocturnal inversions. *Bull. Amer. Meteor. Soc.*, **38**, 283–290.
- Bonner, W. D., 1968: Climatology of the low level jet. *Mon. Wea. Rev.*, **96**, 833–850, [https://doi.org/10.1175/1520-0493\(1968\)096<0833:COTLLJ>2.0.CO;2](https://doi.org/10.1175/1520-0493(1968)096<0833:COTLLJ>2.0.CO;2).
- Businger, J. A., 1973: Turbulent transfer in the atmospheric surface layer. *Workshop on Micrometeorology*, D. H. Haugen, Ed., Amer. Meteor. Soc., 67–100.
- Dee, D. P., and Coauthors, 2011: The ERA-Interim reanalysis: Configuration and performance of the data assimilation system. *Quart. J. Roy. Meteor. Soc.*, **137**, 553–597, <https://doi.org/10.1002/qj.828>.
- Dipankar, A., B. Stevens, R. Heinze, C. Moseley, G. Zängl, M. Giorgetta, and S. Brdar, 2015: Large eddy simulation using the general circulation model ICON. *J. Adv. Model. Earth Syst.*, **7**, 963–986, <https://doi.org/10.1002/2015MS000431>.
- Dörenkämper, M., M. Optis, A. Monahan, and G. Steinfeld, 2015: On the offshore advection of boundary-layer structures and the influence on offshore wind conditions. *Bound.-Layer Meteor.*, **155**, 459–482, <https://doi.org/10.1007/s10546-015-0008-x>.
- Emeis, S., 2017: Upper limit for wind shear in stably stratified conditions expressed in terms of a bulk Richardson number. *Meteor. Z.*, **26**, 421–430, <https://doi.org/10.1127/metz/2017/0828>.
- , M. Harris, and R. M. Banta, 2007: Boundary-layer anemometry by optical remote sensing for wind energy applications. *Meteor. Z.*, **16**, 337–347, <https://doi.org/10.1127/0941-2948/2007/0225>.
- Heinze, R., and Coauthors, 2017: Large-eddy simulations over Germany using ICON: A comprehensive evaluation. *Quart. J. Roy. Meteor. Soc.*, **143**, 69–100, <https://doi.org/10.1002/qj.2947>.
- Higgins, R. W., Y. Yao, E. S. Yarosh, J. E. Janowiak, and K. C. Mo, 1997: Influence of the Great Plains low-level jet on summer-time precipitation and moisture transport over the central United States. *J. Climate*, **10**, 481–507, [https://doi.org/10.1175/1520-0442\(1997\)010<0481:IOTGPL>2.0.CO;2](https://doi.org/10.1175/1520-0442(1997)010<0481:IOTGPL>2.0.CO;2).
- Hirsikko, A., and Coauthors, 2014: Observing wind, aerosol particles, cloud and precipitation: Finland's new ground-based remote-sensing network. *Atmos. Meas. Tech.*, **7**, 1351–1375, <https://doi.org/10.5194/amt-7-1351-2014>.
- Holtstlag, A. A. M., and Coauthors, 2013: Stable atmospheric boundary layers and diurnal cycles: Challenges for weather and climate models. *Bull. Amer. Meteor. Soc.*, **94**, 1691–1706, <https://doi.org/10.1175/BAMS-D-11-00187.1>.
- Jenkinson, A. F., and F. P. Collison, 1977: An initial climatology of gales over the North Sea. Met Office Synoptic Climatology Branch Memo. 62, 18 pp.
- Krause, D., and P. Thörnig, 2016: JURECA: General-purpose supercomputer at Jülich Supercomputing Centre. *J. Large-Scale Res. Facil.*, **2**, A62, <https://doi.org/10.17815/jlsrf-2-121>.
- Lampert, A., B. Bernalte Jimenez, G. Gross, D. Wulff, and T. Kenull, 2015: One-year observations of the wind distribution and low-level jet occurrence at Braunschweig, north German plain. *Wind Energy*, **19**, 1807–1817, <https://doi.org/10.1002/we.1951>.
- , and Coauthors, 2016: A study of local turbulence and anisotropy during the afternoon and evening transition with an unmanned aerial system and mesoscale simulation. *Atmos. Chem. Phys.*, **16**, 8009–8021, <https://doi.org/10.5194/acp-16-8009-2016>.
- Löhnert, U., and Coauthors, 2015: JOYCE: Jülich Observatory for Cloud Evolution. *Bull. Amer. Meteor. Soc.*, **96**, 1157–1174, <https://doi.org/10.1175/BAMS-D-14-00105.1>.
- Macke, A., and Coauthors, 2017: The HD(CP)² Observational Prototype Experiment (HOPE)—An overview. *Atmos. Chem. Phys.*, **17**, 4887–4914, <https://doi.org/10.5194/acp-17-4887-2017>.
- Mahrt, L., and D. Vickers, 2002: Contrasting vertical structures of nocturnal boundary layers. *Bound.-Layer Meteor.*, **105**, 351–363, <https://doi.org/10.1023/A:1019964720989>.
- Mathieu, N., I. Strachan, M. Leclerc, A. Karipot, and E. Pattey, 2005: Role of low-level jets and boundary-layer properties on the NBL budget technique. *Agric. For. Meteorol.*, **135**, 35–43, <https://doi.org/10.1016/j.agrformet.2005.10.001>.
- Mauder, M., M. Cuntz, C. Drüe, A. Graf, C. Rebmann, H. P. Schmid, M. Schmidt, and R. Steinbrecher, 2013: A strategy for quality and uncertainty assessment of long-term eddy-covariance measurements. *Agric. For. Meteorol.*, **169**, 122–135, <https://doi.org/10.1016/j.agrformet.2012.09.006>.
- Mitchell, M. J., R. W. Arritt, and K. Labas, 1995: A climatology of the warm season Great Plains low-level jet using wind profiler observations. *Wea. Forecasting*, **10**, 576–591, [https://doi.org/10.1175/1520-0434\(1995\)010<0576:ACOTWS>2.0.CO;2](https://doi.org/10.1175/1520-0434(1995)010<0576:ACOTWS>2.0.CO;2).
- O'Connor, E. J., A. J. Illingworth, I. M. Brooks, C. D. Westbrook, R. J. Hogan, F. Davies, and B. J. Brooks, 2010: A method for estimating the turbulent kinetic energy dissipation rate from a vertically pointing Doppler lidar, and independent evaluation from balloon-borne in situ measurements. *J. Atmos. Oceanic Technol.*, **27**, 1652–1664, <https://doi.org/10.1175/2010JTECHA1455.1>.
- Päschke, E., R. Leinweber, and V. Lehmann, 2015: An assessment of the performance of a 1.5 μm Doppler lidar for operational vertical wind profiling based on a 1-year trial. *Atmos. Meas. Tech.*, **8**, 2251–2266, <https://doi.org/10.5194/amt-8-2251-2015>.
- Pearson, G., F. Davies, and C. Collier, 2009: An analysis of the performance of the UFAM pulsed Doppler lidar for observing the boundary layer. *J. Atmos. Oceanic Technol.*, **26**, 240–250, <https://doi.org/10.1175/2008JTECHA1128.1>.
- Peña, A., and Coauthors, 2016: Ten years of boundary-layer and wind-power meteorology at Høvsøre, Denmark. *Bound.-Layer Meteor.*, **158**, 1–26, <https://doi.org/10.1007/s10546-015-0079-8>.
- Philipp, A., C. Beck, R. Huth, and J. Jacobeit, 2016: Development and comparison of circulation type classifications using the COST 733 dataset and software. *Int. J. Climatol.*, **36**, 2673–2691, <https://doi.org/10.1002/joc.3920>.
- Prabha, T. V., M. Y. Leclerc, A. Karipot, and D. Y. Hollinger, 2007: Low-frequency effects on eddy covariance fluxes under the influence of a low-level jet. *J. Appl. Meteor. Climatol.*, **46**, 338–352, <https://doi.org/10.1175/JAM2461.1>.
- Schween, J. H., A. Hirsikko, U. Löhnert, and S. Crewell, 2014: Mixing-layer height retrieval with ceilometer and Doppler lidar: From case studies to long-term assessment. *Atmos. Meas. Tech.*, **7**, 3685–3704, <https://doi.org/10.5194/amt-7-3685-2014>.
- Stensrud, D., 1996: Importance of low-level jets to climate: A review. *J. Climate*, **9**, 1698–1711, [https://doi.org/10.1175/1520-0442\(1996\)009<1698:IOLLJT>2.0.CO;2](https://doi.org/10.1175/1520-0442(1996)009<1698:IOLLJT>2.0.CO;2).
- Storm, B., J. Dudhia, S. Basu, A. Swift, and I. Giammanco, 2009: Evaluation of the Weather Research and Forecasting Model on forecasting low-level jets: Implications for wind energy. *Wind Energy*, **12**, 81–90, <https://doi.org/10.1002/we.288>.

- Su, J., M. Felton, L. Lei, M. P. McCormick, R. Delgado, and A. St. Pé, 2016: Lidar remote sensing of cloud formation caused by low-level jets: Cloud formation caused by low-level jets. *J. Geophys. Res. Atmos.*, **121**, 5904–5911, <https://doi.org/10.1002/2015JD024590>.
- Svensson, G., and A. A. M. Holtslag, 2009: Analysis of model results for the turning of the wind and related momentum fluxes in the stable boundary layer. *Bound.-Layer Meteor.*, **132**, 261–277, <https://doi.org/10.1007/s10546-009-9395-1>.
- Tuononen, M., V. A. Sinclair, and T. Vihma, 2015: A climatology of low-level jets in the mid-latitudes and polar regions of the Northern Hemisphere: A climatology of low-level jets. *Atmos. Sci. Lett.*, **16**, 492–499, <https://doi.org/10.1002/asl.587>.
- , E. J. O'Connor, V. A. Sinclair, and V. Vakkari, 2017: Low-level jets over Utö, Finland, based on Doppler lidar observations. *J. Appl. Meteor. Climatol.*, **56**, 2577–2594, <https://doi.org/10.1175/JAMC-D-16-0411.1>.
- Whiteman, C. D., X. Bian, and S. Zhong, 1997: Low-level jet climatology from enhanced rawinsonde observations at a site in the southern Great Plains. *J. Appl. Meteor.*, **36**, 1363–1376, [https://doi.org/10.1175/1520-0450\(1997\)036<1363:LLJCFE>2.0.CO;2](https://doi.org/10.1175/1520-0450(1997)036<1363:LLJCFE>2.0.CO;2).
- Yamartino, R. J., 1984: A comparison of several single-pass estimators of the standard deviation of wind direction. *J. Climate Appl. Meteor.*, **23**, 1362–1366, [https://doi.org/10.1175/1520-0450\(1984\)023<1362:ACOSPE>2.0.CO;2](https://doi.org/10.1175/1520-0450(1984)023<1362:ACOSPE>2.0.CO;2).
- Zängl, G., D. Reinert, P. Rípodas, and M. Baldauf, 2015: The ICON (ICOsahedral Non-hydrostatic) modelling framework of DWD and MPI-M: Description of the non-hydrostatic dynamical core. *Quart. J. Roy. Meteor. Soc.*, **141**, 563–579, <https://doi.org/10.1002/qj.2378>.
- Zhong, S., J. D. Fast, and X. Bian, 1996: A case study of the Great Plains low-level jet using wind profiler network data and a high-resolution mesoscale model. *Mon. Wea. Rev.*, **124**, 785–806, [https://doi.org/10.1175/1520-0493\(1996\)124<0785:ACSOTG>2.0.CO;2](https://doi.org/10.1175/1520-0493(1996)124<0785:ACSOTG>2.0.CO;2).
- Zhou, B., and F. K. Chow, 2012: Turbulence modeling for the stable atmospheric boundary layer and implications for wind energy. *Flow Turbul. Combust.*, **88**, 255–277, <https://doi.org/10.1007/s10494-011-9359-7>.

Copyright of Journal of Applied Meteorology & Climatology is the property of American Meteorological Society and its content may not be copied or emailed to multiple sites or posted to a listserv without the copyright holder's express written permission. However, users may print, download, or email articles for individual use.

4 LAND USE INDUCED WATER VAPOR PATTERNS

DETECTION OF LAND SURFACE INDUCED WATER VAPOR PATTERNS

T. Marke, U. Löhnert, V. Schemann, J. H. Schween, and S. Crewell (2020).
“Detection of land-surface-induced atmospheric water vapor patterns”. In:
Atmospheric Chemistry and Physics 20.3, pp. 1723–1736. DOI: [10.5194/acp-20-1723-2020](https://doi.org/10.5194/acp-20-1723-2020)

© Author(s) 2020. This work is distributed under the Creative Commons Attribution 4.0 License.



Detection of land-surface-induced atmospheric water vapor patterns

Tobias Marke, Ulrich Löhnert, Vera Schemann, Jan H. Schween, and Susanne Crewell

Institute for Geophysics and Meteorology, University of Cologne, Cologne, Germany

Correspondence: Tobias Marke (tmarke@meteo.uni-koeln.de)

Received: 1 April 2019 – Discussion started: 7 May 2019

Revised: 30 November 2019 – Accepted: 26 December 2019 – Published: 12 February 2020

Abstract. Finding observational evidence of land surface and atmosphere interactions is crucial for understanding the spatial and temporal evolution of the boundary layer, as well as for model evaluation, and in particular for large-eddy simulation (LES) models. In this study, the influence of a heterogeneous land surface on the spatial distribution of atmospheric water vapor is assessed. Ground-based remote sensing measurements from a scanning microwave radiometer (MWR) are used in a long-term study over 6 years to characterize spatial heterogeneities in integrated water vapor (IWV) during clear-sky conditions at the Jülich Observatory for Cloud Evolution (JOYCE). The resulting deviations from the mean of the scans reveal a season- and direction-dependent IWV that is visible throughout the day. Comparisons with a satellite-derived spatial IWV distribution show good agreement for a selection of satellite overpasses during convective situations but no clear seasonal signal. With the help of a land use type classification and information on the topography, the main types of regions with a positive IWV deviation were determined to be agricultural fields and nearby open pit mines. Negative deviations occurred mainly above elevated forests and urban areas. In addition, high-resolution large-eddy simulations (LESs) are used to investigate changes in the water vapor and cloud fields for an altered land use input.

sponsible for mesoscale circulations and considerably affect the state of the atmospheric boundary layer in a nonlinear way (e.g., Ookouchi et al., 1984; Pielke et al., 1991; Clark and Arritt, 1995). On a more local scale, the transport of energy and water vapor into the atmosphere can trigger the formation of shallow convective clouds and precipitation (e.g., Rabin et al., 1990; Avissar and Schmidt, 1998). Because this small-scale variability can not be resolved by most weather forecast and climate models, it needs to be parameterized. This requires assumptions near the surface boundaries, which strongly affect exchange processes. Unresolved patterns in the models are crucial, since the resulting gradients directly influence the fluxes and hence the evolution of the model state (Simmer et al., 2015). Monitoring and modeling these spatial patterns and interactions are the main focuses of this study, which is conducted within the framework of the Transregional Collaborative Research Centre 32 (TR32) “Patterns in Soil-Vegetation-Atmosphere Systems: Monitoring, Modelling and Data Assimilation” (<http://www.tr32.de>, last access: 25 November 2019). The scope of TR32, as described in Simmer et al. (2015), is to improve the understanding and prediction capabilities of the spatiotemporal evolution of the terrestrial system across scales, using measurement techniques and modeling platforms and integrating activities of several research groups.

Since the scales of surface heterogeneity and resulting interaction processes with the overlying boundary layer are on the order of meters to kilometers, a frequently used tool for studying these interaction processes on a local scale is conducting high-resolution large-eddy simulations (LES) (e.g., Courault et al., 2007; Huang and Margulis, 2009; Maronga and Raasch, 2013; Shao et al., 2013). By altering the land surface properties, the turbulence-resolving simulations provide estimates of the resulting effect on the boundary-layer structure. In this way Vilà-Guerau De Arellano et al. (2014) show

1 Introduction

Interactions between the land surface and the atmospheric boundary layer can have significant influences on the regional weather and climate. Heterogeneity in land use, among other parameters characterized by soil type, vegetation, and urban areas, induces spatial variability in surface fluxes of momentum, sensible, and latent heat. Numerical studies suggest that contrasts in land surface fluxes are re-

differences in cloud dynamics that can be related to the partitioning of the surface fluxes determined by the plant functional type. In van Heerwaarden and Vilà-Guerau De Arellano (2008), an enhancement of cloud formation over heterogeneous landscapes using different Bowen ratios is indicated.

For a better understanding of the influence of the land surface on the atmospheric state and in order to evaluate model findings, ground-based observations by current state-of-the-art remote sensing instrumentation can be used. Significant effects of heterogeneous land use on the turbulent fluxes and connections to clouds have been shown in several field campaigns with a short-term perspective (Weckwerth et al., 2004; Beyrich et al., 2006; Wulfmeyer et al., 2011, 2018; Späth et al., 2016; Macke et al., 2017). Investigating the influence of land use heterogeneity on boundary-layer characteristics, such as water vapor and clouds from long-term measurements, can play a key role in finding systematically significant patterns in relationships between the local land surface and atmosphere above.

As a key parameter that connects vegetation activity and the boundary layer, atmospheric water vapor plays an important role not only within the hydrological cycle but also for the energy balance at the surface and within the atmosphere. Späth et al. (2016) investigated water vapor fields for a limited amount of time in a campaign with a scanning differential absorption lidar and found gradients related to surface elevation and land cover type. Also, long-term studies of the spatiotemporal variability in water vapor have revealed terrain-related processes in a mountainous area (Adler et al., 2016) by using scans from a passive ground-based microwave radiometer (MWR). Compared to the widely used satellite observations for spatially resolved water vapor estimates, available only for a handful of overpasses per day, the MWR is well suited for continuous and temporally highly resolved measurements at a certain location. While MWR profile measurements of humidity suffer from a coarse resolution, a good agreement between zenith measurements of integrated water vapor (IWV) using the MWR, satellite, and global positioning system (GPS) observations was shown in Steinke et al. (2015). The ability of the MWR to detect horizontal humidity gradients by retrieving IWV values in a scanning configuration has already been proven (Kneifel et al., 2009; Schween et al., 2011).

To address the question whether spatial water vapor distributions can be connected to land surface properties, this observational and modeling study focuses on the long-term pattern of azimuthal IWV deviations derived from satellite and ground-based measurements at the Jülich Observatory of Cloud Evolution (JOYCE; Löhnert et al., 2015) in western Germany (50.91° N, 6.41° E). At JOYCE, various remote sensing instruments, including the scanning MWR, have been deployed since 2011 to continuously monitor water vapor, clouds, and precipitation. For comparing the spatial IWV distribution derived from the MWR with an independent measurement, a satellite water vapor product is used at

a high spatial resolution. In addition, a Doppler wind lidar is available for a characterization of the atmospheric boundary layer in terms of the winds and turbulent mixing processes that control the exchange of water vapor between the surface and the atmosphere. The impact of the land surface on the atmospheric water vapor distribution is evaluated by comparing the derived IWV deviations to a detailed land use map. To better understand the impact of the land surface on the evolution of the cloudy boundary layer, sensitivity studies with high-resolution LES are performed with different land use type settings.

The details of the instruments and data used in this study in Sect. 2 are followed by the description of the data sample derivation used in the long-term analysis. For a better description of the state of the boundary layer during clear-sky conditions and large-scale effects, the results are shown together with wind and turbulence statistics derived from Doppler lidar measurements during the MWR scans and a reanalysis product (Sect. 3.1). Subsequently, the IWV deviations derived from MWR scans and for a collection of satellite overpasses are compared for different seasons (Sect. 3.2) and for a selected single day. A model case study is complemented by the analysis of two large-eddy simulations focusing on the influence of land use on the evolution of the cloudy boundary layer (Sect. 4), and a summary of the results is given in Sect. 5.

2 Instruments and data

2.1 Microwave radiometer

The microwave radiometer HATPRO (Humidity And Temperature PROfiler) at JOYCE utilizes direct detection receivers and measures the brightness temperatures for seven channels in the K band from 22 to 32 GHz and for seven channels also in the V band from 52 to 58 GHz. In this study, the observations of the seven K-band channels with a 1–2 s temporal resolution are taken into account. A statistical approach based on a least squares linear regression model (Löhnert and Crewell, 2003) is applied to derive the IWV, absolute humidity (q), and liquid water path (LWP) using observations of the downwelling microwave radiance along the water vapor absorption line between 22.24 and 27.84 GHz and in the atmospheric window at 31.4 GHz. The instrument is capable of high temporal resolution (Rose et al., 2005), and the absolute error in zenith TB measurements of 0.5 K is mainly determined by the absolute calibration of the instrument (Maschwitz et al., 2013). This accuracy converts into an uncertainty of 0.5–0.8 kg m⁻² in the derived IWV and 20–30 g m⁻² for LWP.

The zenith measurements (IWV_z) alternate with full azimuth scans in 10° steps at a 30° elevation angle. The degrees of freedom for signal (DFS) are usually between 1 and 2 for MWR humidity retrievals, and the highest information

content can be found in the boundary layer. For the zenith retrieval and the 30° (slant path) retrieval, 1.87 DFS and 2.14 DFS were identified, respectively. The scans are available between June 2012 and June 2015 and starting from June 2018. In 2016 and 2017 no MWR scans were performed. The earlier scanning frequency was 15 min, and it was increased to 10 min between 25 June and 18 July 2018 and decreased to 30 min after 18 July 2018. Due to directionally dependent interference in the unprotected 26.24 GHz channel, specific azimuth directions (50, 160, 180, and 260°) are not considered. Since the excluded azimuth directions are not connected, no larger gap is apparent, and a smooth transitions between the gaps can be assumed. Therefore, the missing IWV values are filled using linear interpolation. For all scans, the derived LWP, IWV, and q are air mass corrected to account for the slant angle of the scanning MWR.

2.2 Doppler lidar and boundary layer classification

As a pulsed lidar system, the Halo Photonics Stream Line Doppler lidar (Pearson et al., 2009) provides range-resolved profile measurements of radial Doppler velocity and backscattered signal. With a wavelength of 1.5 μm (near-IR) the instrument is sensitive to the backscatter of aerosols and clouds and is able to scan the full hemisphere. The maximum detectable range depends on the presence of atmospheric particles and the lowest reliable range is at 105 m. At JOYCE the system is set to a range resolution of 30 m and performs plan position indicator scans every 15 min to estimate wind speed and direction profiles based on the velocity–azimuth display (VAD) method using 36 beams at a 75° elevation. In addition the Doppler beam swing (DBS) technique, with three beams and range–height indicator scans, is scheduled every 5 and 30 min, respectively. For the remaining time, the instrument is facing the zenith to derive the vertical velocity with a high temporal resolution (1 s).

To study land surface and atmosphere exchange processes, it is crucial to know the turbulent state of the boundary layer. Therefore, an objective classification of the mixing sources presented by Manninen et al. (2018) is utilized to describe the turbulence characteristics during MWR scans at JOYCE. The method is based on the combination of multiple Doppler lidar quantities including the dissipation rate of turbulent kinetic energy (TKE) derived from vertically pointing observations, using the method presented in O'Connor et al. (2010). The TKE dissipation rate is based on the variance in the observed mean Doppler velocity and allows for a threshold-based estimation of the convective boundary layer (CBL) height by determining the last range bin in each profile with significant turbulence in a bottom-up approach.

2.3 MODIS IWV

The passive imaging Moderate Resolution Imaging Spectroradiometer (MODIS) measures within 36 spectral bands

ranging from 0.4 to 14.4 μm . Two MODIS instruments are currently airborne on NASA's sun-synchronous near-polar-orbiting Earth Observing System Terra and Aqua satellites. A full coverage of the globe is achieved in 1–2 d with an orbit height of 705 km and a scan rate of 20.3 rpm. The swath dimensions of MODIS are 2330 km (cross track) and 10 km (along track at nadir). Within the 36 spectral bands, five channels in the 0.8–1.3 μm near-infrared spectral region can be used for water vapor remote sensing (Gao and Kaufman, 2003). For IWV estimates, the Level-2 (Collection 6.1) near-infrared retrieval (MODIS-NIR) with a 1 km spatial resolution is chosen. The retrieval by Gao and Kaufman (2003) is based on three channels at 0.936, 0.940, and 0.905 μm for the water vapor absorption and at 0.865 and 1.24 μm to correct for atmospheric gaseous absorption. In order to derive the total vertical amount of water vapor, the reflected NIR solar radiation in the water vapor absorption channel is compared to the window channels yielding the atmospheric water vapor transmittance. The amount of water vapor is then obtained from lookup tables derived from a line-by-line atmospheric transmittance code. Reliable estimates of the water vapor total column amount over land areas can only be inferred during daytime and for cloud-free regions. Typical errors of the MODIS-NIR water vapor product range between 5 % and 10 %. Here, a height correction similar to Steinke et al. (2015) of the retrieved values is performed due to the variations in the horizontal and height distance to JOYCE per flight track of MODIS. The height difference is corrected by assuming an exponential decrease in the humidity profile and by using the water vapor density obtained from measurements of temperature, humidity, and pressure from a weather sensor attached to the MWR, and the topography with a 200 m horizontal resolution. Furthermore, the IWV product was resampled to 100 m for calculating the mean values of several overpasses.

2.4 ERA5 data products

To distinguish between local influences and large-scale features regarding the observed spatial pattern of IWV deviations, the reanalysis products of ERA5 with a 31 km horizontal resolution are analyzed (Copernicus Climate Change Service, 2017). Besides the eastward and northward wind components at different pressure levels (1000 and 700 hPa), the direction of the IWV transport (IWVT; in degrees) is also considered at a 3 h temporal resolution for the closest point to JOYCE. The vertical integral of water vapor flux, used to derive IWVT, is calculated utilizing the specific humidity and winds at the model level. The ERA5 IWV is selected at the closest output time to the MWR scans.

2.5 ICON-LEM

As a state-of-the-art atmospheric modeling system, the ICOSahedral Nonhydrostatic model ICON (Zängl et al.,

2015) has been developed by the German Weather Service (DWD) and the Max Planck Institute for Meteorology (MPI-M). The ICON Large-Eddy Model (ICON-LEM) was designed within the framework of the High Definition Clouds and Precipitation for advancing Climate Prediction (HD(CP)²) project for improving moist processes in climate prediction models (Heinze et al., 2017). In this study, the ICON-LEM simulations are used to provide a spatial representation of the IWV field to compare with the measurements obtained from the scanning MWR and the MODIS-NIR water vapor product around JOYCE.

A good agreement between simulations of ICON-LEM using high grid resolutions of up to 156 m and observations was already shown in Heinze et al. (2017) concerning turbulence, column water vapor, and cumulus clouds (compared to satellite observations). The topographic influence on the wind field was also shown in ICON-LEM simulations and observations at JOYCE (Marke et al., 2018). Therefore, a similar setup with a domain radius size of 10 km, 78 m horizontal resolution, and 20 km vertical extent is used in this study. The minimal layer thickness is 20 m, and the lowest 2 km section contains 33 levels. Initial and lateral boundary conditions are created from the output of the ECMWF Integrated Forecasting System (IFS) model. As the IFS and the ICON models do not use identical land surface models, a sensitivity of the simulations to the treatment of soil moisture and other land surface components can not be excluded. But those sensitivities are the same for both simulations, and sensitivity studies suggest that the results are rather robust despite small variations. In addition to the control simulation using a simplified version of the land use input data GlobCover (Bontemps et al., 2011) with 300 m resolution, a second simulation is conducted with one altered land use setting. In this way parameters like leaf area index and roughness length are changed to get a different distribution of potential water vapor sources and sinks at the surface.

2.6 Land use classification and measurement site description

To be able to link atmospheric water vapor measurements to land surface properties, spatial land use information is needed. This is addressed by using a remote-sensing-based regional crop map (Waldhoff et al., 2017) that was applied to a study area in western Germany including the surrounding area of JOYCE. In this method, supervised multitemporal remote sensing data from Sentinel-2, ancillary information, and expert knowledge of crops are combined in a multi-data approach (MDA). The classification is, therefore, able to differentiate between 44 vegetated, urban, and water areas with a spatial resolution of 15 m.

The detailed and highly resolved classification is used to identify areas with a predominant land use type. Therefore, the classified types are condensed into six main types, in particular agricultural areas, grassland, bare ground, urban ar-

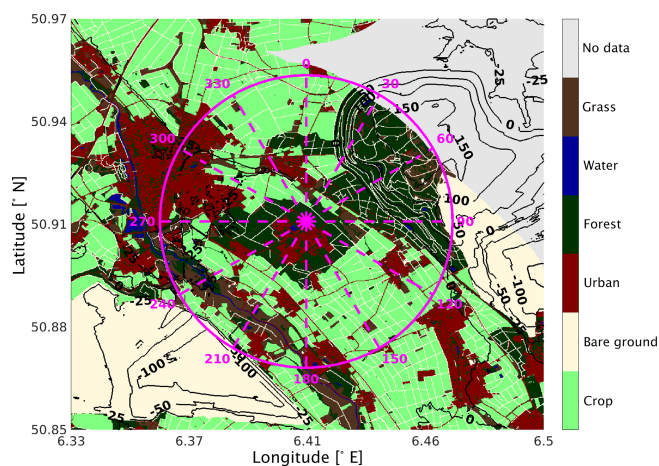


Figure 1. Simplified map (12 km×13 km) of the land use classifications described in Waldhoff et al. (2017) centered around JOYCE (see also Waldhoff and Lusse, 2016). The circle (4.3 km radius) shows the crossing distance and azimuth angles of the MWR scans at the IWV scaling height of 2.5 km. Contours refer to the height relative to JOYCE (111 m a.s.l.).

eas, deciduous forest, and water. These six groups are expected to have a significantly different behavior in terms of transpiration and/or evaporation depending on the season and, therefore, might cause atmospheric water vapor patterns that can be distinguished and related to the appropriate type. In Fig. 1 the simplified land use classification of a 12 km×13 km area centered around JOYCE is shown. The city of Jülich to the northwest and JOYCE at the Research Center Jülich are the largest urban areas in this surrounding. The artificially created pit mine dump hill, Sophienhöhe, located in the northeast direction, is up to 200 m higher than JOYCE and covered mainly by a deciduous forest. In the northern and southeastern part of the selected domain, the sites identified are mostly agricultural. The main crop type between April and June is winter wheat, and sugar beet, maize, and potato are dominant from July until September. A common crop rotation is a 2-year cycle of sugar beet to winter wheat (Waldhoff et al., 2017). Due to this crop rotation and regarding the small field sizes in this domain, no further distinction in crop types is made, but more active crop fields in terms of evapotranspiration are present during the spring season. The southwestern parts are mostly crop fields, but there are also grasslands surrounding the Rur River, with its valley going from southeast to northwest. The pit mines (bare ground) with depressions down to 300 m below JOYCE are located to the east and southwest.

3 Long-term observed directional IWV deviations

3.1 Data sample derivation and characteristics

In order to find patterns in the long-term water vapor scans at JOYCE that can be related to local land surface characteristics, the MWR scans are evaluated during meteorological conditions that are favorable for strong land surface and atmosphere interactions. This excludes overcast situations, and situations with a large-scale advection of moist or dry air as during these times the surface influence is low, which was shown by Steinke et al. (2019) by the amplitude reduction of the diurnal water vapor cycle. The cloud detection is obtained by using the 31.4 GHz channel, which is within an atmospheric window. The signal from this channel is dominated by the presence of liquid water in the case of clouds appearing in field of view of the instrument. During a single scan, the maximum difference in the measured 31.4 GHz brightness temperature for each azimuth direction and the mean of the whole scan must be below 2 K, since liquid water clouds are expected to cause a much higher difference. Furthermore the air-mass-corrected LWP from the statistical retrieval needs to be below 20 g m^{-2} , which is on the order of the retrieval uncertainty. To avoid scenes with large-scale advection of moist or dry air, the difference between the maximum and minimum IWV_z within 1 h around the scan needs to be smaller than 2 kg m^{-2} . This threshold is chosen to be above the instrument sensitivity for IWV. These requirements need to be fulfilled for at least three consecutive scans. The first and last scan of each sequence are neglected to ensure that they are not part of a transition from conditions violating the criteria. The choice of the thresholds was shown to be a good trade-off between excluding apparent cloudy situations but still allowing a sufficient number of scans to generate a large data sample. In order to detect seasonal differences due to different stages of crop development in the growing phase from senescence to harvest, the months of April–June and July–September between 2012 and 2018 are separated. The highest diurnal IWV variability is observed between spring and autumn at JOYCE (Löhnert et al., 2015), and the influence from the land surface is expected to be largest in spring and early summer. Instead of using the total slant column IWV, the humidity profile is integrated up to the CBL height determined by the Doppler lidar (hereafter IWV_{CBL}) for an analysis of the lower tropospheric water vapor patterns. For all scans, the mean value per scan is subtracted to investigate the deviations in each azimuth direction.

In addition, a colocated Doppler lidar is used to gain information on atmospheric turbulence, wind direction, and wind speed during the scans. The temporal resolution of the Doppler lidar VAD scans is 15 min, and the closest measurement to the scan time is selected. For the general development of the wind direction during the day, 6 h averages are calculated. The number of MWR scans per hourly bin that meet the requirements ranges from 127 to 496, with fewer

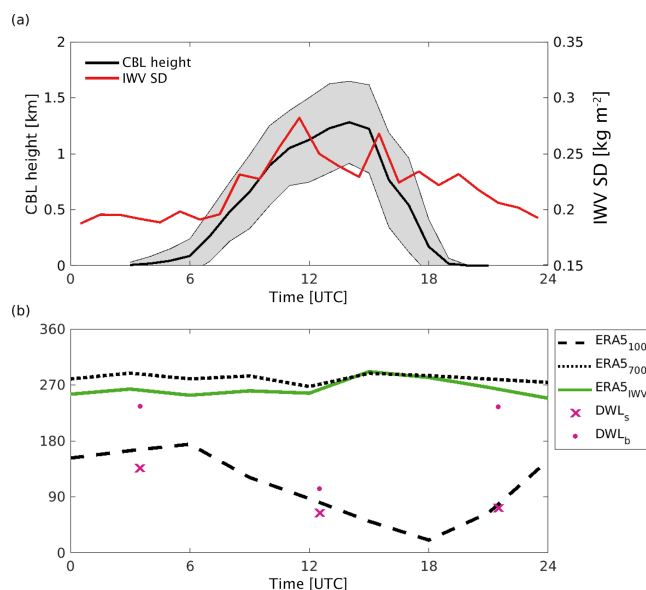


Figure 2. (a) Hourly averaged convective boundary-layer (CBL) height (with standard deviation in shadings) from the Doppler lidar boundary-layer classification at the MWR scan times. The zenith IWV standard deviation (SD) is determined within 1 h around the scans. (b) The lines show the directions (in degree) of the averaged ERA5 wind directions at 1000 hPa (ERA5₁₀₀₀), 700 hPa (ERA5₇₀₀), and the IWV transport (ERA5_{IWVT}). Symbols indicate the mean Doppler lidar wind direction (average times: 01:00–06:00, 10:00–15:00, and 19:00–24:00 UTC) at 105 m (DWL_s) and 1005 m (DWL_b).

scans during midday. The decrease in the number of cases during daytime is due to the formation of convective clouds, since overcast situations would influence the number of cases independent of the time of the day. The mean standard deviation for each scan increases from 1.1 % to 1.94 % during daytime, indicating the influence of convective activity, which is shown by high-TKE dissipation rates and a corresponding mean CBL height of up to 1.28 km (Fig. 2a). Also, the IWV standard deviation from the zenith MWR measurements in Fig. 2a reveals a diurnal cycle during this measurement period of late spring until early autumn, which is in agreement with the seasonal statistics derived in Löhnert et al. (2015). While the IWV standard deviation follows the rate of the CBL height development in the morning hours, an abrupt decrease is only evident in the turbulence measurements in the afternoon transition period. This suggests that water vapor is mixed into the upper layers of the atmosphere during daytime and is still present in the residual layer throughout the night.

For assessing the impact of the large-scale water vapor transport, the ERA5 reanalysis product is used. The ERA5 IWV at the closest output time to the MWR scans compared to the 1 h averaged IWV_z from the MWR shows a high correlation coefficient of 0.98 and a root-mean-square

error (RMSE) of only 1.46 kg m^{-2} . The ERA5 wind direction at 1000 hPa (ERA5₁₀₀₀) is in good agreement with the mean near-surface wind direction (average times: 01:00–06:00, 10:00–15:00, and 19:00–24:00 UTC) derived from the Doppler lidar at 105 m (DWL_s; Fig. 2b). The wind direction ranges from a southerly flow during the night to an east to north direction during the day, corresponding to fair-weather situations and anticyclonic flow at this site. The wind direction turns clockwise with height for the ERA5 product and the Doppler lidar observations but stays relatively constant within the CBL as there is no large difference between DWL_s and the Doppler lidar wind direction at 1005 m (DWL_b) between 10:00 and 15:00 UTC. The wind direction in the free troposphere at 700 hPa shows no significant diurnal cycle. The same applies to the IWVT, which corresponds to the westerly wind direction at 700 hPa, showing the westerlies transport of humid air at the midlatitudes. But at midday and early afternoon (12:00–17:00 UTC), positive IWV_{CBL} deviations in the long-term MWR scans increase and shift to the southeast (not shown). Despite the fact that the ERA5 IWV shows a diurnal cycle, this shift can not be seen in the IWVT, suggesting that local influences also contribute to the observed IWV signal. This is further analyzed in Sect. 3.2.

Separating all cases according to the low-level wind direction from the Doppler lidar, a directional dependence is found related to the wind speed, indicating local transport and a shift between the humidity field and the underlying surface within the MWR scanning beam. To exclude this process and to better connect the spatial IWV deviations with the surrounding land use, the MWR scan analysis is restricted to cases with wind speeds below the median value of 5 m s^{-1} . During the observational period, 161 d out of a total of 1242 single scans are selected with a mean IWV_z of $18.02 \pm 6.43 \text{ kg m}^{-2}$ measured in a 1 h window around the scans. At JOYCE the average year-to-year variability in terms of humidity is rather small, but still a good coverage of relatively dry and wet years is achieved in this study. As an exemplary measure, the mean zenith IWV taken around the selected scans for each year ranges from 15.0 to 21.4 kg m^{-2} . Therefore, the variability in the zenith IWV values for the different years ($4.2\text{--}7.8 \text{ kg m}^{-2}$) is in the range or higher than changes in the mean value.

3.2 Daytime MWR and MODIS-derived IWV deviations and connection to land use

Figure 3a shows the daytime (12:00–17:00 UTC) mean value of the IWV_{CBL} deviation for all 36 azimuth directions of the MWR scans. In this time period a well-mixed CBL has developed, and the highest convective water vapor flux from the land surface into the atmosphere is expected. For the April–June cases, a positive deviation of up to 0.61 % from the mean between 130 and 270° is visible. Also, a positive peak around 75° is present. However, between 270 and 60° mostly negative IWV_{CBL} deviations are present (up to -0.79%). In

contrast, the July–September cases only show a positive deviation between 180 and 270° and a slightly negative deviation between 0 and 120°. Otherwise there is no noticeable deviation during this season. Note that these deviations are median values used to detect the long-term pattern and that single scan deviations from the mean can reach over 5 %.

For a comparison with an independent IWV measurement and to exclude that the patterns are influenced by interference, the MWR results are compared to the MODIS-NIR-derived IWV around JOYCE. The findings presented here could also be valuable for further studies using the MODIS products for assessing spatial IWV differences, which is especially valuable for larger areas. For a fair comparison of the column amount of water vapor from MODIS to the path-integrated water vapor observations from the MWR scans, a virtual MWR scan is derived from the MODIS observations. Therefore, the total IWV is distributed to an absolute humidity profile for each MODIS pixel assuming a linear decrease by 20 % in the CBL and an exponential decrease above this, similar to Schween et al. (2011). The mean CBL height is determined from the Doppler-lidar-based boundary-layer classification (Manninen et al., 2018) around 1 h of each overpass. The CBL height is assumed to be constant in the area of interest, as well as the $1/e$ height for the exponential decrease, which is calculated from the MWR humidity profile of the corresponding overpass. In this way a virtual scan corresponding to the MWR scan configuration can be performed around JOYCE where the amount of water vapor is integrated for each beam up to the CBL height. Only overpasses without missing data due to the MODIS quality checks are considered.

As an additional comparison of the MWR and MODIS, the IWV_z measurements of the MWR (IWV_{z,MWR}) and the MODIS mean total column amount 1 km around JOYCE (IWV_{z,MODIS}) are compared. The zenith IWV values are highly correlated (0.96) with a RMSE of 2.45 kg m^{-2} , which is about 1 kg m^{-2} higher than that found in Steinke et al. (2015). This discrepancy is probably caused by a greater IWV variability shown in Fig. 2a. For larger IWV values, the MODIS observations tend to an overestimation. For the 22 (April–June) and 36 (July–September) MODIS overpasses occurring between 09:00 and 13:00 UTC, the mean IWV deviations from the virtual scans are calculated (Fig. 3b). Note that only showing the MWR scans during the MODIS overpasses does not change the deviation pattern significantly. In general, the relative deviations from the MODIS virtual scans do not show a seasonal pattern as is seen in the MWR scans (Fig. 3b). With both observations, a noticeable negative deviation around 30° is visible, and the agreement in the location of the positive deviations for both seasons around 180–240° is also evident. This area shows a high fraction of grassland, the Rur River, and one of the pit mines, explaining the positive deviations in both seasons, whereas less water vapor seems to be present in the vicinity of the forested hill (Fig. 1). Regarding the MODIS-derived results, the pit mine

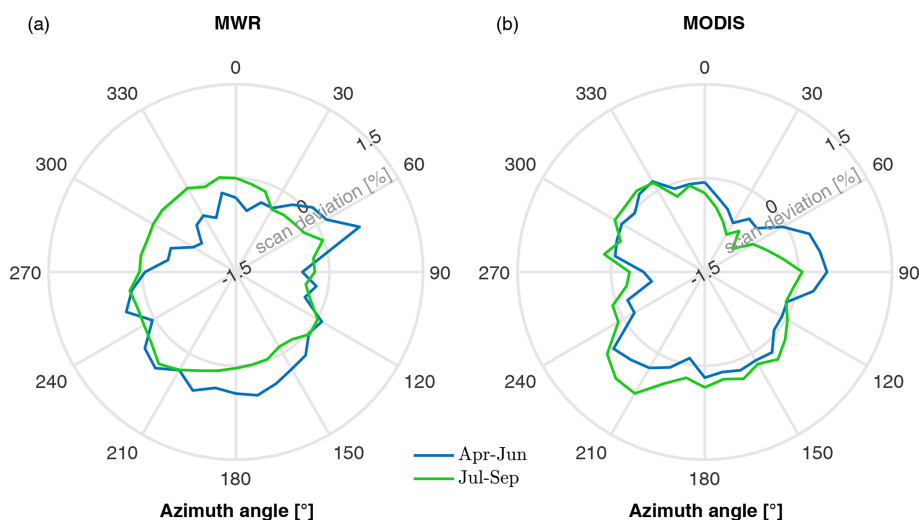


Figure 3. (a) Mean values of the MWR water vapor deviation (integrated up to the CBL height) from the mean per scan between 12:00 and 17:00 UTC for April–June (99 scans) and July–September (123 scans). (b) Same as panel (a) but for the MODIS IWV deviations including 22 overpasses (April–June) and 36 overpasses (July–September), respectively.

around 90° also reveals a positive deviation, but the peak for the MWR is shifted to 70° . This phenomenon might be explained by the orographic flow that is strongly altered by the pit mines as shown in Marke et al. (2018) and the low spatial resolution of the MODIS IWV product.

The results presented here for the MWR and MODIS scans suggest a higher water vapor flux into the atmosphere for the agricultural fields in the southwest due to evapotranspiration (no irrigation), especially in the main crop growing season between April and June. The high amount of water vapor around the pit mines could be caused by irrigation to reduce dust emissions during the day and dew formation at night. In contrast, the forest and urban areas reveal a lower water vapor amount. This can be explained by less water availability in urban areas and a higher water use efficiency for deciduous forests compared to crop fields demonstrated in Tang et al. (2015). A similar difference in the surface fluxes between crops during the main vegetation period and forest (pine trees) was found using surface flux measurements (Beyrich et al., 2006) and in the LES study by Garcia-Carreras et al. (2011). In addition, lower wind speeds due to the topography and a higher roughness length at the forested hill can cause decreased water vapor fluxes into the atmosphere. Thus, spatial water vapor differences can be detected by the scanning MWR, especially with a long-term perspective that uses a composite of carefully selected cases.

4 LES case study analysis for land surface impact

The influence of the land use type on the evolution of the cloudy boundary layer is further investigated in a case study (25 July 2012) by means of a large-eddy simulation using the ICON-LEM model. Due to the spatial resolution of the

land use data and the scale of the land use patches around JOYCE, the crop and grass types are combined. On this day, with a northwesterly wind direction, no clouds are present until 11:30 UTC. The timing of the selected MODIS overpass is 10:15 UTC, and five MWR scans are performed between 09:10 and 11:10 UTC. The results of the observed water vapor deviations are shown in Fig. 4. As already shown in the previous long-term analysis, the maximum positive deviation occurs in a southeasterly to southwesterly direction, with a good agreement in the sign changes between the MWR and MODIS. Although this day is in late July, it still shows similar features when compared to the April–June season, suggesting still-active crop fields (especially sugar beet) in this area. In order to make a general statement about whether the ICON-LEM correctly represents the spatial water vapor distribution, a large number of high-resolution simulations would be needed. Here, the focus is on assessing the impact of different land use data as input for the model on boundary-layer development and cloud formation. In this 2 h time interval the CBL height determined by the Doppler lidar increases from 405 to 1275 m. In the first ICON-LEM simulation (ICON1) that uses the simplified GlobCover land use data (Fig. 5a), the model boundary-layer height reaches these heights about 1 h later than in the observations. The mean IWV_z values are 24.83 kg m^{-2} (MWR), 29.26 kg m^{-2} (MODIS), and 28.22 kg m^{-2} (ICON1), where the ICON1 zenith IWV is averaged within a radius of 1 km around JOYCE, and for MODIS the nearest pixel is chosen. The lower observed IWV value by the MWR and higher CBL height compared to ICON1 suggest that the partitioning of surface heat fluxes is more towards the latent heat flux in the simulation.

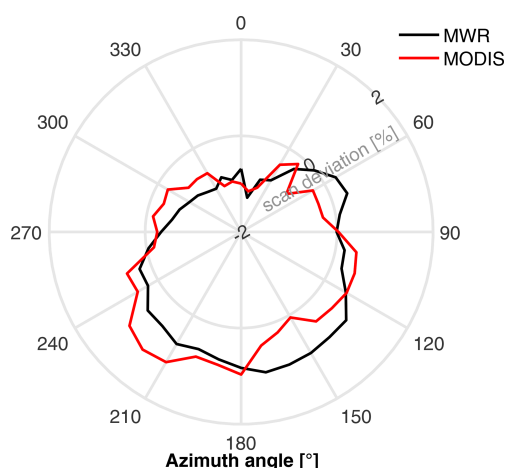


Figure 4. Mean values of the MWR and MODIS water vapor deviation for the 25 July 2012 case study including five MWR scans (09:10–11:10 UTC) and one MODIS overpass at 10:15 UTC.

Using the humidity budget equation, the contribution of local and nonlocal sources to the change in atmospheric humidity within the boundary layer can be estimated using ICON-LEM. The Reynolds-averaged continuity equation with contributions only from advection and turbulent flux divergence (no molecular diffusion or other source terms) for water vapor (incompressible) with the Einstein notation yields

$$\frac{\partial \bar{q}}{\partial t} + \bar{u}_j \frac{\partial \bar{q}}{\partial x_j} = - \frac{\partial (\bar{u}'_j \bar{q}')}{\partial x_j}, \quad (1)$$

where \bar{q} is the averaged specific humidity. Assuming a horizontal homogeneity of the turbulent fluxes ($\frac{\partial}{\partial x} \bar{u}'_j \bar{q}' = \frac{\partial}{\partial y} \bar{v}'_j \bar{q}' = 0$), with $\bar{w} = 0$, expressing the turbulent flux as latent heat flux, $\bar{w}'_j \bar{q}' = LE/(\rho L_v)$, and taking into account that in a well-mixed boundary layer \bar{q} does not vary with height, we can integrate Eq. (1) over height and get

$$\underbrace{\frac{\partial \bar{q}}{\partial t}}_I = - \underbrace{\frac{\Delta \left(\frac{LE}{\rho L_v} \right)}{z_i}}_{II} - \underbrace{\bar{V} \frac{\partial \bar{q}}{\partial x}}_{III}, \quad (2)$$

where ρ is the air density, L_v is the heat of vaporization of water, $\Delta(LE/(\rho L_v))$ is the difference in latent heat flux between the top of the CBL and surface, z_i is the CBL height, \bar{V} is the average wind speed, and $\partial/\partial x$ denotes differentiation along the average wind direction. The turbulent flux at the top of the CBL accounts for entrainment (including subsidence) and can be expressed as (Stull, 1988)

$$LE_{z_i} = \rho L_v w_e \Delta q = \rho L_v w_e [\bar{q}(z_i) - \bar{q}(z_i^+)], \quad (3)$$

where $\bar{q}(z_i)$ is the mean specific humidity in the CBL, $\bar{q}(z_i^+)$ is the specific humidity directly above the CBL, and w_e is the entrainment velocity. Without CBL height advection, the

entrainment velocity is the difference between the local rate of a changing CBL height over time minus subsidence (Stull, 1988):

$$w_e = \frac{\partial z_i}{\partial t} - \bar{w}(z_i), \quad (4)$$

with $\bar{w}(z_i)$ as the vertical velocity at the height of the CBL. This results in the following expression for the difference in latent heat flux between the surface (LE_s) and the top of the CBL,

$$\Delta \left(\frac{LE}{\rho L_v} \right) = [\bar{q}(z_i) - \bar{q}(z_i^+)] \cdot \left(\frac{\partial z_i}{\partial t} - \bar{w}(z_i) \right) - \frac{LE_s}{\rho_s L_v}, \quad (5)$$

where ρ_s is the surface value of the air density. Equation (2) shows the humidity tendency (term I) with term II representing the local (evapotranspiration) and term III representing the nonlocal contribution by horizontal advection. For ICON1 the terms of Eq. (2) are calculated separately and averaged within the CBL for the domain shown in Fig. 5 between 10:00 and 11:00 UTC, where the CBL height increases from 500 to 770 m, and still no clouds are present. During that time the specific humidity in the CBL increases by $0.62 \text{ g kg}^{-1} \text{ h}^{-1}$ on average. The contribution of the local term accounts for 0.21 , and $0.29 \text{ g kg}^{-1} \text{ h}^{-1}$ is advected. This leaves a residual term of $0.12 \text{ g kg}^{-1} \text{ h}^{-1}$, indicating that the assumptions made for the budget equation are not valid, but it can be stated that in this simulation the humidity field is not entirely dominated by advection, and the local source is of the same order of magnitude.

The sensitivity of slant path integrals of the water vapor field up to the CBL height to water vapor transport from the land surface can be evaluated from the local part of the humidity budget. term II of Eq. (2) is calculated for a circular area with a radius corresponding to the projected CBL height of a 30° slant path and divided into sectors of 10° . Similar to the MWR measurements, the integrated water vapor is derived for a 30° slant path and 10° azimuth steps and integrated up to a height h_{int} , which represents the maximum height of the slant path. At the normalized height of $h_{\text{int}}/\text{CBL height} = 1$, the circle described by the slant path corresponds to the area where the local part of the humidity budget is computed. Figure 6 shows the correlation coefficient of the mean (10:00–11:00 UTC) 10° sector estimates of term II of Eq. (2) and the slant-path-integrated water vapor at a 30° elevation and 10° azimuth steps that depends on the integration lengths. At short integration lengths no correlation between the integrated water vapor and the local source of humidity can be found. The correlation coefficient increases with height, reaches a maximum below the CBL height, and decreases strongly above the CBL. This indicates that local sources of humidity at the surface can be detected by means of slant-path-integrated water vapor in a well-mixed boundary layer when integrating up to the CBL height as performed in Sect. 3.2 with the MWR. Note that the values of the cor-

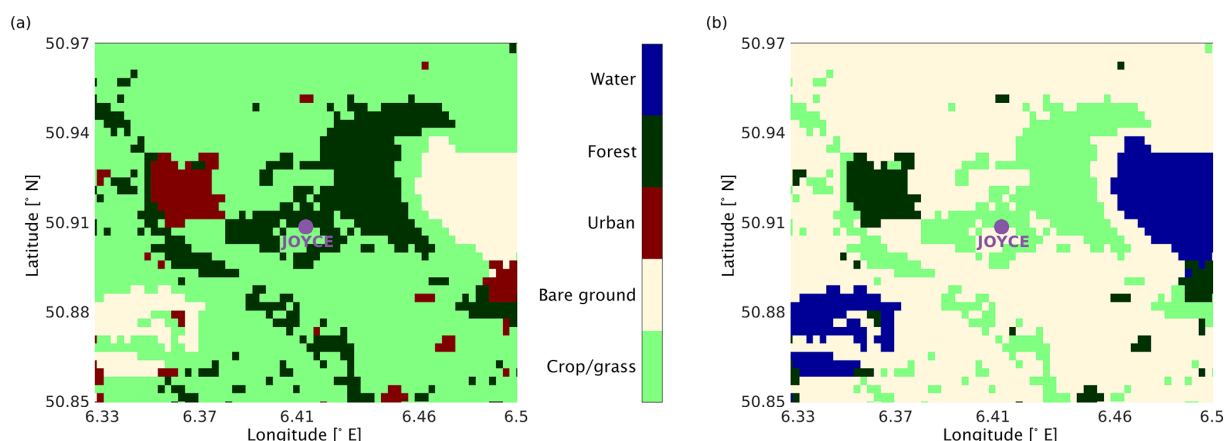


Figure 5. (a) A 12 km × 13 km map of the simplified GlobCover land use data centered around JOYCE used for the first ICON-LEM simulation (ICON1). (b) Same as panel (a) but with altered land use types for the second simulation (ICON2).

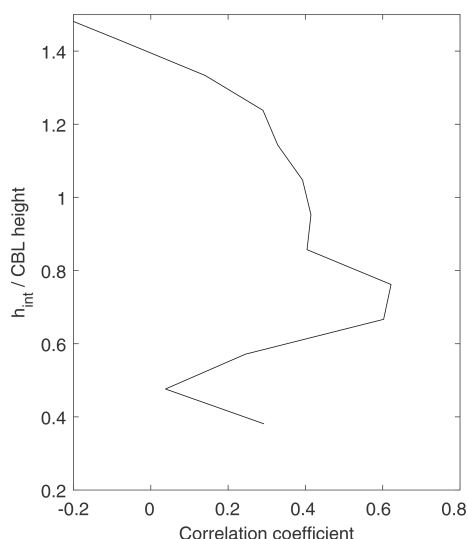


Figure 6. Correlation between 10° sector estimates of term II of Eq. (2) and the slant-path-integrated water vapor at a 30° elevation and 10° azimuth steps. h_{int} is the maximum height of the slant path that is used for the integration and is normalized by the CBL height.

relation coefficient would likely increase for cases with less advection.

Since it can be expected from the analysis of Eq. (2) that humidity transport from the surface is important for this day, changing the land use types is expected to have an influence on the development of the cloudy boundary layer. In a second simulation (ICON2), the land use types are changed according to Fig. 5b (crop–grass to bare ground, bare ground to water, urban to forest, forest to crop–grass and water to urban). In this way, a significant reconstruction of the spatial distribution of the land use types is achieved without changing the scale of heterogeneity, and it keeps all occurring land use types. Also, the partitioning of turbulent surface fluxes

is largely affected by changing crop–grassland to bare soil, but for the whole simulation time the domain-averaged sum of latent and sensible heat only differs by around 10 W m^{-2} between ICON1 and ICON2. The maximum height above ground, where changing the land use types still has a significant influence on model parameters, is around 2.3–2.5 km, which is visible, for example, in the domain-averaged specific humidity difference profile (not shown). Above this height the large-scale forcings are more dominant, which are the same for both simulations. The highest difference occurs in the CBL, which is in agreement with Sühling and Raasch (2013), showing that heterogeneous surface patterns extend throughout the CBL for simulated turbulent heat fluxes. The length scale of land use variability seems to be large enough to cause these differences in the boundary layer according to the blending-height concept (Mahrt, 2000). Also, Shao et al. (2013) found an influence of land-surface heterogeneity well beyond the surface layer using LES.

In order to elaborate on the details of different boundary layer and cloud development, the spatial fields of height- and time-averaged vertical velocity and integrated humidity up to the CBL height (IWV_{CBL}) are analyzed (Fig. 7). The averaging domain is the same as that shown in Fig. 5, and the averaging time is between 12:00 and 13:00 UTC, which is the time range of the first cloud formation in the simulations. Poll et al. (2017) also performed large-eddy simulations of this day in a similar domain and showed the occurrence of clouds around this time in visible satellite data. They found cellular structures in the vertical velocity, which are also evident in Fig. 7a. In addition, the wind is lifted by the hill, and a downdraft above the hill can be seen. This was already discussed in Marke et al. (2018) and might explain parts of the negative scan deviations to the northeast, as discussed in Sect. 3.2, by a suppressed water vapor flux. Moreover the hill serves as a natural border and has an impact by channeling the updraft streak with associated water vapor transport and cloud for-

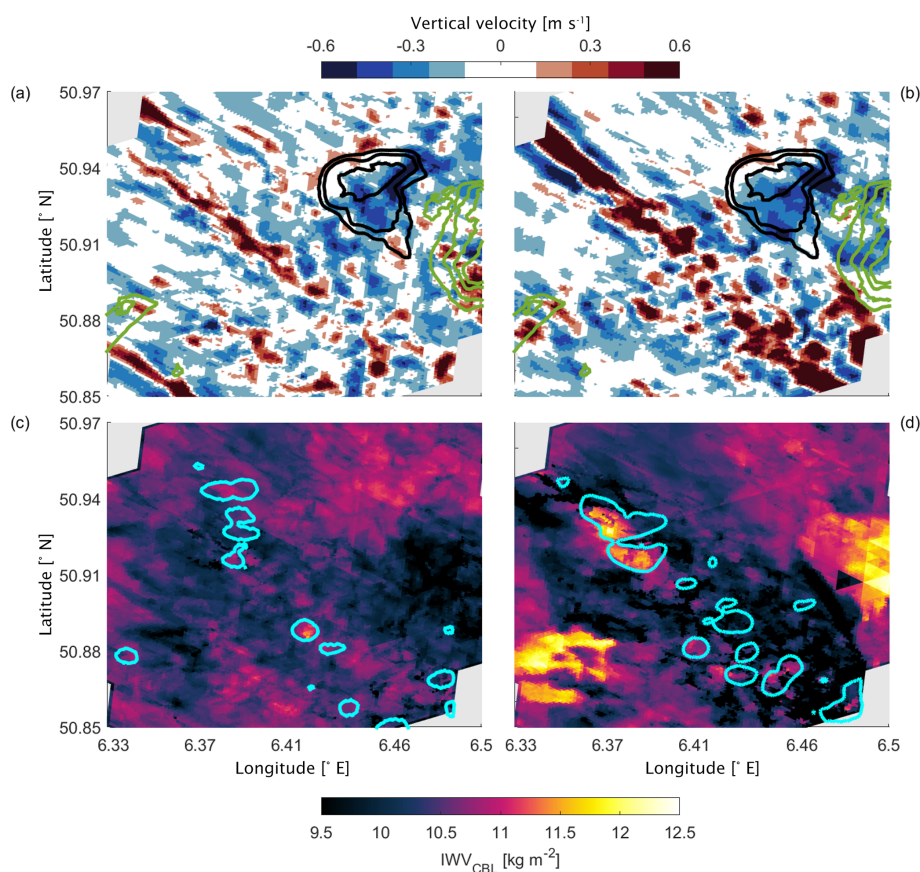


Figure 7. ICON-LEM vertically averaged vertical velocity (**a**, **b**) and integrated humidity (**c**, **d**) up to the CBL height of the ICON1 (**a**, **c**) and ICON2 (**b**, **d**) simulations. Contours in panels (**a**) and (**b**) refer to the topography relative to JOYCE in m a.s.l. between -200 and 0 m (green) and 0 to 200 m (black) in 50 m steps. Contours in panels (**c**) and (**d**) show areas with total column integrated cloud water values above 10 g m^{-2} . The results are averaged between $12:00$ and $13:00$ UTC.

mation going from northwest to southeast. The streaks are also visible in simulations using a larger domain, lower resolution, no topography, and only bare ground (not shown), but the position and strength are strongly altered by the topography and land use input. In the ICON2 simulation the differences in surface properties and the size of the heterogeneous land use patches intensify the vertical velocity streak structure, leading to a higher water vapor transport from the surrounding area into the updraft region and an earlier cloud formation. The water bodies introduced in the second simulation show higher IWV_{CBL} values (Fig. 7d), but the sensible heat flux and CBL height are too low for clouds to form. The mean cloud cover of 8.55% in ICON1 compared to 10.55% in ICON2 is closer to the observed maximum cloud cover of 6% determined by a total sky imager at JOYCE on this day.

Less vegetated areas and hence a lower roughness length in ICON2 also lead to an increase in the mean wind speed of 0.42 m s^{-1} at approximately 200 m above the ground. With higher wind speeds and a higher fraction of bare ground, the domain-averaged sensible heat flux (between $11:00$ and $18:00$ UTC) in ICON2 is increased by 28.72 W m^{-2} , and the

CBL grows deeper (by about 30 m), especially in the south-eastern part of the domain. On the other side, the specific humidity in ICON1 is significantly larger in the CBL (Fig. 6), and clouds grow taller compared to the ICON2 simulation (Fig. 8), which is connected to an increase in latent heat flux by 86.04 W m^{-2} in ICON1 due to more vegetated areas. Also, the maximum integrated cloud water content of these clouds is 36.96 g m^{-2} in ICON1 and only 5.61 g m^{-2} in ICON2 because of the limited moisture supply. The drastic change in the land use data input for ICON2, therefore, causes a shift in the partitioning between sensible and latent heat flux, which has strong implications for the development of convective clouds. Thus, the long-term observed spatial water vapor deviations and high-resolution LES conducted in this study underline the importance of further monitoring and modeling of the local and small-scale interactions between land use, topography, water vapor transport, and the transition to clouds.

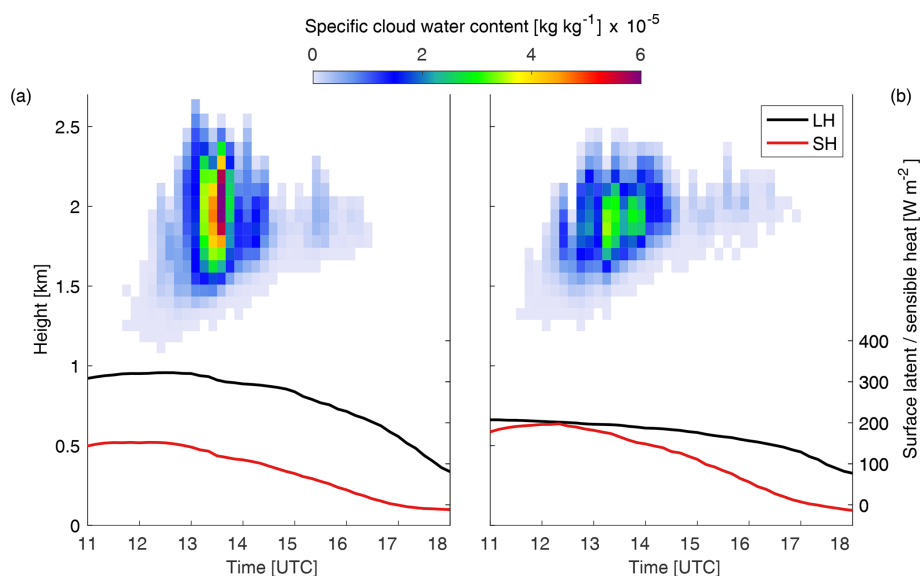


Figure 8. ICON-LEM specific cloud water content for the ICON1 (a) and ICON2 (b) simulation together with the surface fluxes of latent and sensible heat. The results are averaged for the domain shown in Fig. 5.

5 Conclusions

Exchange processes between the land surface and atmosphere are an important controlling factor in the water cycle. Long-term observational evidence of this interaction spanning scales of a few kilometers is still lacking. The scanning microwave radiometer (MWR) at the Jülich Observatory for Cloud Evolution (JOYCE) proved to be suitable for detecting spatial IWV deviations not only for single scans but also in a statistical sense. The atmospheric water vapor pattern can only partly be explained by the large-scale advection and is also attributed to the local transport of water vapor from the surface, especially during convective scenes. This is detected in the long-term analysis of liquid water in cloud-free scans over 6 years of observations.

The comparison with the satellite-based MODIS near-infrared IWV product, as an independent observation, shows features similar to areas with pronounced positive and negative deviations around JOYCE. In a further step, these deviations can be related qualitatively to land surface properties by means of a land use classification. The classification is based on a remote-sensing-derived regional crop map and reveals that positive IWV deviations mainly originate over agricultural areas and open pit mines close to the measurement site, while urban and elevated forest areas show negative deviations. The main locations of the maximum and minimum deviation in the MODIS and MWR measurements are in agreement, but seasonal effects related to the crop development stages are only visible in MWR observations.

In a comprehensive case study, large-eddy simulations with the high-resolution ICON-LEM model were carried out to further assess the impact of the land surface on the devel-

opment of the cloudy boundary layer. While the control simulation is initiated with a realistic land use input, the second simulation with modified land use types revealed changes in convective motions and cloud characteristics according to differences in surface fluxes. These findings suggest that ground-based remote sensing of water vapor supported by high-resolution modeling can be valuable for studying the regional influence of heterogeneous land surfaces on the atmospheric water vapor and the connection between surface fluxes, water vapor, and clouds.

Data availability. The MODIS/Terra Total Precipitable Water Vapor 5-Min L2 Swath 1km dataset was acquired from the Level-1 and Atmosphere Archive & Distribution System (LAADS) Distributed Active Archive Center (DAAC), located in the Goddard Space Flight Center in Greenbelt, Maryland (https://ladsweb.modaps.eosdis.nasa.gov/missions-and-measurements/products/MOD05_L2, last access: 11 November 2019; Borbas et al., 2017).

Author contributions. TM, SC, JHS, and UL designed the experiments and processed the observational data. VS performed the ICON-LEM simulations, and TM prepared the paper with contributions from all coauthors.

Competing interests. The authors declare that they have no conflict of interest.

Acknowledgements. The authors would like to acknowledge the Transregional Collaborative Research Centre (TR32) “Patterns in

Soil-Vegetation-Atmosphere Systems: Monitoring, Modelling and Data Assimilation” funded by the German Research Foundation (DFG), which has continuously contributed to the instrumentation of JOYCE-CF and its maintenance, including the Humidity And Temperature PROfiler (HATPRO), as well as funding Tobias Marke.

Financial support. This research has been supported by the DFG infrastructural programs (grant no. INST 216/681-1). JOYCE observations originate from the DFG funded Core Facility JOYCE-CF (grant no. LO 901/7-1).

Review statement. This paper was edited by Graham Feingold and reviewed by Wayne Angevine and two anonymous referees.

References

- Adler, B., Kalthoff, N., Kohler, M., Handwerker, J., Wieser, A., Corsmeier, U., Kottmeier, C., Lambert, D., and Bock, O.: The variability of water vapour and pre-convective conditions over the mountainous island of Corsica, *Q. J. Roy. Meteor. Soc.*, 142, 335–346, <https://doi.org/10.1002/qj.2545>, 2016.
- Avissar, R. and Schmidt, T.: An Evaluation of the Scale at which Ground-Surface Heat Flux Patchiness Affects the Convective Boundary Layer Using Large-Eddy Simulations, *J. Atmos. Sci.*, 55, 2666–2689, [https://doi.org/10.1175/1520-0469\(1998\)055<2666:aeotsa>2.0.co;2](https://doi.org/10.1175/1520-0469(1998)055<2666:aeotsa>2.0.co;2), 1998.
- Beyrich, F., Leps, J.-P., Mauder, M., Bange, J., Foken, T., Huneke, S., Lohse, H., Lüdi, A., Meijninger, W. M. L., Mironov, D., Weisensee, U., and Zittel, P.: Area-Averaged Surface Fluxes Over the Litfass Region Based on Eddy-Covariance Measurements, *Bound.-Lay. Meteorol.*, 121, 33–65, <https://doi.org/10.1007/s10546-006-9052-x>, 2006.
- Bontemps, S., Defourny, P., Van Bogaert, E., Arino, O., Kalogirou, V., and Ramos Perez, J. J.: GLOBCOVER 2009 Products Description and Validation Report, Université catholique de Louvain (UCL) & European Space Agency (ESA), 2.2, 53 pp., <https://doi.org/10013/epic.39884.d016>, 2011.
- Borbas, E., Menzel, P., and Gao, B.: MODIS Atmosphere L2 Water Vapor Product. NASA MODIS Adaptive Processing System, Goddard Space Flight Center, USA, https://doi.org/10.5067/MODIS/MOD05_L2.061, 2017.
- Clark, C. A. and Arriitt, P. W.: Numerical Simulations of the Effect of Soil Moisture and Vegetation Cover on the Development of Deep Convection, *J. Appl. Meteorol.*, 34, 2029–2045, [https://doi.org/10.1175/1520-0450\(1995\)034<2029:NSOTEO>2.0.CO;2](https://doi.org/10.1175/1520-0450(1995)034<2029:NSOTEO>2.0.CO;2), 1995.
- Copernicus Climate Change Service (C3S): ERA5: Fifth generation of ECMWF atmospheric reanalyses of the global climate, Copernicus Climate Change Service Climate Data Store (CDS), available at: <https://cds.climate.copernicus.eu/cdsapp#!/home> (last access: 3 March 2019), 2017.
- Courault, D., Drobinski, P., Brunet, Y., Lacarrere, P., and Talbot, C.: Impact of surface heterogeneity on a buoyancy-driven convective boundary layer in light winds, *Bound.-Lay. Meteorol.*, 124, 383–403, <https://doi.org/10.1007/s10546-007-9172-y>, 2007.
- Gao, B.-C. and Kaufman, Y. J.: Water vapor retrievals using Moderate Resolution Imaging Spectroradiometer (MODIS) near-infrared channels, *J. Geophys. Res.-Atmos.*, 108, 4389, <https://doi.org/10.1029/2002jd003023>, 2003.
- Garcia-Carreras, L., Parker, D. J., and Marsham, J. H.: What is the Mechanism for the Modification of Convective Cloud Distributions by Land Surface-Induced Flows?, *J. Atmos. Sci.*, 68, 619–634, <https://doi.org/10.1175/2010jas3604.1>, 2011.
- Heinze, R., Dipankar, A., Henken, C. C., Moseley, C., Sourdeval, O., Trömel, S., Xie, X., Adamidis, P., Ament, F., Baars, H., Barthlott, C., Behrendt, A., Blahak, U., Bley, S., Brdar, S., Brueck, M., Crewell, S., Deneke, H., Di Girolamo, P., Evaristo, R., Fischer, J., Frank, C., Friederichs, P., Göcke, T., Gorges, K., Hande, L., Hanke, M., Hansen, A., Hege, H.-C., Hoose, C., Jahns, T., Kalthoff, N., Klocke, D., Kneifel, S., Knippertz, P., Kuhn, A., van Laar, T., Macke, A., Maurer, V., Mayer, B., Meyer, C. I., Muppa, S. K., Neggers, R. A. J., Orlandi, E., Pantillon, F., Pospichal, B., Röber, N., Scheck, L., Seifert, A., Seifert, P., Senf, F., Siligam, P., Simmer, C., Steinke, S., Stevens, B., Wapler, K., Weniger, M., Wulfmeyer, V., Zängl, G., Zhang, D., and Quaas, J.: Large-eddy simulations over Germany using ICON: a comprehensive evaluation: Evaluation of ICON in Realistic LES Configuration, *Q. J. Roy. Meteor. Soc.*, 143, 69–100, <https://doi.org/10.1002/qj.2947>, 2017.
- Huang, H. Y. and Margulis, S. A.: On the impact of surface heterogeneity on a realistic convective boundary layer, *Water Resour. Res.*, 45, W04425, <https://doi.org/10.1029/2008WR007175>, 2009.
- Kneifel, S., Crewell, S., Lohnert, U., and Schween, J.: Investigating Water Vapor Variability by Ground-Based Microwave Radiometry: Evaluation Using Airborne Observations, *IEEE Geosci. Remote S.*, 6, 157–161, <https://doi.org/10.1109/LGRS.2008.2007659>, 2009.
- Löhnert, U. and Crewell, S.: Accuracy of cloud liquid water path from ground-based microwave radiometry 1. Dependency on cloud model statistics, *Radio Sci.*, 38, 8041, <https://doi.org/10.1029/2002rs002654>, 2003.
- Löhnert, U., Schween, J. H., Acquistapace, C., Ebell, K., Maahn, M., Barrera-Verdejo, M., Hirsikko, A., Bohn, B., Knaps, A., O'Connor, E., Simmer, C., Wahner, A., and Crewell, S.: JOYCE: Jülich Observatory for Cloud Evolution, *B. Am. Meteorol. Soc.*, 96, 1157–1174, <https://doi.org/10.1175/BAMS-D-14-00105.1>, 2015.
- Macke, A., Seifert, P., Baars, H., Barthlott, C., Beekmans, C., Behrendt, A., Bohn, B., Brueck, M., Bühl, J., Crewell, S., Damian, T., Deneke, H., Düsing, S., Foth, A., Di Girolamo, P., Hammann, E., Heinze, R., Hirsikko, A., Kalisch, J., Kalthoff, N., Kinne, S., Kohler, M., Löhnert, U., Madhavan, B. L., Maurer, V., Muppa, S. K., Schween, J., Serikov, I., Siebert, H., Simmer, C., Späth, F., Steinke, S., Träummer, K., Trömel, S., Wehner, B., Wieser, A., Wulfmeyer, V., and Xie, X.: The HD(CP)² Observational Prototype Experiment (HOPE) – an overview, *Atmos. Chem. Phys.*, 17, 4887–4914, <https://doi.org/10.5194/acp-17-4887-2017>, 2017.
- Mahrt, L.: Surface Heterogeneity and Vertical Structure of the Boundary Layer, *Bound.-Lay. Meteorol.*, 96, 33–62, <https://doi.org/10.1023/A:1002482332477>, 2000.
- Manninen, A. J., Marke, T., Tuononen, M., and O'Connor, E. J.: Atmospheric Boundary Layer Classification With

- Doppler Lidar, *J. Geophys. Res.-Atmos.*, 123, 8172–8189, <https://doi.org/10.1029/2017JD028169>, 2018.
- Marke, T., Crewell, S., Schemann, V., Schween, J. H., and Tuononen, M.: Long-term observations and high-resolution modeling of midlatitude nocturnal boundary layer processes connected to low-level jets, *J. Appl. Meteorol. Clim.*, 57, 1155–1170, <https://doi.org/10.1175/JAMC-D-17-0341.1>, 2018.
- Maronga, B. and Raasch, S.: Large-Eddy Simulations of Surface Heterogeneity Effects on the Convective Boundary Layer During the LITFASS-2003 Experiment, *Bound.-Lay. Meteorol.*, 146, 17–44, <https://doi.org/10.1007/s10546-012-9748-z>, 2013.
- Maschwitz, G., Löhnert, U., Crewell, S., Rose, T., and Turner, D. D.: Investigation of ground-based microwave radiometer calibration techniques at 530 hPa, *Atmos. Meas. Tech.*, 6, 2641–2658, <https://doi.org/10.5194/amt-6-2641-2013>, 2013.
- O'Connor, E. J., Illingworth, A. J., Brooks, I. M., Westbrook, C. D., Hogan, R. J., Davies, F., and Brooks, B. J.: A method for estimating the turbulent kinetic energy dissipation rate from a vertically pointing doppler lidar, and independent evaluation from balloon-borne in situ measurements, *J. Atmos. Ocean. Tech.*, 27, 1652–1664, <https://doi.org/10.1175/2010JTECHA1455.1>, 2010.
- Ookouchi, Y., Segal, M., Kessler, R. C., and Pielke, R. A.: Evaluation of Soil Moisture Effects on the Generation and Modification of Mesoscale Circulations, *Mon. Weather Rev.*, 112, 2281–2292, [https://doi.org/10.1175/1520-0493\(1984\)112<2281:eosomeo>2.0.co;2](https://doi.org/10.1175/1520-0493(1984)112<2281:eosomeo>2.0.co;2), 1984.
- Pearson, G., Davies, F., and Collier, C.: An Analysis of the Performance of the UFAM Pulsed Doppler Lidar for Observing the Boundary Layer, *J. Atmos. Ocean. Tech.*, 26, 240–250, <https://doi.org/10.1175/2008JTECHA1128.1>, 2009.
- Pielke, R. A., Dalu, G. A., Snook, J. S., Lee, T. J., and Kittel, T. G. F.: Nonlinear Influence of Mesoscale Land Use on Weather and Climate, *J. Climate*, 4, 1053–1069, [https://doi.org/10.1175/1520-0442\(1991\)004<1053:niomlu>2.0.co;2](https://doi.org/10.1175/1520-0442(1991)004<1053:niomlu>2.0.co;2), 1991.
- Poll, S., Shrestha, P., and Simmer, C.: Modelling convectively induced secondary circulations in the textitterra incognita with TerrSysMP: Modelling CISCs in the Terra Incognita with TerrSysMP, *Q. J. Roy. Meteor. Soc.*, 143, 2352–2361, <https://doi.org/10.1002/qj.3088>, 2017.
- Rabin, R. M., Stadler, S., Wetzels, P. J., Stensrud, D. J., and Gregory, M.: Observed Effects of Landscape Variability on Convective Clouds, *B. Am. Meteorol. Soc.*, 71, 272–280, [https://doi.org/10.1175/1520-0477\(1990\)071<0272:oeolvo>2.0.co;2](https://doi.org/10.1175/1520-0477(1990)071<0272:oeolvo>2.0.co;2), 1990.
- Rose, T., Crewell, S., Löhnert, U., and Simmer, C.: A network suitable microwave radiometer for operational monitoring of the cloudy atmosphere, *Atmos. Res.*, 75, 183–200, <https://doi.org/10.1016/j.atmosres.2004.12.005>, 2005.
- Schween, J. H., Crewell, S., and Löhnert, U.: Horizontal-humidity gradient from one single-scanning microwave radiometer, *IEEE Geosci. Remote S.*, 8, 336–340, <https://doi.org/10.1109/LGRS.2010.2072981>, 2011.
- Shao, Y., Liu, S., Schween, J. H., and Crewell, S.: Large-Eddy Atmosphere-Land-Surface Modelling over Heterogeneous Surfaces: Model Development and Comparison with Measurements, *Bound.-Lay. Meteorol.*, 148, 333–356, <https://doi.org/10.1007/s10546-013-9823-0>, 2013.
- Simmer, C., Thiele-Eich, I., Masbou, M., Amelung, W., Bogen, H., Crewell, S., Dieckrüger, B., Ewert, F., Hendricks Franssen, H.-J., Huisman, J. A., Kemna, A., Klitzsch, N., Kollet, S., Langensiepen, M., Löhnert, U., Rahman, A. S. M. M., Rascher, U., Schneider, K., Schween, J., Shao, Y., Shrestha, P., Stiebler, M., Sulis, M., Vanderborght, J., Vereecken, H., van der Kruk, J., Waldhoff, G., and Zerenner, T.: Monitoring and Modeling the Terrestrial System from Pores to Catchments: The Transregional Collaborative Research Center on Patterns in the Soil-Vegetation-Atmosphere System, *B. Am. Meteorol. Soc.*, 96, 1765–1787, <https://doi.org/10.1175/BAMS-D-13-00134.1>, 2015.
- Späth, F., Behrendt, A., Muppa, S. K., Metzendorf, S., Riede, A., and Wulfmeyer, V.: 3-D water vapor field in the atmospheric boundary layer observed with scanning differential absorption lidar, *Atmos. Meas. Tech.*, 9, 1701–1720, <https://doi.org/10.5194/amt-9-1701-2016>, 2016.
- Steinke, S., Eikenberg, S., Löhnert, U., Dick, G., Klocke, D., Di Girolamo, P., and Crewell, S.: Assessment of small-scale integrated water vapour variability during HOPE, *Atmos. Chem. Phys.*, 15, 2675–2692, <https://doi.org/10.5194/acp-15-2675-2015>, 2015.
- Steinke, S., Wahl, S., and Crewell, S.: Benefit of high resolution COSMO reanalysis: The diurnal cycle of column-integrated water vapor over Germany, *Meteorol. Z.*, 28, 165–177, <https://doi.org/10.1127/metz/2019/0936>, 2019.
- Stull, R. B.: *An Introduction to Boundary Layer Meteorology*, Kluwer Academic, Dordrecht, the Netherlands, 1988.
- Sührling, M. and Raasch, S.: Heterogeneity-Induced Heat-Flux Patterns in the Convective Boundary Layer: Can they be Detected from Observations and is There a Blending Height? – A Large-Eddy Simulation Study for the LITFASS-2003 Experiment, *Bound.-Lay. Meteorol.*, 148, 309–331, <https://doi.org/10.1007/s10546-013-9822-1>, 2013.
- Tang, X., Li, H., Desai, A. R., Nagy, Z., Luo, J., Kolb, T. E., Oliosio, A., Xu, X., Yao, L., Kutsch, W., Pilegaard, K., Köstner, B., and Ammann, C.: How is water-use efficiency of terrestrial ecosystems distributed and changing on Earth?, *Sci. Rep.*, 4, 7483, <https://doi.org/10.1038/srep07483>, 2015.
- van Heerwaarden, C. C. and Vilà-Guerau De Arellano, J.: Relative Humidity as an Indicator for Cloud Formation over Heterogeneous Land Surfaces, *J. Atmos. Sci.*, 65, 3263–3277, <https://doi.org/10.1175/2008JAS2591.1>, 2008.
- Vilà-Guerau De Arellano, J., Ouwensloot, H. G., Baldocchi, D., and Jacobs, C. M.: Shallow cumulus rooted in photosynthesis, *Geophys. Res. Lett.*, 41, 1796–1802, <https://doi.org/10.1002/2014GL059279>, 2014.
- Waldhoff, G. and Lussem, U.: Enhanced land use classification of 2015 for the Rur catchment – Update, TR32DB, <https://doi.org/10.5880/TR32DB.19>, 2016.
- Waldhoff, G., Lussem, U., and Bareth, G.: Multi-Data Approach for remote sensing-based regional crop rotation mapping: A case study for the Rur catchment, Germany, *Int. J. Appl. Earth Obs.*, 61, 55–69, <https://doi.org/10.1016/j.jag.2017.04.009>, 2017.
- Weckwerth, T. M., Parsons, D. B., Koch, S. E., Moore, J. A., LeMone, M. A., Demoz, B. B., Flamant, C., Geerts, B., Wang, J., and Feltz, W. F.: An Overview of the International H₂O Project (IHOP_2002) and Some Preliminary Highlights, *B. Am. Meteorol. Soc.*, 83, 1455–1465, 2002.

- rol. Soc., 85, 253–278, <https://doi.org/10.1175/BAMS-85-2-253>, 2004.
- Wulfmeyer, V., Behrendt, A., Kottmeier, C., Corsmeier, U., Barthlott, C., Craig, G. C., Hagen, M., Althausen, D., Aoshima, F., Arpagaus, M., Bauer, H.-S., Bennett, L., Blyth, A., Brandau, C., Champollion, C., Crewell, S., Dick, G., Di Girolamo, P., Dorninger, M., Dufournet, Y., Eigenmann, R., Engelmann, R., Flamant, C., Foken, T., Gorgas, T., Grzeschik, M., Handwerker, J., Hauck, C., Höller, H., Junkermann, W., Kalthoff, N., Kiemle, C., Klink, S., König, M., Krauss, L., Long, C. N., Madonna, F., Mobbs, S., Neininger, B., Pal, S., Peters, G., Pigeon, G., Richard, E., Rotach, M. W., Russchenberg, H., Schmitalla, T., Smith, V., Steinacker, R., Trentmann, J., Turner, D. D., van Baelen, J., Vogt, S., Volkert, H., Weckwerth, T., Wernli, H., Wieser, A., and Wirth, M.: The Convective and Orographically-induced Precipitation Study (COPS): the scientific strategy, the field phase, and research highlights, *Q. J. Roy. Meteor. Soc.*, 137, 3–30, <https://doi.org/10.1002/qj.752>, 2011.
- Wulfmeyer, V., Turner, D. D., Baker, B., Banta, R., Behrendt, A., Bonin, T., Brewer, W. A., Buban, M., Choukulkar, A., Dumas, E., Hardesty, R. M., Heus, T., Ingwersen, J., Lange, D., Lee, T. R., Metzendorf, S., Muppa, S. K., Meyers, T., Newsom, R., Osman, M., Raasch, S., Santanello, J., Senff, C., Späth, F., Wagner, T., and Weckwerth, T.: A New Research Approach for Observing and Characterizing Land-Atmosphere Feedback, *B. Am. Meteorol. Soc.*, 99, 1639–1667, <https://doi.org/10.1175/BAMS-D-17-0009.1>, 2018.
- Zängl, G., Reinert, D., R’ipodas, P., and Baldauf, M.: The ICON (ICOsahedral Non-hydrostatic) modelling framework of DWD and MPI-M: Description of the non-hydrostatic dynamical core, *Q. J. Roy. Meteor. Soc.*, 141, 563–579, <https://doi.org/10.1002/qj.2378>, 2015.

5 STATISTICAL RETRIEVALS OF LIQUID CLOUDS

STATISTICAL RETRIEVAL OF THIN LIQUID CLOUD MICROPHYSICAL PROPERTIES USING GROUND-BASED INFRARED AND MICROWAVE OBSERVATIONS

T. Marke, K. Ebell, U. Löhnert, and D. Turner (2016). “Statistical retrieval of thin liquid cloud microphysical properties using ground-based infrared and microwave observations”. In: *Journal of Geophysical Research* 121.24. DOI: [10.1002/2016JD025667](https://doi.org/10.1002/2016JD025667)

© 2016 American Geophysical Union. All Rights Reserved.

RESEARCH ARTICLE

10.1002/2016JD025667

Key Points:

- Microphysical properties of thin liquid water clouds
- Improving statistical retrieval accuracy by combining microwave and infrared regime
- Evaluation of retrieval performance in a radiative closure study with real measurements

Correspondence to:

T. Marke,
tmarke@meteo.uni-koeln.de

Citation:

Marke, T., K. Ebell, U. Löhnert, and D. D. Turner (2016), Statistical retrieval of thin liquid cloud microphysical properties using ground-based infrared and microwave observations, *J. Geophys. Res. Atmos.*, 121, 14,558–14,573, doi:10.1002/2016JD025667.

Received 18 JUL 2016

Accepted 17 NOV 2016

Accepted article online 23 NOV 2016

Published online 20 DEC 2016

Statistical retrieval of thin liquid cloud microphysical properties using ground-based infrared and microwave observations

Tobias Marke¹ , Kerstin Ebell¹ , Ulrich Löhnert¹ , and David D. Turner² 
¹Institute for Geophysics and Meteorology, University of Cologne, Cologne, Germany, ²National Severe Storms Laboratory, Norman, Oklahoma, USA

Abstract In this article, liquid water cloud microphysical properties are retrieved by a combination of microwave and infrared ground-based observations. Clouds containing liquid water are frequently occurring in most climate regimes and play a significant role in terms of interaction with radiation. Small perturbations in the amount of liquid water contained in the cloud can cause large variations in the radiative fluxes. This effect is enhanced for thin clouds (liquid water path, LWP < 100 g/m²), which makes accurate retrieval information of the cloud properties crucial. Due to large relative errors in retrieving low LWP values from observations in the microwave domain and a high sensitivity for infrared methods when the LWP is low, a synergistic retrieval based on a neural network approach is built to estimate both LWP and cloud effective radius (r_{eff}). These statistical retrievals can be applied without high computational demand but imply constraints like prior information on cloud phase and cloud layering. The neural network retrievals are able to retrieve LWP and r_{eff} for thin clouds with a mean relative error of 9% and 17%, respectively. This is demonstrated using synthetic observations of a microwave radiometer (MWR) and a spectrally highly resolved infrared interferometer. The accuracy and robustness of the synergistic retrievals is confirmed by a low bias in a radiative closure study for the downwelling shortwave flux, even for marginally invalid scenes. Also, broadband infrared radiance observations, in combination with the MWR, have the potential to retrieve LWP with a higher accuracy than a MWR-only retrieval.

1. Introduction

Assessing the impact of clouds on the global circulation represents a major task in improving climate models. Quoting the fifth assessment report (AR5), the Intergovernmental Panel on Climate Change (IPCC) states that clouds and their associated macrophysical and microphysical processes are still responsible for large uncertainties in the estimation and interpretation of the Earth's energy budget [*Intergovernmental Panel on Climate Change*, 2013]. Clouds drive the atmospheric circulation through complex interactions with solar and thermal fluxes from the surface and the atmosphere [Stephens, 2005]. In situations with a low liquid water path (LWP), the radiative fluxes are especially sensitive to liquid water variations [Turner *et al.*, 2007b; Sengupta *et al.*, 2003]. Thus, special emphasis needs to be put on thin liquid water clouds, which are here defined as clouds containing low amounts of liquid water (LWP below 100 g/m²). Furthermore, Turner *et al.* [2007a] revealed that a high frequency of occurrence (between 43% and 67%) of thin liquid water clouds can be observed in most climate regimes, including the Arctic (Barrow, Alaska), a continental midlatitude site (Lamont, Oklahoma), and the tropical Western Pacific (Darwin, Australia). Thus, in order to better represent thin liquid water clouds and their impact on radiative fluxes and heating rates in climate models, it is extremely important to develop instruments and retrieval algorithms that can be used to accurately derive properties of these clouds like LWP and cloud droplet effective radius (r_{eff}) [Löhnert and Crewell, 2003].

Microphysical and optical cloud properties, such as LWP and r_{eff} , can be used to describe the interactions of clouds with radiation [Hu and Stamnes, 1993; Stephens, 1978]. Most notably, the impact of clouds on the radiative flux is mainly dependent on the total amount of condensed water contained in the cloud [Turner *et al.*, 2007a]. The effective radius is also valuable for understanding the mechanisms of cloud formation, dissipation, and interactions with aerosol and drizzle [Kubar *et al.*, 2009].

Ground-based remote sensing instruments, like active cloud radars or passive instruments, are commonly used for observing liquid water clouds [Turner *et al.*, 2007b]. Typically, automated observation methods are

able to obtain long-term records of cloud properties with a high temporal resolution from the radiative energy that is emitted, transmitted, or reflected by the cloud. Passive remote sensing instruments are preferable because they are typically more affordable than active remote sensors [Crewell *et al.*, 2009] but do not provide vertical cloud information.

Comparisons of state-of-the-art retrieval methods show large discrepancies in retrieving LWP and r_{eff} for liquid water clouds. Turner *et al.* [2007b] evaluated different MWR-based LWP algorithms for a cloudy case with a LWP less than 100 g/m² and found a spread of 40 g/m² between the LWP algorithms, which was primarily due to the retrieval technique and the assumptions used in the methods. This result agrees with the conclusions of Marchand *et al.* [2003] and Sengupta *et al.* [2003], both of which included random uncertainties in the microwave brightness temperatures in the retrieval. This emphasizes the demand for improving the accuracy of retrieval algorithms for thin clouds.

The microwave radiometer (MWR) is the most common single-instrument approach to retrieve LWP [Löhnert and Crewell, 2003; Liljegren *et al.*, 2001] and has been used for decades [e.g., Westwater, 1978]. Observations in the microwave region can be used to retrieve LWP, because of the semitransparency of clouds [Löhnert *et al.*, 2004] and the increase of the liquid water contribution in the emitted signal with higher frequency [Crewell *et al.*, 2009]. The MWR is able to retrieve wide ranges of LWP without saturation but with a LWP retrieval error of around 20–30 g/m² [Marchand *et al.*, 2003; Löhnert and Crewell, 2003]. This results in high relative uncertainties for clouds with low LWP values.

Similar to the passive MWR, also, techniques in the infrared domain make use of the energy emitted by the atmosphere to gain information on cloud properties. If the cloud is single layered and contains low amounts of liquid water, the infrared methods are able to obtain simultaneous estimates of LWP and r_{eff} [Turner *et al.*, 2007b]. The infrared domain offers a significantly higher sensitivity to changes in LWP for low amounts of cloud liquid water than the MWR [Turner, 2007]. Note that the infrared observations are also sensitive toward ice clouds. Thus, prior information on the cloud phase must be available, because an incorrect phase determination can lead to errors in the estimates of the single-scattering properties [Turner *et al.*, 2003]. The distinction between liquid water and ice can be achieved by taking advantage of differences in the refraction index of ice and water in the highly resolved infrared spectrum between 11 and 19 μm for a low amount of precipitable water vapor (PWV < 1 cm, according to Turner *et al.* [2003]). This prevents Atmospheric Emitted Radiance Interferometer (AERI) observations from being used in most midlatitude and all tropical locations. Thus, using active remote sensors and an algorithm like the cloud classification scheme Cloudnet [Illingworth *et al.*, 2007], as done in the present study, provides a much more robust and consistent cloud phase identification over the entire PWV range.

Since the interaction of atmospheric constituents with radiation changes with wavelength, spectrally diverse measurements contain different information about the atmospheric composition. Therefore, the optimal instrument and frequency combination needs to be determined [Löhnert *et al.*, 2004]. Ground-based instruments in the infrared domain have the advantage of high sensitivities to clouds with small LWP, when on the other side the uncertainty in the MWR retrievals is relatively large. Conversely, the infrared signal saturates at larger amounts of LWP (around 60 g/m² [Turner, 2007]), leading to large uncertainties in the infrared retrievals. Hence, we focus on LWP and r_{eff} retrievals using a combination of ground-based microwave and infrared observations. These synergistic LWP retrievals show a high sensitivity for low-LWP situations and are still able to retrieve LWP over the entire dynamic range.

A combined LWP retrieval using the microwave and infrared spectral region has been developed by Turner [2007] and showed improved skills in retrieving LWP relative to a MWR-only retrieval approach. That retrieval algorithm was developed for mixed-phase clouds and used the optimal estimation approach [e.g., Rodgers, 2000]. Such physical algorithms are rather complex and computationally expensive, requiring vertical profiles of temperature and humidity as input (e.g., from radiosonde data). This study focuses on statistical retrievals for LWP and r_{eff} , i.e., a neural network approach, where vertical profiles are not required and therefore the derivation of the retrievals is independent of the times of radiosonde ascents. Moreover, the statistical retrievals are easy to handle: applying the retrievals only requires a matrix multiplication of the measured quantity together with the one-time-derived retrieval coefficients. However, it is not readily evident that a statistical retrieval can be derived with a similar accuracy than the physical retrieval, due to the nonlinear response of the downwelling radiation to increasing LWP in the infrared domain [Turner, 2007]. Hereby a neural network approach is chosen to accomplish this goal, and the scientific objectives of this study are

Table 1. Wavenumber Ranges for AERI Microwindows

| # | Wavenumber (cm ⁻¹) | # | Wavenumber (cm ⁻¹) |
|---|--------------------------------|----|--------------------------------|
| 1 | 770.9–774.8 | 8 | 872.2–877.5 |
| 2 | 785.9–790.7 | 9 | 891.9–895.8 |
| 3 | 809.0–812.9 | 10 | 898.2–905.4 |
| 4 | 815.3–824.4 | 11 | 929.6–939.7 |
| 5 | 828.3–834.6 | 12 | 959.9–964.3 |
| 6 | 842.8–848.1 | 13 | 985.0–998.0 |
| 7 | 860.1–864.0 | | |

as follows: performance evaluation for single-instrument and synergy retrievals in the microwave and infrared domains using synthetic data, comparison of the retrievals using spectrally highly resolved or broadband infrared observations, and retrieval validation in a radiative closure study using real measurements.

In the next section, the instruments that are deployed in this study and their specifications are described. In section 3, the methodology is presented including the retrieval development and the compilation of synthetic data for retrieval training and testing. In section 4, the retrievals are tested with the synthetic data, while section 5 deals with the application of the retrievals to real measurements in a radiative closure study.

2. Instruments

This study includes three types of state-of-the-art passive ground-based remote sensing instruments: a microwave Humidity And Temperature PROfiler (HATPRO-MWR), two broadband infrared radiometers (IRRs), and the infrared Atmospheric Emitted Radiance Interferometer (AERI). In the following, the basic principles and characteristics of each instrument are briefly specified. The measurements are taken from the Jülich Observatory for Cloud Evolution (JOYCE) [Löhnert *et al.*, 2015]. JOYCE is operated jointly by the University of Cologne, the Research Centre Jülich, and the Transregional Collaborative Research Centre “Patterns in Soil-Vegetation-Atmosphere Systems: Monitoring, Modelling and Data Assimilation.” The scientific goal of JOYCE is to observe the spatial and temporal variability of atmospheric water cycle variables.

2.1. Infrared Interferometer AERI

The Atmospheric Emitted Radiance Interferometer (AERI) is an operational ground-based spectrometer. The AERI measures the downwelling infrared radiance every 16–17 s at approximately 1 cm⁻¹ resolution from 520 to 3000 cm⁻¹ (corresponding to 3.3–19.2 μm), with a narrow zenith field of view. Since there is no significant infrared emission from space in the downwelling radiance, the entire signal is provided by emission from the atmosphere. Two detectors are used in a “sandwich” configuration, to provide the needed sensitivity across the entire spectral range [Knuteson *et al.*, 2004a]. Approximately 2500 spectral channels for each of its two detectors are provided. This is accomplished by measuring the interference pattern created by the interferometer. The two well-characterized blackbodies (one at ambient air temperature and the other fixed at 60°C) and the application of a nonlinearity correction for the detectors result in the radiometric accuracy of the radiance measurements being better than 1% of the ambient radiance [Knuteson *et al.*, 2004b].

Turner [2005] has shown that the AERI high spectral resolution observations can be used to retrieve microphysical cloud properties, utilizing “microwindows” between gaseous absorption lines and thereby minimizing the effects of atmospheric gases. In this study, 13 microwindows are used (Table 1), which are described in Turner [2005]. They are located between 770.9 cm⁻¹ (13.0 μm) and 998 cm⁻¹ (10.0 μm), which is a spectral region with a high sensitivity to liquid water. The uncertainty in the AERI observations is less than 1 mW/(m² sr cm⁻¹). The study of Turner [2007] shows that the AERI possesses a high sensitivity to changes in LWP until the LWP increases above 60 g/m². At LWP values below 60 g/m², the sensitivity of the downwelling radiance to changes in LWP is higher than the AERI uncertainty. For optically thicker clouds, a further rise in the LWP produces only a slightly increase in the infrared radiance, which can no longer be distinguished from the measurement noise.

2.2. Microwave and Infrared Radiometers

The Humidity And Temperature PROfiler (HATPRO) at JOYCE consists of a passive microwave radiometer utilizing direct detection receivers. Usually, a two-channel statistical or physical retrieval is applied to derive LWP using observations of the downwelling microwave radiance at 23.8 and 31.4 GHz [e.g., Liljegren *et al.*, 2001].

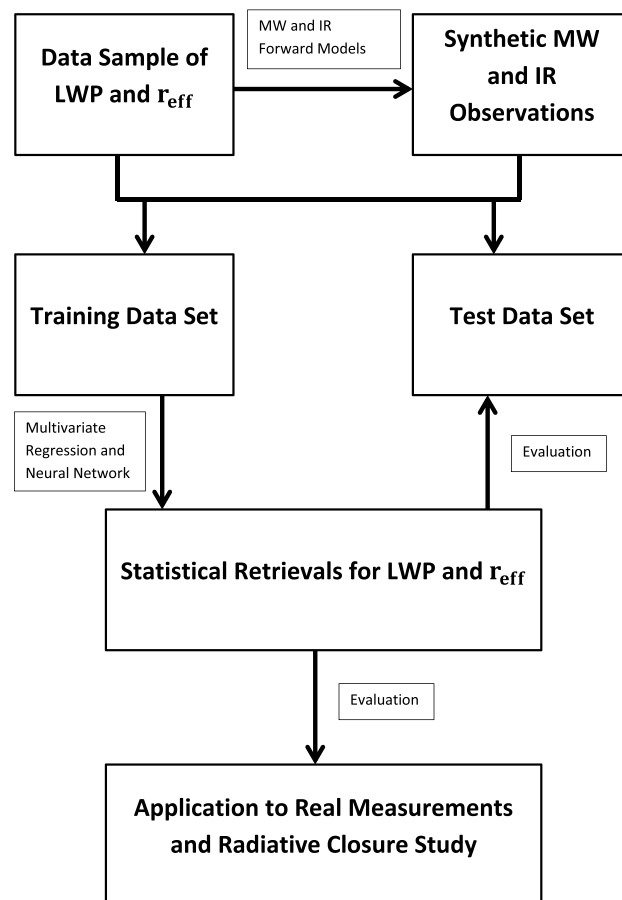


Figure 1. Flow chart of the study setup.

The former frequency is on the wing of the 22.2 GHz water vapor absorption line, and the latter frequency is located in an atmospheric window, where the signal is dominated by liquid water emission when clouds are in the instrument's field of view. The estimated error in the two-channel MWR retrieved LWP is usually considered to be at least 20–30 g/m² because of uncertainties in the microwave absorption model, the applied retrieval method, and the measurement accuracy [Turner *et al.*, 2007b]. Considering the low LWP values of thin clouds (below 100 g/m²), this uncertainty converts into relative errors being 20% or more.

The MWR measures the brightness temperatures (TB) at seven channels in the K band from 22 GHz to 32 GHz and at seven channels also in the V band from 52 GHz to 58 GHz. The instrument was designed to observe liquid water path with a high temporal resolution up to 1 s [Rose *et al.*, 2005]. In this study, only zenith observations of the seven K-band channels with a 1 s temporal resolution are taken into account. The zenith measurements alternate with full hemispheric scans for temperature profiling.

In contrast to the infrared domain, the

absorption has no dependence on the droplet size distribution (DSD) and thus r_{eff} , since the cloud droplets are significantly smaller than the wavelength and are therefore located in the Rayleigh scattering regime [Crewell *et al.*, 2009].

In addition, the microwave radiometer is equipped with two broadband infrared radiometers (IRRs). The first IRR has a maximum sensitivity at around 11.1 μm (bandpass 10.2–11.9 μm), and the second one provides a maximum sensitivity at around 12 μm (bandpass 11.1–12.8 μm), which correspond to wavelength ranges of 840.3–980.4 cm^{-1} and 781.3–900.9 cm^{-1} , respectively. The accuracy is denoted to be about 1 K. The IRR wavelength bands are located in an atmospheric window where the measured longwave radiation is dominated by clouds and saturation is expected to be around 40 g/m². The adjustment of the elevation angle of the IRRs is linked to the MWR. The IRRs in this study are used to examine the potential of broadband infrared measurements to retrieve cloud properties, in comparison to spectrally highly resolved observations of the AERI, which are of much higher cost and have a higher calibration demand.

2.3. Shortwave Broadband Measurements

For the radiative closure study in the last part of this study, the Kipp & Zonen CMP 21 pyranometer is used to measure the downwelling broadband hemispheric irradiance in the solar spectrum (285 to 2800 nm) with a 5 s temporal resolution. The instrument is bias corrected for a nighttime offset and the cosine effect. The error estimation also includes the sensitivity of the data logger and its temperature dependence.

3. Methodology

The methodology of this study is summarized in Figure 1. First, a data sample of single-layer liquid water cloud properties is generated. Using this data sample, MWR and IRR brightness temperatures, as well as

AERI radiances, are simulated. The combined cloud property and measurement data set is separated into a training and test data set. Statistical retrievals are developed based on the training data set, which are in turn evaluated with the test data set. Finally, the retrievals are applied to real measurements. Each step will be explained in detail in the following.

3.1. Data Sample of Single-Layer Liquid Water Cloud Properties

For the derivation of the statistical retrievals, a training and test data sample containing only cases of single-layer liquid water clouds is prepared. These samples include the LWP and the cloud layer mean r_{eff} . In addition to LWP and r_{eff} , a thermodynamic profile of temperature, pressure, and humidity are needed to simulate MWR, AERI, and IRR observations, which are then used for retrieval development. This compiled data set is assumed to represent the characteristics of single-layer water clouds at JOYCE. In order to create the data set of LWP and r_{eff} , cloud radar and MWR measurements are used in combination with simple radar-MWR retrievals for retrieving a r_{eff} training data set. In order to ensure that the training data set contains only the desired single-layer liquid water clouds and the measured signal is not influenced by any other clouds, information on cloud phase and cloud layers is required. Both cloud phase and number of cloud layers can be determined by using the Cloudnet classification product. If the Cloudnet product is not available, a different cloud classification, involving radar and lidar measurements, needs to be applied to allow for a physical interpretation of the retrieval results.

In order to create this data set of LWP and r_{eff} , JOYCE measurements in combination with cloud radar reflectivity/MWR methods are used. First, single-layer liquid clouds are detected using the Cloudnet classification product. The core instruments for Cloudnet are a Doppler cloud radar, a lidar ceilometer, a multiwavelength microwave radiometer, and a rain gauge. The classification product provides vertically resolved information on the cloud phase averaged for 30 s. In addition, profiles of temperature, pressure, and humidity are included, which are from either the European Centre for Medium-Range Weather Forecasting (ECMWF) model or the numerical weather prediction model COSMO-DE [Baldauf and other, 2011]. Further details of the Cloudnet product can be found in Illingworth et al. [2007].

The backscatter targets in each radar/lidar pixel are categorized into a number of different classes, including precipitation. If drizzle or rain is present, the cloud radar reflectivity is dominated by large drops and simple cloud radar reflectivity/MWR methods are not applicable. Thus, in this study, only nonprecipitating clouds are included and determined by using the Cloudnet approach. The identification of clouds containing drizzle can also be achieved by using thresholds in the radar reflectivity only [Krasnov and Russchenberg, 2002] or as a ratio to ceilometer extinction [Frisch et al., 1995] to discriminate drizzle-free clouds. Furthermore, clouds must be present for at least 2 min in order to avoid spurious cloud detection and to ensure full cloud cover in the instrument's field of view.

With the previous described Cloudnet classification, 5780 cases (30 s averages) of single-layer liquid water clouds without precipitation are identified for the JOYCE site in the period of 13 March to 31 December 2012. For the liquid water path, the Cloudnet-derived LWP is used, which is based on a statistical retrieval using microwave observations. Such retrievals may provide physically unrealistic negative values, which have been excluded in this data sample. The LWP distribution shows the expected high occurrence of low LWP values for the liquid water clouds with a median of 28.6 g/m² (not shown). Clouds with a LWP below 100 g/m², which represent the cloud type of main interest in this study, account for 87.9% of all observed single-layer liquid cloud profiles in this period. Note that the statistical retrieval can only be as good as the training data set, which is assumed to encompass the full range of atmospheric conditions. This results in site and cloud type-specific training data set, which could be extended to more cloud types in future studies (mixed-phase clouds). If other sites exhibit similar atmospheric conditions, it is sensible to apply the developed retrievals at these sites. Otherwise, new retrieval coefficients based on a more appropriate training data set have to be found.

In order to have an estimate of mean layer r_{eff} and vertical information on these cloud properties needed for the forward simulations, a cloud radar/microwave radiometer method is deployed. A homogeneous mixing model, described in Knist [2014], is used to derive profiles of LWC and r_{eff} from the cloud layer mean r_{eff} . Homogeneous mixing is described by a faster mixing process than the effects of evaporation. In this case, evaporation reduces uniformly the DSD and the number concentration and the DSD shape parameter does not change. If this process occurs, the microphysical cloud properties consequently change according to Boers et al. [2006] and the impact of mixing accounts for the vertical variation in the radar reflectivity [Knist, 2014].

Table 2. Main Cloud Properties of the Data Sample

| Property | Mean \pm SD | Median | Minimum | Maximum |
|------------------|----------------------------------|----------------------|---|------------------------|
| Base height | 1769.6 \pm 889.9 m | 1985.9 m | 143.9 m | 4000.5 m |
| Thickness | 337.9 \pm 185.6 m | 287.8 m | 86.3 m | 1870.8 m |
| LWP | 51.2 \pm 71.1 g/m ² | 28.6g/m ² | 0.02g/m ² | 1032.2g/m ² |
| LWC | 0.2 \pm 0.2 g/m ³ | 0.2g/m ³ | 1.6 \cdot 10 ⁻⁴ g/m ³ | 1.4g/m ³ |
| r_{eff} | 6.3 \pm 2.2 μ m | 4.0 μ m | 1.0 μ m | 32.4 μ m |

For the homogeneous mixing model a gamma DSD is applied, which is frequently used in liquid cloud studies [Miles *et al.*, 2000] and results in the following equations for the LWC and r_{eff} as used in Knist [2014]:

$$\text{LWC}(h) = \text{LWP} \frac{Z^{1/2}(h)}{\sum_{i=0}^n Z^{1/2}(h_i) \Delta h}, \quad (1)$$

where h is the height above cloud base and Δh is the radar range gate. The radar reflectivity Z is summed up from the base to the top of the cloud. The LWP is taken from the Cloudnet output and is also used to derive the r_{eff} in this approach:

$$r_{\text{eff}}(h) = k_{R_v} \left(\frac{\pi \rho_w \sum_{i=0}^n Z^{1/2}(h_i)}{48 \text{LWP}} \right)^{1/3} Z^{1/6}(h), \quad (2)$$

$$k_{R_v} = \left(\frac{(\nu + 2)^3}{((\nu + 3)(\nu + 4)(\nu + 5))} \right)^{1/3}, \quad \nu = 8.7. \quad (3)$$

The r_{eff} derivation depends on the DSD shape parameter ν through the coefficient k_{R_v} . In this study, continental single-layer liquid water clouds are examined, which are expected to have larger droplet concentrations and smaller particle sizes. Referring to several experimental data of such cloud types, the reported mean value of $\nu = 8.7$ for the gamma DSD shape parameter is used according to Miles *et al.* [2000].

In this study, mean values of the derived data sample are 4.2 μ m for r_{eff} and 0.2g/m³ for LWC. In Chiu *et al.* [2012], who also used the radar reflectivity for deriving r_{eff} , the distribution of the effective radius peaks at 6–8 μ m for single-layer liquid water clouds. The reason for the smaller derived values in this study is most likely the uncertainty in LWP. Since negative values from the MWR-derived LWP are not considered for the radiative transfer calculations, the mean value of the data set is higher than the “true” mean value. This can introduce a negative bias in retrieving r_{eff} in a LWP/ Z relationship-based method, where r_{eff} is inversely proportional to the LWP. A further source of errors is the assumption on the droplet concentration, which is determined by the constant choice of ν and can cause large uncertainties [Zhao *et al.*, 2012]. In order to increase the possible range of the r_{eff} values, the variability of the data set has been increased by 50%, resulting in an increased mean value of 6.3 μ m. An overview of the characteristics of the cloud data sample is given in Table 2.

3.2. Simulated Microwave and Infrared Observations

In this section, the infrared and microwave forward models to simulate the MWR, AERI, and IRR observations using the previously described data sample are presented.

3.2.1. Infrared Forward Model

The LBLDIS [Turner *et al.*, 2003] forward model combines a Line-by-Line Radiative Transfer Model (LBLRTM) [Clough *et al.*, 1992], computing infrared atmospheric emission spectra for gases and the Discrete Ordinate Radiate Transfer (DISORT) [Stamnes *et al.*, 1988] model, accounting for the scattering and absorption properties of the cloud. Input variables are, in addition to the cloud microphysical properties of the data sample, thermodynamic profiles of temperature (T), pressure (p), and humidity (q), which are taken from COSMO-DE model output. Figure 2 shows the simulated AERI spectrum for a clear-sky case and the high sensitivity to increasing LWP values. But also, the saturation effect for higher LWP values is visible. For the simulated infrared observations, the corresponding AERI spectral resolution using the previous described microwindows (grey bars, Figure 2) and IRR spectral response functions (dashed blue and red lines in Figure 2) are taken into account.

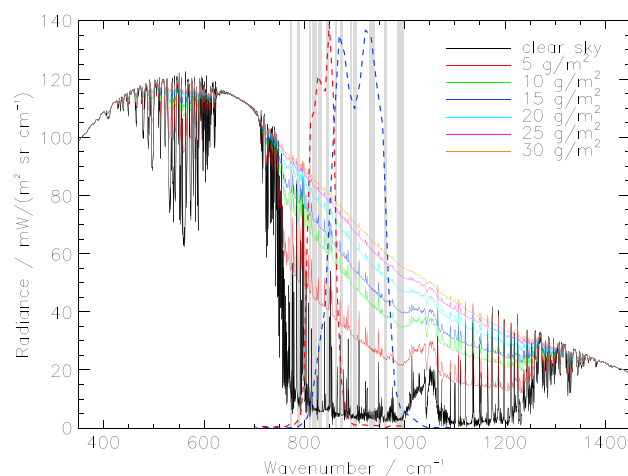


Figure 2. Simulated AERI radiances using LBLDIS for clear sky (solid black line) and different LWP ranging from 5 to 30 g/m² (solid colored lines) with constant effective radius ($r_{\text{eff}} = 7 \mu\text{m}$). Grey bars denote the 13 microwindows and dashed colored lines the IRR spectral response functions.

oxygen is calculated according to Rosenkranz [1998], with adjustments in the water vapor continuum [Turner et al., 2009] and for liquid water according to Liebe et al. [1991].

3.3. Derivation of Statistical Retrievals Using a Neural Network Approach

Statistical retrievals for LWP and mean layer r_{eff} are derived based on the data sets described in sections 3.1 and 3.2, which are divided into training and test parts. The training subset contains 70% of the original data set, and 15% are used for the testing and 15% for validation within the neural network retrieval development. In order to maintain the statistical properties, the original data set was divided randomly. This resulted in data sets with similar statistical properties. For example, the median LWP (r_{eff}) values for the training and testing data subsets are 28.52 g/m² (6.0 μm) and 29.79 g/m² (5.9 μm), respectively. Due to the limited sensitivity of the infrared methods, saturation occurs for LWP values larger than 40–60 g/m². This nonlinear effect cannot be represented by a multivariate linear regression scheme. Therefore, a neural network (NNET) approach is chosen in this study. Since the infrared observations are saturated above 60 g/m², they are only used in combination with the MWR. An overview of all retrievals that are derived and applied in this study is given in Table 3. In the following only the short names will be used.

Neural network retrievals have been widely used for cloud property retrievals [e.g., Cadeddu et al., 2009; Turner and Gero, 2011]. The NNET architecture possesses the advantage of finding nonlinear statistical relationships between input parameters and target values [Faure et al., 2001]. The network in this study consists of a two-layer feedforward network with sigmoid hidden neurons and linear output neurons. The input parameters p contain the linear and quadratic simulated brightness temperatures of the MWR (seven channels), the IRRs and the AERI radiances in the selected 13 microwindows. For the MWR 0.5 K was added to the brightness temperatures as random noise. The noise contributions for the simulated infrared radiances are 1 K (IRRs) and 0.2 mW (m² sr cm⁻¹)⁻¹ (AERI). In the first layer (hidden layer), the input is weighted (\mathbf{W}_1) and a bias b_1 is added using the sigmoid function, giving an output a_1 in the range of 0 to 1:

$$a_1 = \text{logsig}(\mathbf{W}_1 p + b_1). \quad (5)$$

The weights and biases need to be adjusted in several iterations, in order to optimize the performance of the network in terms of the root-mean-square (RMS) error. In order to avoid overtraining, a validation set is used to decide when to stop the network training (according to Hagan et al. [2014]). The training set is used to compute the gradients and to determine the updated weight at each iteration. The error of the validation set is monitored during the training: if the error increases or remains the same for six iterations, the training is stopped. The testing data set is used as a further check that the network generalizes well. The number of weights and bias values can be adjusted to optimize the network performance. After testing several

3.2.2. Microwave Forward Model

A radiative transfer operator is used to simulate the brightness temperatures for the seven MWR frequencies f_i between 22 and 32 GHz Löhnert et al. [2004].

$$\text{TB}_i = \text{RTO}(\mathbf{T}, \mathbf{p}, \mathbf{q}, \text{LWC}, f_i), \quad (4)$$

with i from 1 to 7, denoting the MWR frequencies, and the COSMO-DE given atmospheric state vectors (\mathbf{T} , \mathbf{p} , \mathbf{q} , and LWC).

The forward model performing the radiative transfer calculation (RTO is the radiative transfer operator) is only valid for nonscattering cases. Therefore, the approximation is only applicable for nonprecipitating clouds and for frequencies below 100 GHz [Simmer, 1994]. The microwave absorption for water vapor and

Table 3. Neural Network Retrievals Developed in This Study

| Instrument(s) | Variable | Short Name |
|---------------|------------------|------------|
| MWR | LWP | MW_LWP |
| MWR + AERI | LWP | MW+AE_LWP |
| MWR + IRRs | LWP | MW+IR_LWP |
| MWR | r_{eff} | MW_reff |
| MWR + AERI | r_{eff} | MW+AE_reff |
| MWR + IRRs | r_{eff} | MW+IR_reff |

configurations, the number was set to 20. In the second layer, the retrieval output a_2 , which represents the LWP or r_{eff} , is computed with a linear transformation:

$$a_2 = \text{lin}(\mathbf{W}_2 a_1 + b_2). \quad (6)$$

The Levenberg-Marquardt algorithm was used for the back propagation in the MATLAB neural network toolbox, explained in detail in *Hagan et al.* [2014].

3.4. Setup of Shortwave Radiation Closure Study

While for the synthetic data study the retrieval performance can directly be evaluated, since the “truth” is known, it is more difficult to assess the retrieval performance using real measurements. To this end, a shortwave downwelling radiation closure study is performed (section 5). In this closure study, the measured shortwave radiation from the CMP 21 pyranometer at JOYCE is compared to the output of a broadband radiative transfer model using the retrieved LWP and r_{eff} as input. The deployed model is the broadband rapid radiative transfer model RRTMG, which has been developed by the Atmospheric and Environmental Research (AER) Incorporated [Clough et al., 2005]. RRTMG provides accurate atmospheric fluxes and heating rates in the shortwave and longwave spectral regime and is widely used in numerical weather prediction and climate models. The accuracy has been extensively validated, in particular with comparisons between the RRTMG and the LBLRTM line-by-line calculations. The differences in shortwave fluxes in Clough et al. [2005] are found to be less than 1.5 W/m^2 for the net flux in the troposphere. In the following, all crucial input variables used in this study are described in detail.

For the concentrations of ozone, methane, and oxygen, profiles of the midlatitude standard atmosphere are applied. Also, the thermodynamic profiles of temperature, pressure, and humidity from COSMO-DE are included. The effects of aerosols on the shortwave fluxes need to be accounted for. Therefore, vertical profiles of aerosol optical depth (AOD), single-scattering albedo, and asymmetry parameter are inserted in RRTMG. Values for the aerosol optical depths have been derived from AErosol RObotic NETwork (AERONET) [Holben et al., 1998] measurements: The aerosol optical depths are calculated for all RRTMG midinterval wavelengths via the measured aerosol optical depths and Angstrom exponent at 870nm, which describes the spectral dependence of the aerosol optical depth. Here 870nm is taken as the reference wavelength, because of the high sensitivity to LWP in this spectral area. In this study a monthly mean AOD is assumed, which is vertically scaled using an exponential weighting function with a scaling height of about 1.3km. For the single-scattering albedo and the asymmetry parameter, values for urban aerosol are applied, which were computed from the Optical Properties of Aerosols and Clouds (OPAC) database [Hess et al., 1998].

The direct-beam and diffuse shortwave surface albedo are included by using the Collection 5 products of the Terra and Aqua Moderate Resolution Imaging Spectroradiometer (MODIS) combined data set at 500 m resolution [Schaaf et al., 2002].

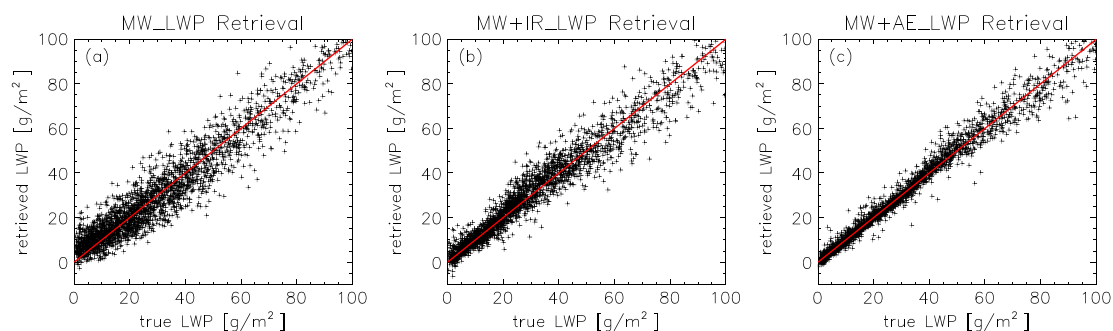


Figure 3. Scatterplots of the true (test data set) and retrieved LWP of the NNET-LWP retrievals (a) MW_LWP, (b) MW+IR_LWP, and (c) MW+AE_LWP. The legend describes the retrieval performance for low (LWP < 50 g/m²) and high (LWP > 50 g/m²) LWP situations to emphasize the different sensitivities of the infrared and microwave retrievals. The 1:1 line is given in red.

Table 4. Statistics (Correlation, Bias, and RMSE) for LWP and r_{eff} Retrievals of the Synthetic Study for LWP Values Below and Above 50 g/m²

| | MW_LWP | MW+IR_LWP | MW+AE_LWP | MW_reff | MW+IR_reff | MW+AE_reff |
|---------------------------|----------------------|----------------------|----------------------|---------|------------|------------|
| LWP < 50 g/m ² | | | | | | |
| Correlation | 0.88 | 0.95 | 0.99 | 0.36 | 0.80 | 0.95 |
| Bias | 0.5g/m ² | 1.0g/m ² | 0.2g/m ² | 0.04μm | −0.05μm | 0.01μm |
| RMSE | 6.5g/m ² | 4.4g/m ² | 2.4g/m ² | 2.2μm | 1.4μm | 0.7μm |
| LWP > 50 g/m ² | | | | | | |
| Correlation | 0.996 | 0.996 | 0.997 | 0.35 | 0.55 | 0.62 |
| Bias | −1.6g/m ² | −1.9g/m ² | −0.8g/m ² | −0.2μm | −0.1μm | 0.02μm |
| RMSE | 8.7g/m ² | 9.1g/m ² | 7.4g/m ² | 1.8μm | 1.6μm | 1.5μm |

4. Retrieval Test With Synthetic Data

In this section, the previously described retrievals for LWP and r_{eff} are tested with the simulated observations of MWR, AERI, and IRRs. Since the microwave and infrared spectral domains have distinct sensitivities for different LWP regimes, the performance of the single instrument and synergy retrievals is analyzed with respect to varying LWP values.

4.1. Retrieval Results for LWP

Comparing the MW_LWP retrieval to the synergy retrievals (MW+IR_LWP and MW+AE_LWP), the wide spread for low-LWP cases is noticeable in Figure 3a. If the IRR and AERI simulated radiances are combined with the MWR in the NNET approach, the benefit of the infrared domain is visible for low LWP values (Figures 3b and 3c). The absolute root-mean-square error (RMSE) is reduced by 2.1g/m² for the MW+IR_LWP retrieval in the LWP range up to 50g/m² and by 4.1g/m² for the MW+AE_LWP retrieval (Table 4). In the range of higher LWP values, only the MWR and AERI synergy is able to improve the RMSE compared to the MWR-only retrieval (by 1.3g/m²). Note that the axis range in Figure 3 was limited to 100g/m², but higher values do occur and the statistics in Table 4 encompass all values.

In order to get a better insight into the retrieval performance, the relative RMSE of the different retrievals is analyzed depending on the LWP for thin liquid water clouds up to 100g/m². Figure 4 shows a decrease in relative RMSE with increasing LWP for all retrievals. The expected high errors for the MW_LWP retrieval for low LWP values are also revealed, i.e., above 50%. At 100g/m² the relative error is decreased to around 8%. There is a distinct improvement for the combination of microwave and infrared simulated observations compared to the retrieval using only the MWR. Below 90g/m² the MW+AE_LWP retrieval shows a reduction in relative RMSE up to 37 percentage points (pp) compared to the MW_LWP retrieval results. For the entire LWP range of thin liquid water clouds, the MW+AE_LWP retrieval reveals the lowest relative RMSE of 7–17%, which translates into absolute errors of only 1.7–8.8g/m². Note that the relative error in the MW+AE_LWP retrieval, which uses a NNET retrieval approach, is almost identical to the relative error in the physical retrieval method of Turner [2007].

It has been demonstrated that the combination of the MWR and the highly spectrally resolved infrared measurements of the AERI are very beneficial in retrieving LWP. The question is if also the simulated broadband

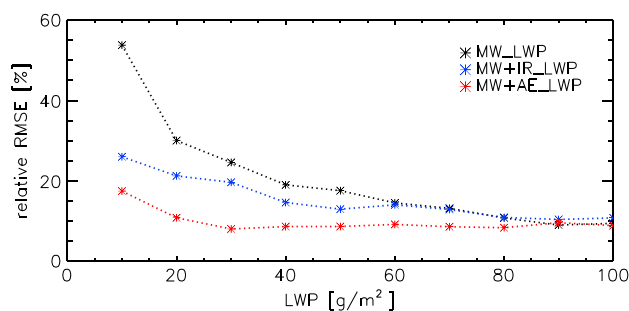


Figure 4. Relative root-mean-square error as a function of LWP for the different NNET-LWP retrievals.

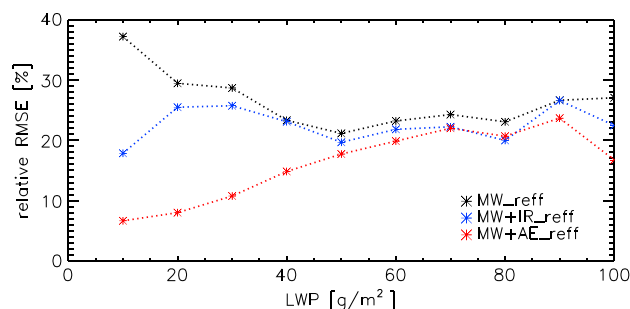


Figure 5. Relative root-mean-square error as a function of LWP for the different NNET r_{eff} retrievals.

infrared observations of the IRRs improve the MWR-derived LWP. In general, the relative RMSE increases if IRR instead of AERI observations are used (Figure 4). Replacing the AERI with the IRR simulated observations in a retrieval synergy leads to a reduced accuracy up to 9 pp in the retrieved LWP, with the larger impact at smaller LWP values. For the low LWP values the IRR and MWR retrieval combination still performs better than the MWR alone (up to 28 pp lower relative RMSE).

4.2. Retrieval Results for r_{eff}

In the following, the r_{eff} retrievals are discussed. In contrast to the NNET-LWP retrieval results in Figure 4, the RMSEs of the r_{eff} retrievals only show a strong dependence on the LWP for the MW+AE_reff retrieval (Figure 5). The RMSE increases from 0.7 below 50 g/m² to 1.5 above 50 g/m² (Figure 6c). As expected, the MWR observations reveal no sensitivity to r_{eff} (Figure 6a), which results in higher absolute errors of 1.3–2.4 μm . However, the brightness temperatures are additionally used in combination with infrared measurements to retrieve r_{eff} , in order to examine if the MWR indirectly improves the r_{eff} estimation through constraining the LWP information.

For the MW+AE_reff retrievals a relative RMSE below 15% (absolute error = 0.4–0.8 μm) can be seen up to 40 g/m² in Figure 5, which is similar to the error only using the AERI (not shown). For higher LWP values, the combined retrieval MW+AE_reff shows an improvement of about 0.2 μm . The average relative error of the MW+IR_reff retrieval is around 22.5% in the LWP range up to 100 g/m². In terms of absolute errors the combination of IRR and MWR is on average 0.2 μm lower than for the IRR alone. This implies that the brightness temperatures of the MWR provide some additional information to improve the r_{eff} retrieval accuracy via constraining the LWP. Using the spectrally highly resolved AERI observations instead of the broadband IRR ones, a significant improvement in the retrieval performance can be observed below 50 g/m² (lower absolute error by 1.5 μm).

5. Application to Real Measurements

With respect to synthetic data, the statistical NNET retrievals using the synergy of MWR and AERI show potential for retrieving LWP and r_{eff} for thin liquid water clouds. For this study it can be stated that the spectrally highly resolved AERI observations are favorable over the broadband IRR observations in a retrieval

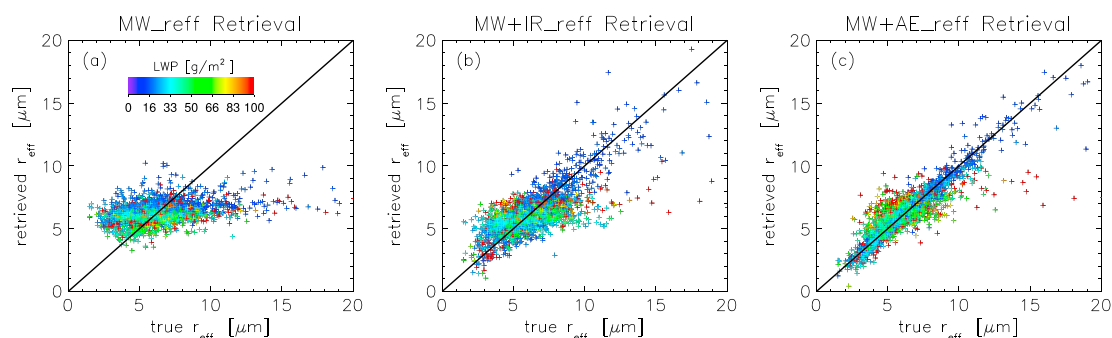


Figure 6. Same as Figure 3 for the NNET r_{eff} retrievals (a) MW_reff, (b) MW+IR_reff, and (c) MW+AE_reff. The data points are colored with the corresponding LWP from the test data set. The 1:1 line is given in black.

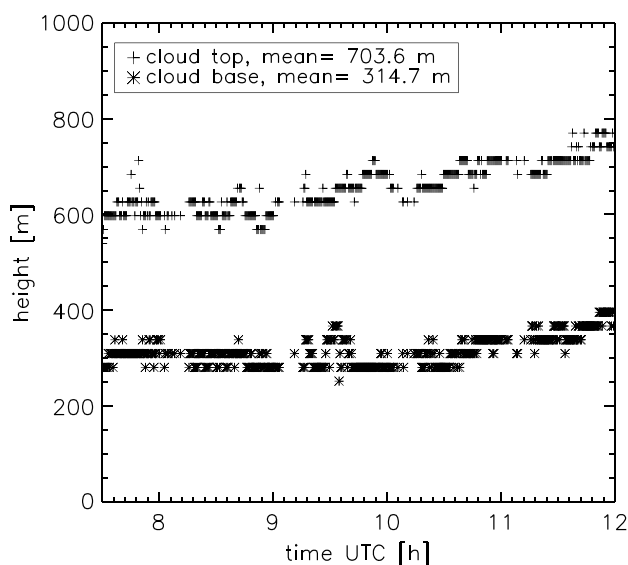


Figure 7. Cloudnet-derived cloud base and cloud top height. Results shown for 8 April 2015 (7.5–12 UTC).

combination with the MWR, especially for deriving the effective radius, although the combination of MWR and IRRs exhibits only a minor difference in retrieving the LWP compared to the MW+AE_LWP retrieval and displayed an improvement to the single instrument MWR retrieval. Thus, the LWP and r_{eff} retrievals of MWR, MWR+IR, and MWR+AERI have been chosen to be applied to real measurements at JOYCE. Since there is no truth for the cloud properties at JOYCE, the retrieval performance is evaluated in terms of a radiative closure study in this section. The focus is to show the potential of using both the LWP and r_{eff} retrievals for the closure.

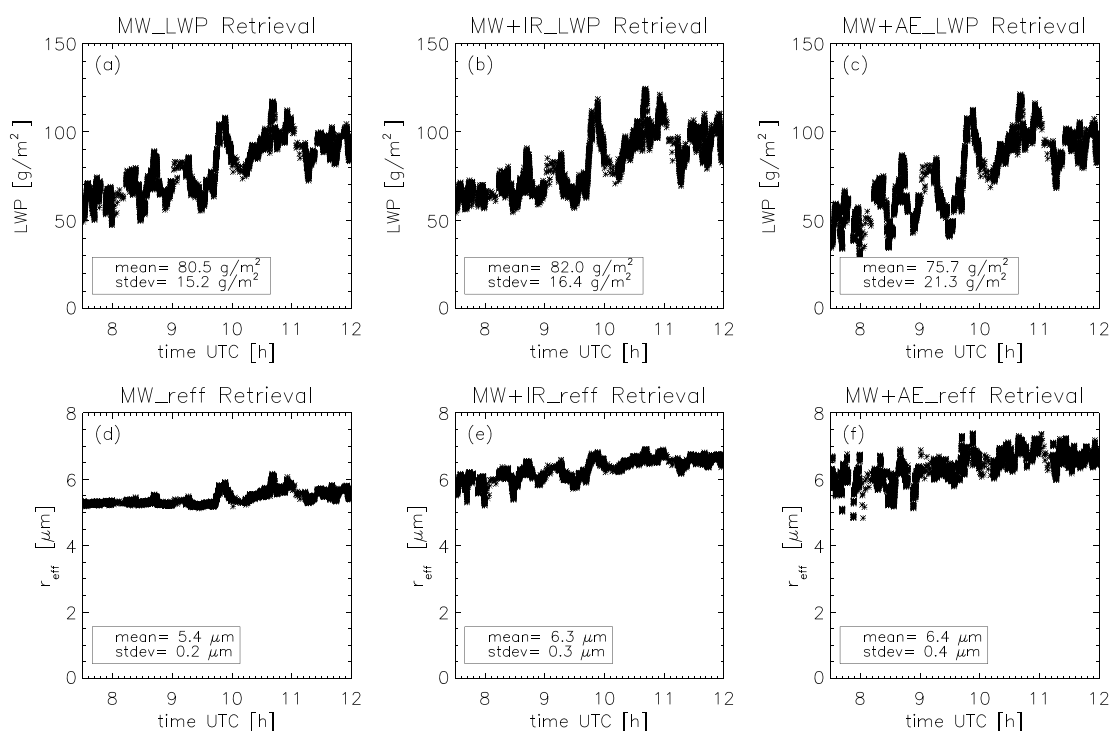


Figure 8. (a–c) LWP and (d–f) r_{eff} time series derived with the MWR (Figures 8a and 8d), MWR+IRR (Figures 8b and 8e), and MWR+AERI (Figures 8c and 8f) retrievals. Gaps in the measurements are due to MWR scans. Results shown for 8 April 2015 (7.5–12 UTC).

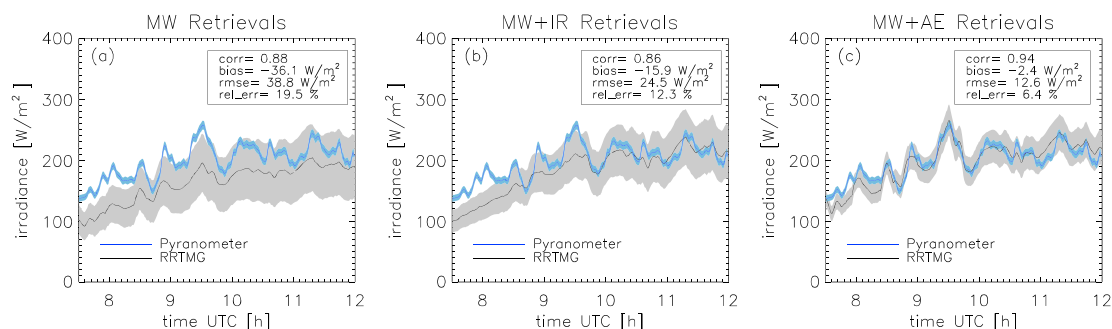


Figure 9. Time series for the RRTMG-derived shortwave downward flux (black line) averaged over 5 min and the measured shortwave downward flux for the CMP 21 pyranometer (blue line). (a) RRTMG calculation using the derived MW_LWP and MW_reff retrievals, (b) MW+IR_LWP and MW+IR_reff retrievals, and (c) MW+AE_LWP and MW+AE_reff retrievals. Shaded areas are due to measurement errors of the pyranometer and a LWP error of $\pm 18\%$ for the MW_LWP retrieval (MW+IR_LWP: $\pm 14\%$, MW+AE_LWP: $\pm 9\%$). Results shown for 8 April 2015 (7.5–12 UTC).

5.1. Ideal Case Study Description

For the application of the retrievals to real measurements at JOYCE we will focus on a case on 8 April 2012 with a persistent single-layer liquid water cloud between 7.5 and 12 UTC (Figure 7). This time period of rather homogeneous cloud overcast condition has been chosen to minimize uncertainties in the radiative closure study due to three-dimensional radiation effects, which can introduce large errors in the shortwave radiation estimates based on 1-D radiative transfer calculations. Although the retrievals can be applied to broken cloud scenes, which are common for low-LWP scenes, they cannot be evaluated in this way. The derived LWP and r_{eff} from the NNET retrievals are used to calculate the shortwave flux in the radiative transfer model RRTMG.

The retrieved LWP values show an increase with time (Figures 8a–8c) corresponding to a higher cloud thickness. The lowest LWP mean value of 75.7 g/m^2 and highest standard deviation (by about 6 g/m^2) is retrieved by the MW+AE_LWP retrieval. The r_{eff} retrieval results are typically between 5 and $7 \mu\text{m}$ and show a low variability. The combination of MWR and AERI (MW+AE_reff) shows the highest variations in r_{eff} , especially in the beginning of the time series where the LWP is still low. As expected, the MW_reff-derived r_{eff} is almost constant around $5.3 \mu\text{m}$, which is caused by the low sensitivity of the MWR to the r_{eff} (Figures 8d–8f).

5.2. Shortwave Radiative Closure Study

Since the shortwave fluxes of the CMP 21 pyranometer represent instantaneous hemispheric measurements, the calculated shortwave fluxes based on the cloud properties from the narrow field of view of AERI, IRR, and MWR are averaged over 5 min in order to improve the comparability. Using the derived LWP uncertainty from the synthetic data study, i.e., 18% for MW_LWP, 14% for MW+IR_LWP, and 9% for the MW+AE_LWP retrieval, the related bias error in the shortwave downwelling fluxes is assessed as an estimate for the uncertainty in the shortwave downwelling flux.

Using the MWR retrievals, a clear underestimation of the measured shortwave flux is visible (Figure 9a), resulting in a bias value of -36.1 W/m^2 . Adding broadband infrared observations in the LWP and r_{eff} retrievals (MWR+IRR approach), the calculated flux values are also lower than measured by the pyranometer, especially between 7.5 and 8.5 UTC. During this time, Figures 8b and 8e show higher LWP values combined with a lower variability in r_{eff} than in the MWR and MWR+AERI cases, causing the high negative bias. However, the MWR+IRR combination is still able to reduce the error in the shortwave flux to 12.3% compared to the RRTMG

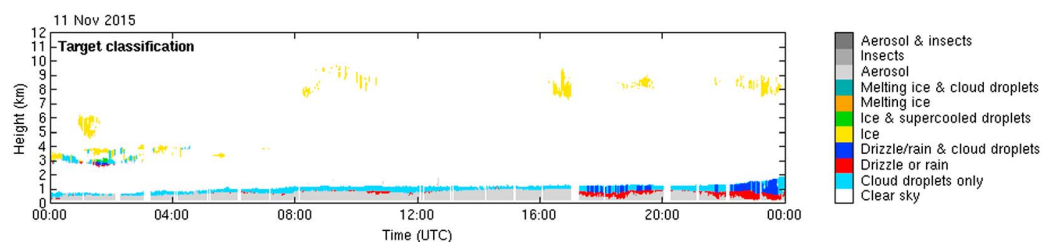


Figure 10. Cloudnet target classification for 11 November 2015. Gaps in the measurements are due to cloud radar scanning times.

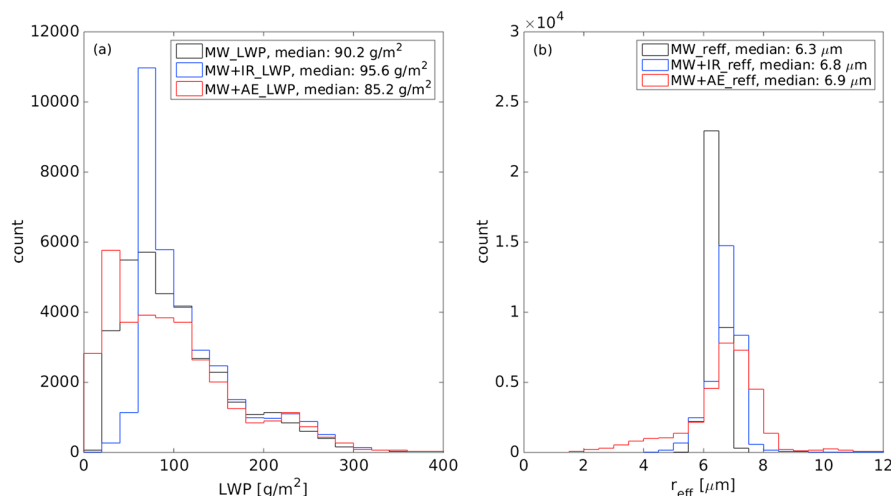


Figure 11. Histograms of (a) LWP and (b) r_{eff} derived with the MW (black), MW+IR (blue), and MW+AE (red) retrievals. Results shown for 11 November 2015 (0–24 UTC).

results using the MWR retrievals (relative RMSE of 19.5%). The derived shortwave downward flux using the MWR+AERI retrievals (Figure 9c) in the RRTMG calculations shows the best agreement within the retrieval uncertainties for the whole time period in comparison to the measured flux values (relative RMSE of 6.4%). The good shortwave closure for the MWR+AERI approach confirms the high accuracy for a combined retrieval using microwave and infrared observations for single-layer liquid water clouds with low LWP values.

5.3. Retrieval Robustness Analysis

In the previous section, an ideal case was selected to investigate the potential of the retrievals in a radiative closure study for a single-layer liquid water cloud. In order to demonstrate the robustness, the retrievals are applied to a full day of measurements including scenes which were not included in the retrieval training process (e.g., multilayer clouds, mixed-phase clouds, and drizzle; Figure 10). To increase the comparability, the MWR temporal resolution (1 s) was used for all LWP and r_{eff} retrievals for the whole day, resulting in 34,395 retrieved values.

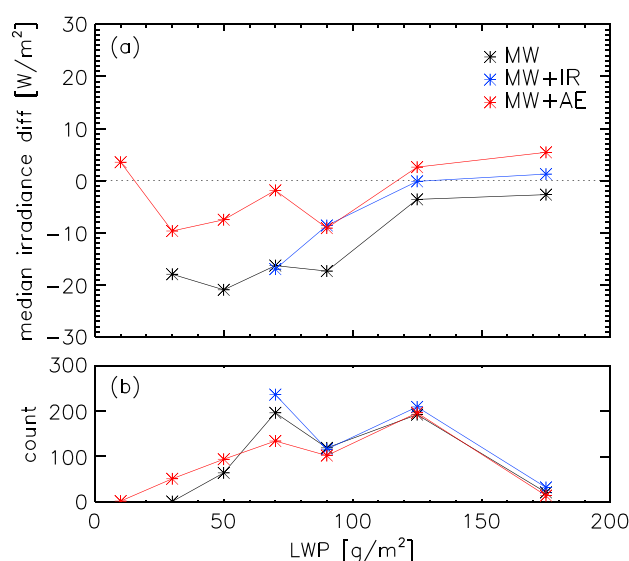


Figure 12. (a) Median calculated-observed shortwave irradiance difference (RRTMG – Pyranometer) and (b) number of occurrences as a function of LWP for the MW (black), MW+IR (blue), and MW+AE (red) retrievals. Results shown for 11 November 2015 (7–13 UTC).

The MW+AE_LWP retrieval provides the lowest values peaking at 10–20 g/m², whereas the MW+IR_LWP and MW_LWP retrievals peak around 60–80 g/m² and display a 5–10 g/m² higher median (Figure 11a). For LWP values above 150 g/m² all LWP distributions are in a similar range. The MWR+AERI combination also shows the broadest distribution for the retrieved r_{eff} values (Figure 11b). All median values are within 1 μm , but the variability of the MW_reff and MW+IR_reff retrievals is much smaller, with no values below 4 μm .

For the shortwave radiative closure study the time period from 7 UTC to 13 UTC was chosen due to sufficient sunlight and a measurement gap between 13 to 14 UTC. In this time period light drizzle and ice clouds were apparent. The differences of the computed and measured fluxes are analyzed in dependence of the retrieved LWP. For LWP below 80 g/m² the MWR+AERI retrieval approach shows a clear improvement, first of all due to lower retrieved LWP values (Figure 12b) and with only a median difference around $\pm 10 \text{ W/m}^2$. In the range of higher LWP values, all retrieval approaches show a good closure. Above 100 g/m², where the infrared methods are not improving the retrieval performance and the MWR information dominates, the retrieved LWP values of all retrievals fall within a 5% mean difference. The deviations between measured and calculated fluxes are thus caused by the higher uncertainty in the r_{eff} , with a 12% mean difference among the r_{eff} retrievals in this range.

6. Summary and Conclusions

Regarding the large impact of thin liquid water clouds on the interaction with radiation, there is a great demand for accurate retrieval representation of cloud microphysical properties. In this context, widely used microwave radiometer retrieval showed large uncertainties for low amounts of cloud liquid water. Therefore, the high sensitivity of the infrared spectral domain can be used to improve the retrieval performance in low-LWP situations.

In this study, we focused on statistical retrievals based on a neural network approach in order to retrieve microphysical properties of liquid water clouds using infrared and microwave observations. The derivation of robust and fast applicable LWP and r_{eff} retrievals for single-layer thin liquid water clouds ($\text{LWP} < 100 \text{ g/m}^2$) was achieved using a synthetic data set of microwave observations and additional spectrally highly resolved and broadband infrared observations.

For the synthetic study, the retrievals based on the microwave and infrared synergy showed a high sensitivity and good performance for cases with low amounts of liquid water (relative error of 9–17%). In contrast, the MWR retrieval provides reasonable low errors beyond the point of saturation for the infrared retrievals (40–60 g/m²). For the combined microwave and infrared LWP retrievals, the application of simulated broadband IRR observations showed on average a 5 pp higher relative error compared to the spectral highly resolved ones from AERI but is still performing better than the MWR alone.

Considering the r_{eff} retrieval performance, the higher spectral resolution of the AERI infrared observations showed a clear improvement to the broadband IRR ones with a relative error below 20% ($\text{LWP} < 60 \text{ g/m}^2$). As expected, there was no dependence on the r_{eff} for the microwave retrieval results, but the MWR brightness temperatures can still be used in combination with the infrared observations to improve the retrieval errors.

After applying the retrievals to real measurements at the Jülich Observatory for Cloud Evolution (JOYCE), the retrieval results need to be evaluated. In order to test the consistency of the retrieval results, a radiative closure study for the shortwave downwelling flux using a radiative transfer model (RRTMG) was performed. The best closure, compared to pyranometer measurements, is achieved for the MWR+AERI retrievals with only a 6.4% relative error in an ideal case. This retrieval also showed robust results for marginally invalid scenes, which encourages to include scenes which are currently not supported by the retrieval approach (e.g. clouds that partially fill the field of view of the instrument, mixed-phase clouds and drizzling clouds) in future studies. However, estimates of LWP are more uncertain and thus hard to interpret in complicated scenes. More detailed instrument system simulation experiments need to be conducted to fully understand the impacts of different “nonideal” physical conditions on the retrieval. For future field campaign deployments, independent observations of LWP and especially r_{eff} gathered from in situ or Sun photometer [Chiu *et al.*, 2012] measurements could help to further evaluate the retrievals and derive a more site-specific training data set of r_{eff} .

For the frequently occurring thin liquid water clouds, the neural network approach combining microwave and infrared observations can provide good estimates of the LWP and r_{eff} with orders of magnitude less computational demand compared to physical retrievals [Turner, 2007]. In order to apply the retrievals, only information

on the cloud phase must be available and nondrizzling water cloud cases need to be identified, since the training data set could only be derived for these conditions. Cloud phase determination can be obtained directly from the AERI [Turner *et al.*, 2003] or an additional data product like the Cloudnet algorithm, which is already available at many atmospheric supersites like JOYCE.

Acknowledgments

The authors would like to thank the Transregional Collaborative Research Center (TR32) "Patterns in Soil-Vegetation-Atmosphere Systems," which is funded by the German Science Foundation (DFG) and has continuously contributed to the instrumentation of JOYCE and its maintenance. Further, the Humidity And Temperature Profiler (HATPRO) and the Atmospheric Emitted Radiance Interferometer (AERI) used in this study have been funded by DFG infrastructural programs under grants INST 216/681-1 and INST 216/519-1. Data management as well as the closure study were incorporated by the research initiative "High Definition Clouds and Precipitation for advancing Climate Prediction HD(CP)2 - Supersites" (first phase 2012–2016) funded by the German Ministry for Education and Research (BMBF). The work by Tobias Marke was funded by the TR32 project "Experimental study of spatiotemporal structures in atmosphere-land surface energy, water and CO₂ exchange (2014–2018)." The MODIS albedo MCD43A1.005 data product was retrieved from the online Data Pool, courtesy of the NASA Land Processes Distributed Active Archive Center (LP DAAC), USGS/ Earth Resources Observation and Science (EROS) Center, Sioux Falls, South Dakota. Access to the aerosol optical depths was made possible through AERONET and Birger Bohn from the Research Centre Jülich (b.bohn@fz-juelich.de).

References

- Baldauf, M., and other (2011), *Kurze Beschreibung des Lokal-Modells Kurzzeitfrst LMK und seiner Datenbanken auf dem Datenserver des DWD*, German Weather Service (DWD) Geschäftsbereich Forschung und Entwicklung, 63004 Offenbach, Germany.
- Boers, R., J. R. Acarreta, and J. L. Gras (2006), Satellite monitoring of the first indirect aerosol effect: Retrieval of the droplet concentration of water clouds, *J. Geophys. Res.*, **111**, D22208, doi:10.1029/2005JD006838.
- Cadeddu, M. P., D. D. Turner, and J. C. Liljegren (2009), A neural network for real-time retrievals of PWV and LWP from Arctic millimeter-wave ground-based observations, *IEEE Trans. Geosci. Remote Sens.*, **47**(7), 1887–1900, doi:10.1109/TGRS.2009.2013205.
- Chiu, J. C., et al. (2012), Cloud droplet size and liquid water path retrievals from zenith radiance measurements: Examples from the atmospheric radiation measurement program and the aerosol robotic network, *Atmos. Chem. Phys.*, **12**, 10313–10329, doi:10.5194/acp-12-10313-2012.
- Clough, S. A., M. J. Iacono, and J. L. Moncet (1992), Line-by-line calculations of atmospheric fluxes and cooling rates: Application to water vapor, *J. Geophys. Res.*, **97**(D14), 761–785, doi:10.1029/92JD01419.
- Clough, S. A., M. W. Shepard, E. J. Mlawer, J. S. Delamere, M. J. Iacono, K. Cady-Pereira, S. Boukabara, and P. D. Brown (2005), Atmospheric radiative transfer modeling: A summary of the AER codes, *J. Quant. Spectrosc. Radiat. Transfer*, **91**, 233–244, doi:10.1016/j.jqsrt.2004.05.058.
- Crewell, S., K. Ebell, U. Löhnert, and D. D. Turner (2009), Can liquid water profiles be retrieved from passive microwave zenith observations?, *Geophys. Res. Lett.*, **36**, L06803, doi:10.1029/2008GL036934.
- Faure, T., H. Isaka, and B. Guillemet (2001), Neural network retrieval of cloud parameters of inhomogeneous and fractional clouds: Feasibility study, *Remote Sens. Environ.*, **77**, 123–138, doi:10.1016/S0034-4257(01)00199-7.
- Frisch, A. S., C. W. Fairall, and J. B. Snider (1995), Measurement of stratus cloud and drizzle parameters in ASTEX with a K-band Doppler radar and microwave radiometer, *J. Atmos. Sci.*, **52**, 2788–2799.
- Hagan, M. T., H. B. Demuth, M. H. Beale, and O. De Jesús (2014), *Neural Network Design*, 2nd edn., Oklahoma State Univ., Stillwater, Okla.
- Hess, M., P. Koepke, and I. Schult (1998), Optical properties of aerosols and clouds: The software package OPAC, *Bull. Am. Meteorol. Soc.*, **79**, 831–844, doi:10.1175/1520-0477(1998)079<0831:OPOAAC>2.0.CO;2.
- Holben, B. N., et al. (1998), AERONET—A federated instrument network and data archive for aerosol characterization, *Remote Sens. Environ.*, **66**, 1–16, doi:10.1016/S0034-4257(98)00031-5.
- Hu, Y. X., and K. Stamnes (1993), An accurate parameterization of the radiative properties of water clouds suitable for use in climate models, *J. Clim.*, **6**, 728–742, doi:10.1175/1520-0442(1993)006<0728:AAPOTR>2.0.CO;2.
- Illingworth, A. J., et al. (2007), Cloudnet continuous evaluation of cloud profiles in seven operational models using ground-based observations, *Bull. Am. Meteorol. Soc.*, **88**, 883–898, doi:10.1175/BAMS-88-6-883.
- Intergovernmental Panel on Climate Change (2013), *Climate Change 2013: The Physical Science Basis. Contribution of Working Group 1 to the Fifth Assessment Report of the Intergovernmental Panel on Climate Change*, Cambridge Univ. Press, Cambridge, U. K.
- Knist, C. L. (2014), *Retrieval of liquid water cloud properties from ground-based remote sensing observations*, dissertation at Delft Univ. of Technology, Delft, Netherlands.
- Knuteson, R. O., et al. (2004a), Atmospheric emitted radiance interferometer. Part I: Instrument design, *J. Atmos. Oceanic Technol.*, **21**, 1763–1776, doi:10.1175/JTECH-1662.1.
- Knuteson, R. O., et al. (2004b), Atmospheric emitted radiance interferometer. Part II: Instrument performance, *J. Atmos. Oceanic Technol.*, **21**, 1777–1789, doi:10.1175/JTECH-1663.1.
- Krasnov, O. A., and H. W. J. Russchenberg (2002), An enhanced algorithm for the retrieval of liquid water cloud properties from simultaneous radar and lidar measurements, in *European Conference on Radar Meteorology (ERAD) 2002 Proceedings*, vol. 1, pp. 173–183, ERAD Publication Series, Delft, The Netherlands.
- Kubar, T. L., D.-L. Hartmann, and R. Wood (2009), Understanding the importance of microphysics and macrophysics for warm rain in marine low clouds. Part I: Satellite observations, *J. Atmos. Sci.*, **66**, 2953–2972, doi:10.1175/2009JAS3071.1.
- Liebe, H., G. Hufford, and T. Manabe (1991), A model for the complex permittivity of water at frequencies below 1 THz, *Int. J. Infrared Millimeter Waves*, **12**, 659–675, doi:10.1007/BF01008897.
- Liljegren, J. C., E. E. Clothiaux, G. G. Mace, S. Kato, and X. Dong (2001), A new retrieval for cloud liquid water path using a ground-based microwave radiometer and measurements of cloud temperature, *J. Geophys. Res.*, **106**(D13), 485–500, doi:10.1029/2000JD900817.
- Löhnert, U., and S. Crewell (2003), Accuracy of cloud liquid water path from ground-based microwave radiometry, 1. Dependency on cloud model statistics, *Radio Science*, **38**(3), 8041, doi:10.1029/2002RS002654.
- Löhnert, U., S. Crewell, and C. Simmer (2004), An integrated approach toward retrieving physically consistent profiles of temperature, humidity, and cloud liquid water, *J. Appl. Meteorol.*, **43**, 1295–1307, doi:10.1175/1520-0450(2004)043<1295:AIATRP>2.0.CO;2.
- Löhnert, U., et al. (2015), JOYCE: Jülich Observatory for Cloud Evolution, *Bull. Am. Meteorol. Soc.*, **96**, 1157–1174, doi:10.1175/BAMS-D-14-00105.1.
- Marchand, R., T. Ackerman, E. D. Westwater, S. A. Clough, K. Cady-Pereira, and J. C. Liljegren (2003), An assessment of microwave absorption models and retrievals of cloud liquid water using clear-sky data, *J. Geophys. Res.*, **108**(D24), 4773, doi:10.1029/2003JD003843.
- Miles, N. L., J. Verlinde, and E. E. Clothiaux (2000), Cloud droplet size distributions in low-level stratiform clouds, *J. Atmos. Sci.*, **57**, 295–311, doi:10.1175/1520-0469(2000)057<0295:CDSIL>2.0.CO;2.
- Rodgers, C. D. (2000), *Inverse Methods for Atmospheric Sounding: Theory and Practice*, 238 pp., World Scientific, Singapore.
- Rose, T., S. Crewell, U. Löhnert, and C. Simmer (2005), A network suitable microwave radiometer for operational monitoring of the cloudy atmosphere, *Atmos. Res.*, **75**, 183–200, doi:10.1016/j.jatmosres.2004.12.005.
- Rosenkranz, P. W. (1998), Water vapor microwave continuum absorption: A comparison of measurements and models, *Radio Sci.*, **33**, 919–928, doi:10.1029/98RS01182.
- Schaaf, C. B., et al. (2002), First operational BRDF, albedo nadir reflectance products from MODIS, *Remote Sens. Environ.*, **83**, 135–148, doi:10.1016/S0034-4257(02)00091-3.

- Sengupta, M., E. E. Clothiaux, T. P. Ackerman, S. Kato, and Q. Min (2003), Importance of accurate liquid water path for estimation of solar radiation in warm boundary layer clouds: An observational study, *J. Clim.*, *16*, 2997–3009, doi:10.1175/1520-0442(2003)016<2997:IOALWP>2.0.CO;2.
- Simmer, C. (1994), *Satellitenfernerkundung Hydrologischer Parameter der Atmosphäre mit Mikrowellen*, 13 pp., Verlag Dr. Kovac, Hamburg, Germany.
- Stamnes, K., S.-C. Tsay, and K. Jayaweera (1988), Numerically stable algorithm for discrete-ordinate-method radiative transfer in multiple scattering and emitting layered media, *Appl. Opt.*, *27*, 2502–2509, doi:10.1364/AO.27.002502.
- Stephens, G. L. (1978), Radiation profiles in extended water clouds. I: Theory, *J. Atmos. Sci.*, *35*, 2111–2122, doi:10.1175/1520-0469(1978)035<2111:RPIEWC>2.0.CO;2.
- Stephens, G. L. (2005), Cloud feedbacks in the climate system: A critical review, *J. Clim.*, *18*, 237–273, doi:10.1175/JCLI-3243.1.
- Turner, D. D. (2005), Arctic mixed-phase cloud properties from AERI lidar observations: Algorithm and results from SHEBA, *J. Appl. Meteorol.*, *44*, 427–444, doi:10.1175/JAM2208.1.
- Turner, D. D. (2007), Improved ground-based liquid water path retrievals using a combined infrared and microwave approach, *J. Geophys. Res.*, *112*, D15204, doi:10.1029/2007JD008530.
- Turner, D. D., and P. J. Gero (2011), Downwelling 10 μ m radiance temperature climatology for the Atmospheric Radiation Measurement Southern Great Plains site, *J. Geophys. Res.*, *116*, D08212, doi:10.1029/2010JD015135.
- Turner, D. D., S. A. Ackerman, B. A. Baum, H. E. Revercomb, and P. Yang (2003), Cloud phase determination using ground-based AERI observations at SHEBA, *J. Appl. Meteorol.*, *42*, 701–715, doi:10.1175/1520-0450(2003)042<0701:CPDUGA>2.0.CO;2.
- Turner, D. D., A. Shepard, J. C. Liljegren, E. E. Clothiaux, K. Cady-Pereira, and K. L. Gaustad (2007a), Retrieving liquid water path and precipitable water vapor from the Atmospheric Radiation Measurement (ARM) microwave radiometers, *IEEE Trans. Geosci. Remote Sens.*, *45*(11), 3680–3690, doi:10.1109/TGRS.2007.903703.
- Turner, D. D., et al. (2007b), Thin liquid water clouds: Their importance and our challenge, *Bull. Am. Meteorol. Soc.*, *88*, 177–190, doi:10.1175/BAMS-88-2-177.
- Turner, D. D., M. P. Cadetdu, U. Löhnert, S. Crewell, and A. M. Vogelmann (2009), Modifications to the water vapor continuum in the microwave suggested by ground-based 150-GHz observations, *IEEE Trans. Geosci. Remote Sens.*, *47*(10), 3326–3337, doi:10.1109/TGRS.2009.2022262.
- Westwater, E. (1978), The accuracy of water vapor and cloud liquid determination by dual-frequency ground-based microwave radiometry, *Radio Sci.*, *13*, 667–685, doi:10.1029/RS013i004p00677.
- Zhao, C., et al. (2012), Toward understanding of differences in current cloud retrievals of ARM ground-based measurements, *J. Geophys. Res.*, *117*, D10206, doi:10.1029/2011JD016792.

6 DISCUSSION AND OUTLOOK

In the following chapter, the main findings of [Publication I](#), [Publication II](#), [Publication III](#) and [Publication IV](#) are discussed and an outlook on potential improvements and future work is given subsequently.

6.1 Publication I: Boundary-layer classification

[Publication I](#) ([Manninen et al., 2018](#)) presents a method for an objective classification of turbulence within the atmospheric boundary layer (ABL). The method, as advancement of the study by [Harvey et al. \(2013\)](#), is based on measured Doppler wind lidar (DWL) quantities in order to detect turbulent regions and distinguish between different sources of mixing, which can be surface, cloud or wind driven.

The classification demonstrated the potential to gain insights into diurnal and seasonal ABL characteristics in various climate regimes in an operational mode as well as for the application to long-term data sets. [Figure 6.1](#) shows the strong diurnal variation in surface driven convection at the Jülich ObservatorY for Cloud Evolution (JOYCE), with decreasing intensity for higher levels. Due to less aerosols present in higher altitudes, the amount of missing data increases. Cloud cover is rather homogeneous in winter, but shows a peak before midday in summer corresponding to fair weather cumulus clouds. During night, more shear driven turbulence is probably connected to LLJ and further analyzed in [Publication II](#).

Except for situations with fog and precipitation, that is identified with vertical velocity observations, the robust method operates in most atmospheric conditions and covers the full diurnal cycle of turbulent ABL development. The bit field design of the classification, with a decision tree containing thresholds for different DWL quantities, allows for a future combination with additional instruments like radar to make use of their synergy and to complement and improve the method for example in rainy cases. Further benefits could

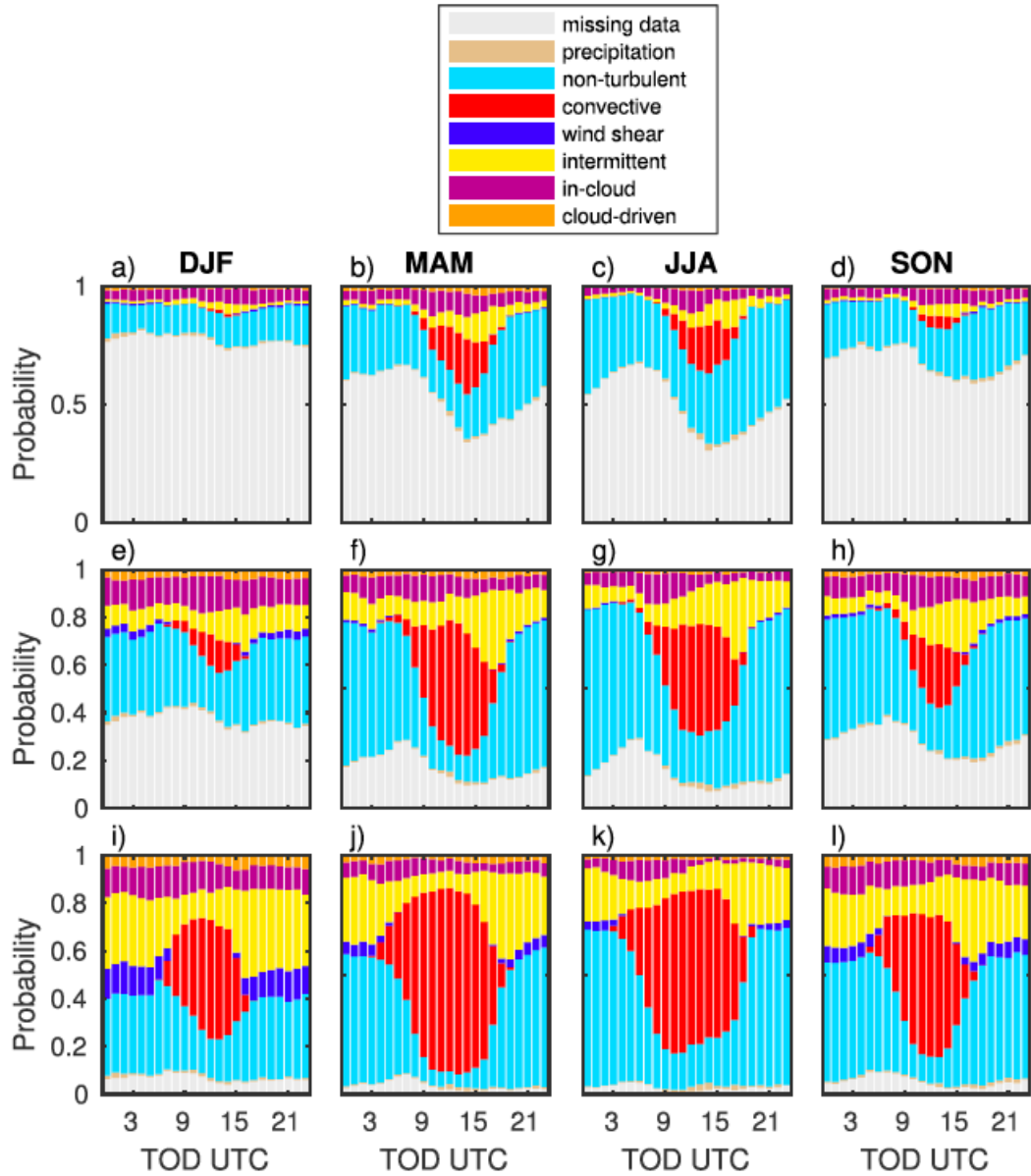


FIGURE 6.1: Seasonal average diurnal cycle of the probability for each identified source causing mixing in the ABL over JOYCE for three different height ranges and for over one year of observations. Source [Manninen et al. \(2018\)](#).

also arise from process studies, for example on the morning transition zone, helping to understand at which point surface driven convection is dominating shear driven turbulence. Similar to [Harvey et al. \(2015\)](#), the classification can be used to evaluate weather forecast models in order to improve ABL schemes. In this thesis, the classification already demonstrated its ability to characterize ABL turbulence in [Publication III](#).

6.2 Publication II: Low-level jet climatology

In **Publication II** (Marke et al., 2018) a low-level jet (LLJ) climatology from long-term DWL data at JOYCE is obtained. The LLJ detection is realized with applying the robust algorithm of Tuononen et al. (2017) to DWL velocity azimuth display (VAD) scans, which were extended with tower observations to fill the observational gap of the DWL below 105 m. Additional consistency checks were applied to distinguish between a LLJ continuation and newly formed jets. Also, single profiles showing LLJ characteristics are not considered, since only coherent jets that are present over one hour are included into the climatology.

LLJ occurrence was found to be dominant during night with a strong directional dependence and jets are detected in 13% of the observational period. Regarding the seasonal cycle, differences related to the development of LLJs at this site could be identified, since the wintertime diurnal cycle is less pronounced due to the presence of clouds and lower solar forcing. In the assessment of LLJ turbulence, the jets are classified according to the bulk wind shear below the jet, resulting in two distinct classes. The high wind shear jets show strong mixing below the LLJ nose. This has large implications for wind turbine safety, since 16% of the jets have the wind speed maximum below 200 m. A stable surface layer during nighttime LLJ cases, with an accumulation of atmospheric constituents, could be identified with surface flux measurements of a near-by eddy-covariance (EC) station. This accumulation is especially important during LLJ breakdown in the morning hours, when uplifting of polluted air can lead to cloud formation (Su et al., 2016). Turbulence measurements at the EC station suggest that intermittent turbulence generated by LLJs penetrates the stable layer.

For strong winds also the interaction with the surrounding topography is an important factor for decisions on instrument placement and interpretation of observations depending on the wind direction. In this study a high resolution large-eddy simulation (LES) model was used to investigate the interaction of the three-dimensional wind field with the scaled topography during a LLJ case. In general, a small mismatch of LLJ direction and speed is identified between LES, DWL and radiosonde observations and it was demonstrated that even small topographic perturbations can induce changes in the wind flow. The near-by open cast pit mine and pit mine dump hill induced wave-like motions in the vertical velocity. This was also validated with long-term DWL measurements showing a direction dependent updraft coinciding with the topographic disturbance.

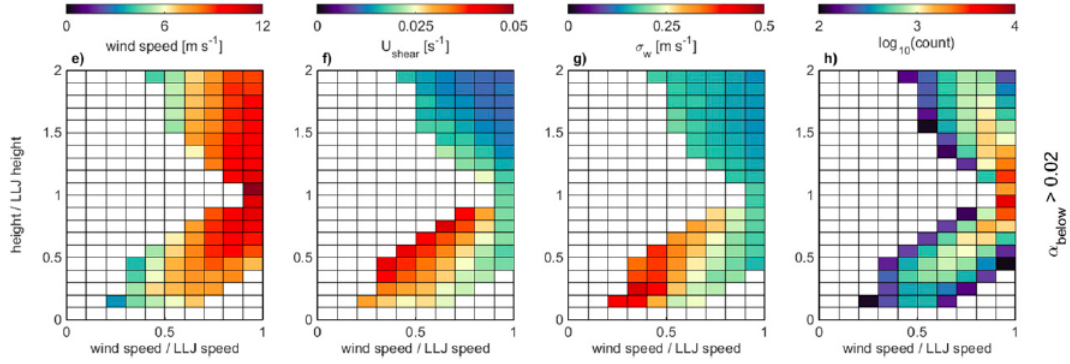


FIGURE 6.2: Distributions of average wind speed, vector wind shear, vertical velocity standard deviation and number of observations as a function of normalized wind speed and height of LLJ cases with strong wind shear. Adapted from Marke et al. (2018).

6.3 Publication III: Land use induced water vapor patterns

Apart from topographic influences shown in Publication II, also the land surface properties like land use can be responsible for land surface-atmosphere interaction processes. Especially transport mechanisms of water vapor are important in terms of the hydrological cycle, surface energy balance and the transition to clouds and hence precipitation. This exchange takes place on small scales that are not resolved by most weather forecast and climate models, but the resulting patterns are crucial, since gradients directly influence fluxes and therefore the evolution of the model state (Simmer et al., 2015).

Monitoring and modeling these spatial patterns and compartment interactions is the main focus of Publication III (Marke et al., 2020) and is also in agreement with the goals of the Transregional Collaborative Research Centre 32 (TR32). In particular, long-term microwave radiometer (MWR) scans are used to assess the spatial variability of integrated water vapor (IWV). Due to the expected high land surface-atmosphere interactions, conditions without liquid water clouds between April and September are selected with criteria based on MWR observations. The pattern found in the scans is partly attributed to the local land surface heterogeneity by regarding the large scale water vapor transport and a comparison to a detailed land use classification by Waldhoff et al. (2017). The statistical scan deviations from the mean is in the order of $\pm 1\%$ and a quantification of the local influence during convective situations is difficult to obtain for single scans. Instead, the MWR derived results are compared to a satellite based water vapor product as an

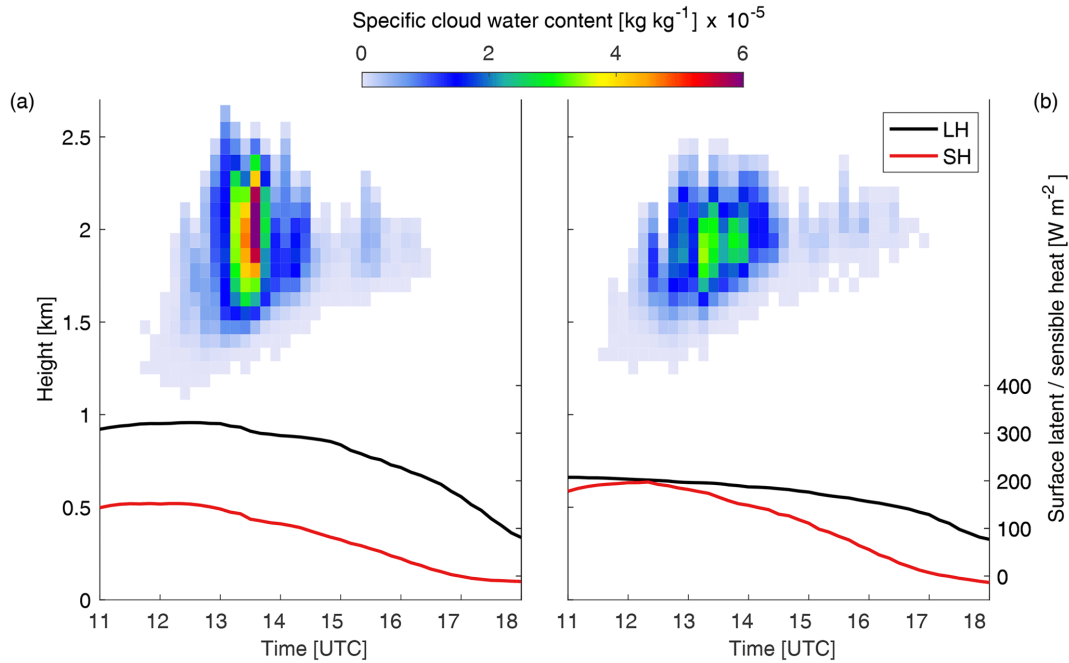


FIGURE 6.3: Domain averaged specific cloud water content for the LES control simulation (a) and a simulation with altered land use types (b) together with the surface fluxes of latent and sensible heat. Source Marke et al. (2020)

independent measurement for a selection of satellite overpasses. Despite the spatial resolution of 1 km, the main directions of positive and negative IWP deviations are in agreement to the MWR.

Simulations of a high resolution LES model for case study, with a similar setup as in Publication II, enables a sensitivity analysis to evaluate atmospheric changes due to a different land use type input. Replacing crop and grass land with bare ground revealed significant effects in the simulation. Vertical velocity structures switched from patchy to a streak dominated pattern generated by a higher surface contrast. This change in the circulation pattern shows to be important for locations of cloud formation, which showed different characteristics because of the surface flux partitioning. For higher latent heat fluxes also more cloud water content and a higher cloud top can be seen in the control simulation, whereas an increased portion of bare ground leads to a higher sensible heat flux (Figure 6.3).

6.4 Publication IV: Statistical retrievals of liquid clouds

Publication III showed the typical development of fair weather cumulus clouds containing low amounts of liquid water. This type of cloud is common in most climate regimes and important in terms of the interaction with radiation (Turner et al., 2007a; Turner et al., 2007b). In order to describe cloud related interactions with radiation, the microphysical and optical properties, such as liquid water path (LWP) and effective radius, of clouds can be used (Stephens, 1978; Hu and Stamnes, 1993; Turner et al., 2007b). These quantities describe the impact on the radiative flux and mechanisms of cloud formation, drizzle and dissipation (Kubar et al., 2009). Therefore **Publication IV** (Marke et al., 2016) deals with deriving retrievals of LWP and effective radius for thin liquid water clouds (LWP below 100 g m^{-2}).

MWR is a common instrument type to derive LWP information. Although, retrieval errors of around $20\text{--}30 \text{ g m}^{-2}$ (Löhnert and Crewell, 2003) lead to large relative errors for thin liquid water clouds. On the other hand, observations in the infrared regime reveal a high sensitivity for thin clouds, but show saturation effects for higher amounts of liquid water contained in the clouds. Turner (2007) already showed a combined microwave and infrared retrieval, but with a computational expensive physical approach. This study evaluates the potential of a statistical method, namely neural network, to account for the nonlinear saturation effects and to obtain LWP and effective radius retrievals.

Neural network retrievals are derived for single instrument and synergistic approach of MWR, broadband infrared and the spectral highly resolved infrared atmospheric emitted radiance interferometer (AERI). As a prior constraint, information on cloud phase and cloud layering are required to allow for a physical interpretation of the retrieval results. For this purpose, a training data set consisting of single layer water clouds, identified by the cloud classification approach Cloudnet (Illingworth et al., 2007), is utilized. Then, synthetic microwave and infrared observations are derived from forward model simulations. Necessary input data and assumptions for the retrieval derivation and forward model operators include homogeneous mixing within the cloud layer for effective radius estimates and thermodynamic profiles taken from COSMO-DE (Baldauf et al., 2011).

In **Figure 6.4** the difference in LWP retrieval error as a function of LWP shows the benefit of the MWR+AERI synergy for the whole range of thin cloud LWP

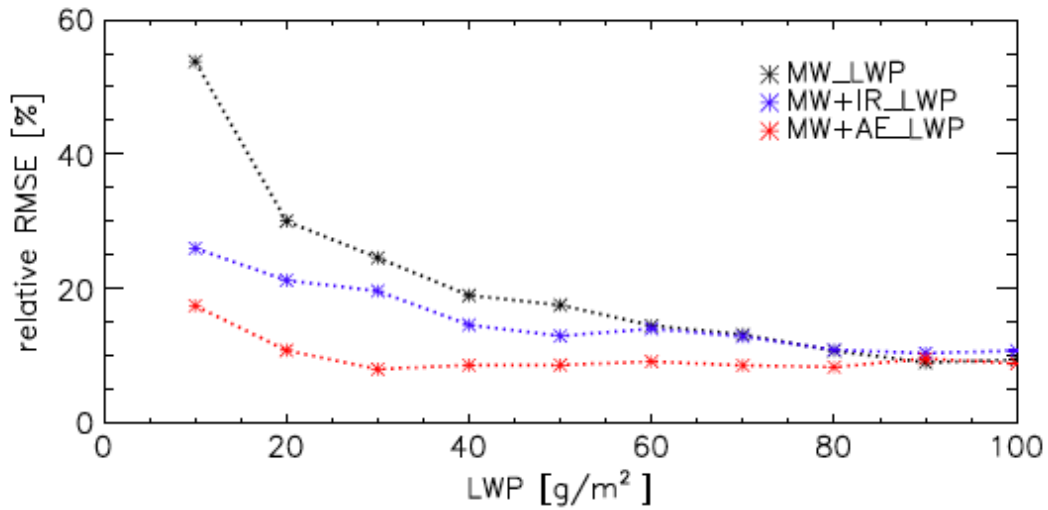


FIGURE 6.4: Relative root-mean-square error as a function of LWP for the different neural network retrievals in the synthetic study. Source [Marke et al. \(2016\)](#)

values. Relative errors above 50% for the single MWR retrieval can be significantly reduced to below 20% and the neural network approach is able to account for the non-linearity arising from saturation effects in the infrared regime. Also the broadband infrared radiometers show improvements, but only until 60 g m^{-2} . The effective radius revealed no strong dependence on simulated MWR observations. Although, comparisons of the single and combined retrievals suggest that the MWR can add to the effective radius retrieval accuracy via constraining the LWP, resulting in a lower retrieval error for the MWR+AERI combination.

Furthermore, the retrieval accuracy is assessed with a shortwave radiative closure study. Retrieved LWP and effective radius values are used as input for the broadband rapid radiative transfer model RRTMG ([Clough et al., 2005](#)). To simulate shortwave fluxes the effects of aerosols need to be accounted for. This is achieved by including the aerosol optical depth (AOD), single scattering albedo and asymmetry parameter into RRTMG. Also the direct-beam and diffuse shortwave surface albedo is described by satellite observations. Statistical neural network retrievals using the synergy of MWR and AERI show again the highest potential in terms of the best radiative closure and more realistic variability of the retrieved values using real measurements. With a larger data set for retrieval training, a better retrieval accuracy and an operational application with constraints in prior knowledge of the retrievals could be obtained.

6.5 Outlook

Atmospheric boundary layer processes are essential to understand and play a key role in the weather and climate system. Weather phenomena, the distribution of pollutants and issues for wind turbine and aviation security can be attributed to the ABL, where almost all life on Earth is contained in. The small relevant scales in the temporal and spatial domain make monitoring and modeling challenging. In this study, tools and process studies are provided to improve understanding of land surface-atmosphere interactions in order to guide towards better a representation in models.

Publication I presents an objective ABL classification to identify turbulent regions and assigning a mixing source. The method already showed to be valuable in deriving long-term statistics of the diurnal and seasonal ABL development at different sites. Including more sites in climatic diverse regions and increasing the data sample for existing sites would further improve the method by adding atmospheric conditions that show a distinct ABL behavior. Although the method is built up solely on DWL observations, the design allows for future implementation of additional instruments. Radar observations are sensitive to larger particles and could complement the classification in drizzle and rain cases. The identification of such periods is important to distinguish between cloud driven turbulence by cloud top cooling and turbulence generated by drizzle evaporation or variations in particle fall speeds. Currently a threshold based method is used to flag rainy situations. A combination with the cloud classification approach Cloudnet ([Illingworth et al., 2007](#)) represents one way to achieve a more complete picture of ABL turbulence and cloud processes. A further critical aspect of the classification is the transition between wind shear induced turbulence and surface driven convection close to the ground. This transition could be better characterized with surface flux measurements or vertically resolved temperature and humidity measurements to obtain the stability at the surface and in the atmosphere. A climatology of boundary layer types derived from continuous DWL measurements has been already utilized to verify weather prediction ABL parameterization schemes ([Harvey et al., 2015](#)). Model related issues like resolution, lead time and seasonality could be evaluated in a similar way using the ABL classification in **Publication I**.

Process studies of land surface-atmosphere interactions as in **Publication II** and **Publication III** benefit from high resolution LES models. The ability to scale the topography or changing land use input data is valuable to assess

the sensitivity of the atmospheric state to these changes. Therefore, conducting more simulations for carefully selected cases that are suited for the regarded process is crucial. The algorithm developed by [Tuononen et al. \(2017\)](#) showed the potential in detecting single LLJs, but also over a longer time period. DWL observations are well suited to obtain turbulence characteristics of the jets, that are frequently occurring during night and in low altitudes. Seasonal variations in LLJ occurrence and wind direction suggest different mechanisms of LLJ development, where further studies are needed with an emphasis on comparing climatic similar sites. The analysis of LLJ development could further benefit from temperature and humidity profiles with high vertical resolution to capture small scale effects around the stable surface layer that are not resolved by microwave radiometer (MWR) measurements. Interactions of the wind field with the topography revealed implications for future deployment of instruments and can be helpful especially for short-term field campaigns.

Field campaigns with various ground-based remote sensing systems could also be planned for evaluating the findings in [Publication III](#). Like in [Späth et al. \(2016\)](#), low-elevation scans of the water vapor field with differential absorption lidar showed differences related to land surface properties. The high sensitivity and line-of-sight resolution can be used to determine differences in evapotranspiration between land use borders. Having more simulations with diverse atmospheric conditions would definitely help to gain more insights into processes like liquid water cloud formation and feedback on the surface fluxes. In addition, more research is needed on the contribution of single soil and vegetation parameters on the interaction process.

The tool for retrieving cloud optical and microphysical properties (LWP and effective radius) in [Publication IV](#) proves the benefit of combining the microwave and infrared spectral regime for thin liquid water clouds. Comparable retrieval accuracy of the neural network retrievals to a physical retrieval approach in [Turner \(2007\)](#) is achieved. Using a longer time series of data to derive the training data set, as well as evaluating the impact on forward model assumptions could further improve the results. When combined with Cloudnet, cloud phase and layering can be obtained, fostering an operational application of the retrievals.

LIST OF FIGURES

| | | |
|-----|--|-----|
| 1.1 | Schematic diurnal cycle of ABL development in fair weather (high pressure) situations (Stull, 2012). | 8 |
| 1.2 | Overview of the thesis including all publications. | 12 |
| 1.3 | Schematic of a VAD scan with 12 beams (Päschke et al., 2015). The angle α corresponds to θ in the text. | 18 |
| 1.4 | "Schematic of vertical velocity energy density spectra vs frequency conforming to Kolmogorov's hypothesis." O'Connor et al. (2010) | 20 |
| 1.5 | Extinction coefficient in the microwave spectral range, with contributions of oxygen, water vapor and liquid water. Löhnert et al. (2004) | 21 |
| 1.6 | "Simulated cloudy minus clear sky radiance difference at 11 μm and 31.4 GHz for a range of LWP. [...] " Turner (2007) | 23 |
| 6.1 | Seasonal average diurnal cycle of the probability for each identified source causing mixing in the ABL over JOYCE for three different height ranges and for over one year of observations. Source Manninen et al. (2018). | 98 |
| 6.2 | Distributions of average wind speed, vector wind shear, vertical velocity standard deviation and number of observations as a function of normalized wind speed and height of LLJ cases with strong wind shear. Adapted from Marke et al. (2018). . . | 100 |
| 6.3 | Domain averaged specific cloud water content for the LES control simulation (a) and a simulation with altered land use types (b) together with the surface fluxes of latent and sensible heat. Source Marke et al. (2020) | 101 |
| 6.4 | Relative root-mean-square error as a function of LWP for the different neural network retrievals in the synthetic study. Source Marke et al. (2016) | 103 |

LIST OF ABBREVIATIONS

| | |
|-----------------|---|
| ABL | A tmospheric B oundary L ayer |
| AERI | A tmospheric E mitted R adiance I nterferometer |
| AOD | A ersol O ptical D epth |
| BT | B rightness T emperature |
| DSD | D roplet S ize D istribution |
| DWL | D oppler W ind L idar |
| EC | E ddy C ovariance |
| GCM | G eneral C irculation M odel |
| GPS | G lobal P ositioning S ystem |
| IWV | I ntegrated W ater V apor |
| JOYCE-CF | J ülich O bservatory for C loud E volution - C entral F acility |
| LES | L arge E ddy S imulation |
| Lidar | L ight D etection and R anging |
| LLJ | L ow- L evel J et |
| LSM | L and S urface M odel |
| LWP | L iquid W ater P ath |
| MWR | M icro W ave R adiometer |
| NWP | N umerical W eather P rediction |
| PBL | P lanetary B oundary L ayer |
| Radar | R adiation D etection and R anging |
| RRTMG | R apid R adiative T ransfer M odel for G lobal models |
| RU | R adiance U nit |
| BT | B rightness T emperature |
| TR32 | T ransregional C ollaborative R esearch C entre 32 |

LIST OF SYMBOLS

| | |
|----------------|--|
| A | Area of receiver optics |
| \mathbf{A} | Matrix of unit vectors |
| a | Kolmogorov constant |
| c | Speed of light |
| Δf | Doppler frequency shift |
| f_0 | Frequency of emitted laser pulse |
| f_{LO} | Frequency of local oscillator |
| h | Height above cloud base |
| k | Wave number |
| k_{r_v} | Coefficient containing the DSD shape parameter |
| L | Length scale |
| L_1 | Length scale of individual sample |
| $n(r)$ | Droplet size distribution |
| $O(R)$ | Overlap function |
| P | Received power |
| P_0 | Average power of laser pulse |
| R | Distance of scatterer |
| r | Droplet radius |
| r_{eff} | Effective radius |
| $S(k)$ | Turbulent energy spectrum |
| t | Laser pulse duration |
| u | Eastward wind component |
| \mathbf{V}_r | Radial velocity vector |
| V | Horizontal wind |
| v | Northward wind component |
| \mathbf{v} | Wind vector |
| v_r | Radial velocity |
| w | Vertical wind |
| Z | Radar reflectivity |
| α | Extinction coefficient |

| | |
|--------------------|---|
| β | Backscatter coefficient |
| ϵ | Dissipation rate |
| η | System efficiency |
| θ | Azimuth angle |
| λ | Wavelength |
| ν | DSD shape parameter |
| π | Archimedes' constant |
| ρ_l | Liquid water density |
| $\sigma_{\bar{v}}$ | Standard deviation of mean Doppler velocity |
| τ | Optical depth |
| ϕ | Zenith angle |

LITERATURE

- Adler, B., N. Kalthoff, M. Kohler, J. Handwerker, A. Wieser, U. Corsmeier, C. Kottmeier, D. Lambert, and O. Bock (Aug. 2016). "The variability of water vapour and pre-convective conditions over the mountainous island of Corsica". In: *Quarterly Journal of the Royal Meteorological Society* 142, pp. 335–346. DOI: [10.1002/qj.2545](https://doi.org/10.1002/qj.2545).
- Baldauf, M., A. Seifert, J. Förstner, D. Majewski, M. Raschendorfer, and T. Reinhardt (Dec. 2011). "Operational Convective-Scale Numerical Weather Prediction with the COSMO Model: Description and Sensitivities". In: *Monthly Weather Review* 139.12, pp. 3887–3905. DOI: [10.1175/MWR-D-10-05013.1](https://doi.org/10.1175/MWR-D-10-05013.1).
- Banakh, V. A., I. Smalikho, F. Köpp, and C. Werner (Aug. 1999). "Measurements of Turbulent Energy Dissipation Rate with a CW Doppler Lidar in the Atmospheric Boundary Layer". In: *Journal of Atmospheric and Oceanic Technology* 16.8, pp. 1044–1061. DOI: [10.1175/1520-0426\(1999\)016<1044:MOTEDR>2.0.CO;2](https://doi.org/10.1175/1520-0426(1999)016<1044:MOTEDR>2.0.CO;2).
- Banta, R., R. K. Newsom, J. K. Lundquist, Y. L. Pichugina, R. L. Coulter, and L. Mahrt (2002). "Nocturnal Low-Level Jet Characteristics Over Kansas During Cases-99". In: *Boundary-Layer Meteorology* 105.2, pp. 221–252. DOI: [10.1023/A:1019992330866](https://doi.org/10.1023/A:1019992330866).
- Beesley, J. A., C. S. Bretherton, C. Jakob, E. L. Andreas, J. M. Intrieri, and T. A. Uttal (May 2000). "A comparison of cloud and boundary layer variables in the ECMWF forecast model with observations at Surface Heat Budget of the Arctic Ocean (SHEBA) ice camp". In: *Journal of Geophysical Research: Atmospheres* 105.D10, pp. 12337–12349. DOI: [10.1029/2000JD900079](https://doi.org/10.1029/2000JD900079).
- Bertoldi, G., J. D. Albertson, W. P. Kustas, F. Li, and M. C. Anderson (Oct. 2007). "On the opposing roles of air temperature and wind speed variability in flux estimation from remotely sensed land surface states". In: *Water Resources Research* 43.10. DOI: [10.1029/2007WR005911](https://doi.org/10.1029/2007WR005911).
- Betts, A. K. (2002). "Evaluation of the diurnal cycle of precipitation, surface thermodynamics, and surface fluxes in the ECMWF model using LBA data". In: *Journal of Geophysical Research* 107.D20. DOI: [10.1029/2001JD000427](https://doi.org/10.1029/2001JD000427).

- Betts, A. K. (Nov. 2004). "Understanding Hydrometeorology Using Global Models". In: *Bulletin of the American Meteorological Society* 85.11, pp. 1673–1688. DOI: [10.1175/BAMS-85-11-1673](https://doi.org/10.1175/BAMS-85-11-1673).
- (Mar. 2009). "Land-Surface-Atmosphere Coupling in Observations and Models". In: *Journal of Advances in Modeling Earth Systems* 1.3. DOI: [10.3894/JAMES.2009.1.4](https://doi.org/10.3894/JAMES.2009.1.4).
- Bevis, M., S. Businger, T. A. Herring, C. Rocken, R. A. Anthes, and R. H. Ware (1992). "GPS meteorology: Remote sensing of atmospheric water vapor using the global positioning system". In: *Journal of Geophysical Research: Atmospheres* 97.D14, pp. 15787–15801. DOI: [10.1029/92JD01517](https://doi.org/10.1029/92JD01517).
- Beyrich, F. (1997). "Mixing height estimation from sodar data — A critical discussion". In: *Atmospheric Environment* 31.23, pp. 3941–3953. DOI: [10.1016/S1352-2310\(97\)00231-8](https://doi.org/10.1016/S1352-2310(97)00231-8).
- Beyrich, F., J.-P. Leps, M. Mauder, J. Bange, T. Foken, S. Huneke, H. Lohse, A. Lüdi, W. M. L. Meijninger, D. Mironov, U. Weisensee, and P. Zittel (Oct. 2006). "Area-Averaged Surface Fluxes Over the Litfass Region Based on Eddy-Covariance Measurements". In: *Boundary-Layer Meteorology* 121.1, pp. 33–65. DOI: [10.1007/s10546-006-9052-x](https://doi.org/10.1007/s10546-006-9052-x).
- Blackadar, A. K. (1957). "Boundary Layer Wind Maxima and their Significance for the Growth of Nocturnal Inversions". In: *Bull. Amer. Meteorol. Soc.* 38, pp. 283–290.
- Bonin, T. A., W. G. Blumberg, P. M. Klein, and P. B. Chilson (Dec. 2015). "Thermodynamic and Turbulence Characteristics of the Southern Great Plains Nocturnal Boundary Layer Under Differing Turbulent Regimes". In: *Boundary-Layer Meteorology* 157.3, pp. 401–420. DOI: [10.1007/s10546-015-0072-2](https://doi.org/10.1007/s10546-015-0072-2).
- Bony, S., R. Colman, V. M. Kattsov, R. P. Allan, C. S. Bretherton, J.-L. Dufresne, A. Hall, S. Hallegatte, M. M. Holland, W. Ingram, D. A. Randall, B. J. Soden, G. Tselioudis, and M. J. Webb (Aug. 2006). "How Well Do We Understand and Evaluate Climate Change Feedback Processes?" In: *Journal of Climate* 19.15, pp. 3445–3482. DOI: [10.1175/JCLI3819.1](https://doi.org/10.1175/JCLI3819.1).
- Bouniol, D, A Illingworth, and R Hogan (2004). "Deriving turbulent kinetic energy dissipation rate within clouds using ground based radar". In: *Proceedings of ERAD*. Vol. 281. 285.
- Brunsell, N. A., D. B. Mechem, and M. C. Anderson (Apr. 2011). "Surface heterogeneity impacts on boundary layer dynamics via energy balance partitioning". In: *Atmospheric Chemistry and Physics* 11.7, pp. 3403–3416. DOI: [10.5194/acp-11-3403-2011](https://doi.org/10.5194/acp-11-3403-2011).

- Cadeddu, M. P., D. D. Turner, and J. C. Liljegren (2009). "A Neural Network for Real-Time Retrievals of PWV and LWP From Arctic Millimeter-Wave Ground-Based Observations". In: *IEEE Transactions on Geoscience and Remote Sensing* 47, No. 7. DOI: [10.1109/TGRS.2009.2013205](https://doi.org/10.1109/TGRS.2009.2013205).
- Cess, R., M. Zhang, W. Ingram, G. Potter, V. Alekseev, H. Barker, E. Cohen-Solal, R. Colman, D. Dazlich, A. Del Genio, et al. (1996). "Cloud feedback in atmospheric general circulation models: An update". In: *Journal of Geophysical Research: Atmospheres* 101.D8, pp. 12791–12794.
- Clough, S. A., M. W. Shepard, E. J. Mlawer, J. S. Delamere, M. J. Iacono, K. Cady-Pereira, S. Boukabara, and P. D. Brown (2005). "Atmospheric radiative transfer modeling: a summary of the AER codes". In: *Journal of Quantitative Spectroscopy and Radiative Transfer* Vol. 91, pp. 233–244. DOI: [10.1016/j.jqsrt.2004.05.058](https://doi.org/10.1016/j.jqsrt.2004.05.058).
- Cohen, A. E., S. M. Cavallo, M. C. Coniglio, and H. E. Brooks (June 2015). "A Review of Planetary Boundary Layer Parameterization Schemes and Their Sensitivity in Simulating Southeastern U.S. Cold Season Severe Weather Environments". In: *Weather and Forecasting* 30.3, pp. 591–612. DOI: [10.1175/WAF-D-14-00105.1](https://doi.org/10.1175/WAF-D-14-00105.1).
- Courault, D., P. Drobinski, Y. Brunet, P. Lacarrere, and C. Talbot (July 2007). "Impact of surface heterogeneity on a buoyancy-driven convective boundary layer in light winds". In: *Boundary-Layer Meteorology* 124.3, pp. 383–403. DOI: [10.1007/s10546-007-9172-y](https://doi.org/10.1007/s10546-007-9172-y).
- Draxl, C., A. N. Hahmann, A. Peña, and G. Giebel (Jan. 2014). "Evaluating winds and vertical wind shear from Weather Research and Forecasting model forecasts using seven planetary boundary layer schemes". In: *Wind Energy* 17.1, pp. 39–55. DOI: [10.1002/we.1555](https://doi.org/10.1002/we.1555).
- Ecklund, W. L., D. A. Carter, and B. B. Balsley (1988). "A UHF Wind Profiler for the Boundary Layer: Brief Description and Initial Results". In: *Journal of Atmospheric and Oceanic Technology* 5.3, pp. 432–441. DOI: [10.1175/1520-0426\(1988\)005<0432:AUWPFT>2.0.CO;2](https://doi.org/10.1175/1520-0426(1988)005<0432:AUWPFT>2.0.CO;2).
- Emeis, S., M. Harris, and R. M. Banta (Aug. 2007). "Boundary-layer anemometry by optical remote sensing for wind energy applications". In: *Meteorologische Zeitschrift* 16.4, pp. 337–347. DOI: [10.1127/0941-2948/2007/0225](https://doi.org/10.1127/0941-2948/2007/0225).
- Freedman, J. M., D. R. Fitzjarrald, K. E. Moore, and R. K. Sakai (Jan. 2001). "Boundary Layer Clouds and Vegetation–Atmosphere Feedbacks". In: *Journal of Climate* 14.2, pp. 180–197. DOI: [10.1175/1520-0442\(2001\)013<0180:BLCAVA>2.0.CO;2](https://doi.org/10.1175/1520-0442(2001)013<0180:BLCAVA>2.0.CO;2).
- Frehlich, R. G. and M. J. Yadlowsky (1994). "Performance of Mean-Frequency Estimators for Doppler Radar and Lidar". In: *Journal of Atmospheric and*

- Oceanic Technology* 11.5, pp. 1217–1230. DOI: [10.1175/1520-0426\(1994\)011<1217:POMFEF>2.0.CO;2](https://doi.org/10.1175/1520-0426(1994)011<1217:POMFEF>2.0.CO;2).
- Frehlich, R. and L. Cornman (Mar. 2002). “Estimating Spatial Velocity Statistics with Coherent Doppler Lidar”. In: *Journal of Atmospheric and Oceanic Technology* 19.3, pp. 355–366. DOI: [10.1175/1520-0426-19.3.355](https://doi.org/10.1175/1520-0426-19.3.355).
- Frisch, A. S., C. W. Fairall, and J. B. Snider (Aug. 1995). “Measurement of Stratus Cloud and Drizzle Parameters in ASTEX with a K_a -Band Doppler Radar and a Microwave Radiometer”. In: *Journal of the Atmospheric Sciences* 52.16, pp. 2788–2799. DOI: [10.1175/1520-0469\(1995\)052<2788:MOSCAD>2.0.CO;2](https://doi.org/10.1175/1520-0469(1995)052<2788:MOSCAD>2.0.CO;2).
- Gao, B.-C. and Y. J. Kaufman (July 2003). “Water vapor retrievals using Moderate Resolution Imaging Spectroradiometer (MODIS) near-infrared channels”. In: *Journal of Geophysical Research: Atmospheres* 108.D13. DOI: [10.1029/2002JD003023](https://doi.org/10.1029/2002JD003023).
- Guo, Z., P. A. Dirmeyer, R. D. Koster, Y. C. Sud, G. Bonan, K. W. Oleson, E. Chan, D. Versegny, P. Cox, C. T. Gordon, J. L. McGregor, S. Kanae, E. Kowalczyk, D. Lawrence, P. Liu, D. Mocko, C.-H. Lu, K. Mitchell, S. Malyshev, B. McAvaney, T. Oki, T. Yamada, A. Pitman, C. M. Taylor, R. Vasic, and Y. Xue (Aug. 2006). “GLACE: The Global Land-Atmosphere Coupling Experiment. Part II: Analysis”. In: *Journal of Hydrometeorology* 7.4, pp. 611–625. DOI: [10.1175/JHM511.1](https://doi.org/10.1175/JHM511.1).
- Hansen, J. E. and L. D. Travis (Oct. 1974). “Light scattering in planetary atmospheres”. In: *Space Science Reviews* 16.4, pp. 527–610.
- Harvey, N. J., R. J. Hogan, and H. F. Dacre (Apr. 2015). “Evaluation of boundary-layer type in a weather forecast model utilizing long-term Doppler lidar observations: Evaluation of Boundary-Layer Type Forecasts”. In: *Quarterly Journal of the Royal Meteorological Society* 141.689, pp. 1345–1353. DOI: [10.1002/qj.2444](https://doi.org/10.1002/qj.2444).
- Harvey, N. J., R. J. Hogan, and H. F. Dacre (Oct. 2013). “A method to diagnose boundary-layer type using Doppler lidar”. In: *Quarterly Journal of the Royal Meteorological Society* 139.676, pp. 1681–1693. DOI: [10.1002/qj.2068](https://doi.org/10.1002/qj.2068).
- Heerwaarden, C. C. van, J. Vilà-Guerau de Arellano, and A. J. Teuling (2010). “Land-atmosphere coupling explains the link between pan evaporation and actual evapotranspiration trends in a changing climate”. In: *Geophysical Research Letters* 37.21. DOI: [10.1029/2010GL045374](https://doi.org/10.1029/2010GL045374).
- Heerwaarden, C. C. van and J. V. Guerau de Arellano (Oct. 2008). “Relative Humidity as an Indicator for Cloud Formation over Heterogeneous Land Surfaces”. In: *Journal of the Atmospheric Sciences* 65.10, pp. 3263–3277. DOI: [10.1175/2008JAS2591.1](https://doi.org/10.1175/2008JAS2591.1).

- Higgins, R. W., Y. Yao, E. S. Yarosh, J. E. Janowiak, and K. C. Mo (Mar. 1997). "Influence of the Great Plains Low-Level Jet on Summertime Precipitation and Moisture Transport over the Central United States". In: *Journal of Climate* 10.3, pp. 481–507. DOI: [10.1175/1520-0442\(1997\)010<0481:IOTGPL>2.0.CO;2](https://doi.org/10.1175/1520-0442(1997)010<0481:IOTGPL>2.0.CO;2).
- Hogan, R. J., A. L. M. Grant, A. J. Illingworth, G. N. Pearson, and E. J. O'Connor (Apr. 2009). "Vertical velocity variance and skewness in clear and cloud-topped boundary layers as revealed by Doppler lidar". In: *Quarterly Journal of the Royal Meteorological Society* 135.640, pp. 635–643. DOI: [10.1002/qj.413](https://doi.org/10.1002/qj.413).
- Holtslag, A. A. M., G. Svensson, P. Baas, S. Basu, B. Beare, A. C. M. Beljaars, F. C. Bosveld, J. Cuxart, J. Lindvall, G. J. Steeneveld, M. Tjernström, and B. J. H. Van De Wiel (Nov. 2013). "Stable Atmospheric Boundary Layers and Diurnal Cycles: Challenges for Weather and Climate Models". In: *Bulletin of the American Meteorological Society* 94.11, pp. 1691–1706. DOI: [10.1175/BAMS-D-11-00187.1](https://doi.org/10.1175/BAMS-D-11-00187.1).
- Hu, X.-M., J. W. Nielsen-Gammon, and F. Zhang (Sept. 2010). "Evaluation of Three Planetary Boundary Layer Schemes in the WRF Model". In: *Journal of Applied Meteorology and Climatology* 49.9, pp. 1831–1844. DOI: [10.1175/2010JAMC2432.1](https://doi.org/10.1175/2010JAMC2432.1).
- Hu, Y. X. and K. Stamnes (1993). "An Accurate Parameterization of the Radiative Properties of Water Clouds Suitable for Use in Climate Models". In: *Journal of Climate* Vol. 6, pp. 728–742. DOI: [10.1175/1520-0442\(1993\)006<0728:AAPOTR>2.0.CO;2](https://doi.org/10.1175/1520-0442(1993)006<0728:AAPOTR>2.0.CO;2).
- Huang, H.-Y. and S. A. Margulis (June 2010). "Evaluation of a fully coupled large-eddy simulation-land surface model and its diagnosis of land-atmosphere feedbacks". In: *Water Resources Research* 46.6. DOI: [10.1029/2009WR008232](https://doi.org/10.1029/2009WR008232).
- Illingworth, A. J., R. J. Hogan, E. O'Connor, D. Bouniol, M. E. Brooks, J. Delanoé, D. P. Donovan, J. D. Eastment, N. Gaussiat, J. W. F. Goddard, M. Haefelin, H. K. Baltink, O. A. Krasnov, J. Pelon, J.-M. Piriou, A. Protat, H. W. J. Russchenberg, A. Seifert, A. M. Tompkins, G.-J. van Zadelhoff, F. Vinit, U. Willén, D. R. Wilson, and C. L. Wrench (2007). "Cloudnet Continuous Evaluation of Cloud Profiles in Seven Operational Models Using Ground-Based Observations". In: *Bulletin of the American Meteorological Society*, pp. 883–898. DOI: [10.1175/BAMS-88-6-883](https://doi.org/10.1175/BAMS-88-6-883).
- IPCC (2013). *Climate Change 2013: The Physical Science Basis. Contribution of Working Group I to the Fifth Assessment Report of the Intergovernmental Panel*

- on *Climate Change*. Cambridge, United Kingdom and New York, NY, USA: Cambridge University Press, p. 1535. DOI: [10.1017/CB09781107415324](https://doi.org/10.1017/CB09781107415324).
- Knist, C. L. (2014). "Retrieval of liquid water cloud properties from ground-based remote sensing observations". In: *Dissertation at Delft University of Technology*. DOI: [10.4233/uuid:2a844dc9-0e89-43c7-a150-a89db0c8327b](https://doi.org/10.4233/uuid:2a844dc9-0e89-43c7-a150-a89db0c8327b).
- Kolmogorov, A. N. (July 1991). "Dissipation of Energy in the Locally Isotropic Turbulence". In: *Proceedings of the Royal Society A: Mathematical, Physical and Engineering Sciences* 434.1890, pp. 15–17. DOI: [10.1098/rspa.1991.0076](https://doi.org/10.1098/rspa.1991.0076).
- Krogsæter, O. and J. Reuder (May 2015). "Validation of boundary layer parameterization schemes in the weather research and forecasting model under the aspect of offshore wind energy applications- Part I: Average wind speed and wind shear". In: *Wind Energy* 18.5, pp. 769–782. DOI: [10.1002/we.1727](https://doi.org/10.1002/we.1727).
- Kubar, T. L., D.-L. Hartmann, and R. Wood (2009). "Understanding the importance of microphysics and macrophysics for warm rain in marine low clouds. Part I: Satellite observations". In: *Journal of Atmospheric Sciences* Vol. 66, pp. 2953–2972. DOI: [10.1175/2009JAS3071.1](https://doi.org/10.1175/2009JAS3071.1).
- Liebe, H., G. Hufford, and T. Manabe (1991). "A model for the complex permittivity of water at frequencies below 1 THz". In: *International Journal of Infrared and Millimeter Waves* Vol. 12, pp. 659–675. DOI: [10.1007/BF01008897](https://doi.org/10.1007/BF01008897).
- Löhnert, U. and S. Crewell (2003). "Accuracy of cloud liquid water path from ground-based microwave radiometry 1. Dependency on cloud model statistics". In: *Radio Science* Vol. 38, No. 3.8041. DOI: [10.1029/2002RS002654](https://doi.org/10.1029/2002RS002654).
- Löhnert, U., S. Crewell, and C. Simmer (2004). "An Integrated Approach toward Retrieving Physically Consistent Profiles of Temperature, Humidity, and Cloud Liquid Water". In: *Journal of Applied Meteorology* Vol. 43, pp. 1295–1307. DOI: [10.1175/1520-0450\(2004\)043<1295:AIATRP>2.0.CO;2](https://doi.org/10.1175/1520-0450(2004)043<1295:AIATRP>2.0.CO;2).
- Löhnert, U., J. H. Schween, C. Acquistapace, K. Ebell, M. Maahn, M. Barrera-Verdejo, A. Hirsikko, B. Bohn, A. Knaps, E. O'Connor, C. Simmer, A. Wahner, and S. Crewell (July 2015). "JOYCE: Jülich Observatory for Cloud Evolution". In: *Bulletin of the American Meteorological Society* 96.7, pp. 1157–1174. DOI: [10.1175/BAMS-D-14-00105.1](https://doi.org/10.1175/BAMS-D-14-00105.1).
- Macke, A., P. Seifert, H. Baars, C. Barthlott, C. Beekmans, A. Behrendt, B. Bohn, M. Brueck, J. Bühl, S. Crewell, T. Damian, H. Deneke, S. Düsing, A. Foth, P. Di Girolamo, E. Hammann, R. Heinze, A. Hirsikko, J. Kalisch, N. Kalthoff, S. Kinne, M. Kohler, U. Löhnert, B. L. Madhavan, V. Maurer, S. K. Muppa, J. Schween, I. Serikov, H. Siebert, C. Simmer, F. Späth, S. Steinke,

- K. Träumner, S. Trömel, B. Wehner, A. Wieser, V. Wulfmeyer, and X. Xie (Apr. 2017). “The HD(CP)² Observational Prototype Experiment (HOPE) – an overview”. In: *Atmospheric Chemistry and Physics* 17.7, pp. 4887–4914. DOI: [10.5194/acp-17-4887-2017](https://doi.org/10.5194/acp-17-4887-2017).
- Manninen, A., T. Marke, M. Tuononen, and E. O’Connor (2018). “Atmospheric Boundary Layer Classification With Doppler Lidar”. In: *Journal of Geophysical Research: Atmospheres* 123.15. DOI: [10.1029/2017JD028169](https://doi.org/10.1029/2017JD028169).
- Manninen, A. J., E. J. O’Connor, V. Vakkari, and T. Petäjä (2016). “A generalised background correction algorithm for a Halo Doppler lidar and its application to data from Finland”. In: *Atmospheric Measurement Techniques* 9.2, pp. 817–827. DOI: [10.5194/amt-9-817-2016](https://doi.org/10.5194/amt-9-817-2016).
- Marchand, R., T. Ackerman, E. D. Westwater, S. A. Clough, K. Cady-Pereira, and J. C. Liljegren (2003). “An assessment of microwave absorption models and retrievals of cloud liquid water using clear-sky data”. In: *Journal of Geophysical Research* Vol. 108, No. D24.4773. DOI: [10.1029/2003JD003843](https://doi.org/10.1029/2003JD003843).
- Marke, T., S. Crewell, V. Schemann, J. Schween, and M. Tuononen (2018). “Long-term observations and high-resolution modeling of midlatitude nocturnal boundary layer processes connected to low-level jets”. In: *Journal of Applied Meteorology and Climatology* 57.5. DOI: [10.1175/JAMC-D-17-0341.1](https://doi.org/10.1175/JAMC-D-17-0341.1).
- Marke, T., K. Ebell, U. Löhnert, and D. Turner (2016). “Statistical retrieval of thin liquid cloud microphysical properties using ground-based infrared and microwave observations”. In: *Journal of Geophysical Research* 121.24. DOI: [10.1002/2016JD025667](https://doi.org/10.1002/2016JD025667).
- Marke, T., U. Löhnert, V. Schemann, J. H. Schween, and S. Crewell (2020). “Detection of land-surface-induced atmospheric water vapor patterns”. In: *Atmospheric Chemistry and Physics* 20.3, pp. 1723–1736. DOI: [10.5194/acp-20-1723-2020](https://doi.org/10.5194/acp-20-1723-2020).
- Maschwitz, G., U. Löhnert, S. Crewell, T. Rose, and D. D. Turner (Oct. 2013). “Investigation of ground-based microwave radiometer calibration techniques at 530 hPa”. In: *Atmospheric Measurement Techniques* 6.10, pp. 2641–2658. DOI: [10.5194/amt-6-2641-2013](https://doi.org/10.5194/amt-6-2641-2013).
- McFarlane, N. (July 2011). “Parameterizations: representing key processes in climate models without resolving them”. In: *Wiley Interdisciplinary Reviews: Climate Change* 2.4, pp. 482–497. DOI: [10.1002/wcc.122](https://doi.org/10.1002/wcc.122).
- McNider, R. T., G. J. Steeneveld, A. A. M. Holtslag, R. A. Pielke Sr., S. Mackaro, A. Pour-Biazar, J. Walters, U. Nair, and J. Christy (2012). “Response and sensitivity of the nocturnal boundary layer over land to added longwave

- radiative forcing". In: *Journal of Geophysical Research: Atmospheres* 117.D14. DOI: [10.1029/2012JD017578](https://doi.org/10.1029/2012JD017578).
- Milovac, J., K. Warrach-Sagi, A. Behrendt, F. Späth, J. Ingwersen, and V. Wulfmeyer (Jan. 2016). "Investigation of PBL schemes combining the WRF model simulations with scanning water vapor differential absorption lidar measurements". In: *Journal of Geophysical Research: Atmospheres* 121.2, pp. 624–649. DOI: [10.1002/2015JD023927](https://doi.org/10.1002/2015JD023927).
- Moeng, C.-H. (July 1984). "A Large-Eddy-Simulation Model for the Study of Planetary Boundary-Layer Turbulence". In: *Journal of the Atmospheric Sciences* 41.13, pp. 2052–2062. DOI: [10.1175/1520-0469\(1984\)041<2052:ALESMF>2.0.CO;2](https://doi.org/10.1175/1520-0469(1984)041<2052:ALESMF>2.0.CO;2).
- Muñoz-Esparza, D., B. Cañadillas, T. Neumann, and J. van Beeck (Nov. 2012). "Turbulent fluxes, stability and shear in the offshore environment: Meso-scale modelling and field observations at FINO1". In: *Journal of Renewable and Sustainable Energy* 4.6, p. 063136. DOI: [10.1063/1.4769201](https://doi.org/10.1063/1.4769201).
- O'Connor, E. J., A. J. Illingworth, I. M. Brooks, C. D. Westbrook, R. J. Hogan, F. Davies, and B. J. Brooks (Oct. 2010). "A Method for Estimating the Turbulent Kinetic Energy Dissipation Rate from a Vertically Pointing Doppler Lidar, and Independent Evaluation from Balloon-Borne In Situ Measurements". In: *Journal of Atmospheric and Oceanic Technology* 27.10, pp. 1652–1664. DOI: [10.1175/2010JTECHA1455.1](https://doi.org/10.1175/2010JTECHA1455.1).
- Paquin, J. E. and S. Pond (Nov. 1971). "The determination of the Kolmogoroff constants for velocity, temperature and humidity fluctuations from second- and third-order structure functions". In: *Journal of Fluid Mechanics* 50.02, p. 257. DOI: [10.1017/S0022112071002568](https://doi.org/10.1017/S0022112071002568).
- Patton, E. G., P. P. Sullivan, and C.-H. Moeng (July 2005). "The Influence of Idealized Heterogeneity on Wet and Dry Planetary Boundary Layers Coupled to the Land Surface". In: *Journal of the Atmospheric Sciences* 62.7, pp. 2078–2097. DOI: [10.1175/JAS3465.1](https://doi.org/10.1175/JAS3465.1).
- Pearson, G., F. Davies, and C. Collier (Feb. 2009). "An Analysis of the Performance of the UFAM Pulsed Doppler Lidar for Observing the Boundary Layer". In: *Journal of Atmospheric and Oceanic Technology* 26.2, pp. 240–250. DOI: [10.1175/2008JTECHA1128.1](https://doi.org/10.1175/2008JTECHA1128.1).
- Perez, R., S. Kivalov, J. Schlemmer, K. Hemker, D. Renné, and T. E. Hoff (Dec. 2010). "Validation of short and medium term operational solar radiation forecasts in the US". In: *Solar Energy* 84.12, pp. 2161–2172. DOI: [10.1016/j.solener.2010.08.014](https://doi.org/10.1016/j.solener.2010.08.014).
- Peña, A., R. Floors, A. Sathe, S.-E. Gryning, R. Wagner, M. S. Courtney, X. G. Larsén, A. N. Hahmann, and C. B. Hasager (Jan. 2016). "Ten Years of

- Boundary-Layer and Wind-Power Meteorology at Høvsøre, Denmark". In: *Boundary-Layer Meteorology* 158.1, pp. 1–26. DOI: [10.1007/s10546-015-0079-8](https://doi.org/10.1007/s10546-015-0079-8).
- Päschke, E., R. Leinweber, and V. Lehmann (June 2015). "An assessment of the performance of a 1.5 μm Doppler lidar for operational vertical wind profiling based on a 1-year trial". In: *Atmospheric Measurement Techniques* 8.6, pp. 2251–2266. DOI: [10.5194/amt-8-2251-2015](https://doi.org/10.5194/amt-8-2251-2015).
- Rabin, R. M., D. J. Stensrud, S. Stadler, P. J. Wetzel, and M. Gregory (Mar. 1990). "Observed Effects of Landscape Variability on Convective Clouds". In: *Bulletin of the American Meteorological Society* 71.3, pp. 272–280. DOI: [10.1175/1520-0477\(1990\)071<0272:OEOLVO>2.0.CO;2](https://doi.org/10.1175/1520-0477(1990)071<0272:OEOLVO>2.0.CO;2).
- Rodgers, C. D. (2000). "Inverse Methods for Atmospheric Sounding". In: *World Scientific, Sin*, 238 pp.
- Rose, T., S. Crewell, U. Löhnert, and C. Simmer (2005). "A network suitable microwave radiometer for operational monitoring of the cloudy atmosphere". In: *Atmospheric Research* Vol. 75, pp. 183–200. DOI: [10.1016/j.atmosres.2004.12.005](https://doi.org/10.1016/j.atmosres.2004.12.005).
- Rosenkranz, P. W. (1998). "Water vapor microwave continuum absorption: A comparison of measurements and models". In: *Radio Science* Vol. 33, pp. 919–928. DOI: [10.1029/98RS01182](https://doi.org/10.1029/98RS01182).
- Rye, B. and R. Hardesty (Jan. 1993a). "Discrete spectral peak estimation in incoherent backscatter heterodyne lidar. I. Spectral accumulation and the Cramer-Rao lower bound". In: *IEEE Transactions on Geoscience and Remote Sensing* 31.1, pp. 16–27. DOI: [10.1109/36.210440](https://doi.org/10.1109/36.210440).
- (Jan. 1993b). "Discrete spectral peak estimation in incoherent backscatter heterodyne lidar. II. Correlogram accumulation". In: *IEEE Transactions on Geoscience and Remote Sensing* 31.1, pp. 28–35. DOI: [10.1109/36.210441](https://doi.org/10.1109/36.210441).
- Santanello, J. A., P. A. Dirmeyer, C. R. Ferguson, K. L. Findell, A. B. Tawfik, A. Berg, M. Ek, P. Gentine, B. P. Guillod, C. van Heerwaarden, J. Roundy, and V. Wulfmeyer (June 2018). "Land-Atmosphere Interactions: The LoCo Perspective". In: *Bulletin of the American Meteorological Society* 99.6, pp. 1253–1272. DOI: [10.1175/BAMS-D-17-0001.1](https://doi.org/10.1175/BAMS-D-17-0001.1).
- Santanello, J. A., C. D. Peters-Lidard, A. Kennedy, and S. V. Kumar (Feb. 2013). "Diagnosing the Nature of Land-Atmosphere Coupling: A Case Study of Dry/Wet Extremes in the U.S. Southern Great Plains". In: *Journal of Hydrometeorology* 14.1, pp. 3–24. DOI: [10.1175/JHM-D-12-023.1](https://doi.org/10.1175/JHM-D-12-023.1).
- Santanello, J. A., C. D. Peters-Lidard, and S. V. Kumar (Oct. 2011). "Diagnosing the Sensitivity of Local Land-Atmosphere Coupling via the Soil

- Moisture-Boundary Layer Interaction". In: *Journal of Hydrometeorology* 12.5, pp. 766–786. DOI: [10.1175/JHM-D-10-05014.1](https://doi.org/10.1175/JHM-D-10-05014.1).
- Santanello, J. A., C. D. Peters-Lidard, S. V. Kumar, C. Alonge, and W.-K. Tao (June 2009). "A Modeling and Observational Framework for Diagnosing Local Land-Atmosphere Coupling on Diurnal Time Scales". In: *Journal of Hydrometeorology* 10.3, pp. 577–599. DOI: [10.1175/2009JHM1066.1](https://doi.org/10.1175/2009JHM1066.1).
- Schween, J. H., S. Crewell, and U. Lohnert (Mar. 2011). "Horizontal-Humidity Gradient From One Single-Scanning Microwave Radiometer". In: *IEEE Geoscience and Remote Sensing Letters* 8.2, pp. 336–340. DOI: [10.1109/LGRS.2010.2072981](https://doi.org/10.1109/LGRS.2010.2072981).
- Schär, C., D. Lüthi, U. Beyerle, and E. Heise (Mar. 1999). "The Soil–Precipitation Feedback: A Process Study with a Regional Climate Model". In: *Journal of Climate* 12.3, pp. 722–741. DOI: [10.1175/1520-0442\(1999\)012<0722:TSPFAP>2.0.CO;2](https://doi.org/10.1175/1520-0442(1999)012<0722:TSPFAP>2.0.CO;2).
- Sengupta, M., E. E. Clothiaux, T. P. Ackerman, S. Kato, and Q. Min (2003). "Importance of Accurate Liquid Water Path for Estimation of Solar Radiation in Warm Boundary Layer Clouds: An Observational Study". In: *Journal of Climate* Vol. 16, pp. 2997–3009. DOI: [10.1175/1520-0442\(2003\)016<2997:IOALWP>2.0.CO;2](https://doi.org/10.1175/1520-0442(2003)016<2997:IOALWP>2.0.CO;2).
- Sengupta, M., E. E. Clothiaux, and T. P. Ackerman (Dec. 2004). "Climatology of Warm Boundary Layer Clouds at the ARM SGP Site and Their Comparison to Models". In: *Journal of Climate* 17.24, pp. 4760–4782. DOI: [10.1175/JCLI-3231.1](https://doi.org/10.1175/JCLI-3231.1).
- Shao, Y., S. Liu, J. H. Schween, and S. Crewell (Aug. 2013). "Large-Eddy Atmosphere-Land-Surface Modelling over Heterogeneous Surfaces: Model Development and Comparison with Measurements". In: *Boundary-Layer Meteorology* 148.2, pp. 333–356. DOI: [10.1007/s10546-013-9823-0](https://doi.org/10.1007/s10546-013-9823-0).
- Shrestha, P., M. Sulis, M. Masbou, S. Kollet, and C. Simmer (Sept. 2014). "A Scale-Consistent Terrestrial Systems Modeling Platform Based on COSMO, CLM, and ParFlow". In: *Monthly Weather Review* 142.9, pp. 3466–3483. DOI: [10.1175/MWR-D-14-00029.1](https://doi.org/10.1175/MWR-D-14-00029.1).
- Simmer, C. (1994). "Satellitenfernerkundung hydrologischer Parameter der Atmosphäre mit Mikrowellen". In: *Verlag Dr. Kovac, Hamburg, Germany* 13.
- Simmer, C., I. Thiele-Eich, M. Masbou, W. Amelung, H. Bogen, S. Crewell, B. Diekkrüger, F. Ewert, H.-J. Hendricks Franssen, J. A. Huisman, A. Kemna, N. Klitzsch, S. Kollet, M. Langensiepen, U. Lohnert, A. S. M. M. Rahman, U. Rascher, K. Schneider, J. Schween, Y. Shao, P. Shrestha, M. Stiebler, M. Sulis, J. Vanderborght, H. Vereecken, J. van der Kruk, G. Waldhoff, and T.

- Zerenner (2015). "Monitoring and Modeling the Terrestrial System from Pores to Catchments: The Transregional Collaborative Research Center on Patterns in the Soil–Vegetation–Atmosphere System". In: *Bulletin of the American Meteorological Society* 96.10, pp. 1765–1787. DOI: [10.1175/BAMS-D-13-00134.1](https://doi.org/10.1175/BAMS-D-13-00134.1).
- Späth, F., A. Behrendt, S. K. Muppa, S. Metzendorf, A. Riede, and V. Wulfmeyer (Apr. 2016). "3-D water vapor field in the atmospheric boundary layer observed with scanning differential absorption lidar". In: *Atmospheric Measurement Techniques* 9.4, pp. 1701–1720. DOI: [10.5194/amt-9-1701-2016](https://doi.org/10.5194/amt-9-1701-2016).
- Steinke, S., S. Eikenberg, U. Löhnert, G. Dick, D. Klocke, P. Di Girolamo, and S. Crewell (Mar. 2015). "Assessment of small-scale integrated water vapour variability during HOPE". In: *Atmospheric Chemistry and Physics* 15.5, pp. 2675–2692. DOI: [10.5194/acp-15-2675-2015](https://doi.org/10.5194/acp-15-2675-2015).
- Stensrud, D. J. and S. J. Weiss (June 2002). "Mesoscale Model Ensemble Forecasts of the 3 May 1999 Tornado Outbreak". In: *Weather and Forecasting* 17.3, pp. 526–543. DOI: [10.1175/1520-0434\(2002\)017<0526:MMEFOT>2.0.CO;2](https://doi.org/10.1175/1520-0434(2002)017<0526:MMEFOT>2.0.CO;2).
- Stephens, G. L. (Nov. 1978). "Radiation Profiles in Extended Water Clouds. II: Parameterization Schemes". In: *Journal of the Atmospheric Sciences* 35.11, pp. 2123–2132. DOI: [10.1175/1520-0469\(1978\)035<2123:RPIEWC>2.0.CO;2](https://doi.org/10.1175/1520-0469(1978)035<2123:RPIEWC>2.0.CO;2).
- (2005). "Cloud Feedbacks in the Climate System: A Critical Review". In: *Journal of Climate* Vol. 18, pp. 237–273. DOI: [10.1175/JCLI-3243.1](https://doi.org/10.1175/JCLI-3243.1).
- Stevens, B. and D. H. Lenschow (Feb. 2001). "Observations, Experiments, and Large Eddy Simulation". In: *Bulletin of the American Meteorological Society* 82.2, pp. 283–294. DOI: [10.1175/1520-0477\(2001\)082<0283:OEALLES>2.3.CO;2](https://doi.org/10.1175/1520-0477(2001)082<0283:OEALLES>2.3.CO;2).
- Storm, B., J. Dudhia, S. Basu, A. Swift, and I. Giammanco (Jan. 2009). "Evaluation of the Weather Research and Forecasting model on forecasting low-level jets: implications for wind energy". In: *Wind Energy* 12.1, pp. 81–90. DOI: [10.1002/we.288](https://doi.org/10.1002/we.288).
- Stull, R. B. (Dec. 2012). *An Introduction to Boundary Layer Meteorology*. Springer Science & Business Media.
- Su, J., M. Felton, L. Lei, M. P. McCormick, R. Delgado, and A. St. Pé (May 2016). "Lidar remote sensing of cloud formation caused by low-level jets". In: *Journal of Geophysical Research: Atmospheres* 121.10, pp. 5904–5911. DOI: [10.1002/2015JD024590](https://doi.org/10.1002/2015JD024590).

- Taylor, G. I. (Sept. 1935). "Statistical Theory of Turbulence". In: *Proceedings of the Royal Society of London. Series A - Mathematical and Physical Sciences* 151.873, pp. 421–444. DOI: [10.1098/rspa.1935.0158](https://doi.org/10.1098/rspa.1935.0158).
- Tuononen, M., E. J. O'Connor, V. A. Sinclair, and V. Vakkari (July 2017). "Low-level jets over Utö, Finland, based on Doppler lidar observations". In: *Journal of Applied Meteorology and Climatology*. DOI: [10.1175/JAMC-D-16-0411.1](https://doi.org/10.1175/JAMC-D-16-0411.1).
- Turner, D. D. (2007). "Improved ground-based liquid water path retrievals using a combined infrared and microwave approach". In: *Journal of Geophysical Research* Vol. 112. DOI: [10.1029/2007JD008530](https://doi.org/10.1029/2007JD008530).
- Turner, D. D., A. Shepard, J. C. Liljegren, E. E. Clothiaux, K. Cady-Pereira, and K. L. Gaustad (2007a). "Retrieving Liquid Water Path and Precipitable Water Vapor From the Atmospheric Radiation Measurement (ARM) Microwave Radiometers". In: *Transactions on Geoscience and Remote Sensing* Vol. 45, No. 11. DOI: [10.1109/TGRS.2007.903703](https://doi.org/10.1109/TGRS.2007.903703).
- Turner, D. D., A. M. Vogelmann, R. T. Austin, J. C. Barnard, K. Cady-Pereira, J. C. Chiu, S. A. Clough, C. Flynn, M. M. Khaiyer, J. Liljegren, K. Johnson, B. Lin, C. Long, A. Marshak, S. Y. Matrosov, S. A. McFarlane, M. Miller, Q. Min, P. Minimis, W. O'Hirok, Z. Wang, and W. Wiscombe (2007b). "Thin Liquid Water Clouds Their Importance and Our Challenge". In: *Bulletin of the American Meteorological Society*. 177–190. DOI: [10.1175/BAMS-88-2-177](https://doi.org/10.1175/BAMS-88-2-177).
- Vilà-Guerau de Arellano, J., H. G. Ouwersloot, D. Baldocchi, and C. M. J. Jacobs (Mar. 2014). "Shallow cumulus rooted in photosynthesis". In: *Geophysical Research Letters* 41.5, pp. 1796–1802. DOI: [10.1002/2014GL059279](https://doi.org/10.1002/2014GL059279).
- Waldhoff, G., U. Lussem, and G. Bareth (Sept. 2017). "Multi-Data Approach for remote sensing-based regional crop rotation mapping: A case study for the Rur catchment, Germany". In: *International Journal of Applied Earth Observation and Geoinformation* 61, pp. 55–69. DOI: [10.1016/j.jag.2017.04.009](https://doi.org/10.1016/j.jag.2017.04.009).
- Webb, M. J., C. A. Senior, D. M. H. Sexton, W. J. Ingram, K. D. Williams, M. A. Ringer, B. J. McAvaney, R. Colman, B. J. Soden, R. Gudgel, T. Knutson, S. Emori, T. Ogura, Y. Tsushima, N. Andronova, B. Li, I. Musat, S. Bony, and K. E. Taylor (July 2006). "On the contribution of local feedback mechanisms to the range of climate sensitivity in two GCM ensembles". In: *Climate Dynamics* 27.1, pp. 17–38. DOI: [10.1007/s00382-006-0111-2](https://doi.org/10.1007/s00382-006-0111-2).
- Weckwerth, T. M., D. B. Parsons, S. E. Koch, J. A. Moore, M. A. LeMone, B. B. Demoz, C. Flamant, B. Geerts, J. Wang, and W. F. Feltz (Feb. 2004). "An Overview of the International H₂O Project (IHOP_2002) and Some

- Preliminary Highlights". In: *Bulletin of the American Meteorological Society* 85.2, pp. 253–278. DOI: [10.1175/BAMS-85-2-253](https://doi.org/10.1175/BAMS-85-2-253).
- Weatkamp, C., ed. (2005). *Lidar*. Vol. 102. Springer Series in Optical Sciences. New York: Springer-Verlag. ISBN: 978-0-387-40075-4. DOI: [10.1007/b106786](https://doi.org/10.1007/b106786).
- Westwater, E. (1978). "The accuracy of water vapor and cloud liquid determination by dual-frequency ground-based microwave radiometry". In: *Radio Science* Vol. 13, pp. 667–685. DOI: [10.1029/RS013i004p00677](https://doi.org/10.1029/RS013i004p00677).
- Wulfmeyer, V., A. Behrendt, C. Kottmeier, U. Corsmeier, C. Barthlott, G. C. Craig, M. Hagen, D. Althausen, F. Aoshima, M. Arpagaus, H.-S. Bauer, L. Bennett, A. Blyth, C. Brandau, C. Champollion, S. Crewell, G. Dick, P. Di Girolamo, M. Dorninger, Y. Dufournet, R. Eigenmann, R. Engelmann, C. Flamant, T. Foken, T. Gorgas, M. Grzeschik, J. Handwerker, C. Hauck, H. Höller, W. Junkermann, N. Kalthoff, C. Kiemle, S. Klink, M. König, L. Krauss, C. N. Long, F. Madonna, S. Mobbs, B. Neininger, S. Pal, G. Peters, G. Pigeon, E. Richard, M. W. Rotach, H. Russchenberg, T. Schwitalla, V. Smith, R. Steinacker, J. Trentmann, D. D. Turner, J. van Baelen, S. Vogt, H. Volkert, T. Weckwerth, H. Wernli, A. Wieser, and M. Wirth (Jan. 2011). "The Convective and Orographically-induced Precipitation Study (COPS): the scientific strategy, the field phase, and research highlights". In: *Quarterly Journal of the Royal Meteorological Society* 137.S1, pp. 3–30. DOI: [10.1002/qj.752](https://doi.org/10.1002/qj.752).
- Wulfmeyer, V., D. D. Turner, B. Baker, R. Banta, A. Behrendt, T. Bonin, W. A. Brewer, M. Buban, A. Choukulkar, E. Dumas, R. M. Hardesty, T. Heus, J. Ingwersen, D. Lange, T. R. Lee, S. Metzendorf, S. K. Muppa, T. Meyers, R. Newsom, M. Osman, S. Raasch, J. Santanello, C. Senff, F. Späth, T. Wagner, and T. Weckwerth (Aug. 2018). "A New Research Approach for Observing and Characterizing Land-Atmosphere Feedback". In: *Bulletin of the American Meteorological Society* 99.8, pp. 1639–1667. DOI: [10.1175/BAMS-D-17-0009.1](https://doi.org/10.1175/BAMS-D-17-0009.1).
- Zampieri, M, P Malguzzi, and A Buzzi (2005). "Sensitivity of quantitative precipitation forecasts to boundary layer parameterization: a flash flood case study in the Western Mediterranean". In: *Natural Hazards and Earth System Science* 5.4, pp. 603–612.
- Zhou, B. and F. K. Chow (Mar. 2012). "Turbulence Modeling for the Stable Atmospheric Boundary Layer and Implications for Wind Energy". In: *Flow, Turbulence and Combustion* 88.1-2, pp. 255–277. DOI: [10.1007/s10494-011-9359-7](https://doi.org/10.1007/s10494-011-9359-7).

DANKSAGUNG

Danke an alle im TR32 die es mir ermöglicht haben diese Forschung zu betreiben und die Organisation während meiner Zeit als PhD Student (Clemens, Insa). Dazu gehört natürlich auch der Support aus den Graduate Schools IRTG (Nadine) und GSGS (Karin) und dem Sekretariat (Dagmar und Annette).

Thanks to all Infernos for the company along my way, the scientific and non-scientific discussions.

Ein besonderer Dank aufgrund der exzellenten und langjährigen Betreuung auch als Student geht an Susanne und Uli und natürlich auch an Uwe als weiteres Mitglied in meinem Doctoral Committee. Danke für eure Beratung und Ideen!

Danke Kerstin, dass du mir unter anderem geholfen hast als SHK erste Erfahrungen in der Wissenschaft zu sammeln.

Danke Mario für alle Probleme die du lösen konntest.

Vielen Dank Vera und Thirza für eure Zeit, Geduld, Simulationen und den Einblick in die Welt der Modelle.

Danke auch an Rainer und Jan, dass ihr euer Wissen und eure Erfahrung mit mir geteilt habt.

Nils, danke für deine Unterstützung. Ich habe in der ganzen Zeit viel gelernt.

Thanks to all my current and former offices mates and sorry for talking so much..

Thank you Dave for sharing your knowledge and always helping me out.

Thanks a lot Ewan, Antti and Minttu for this fruitful collaboration and for hosting me in Finland.

Vor allem danke ich meiner Familie und Natascha für den Rückhalt auch in schwierigen Zeiten.

ERKLÄRUNG

Ich versichere, dass ich die von mir vorgelegte Dissertation selbständig angefertigt, die benutzten Quellen und Hilfsmittel vollständig angegeben und die Stellen der Arbeit - einschließlich Tabellen, Karten und Abbildungen -, die anderen Werken im Wortlaut oder dem Sinn nach entnommen sind, in jedem Einzelfall als Entlehnung kenntlich gemacht habe; dass diese Dissertation noch keiner anderen Fakultät oder Universität zur Prüfung vorgelegen hat; dass sie - abgesehen von unten angegebenen Teilpublikationen - noch nicht veröffentlicht worden ist, sowie, dass ich eine solche Veröffentlichung vor Abschluss des Promotionsverfahrens nicht vornehmen werde. Die Bestimmungen der Promotionsordnung sind mir bekannt. Die von mir vorgelegte Dissertation ist von Prof. Dr. Susanne Crewell betreut worden.

Köln, April 2020



Tobias Marke

Teilpublikationen

A. Manninen, T. Marke, M. Tuononen, and E. O'Connor (2018). "Atmospheric Boundary Layer Classification With Doppler Lidar". In: *Journal of Geophysical Research: Atmospheres* 123.15. DOI: [10.1029/2017JD028169](https://doi.org/10.1029/2017JD028169)

Eigene Beteiligung: Als geteilter Erstautor wurde die Konzeption der Studie zu gleichen Teilen mit A. J. Manninen erstellt. Die Ausarbeitung der Klassifikation wurde zusammen mit E. J. O'Connor, auch während einiger Aufenthalte in Helsinki, erarbeitet. Die Anwendung der Klassifikation auf Langzeitmessungen der beiden Messorte wurde auf A. J. Manninen (Hyytiälä) und mich

(Jülich) aufgeteilt. M. Tuononen hat sowohl bei der Diskussion der Ergebnisse, als auch mit der Anwendung des LLJ Algorithmus geholfen.

T. Marke, S. Crewell, V. Schemann, J. Schween, and M. Tuononen (2018). “Long-term observations and high-resolution modeling of midlatitude nocturnal boundary layer processes connected to low-level jets”. In: *Journal of Applied Meteorology and Climatology* 57.5. DOI: [10.1175/JAMC-D-17-0341.1](https://doi.org/10.1175/JAMC-D-17-0341.1)

Eigene Beteiligung: Für diese Studie wurden von V. Schemann die Simulationen und von M. Tuononen der LLJ Algorithmus bereitgestellt. Die gesamten Berechnungen, sowie die Abbildungen und der Textentwurf wurden von mir erstellt. S. Crewell und J. H. Schween waren bei der Diskussion und der Überarbeitung der Ergebnisse und des Textes beteiligt.

T. Marke, U. Löhnert, V. Schemann, J. H. Schween, and S. Crewell (2020). “Detection of land-surface-induced atmospheric water vapor patterns”. In: *Atmospheric Chemistry and Physics* 20.3, pp. 1723–1736. DOI: [10.5194/acp-20-1723-2020](https://doi.org/10.5194/acp-20-1723-2020)

Eigene Beteiligung: Das Konzept zu dieser Studie und Korrekturen am finalen Text wurden mit Hilfe von S. Crewell und U. Löhnert erarbeitet. Neben den Simulationen, die von V. Schemann durchgeführt wurde, erfolgte die gesamte Analyse der Daten und die Erstellung der Abbildungen durch mich.

T. Marke, K. Ebell, U. Löhnert, and D. Turner (2016). “Statistical retrieval of thin liquid cloud microphysical properties using ground-based infrared and microwave observations”. In: *Journal of Geophysical Research* 121.24. DOI: [10.1002/2016JD025667](https://doi.org/10.1002/2016JD025667)

Eigene Beteiligung: Die Idee zu dieser Studie basiert auf meiner Masterarbeit. Zusammen mit K. Ebell wurden die Strahlungstransportrechnungen durchgeführt und bei der Konzeption und Interpretation der Ergebnisse waren U. Löhnert und D. D. Turner beteiligt. Die Abbildungen und der erste Textentwurf wurden von mir erstellt.